

A Search for Cosmic Microwave Background Anisotropies on Arcminute Scales

Thesis by
Jack Sayers

In Partial Fulfillment of the Requirements
for the Degree of
Doctor of Philosophy

California Institute of Technology
Pasadena, California

2007

(Submitted December 5, 2007)

© 2007

Jack Sayers

All Rights Reserved

Abstract

This thesis describes the results of two sets of observations made in 2003 and 2004 using Bolocam from the Caltech Submillimeter Observatory (CSO), along with a description of the design and performance of the instrument. Bolocam is a large format camera consisting of 144 bolometers with an eight arcminute field of view at the CSO, and can be operated non-simultaneously at 1.1, 1.4, or 2.1 mm. All of the data described in this thesis was collected at 2.1 mm, where the individual beams are approximately one arcminute in size. The observations were made over a total of seventy-nine nights, and consisted of surveys of two science fields, Lynx and the Subaru/XMM Deep Field (SDS1), covering a total area of approximately 1 square degree. The noise properties of the maps are extremely uniform, with RMS variations in coverage of approximately 1.5% for twenty arcsecond map pixels. The point source sensitivity of the maps is approximately $100 \mu\text{K}_{CMB}$ per beam. Fluctuations in emission from the atmosphere limited the sensitivity of our measurements, and several algorithms designed to remove these fluctuations are described. These algorithms also removed astronomical flux, and simulations were used to determine the effect of this attenuation on a CMB power spectrum. Assuming a flat CMB band power in \mathcal{C}_ℓ , our data corresponds to an effective angular multipole of $\ell_{eff} = 5700$, with a $\text{FWHM}_\ell = 2800$. At these scales the CMB power spectrum is expected to be dominated by anisotropies induced by the Sunyaev-Zel'dovich effect (SZE), and have a reasonably flat spectrum. Our data is consistent with a band power of $\mathcal{C}_\ell = 0 \mu\text{K}_{CMB}^2$, and an upper limit of $\mathcal{C}_\ell < 755 \mu\text{K}_{CMB}^2$ at a confidence level of 90%. From this result we find that $\sigma_8 < 1.55$ at a confidence level of 90%.

Acknowledgments

My parents allowed me the freedom to pursue my interests when I was younger, and provided me with the support I needed to develop those interests. With their help, my brother Ryan and I became fascinated with math and science, and we were able to push each other in a never ending quest to see who was smarter. Along the way I was fortunate to have some great teachers, especially my high school physics teacher, Bernie Gordon. As an undergraduate at the Colorado School of Mines I was blessed with amazing professors, including Ed Cecil, Willy Hereman, and James McNeil. Numerous people at Caltech have directly helped me with this project. Kathy, Diana, and Bryanne have taken care of all the logistics, and the graduate students and postdocs in the Lange and Golwala groups have been there with advice and support. Also, the CSO staff and the Bolocam team have provided countless hours of help. Sunil has shown an unbelievable amount of patience for my questions and mistakes, and I couldn't have asked for a better advisor. And, of course, my wife Lindsey has loved and supported me throughout this process.



This thesis is dedicated to the memory of my brother Ryan (1982 - 2003)

Contents

Abstract	iii
Acknowledgments	iv
1 Introduction	1
1.1 A Brief History of Cosmology	1
1.2 Our Current Understanding of the Universe	7
1.3 The Sunyaev-Zel'dovich Effect and Cosmology	9
1.3.1 Background	9
1.3.2 Applications	12
1.3.3 Current Observational Status	16
1.3.4 Summary	18
2 The Bolocam Instrument	20
2.1 Overview	20
2.2 Cryogenics	20
2.2.1 Refrigerator	21
2.2.2 Dewar	21
2.3 Detectors	22
2.3.1 Overview	22
2.3.2 Characterization	24
2.4 Electronics	27
2.4.1 Design	28
2.5 Optics	31
2.5.1 Physical Components	31
2.5.2 Measured Performance	37
3 Observations and Performance	44
3.1 Observing Site	44

3.1.1	Telescope	44
3.1.2	Typical Conditions	44
3.1.3	Actual Conditions	46
3.2	Observing Strategy	48
3.2.1	Science Fields	48
3.2.2	Scan Pattern	50
3.3	Contrasts Between 2003 and 2004	51
3.4	Pointing Reconstruction	52
3.4.1	Relative Beam Offsets	52
3.4.2	Developing a Model of the Array Center Location	53
3.4.3	Uncertainties in the Pointing Model	56
3.5	Flux Calibration	59
3.5.1	Overall Theory	61
3.5.2	Relative Calibration of the Detectors	64
3.5.3	Absolute Calibration	67
3.5.4	Uncertainty in the Flux Calibration	70
3.5.5	Derived Source Fluxes	71
3.6	Beam Profiles	75
3.6.1	Overview	75
3.6.2	Consistency Tests	77
3.6.3	Results	81
4	Noise	85
4.1	Photon Noise	85
4.1.1	Theory	85
4.1.2	Measured Values	86
4.2	Bolometer and Electronics Noise	91
4.2.1	Bolometer Noise	91
4.2.2	Electronics Noise	92
4.3	Non-Optical Noise	95
4.4	Extra Noise During the 2004 Observing Season	97
4.5	Atmospheric Noise: Theory	97

4.5.1	Kolmogorov/Thin-Screen Model	100
4.5.2	Comparison to Data: Instantaneous Correlations	101
4.5.3	Comparison to Data: Time-Lagged Correlations	105
4.5.4	Comparison to Data: Summary	108
4.6	Atmospheric Noise: Removal	108
4.6.1	Average Template Subtraction	108
4.6.2	Wind Model	112
4.6.3	Higher-Order Template Subtraction	112
4.6.4	Adaptive Principal Component Analysis (PCA)	117
4.6.5	Nearest-Neighbor Bolometer Correlations	117
4.7	Sensitivity Losses Due to Correlations and Atmospheric Noise	119
4.8	Atmospheric Noise as a Function of Atmospheric Opacity	125
4.9	Summary of Atmospheric Noise	127
5	Data Processing	129
5.1	Merging and Parsing the Data Time-Streams	129
5.2	Filtering and Down-Sampling	130
5.3	Noise Removal	131
5.3.1	Observations of Bright Point-Like Sources	134
5.3.2	Observations of Science Fields	135
5.4	Map Making	135
5.4.1	Least Squares Map Making Theory	135
5.4.2	The Bolocam Algorithm: Theory	137
5.4.3	The Bolocam Algorithm: Implementation	141
5.5	Transfer Functions	144
5.6	Optimal Sky Subtraction	150
5.7	Final Map Properties	153
5.7.1	Noise PSDs	154
5.7.2	Astronomical Signal Attenuation	154
5.7.3	Noise from Astronomical Sources	157
6	Science Analysis	166
6.1	Procedure	166

6.2	CMB Anisotropy Results	171
6.3	SZE-Induced CMB Anisotropy Results	175
6.4	Conclusions	178
7	Other Bolocam Science	181
7.1	Surveys for Dusty Submillimeter Galaxies	181
7.2	Molecular Cloud Surveys	183
7.3	Targeted Cluster Observations	183
	Bibliography	187
A	Astronomical Flux and Surface Brightness Conversion Factors	209
B	Data Synchronization	211
B.1	Data Acquisition System Multiplexer	211
B.2	Aligning the Telescope and DAS Computer Data Streams	214
B.2.1	Results	214
B.2.2	Details of the Simulation	216
C	Computing Power Spectra and Cross Power Spectra	218
D	Atmospheric Noise Removal Algorithms	222
D.1	Average/Planar/Quadratic Subtraction	222
D.2	Adaptive PCA Subtraction	223
E	Data Processing: Signal Attenuation Versus Signal Amplitude	227
E.1	Theory	227
E.2	Results From Simulations	229
F	Algorithm for Calculating An Excess Map Variance	234

List of Figures

1.1	Hubble's velocity versus distance plot	2
1.2	Primordial light element abundances	3
1.3	COBE spectrum of the CMB	4
1.4	Current CMB power spectrum measurements	6
1.5	Spectral shift caused by the SZE	11
1.6	SZE distortion of the CMB	12
1.7	Cosmology with the SZE	15
1.8	SZE Image of CL0016+1609	17
1.9	SuZIE II cluster spectra	18
2.1	Bolocam refrigerator	22
2.2	The Bolocam dewar	23
2.3	Photograph of the Bolocam detector array	23
2.4	Mapping speed versus bolometer thermal conductance	26
2.5	Bolometer parameters	27
2.6	Simplified schematic of the Bolocam electronics	28
2.7	Photograph of the Bolocam dewar	30
2.8	Integrating cavity	32
2.9	The Bolocam horn-plate	32
2.10	An image of Bolocam mounted at the CSO	34
2.11	Schematic of Bolocam optics box	35
2.12	Bolocam optical system	36
2.13	Bolocam spectral transmission	39
2.14	Optical efficiency	41
2.15	Bolocam beam profiles at various points in the optics	43
3.1	The Caltech Submillimeter Observatory	45
3.2	Atmospheric opacity comparison	46
3.3	Observed atmospheric opacity	49

3.4	Scan speed comparison	52
3.5	Detector beam locations relative to the array center	54
3.6	Residual pointing error versus polynomial order of fit	57
3.7	Final pointing model	58
3.8	Pointing residual versus time of day	59
3.9	Summary of the uncertainty in the pointing model	61
3.10	Relative flux calibration determined from atmospheric emission	66
3.11	Contrasts in relative calibration derived from point versus beam filling sources	68
3.12	Planet temperatures and Bolocam transmission	71
3.13	Absolute flux calibration versus lockin DC output	72
3.14	Difference in beam areas derived from different planets	79
3.15	Histogram of individual bolometer beam areas	82
3.16	Bolocam beam profile	83
3.17	Bolocam beam contour plots	84
4.1	Measured optical loading from inside the dewar	88
4.2	Optical loading from the telescope and optics box	89
4.3	PSD of read-out electronics	93
4.4	PSD of a typical observation made from the CSO	96
4.5	PSD of the dark bolometers	98
4.6	Comparison of 2003 and 2004 time-streams	99
4.7	Lay-Halverson atmospheric model	101
4.8	Correlation versus separation for atmospheric emission	103
4.9	Time-stream correlations versus bolometer separation	104
4.10	Fits of atmospheric model to data	105
4.11	Fits of time-lagged correlations versus bolometer angle	107
4.12	Data before and after average sky subtraction	110
4.13	PSD before and after subtracting atmospheric noise	111
4.14	Results of atmospheric noise removal after accounting for wind velocity . .	113
4.15	Comparison of time-stream PSDs for higher-order atmospheric noise removal	115
4.16	Comparison of map-space PSDs for higher-order atmospheric noise removal	116

4.17	Comparison of time-stream PSDs for quadratic and PCA atmospheric noise removal	118
4.18	Separation of bolometer pairs with highly correlated time-streams	119
4.19	Cross power spectra for single observations	120
4.20	Nearest neighbor bolometer pair correlations before and after sky subtraction	121
4.21	Non-nearest neighbor bolometer pair correlations	122
4.22	Map PSDs from simulated data realizations	124
4.23	Sensitivity versus atmospheric opacity	126
5.1	Lockin filter profiles	132
5.2	Pre-down-sampled time-stream PSD showing 60 Hz pickup	133
5.3	Map coverage	142
5.4	Map-space PSDs for single observations	144
5.5	Measured PDF for the map-space PSD of a single observation	145
5.6	Transfer function, RA scan observations	147
5.7	Transfer function, dec scan observations	148
5.8	Single observation transfer functions	150
5.9	Sky subtraction figure of merit (FOM)	152
5.10	Map-space PSDs of final maps	155
5.11	Noise properties of final maps	156
5.12	Astronomical signal attenuation in final maps	158
5.13	Azimuthally averaged signal attenuation in the final maps	159
5.14	Galactic dust emission maps	160
5.15	Map-space PSD of the dust emission	161
5.16	Power spectra of various astronomical signals	165
6.1	Bayesian likelihood of CMB amplitude	168
6.2	CMB amplitude confidence intervals	171
6.3	CMB amplitude confidence belts for each science field for each observing season	172
6.4	Final CMB amplitude confidence belts	174
6.5	Band power window function	175
6.6	Comparison to other results	176
6.7	Final SZE-induced CMB amplitude confidence belts	178

6.8	Various analytic and simulated SZE spectra	179
7.1	Lockman Hole survey	182
7.2	Differential number counts from Lockman Hole survey	182
7.3	Molecular cloud maps	184
7.4	Signal attenuation for targeted cluster observations	185
7.5	Targeted cluster images	186
B.1	Scatter plot of time offsets for capped observations	212
B.2	Time offset versus bolometer angle for capped observations	213
C.1	Relative cross power spectra versus relative amplitude of correlated signal	220
D.1	PSDs of the templates for quadratic sky subtraction	224
D.2	Comparison of the average sky subtraction template to the leading order adaptive PCA basis vector	226
E.1	Change in atmospheric noise removal as a function of signal amplitude	230
E.2	Histogram of the change in the atmospheric noise correlation coefficients for two different signal amplitudes	231
E.3	Transfer function of the Bolocam data processing	233

List of Tables

2.1	Bolocam optical filters	37
2.2	Summary of Bolocam optical properties	40
3.1	Observing efficiencies	47
3.2	Sensitivity of various scan speeds	51
3.3	Centroiding uncertainty for pointing calibrators	55
3.4	Summary of the uncertainties in the pointing model	60
3.5	Relative calibration errors	66
3.6	Flux calibration uncertainties	73
3.7	Derived fluxes	74
3.8	Deviations in planets from ideal point sources	76
3.9	Consistency checks on beam areas	77
3.10	Full list of individual bolometer beam areas	78
3.11	Statistics on beam areas	81
4.1	Summary of optical loading	90
4.2	Summary of optical, bolometer, and electronics noise	95
4.3	Comparison of observed noise to ideal noise	97
4.4	Uncertainty on CMB amplitude from various simulations	125
5.1	Effective bandwidth of the transfer function	150
5.2	Optimal sky subtraction for each science field	152
5.3	Effective constant band power of various astronomical signals	164
6.1	SZE-induced CMB anisotropy results	180
B.1	Comparison of simulated and real scan data	217
E.1	Change in atmospheric noise removal as a function of signal amplitude	230

Chapter 1 Introduction

Cosmology involves studying the global properties of the universe. Fundamentally, cosmology is concerned with understanding what type of matter/energy composes our universe, along with how this matter/energy has been distributed throughout history. Additionally, cosmology attempts to predict how the distribution of matter/energy will evolve in the future.

1.1 A Brief History of Cosmology

Modern cosmology began with the development of the General Theory of Relativity in 1915 by Albert Einstein, which enabled construction of self-consistent models of the entire universe [85]. If we assume that the universe is isotropic and homogeneous on the largest scales¹, then the Robertson-Walker metric describes the evolution of the universe, with

$$\frac{\ddot{a}(t)}{a(t)} = \frac{-4\pi G}{3} \left(\rho + \frac{3p}{c^2} \right) + \frac{\Lambda}{3} \quad (1.1)$$

and

$$\left(\frac{\dot{a}(t)}{a(t)} \right)^2 = \frac{8\pi G\rho + \Lambda}{3} - \frac{c^2\kappa}{a(t)^2}, \quad (1.2)$$

where G is the gravitational constant, ρ is the density of the matter and radiation in the universe, p is the total pressure of this matter and radiation², κ is the curvature of the universe, Λ is the cosmological constant, and $a(t)$ is the scale factor of the universe at time t . In general, the solution satisfying these equations, $a(t)$, will not be static, so the universe will be either expanding or contracting. In 1929 Edwin Hubble provided the first observational evidence for an expanding universe, when he showed that all extra-galactic nebulae are moving away from our galaxy with a velocity proportional to their distance from us [66]. See Figure 1.1. This result is known as Hubble's Law, and the recessional

¹This assumption is known as the cosmological principle.

²The pressure is assumed to be of the form $p = w\rho c^2$. For non-relativistic particles, like baryons, $w = 0$ and for relativistic particles, like photons, $w = 1/3$. For a cosmological constant, w is defined to be equal to -1. The most recent results from the Wilkinson Microwave Anisotropy Probe (WMAP) suggest that the dark energy equation of state, w , is close to -1 [132].

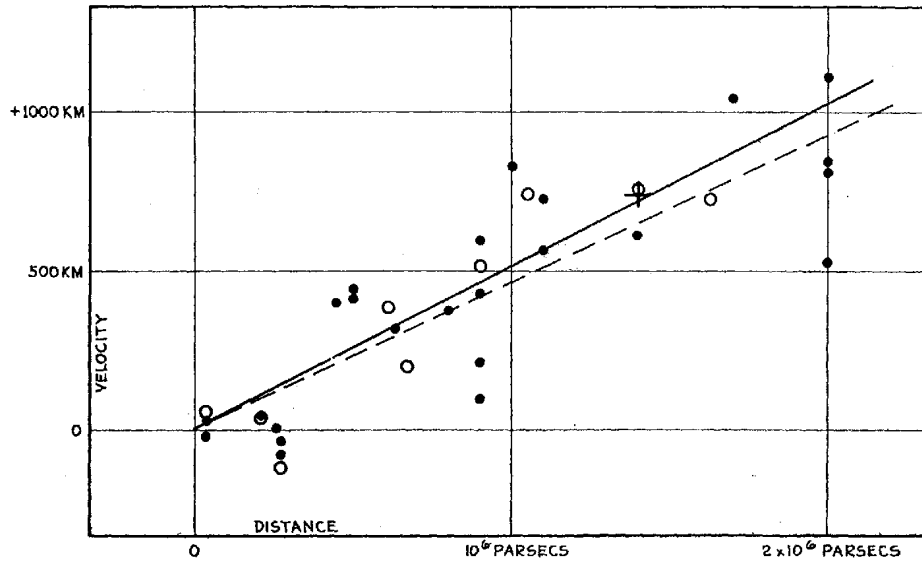


Figure 1.1: Hubble's velocity versus distance relation for extra-galactic nebulae. Figure taken from Hubble [66].

velocities are given by Hubble's constant, H_0 , which is $\simeq 70 \text{ km s}^{-1} \text{ Mpc}^{-1}$.

In 1948 George Gamow and Ralph Alpher determined that the expanding universe must have been extremely hot in its early stages. They showed that the amount of hydrogen and helium in the present universe could be explained by big bang nucleosynthesis (BBN), through a series of reactions in the early universe [5]. Fred Hoyle and Roger Tayler, in 1964, determined from Gamow and Alpher's theory that the primordial abundance of helium should be near 24%, which is consistent with observed amounts [65]. The abundances of other light elements, including ^3He , D, and ^7Li , were predicted from the same theory by Robert Wagoner, Hoyle, and Fowler [151]. The BBN predicted abundances of these light elements have been confirmed observationally, and would be difficult to account for with stellar nucleosynthesis [99,137]. Additionally, the primordial abundances of these elements are sensitive to the number of baryons in the universe, and can be used to estimate the universal baryon density, Ω_b . See Figure 1.2. Of the four light elements, the abundance of D provides the best constraint on the baryon density because its post BBN evolution is simple and it is fairly sensitive to the number of baryons [137]. Currently, observations of high redshift, low metallicity quasar absorption line systems provide the best constraints on the D abundance, and show that the baryon density in the universe is less than 5% of the critical density required to close the universe [137].

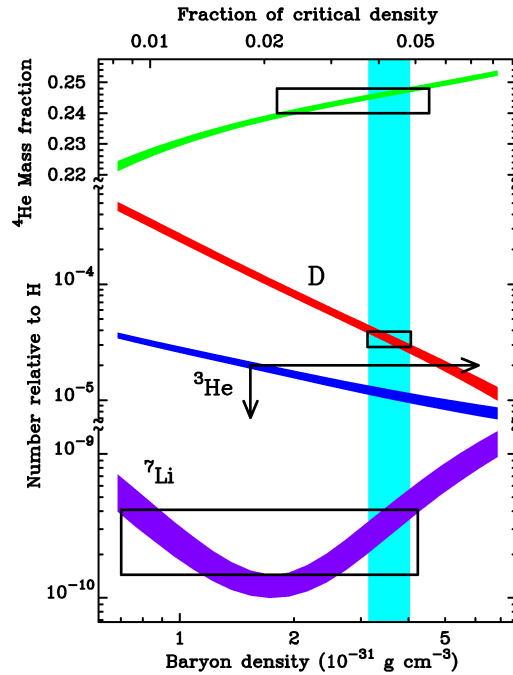


Figure 1.2: Primordial light element abundances as a function of the baryon density. The widths of the bands represent uncertainties in the predicted abundances, and the black boxes represent uncertainties on the measured values. Figure taken from Tytler, et al. [147].

In addition to developing the BBN theory, Gamow and Alpher also predicted a residual cosmic microwave background (CMB) radiation that is nearly isotropic with a blackbody temperature of $\simeq 5 \text{ K}$ [5]. This background radiation was finally detected in 1965 by Arno Penzias and Robert Wilson, with a temperature of approximately 3.5 K [103]³. With observational evidence supporting the predicted primordial element abundances, the CMB, and Hubble’s Law, the big bang theory has become part of the standard cosmological model.

However, the big bang theory does not provide a complete description of the universe. Although the universe is homogeneous on the largest scales, the presence of stars, galaxies, etc., clearly indicate that the universe is highly non-uniform on smaller scales. Therefore, there must have been slight departures from homogeneity in the early universe, which then developed under gravitational collapse. The first theory outlining the gravitational collapse of a bound object was given by James Jean in 1902, when he showed that to form a bound object a density perturbation must exceed the Jean’s length, $\Lambda_J = c_s / \sqrt{G\rho/\pi}$, where ρ is the density of the perturbation relative to the background and c_s is the speed of sound in the medium [85]. After some intervening developments that generalized Jean’s equations

³Subsequent measurements have shown that the temperature is 2.73 K [91]. See Figure 1.3.

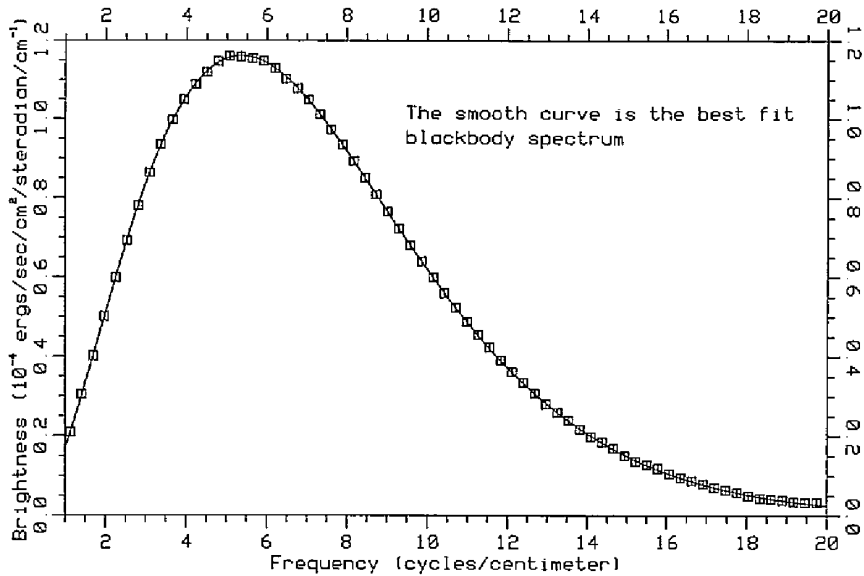


Figure 1.3: Spectrum of the CMB measured by COBE. Overlaid is a blackbody spectrum with a temperature of 2.73 K. Figure taken from Mather, et al. [91].

for an expanding medium, Igor Novikov was able to determine the amplitude of these perturbations. In 1964 he showed that if the modern bound structures are traced back to the time when the Jean's length is comparable to the horizon scale for the universe, then they must have had a density contrast of about 1 part in 10^4 [85]. Later, in the early 1970s, Yakov Zel'dovich and Edward Harrison independently showed that the power spectrum of these initial fluctuations should be approximately scale free, with $P(k) \propto k^n$ for $n = 1$ [62, 161]⁴.

Information about these primordial density fluctuations can be obtained from the CMB. Until the universe had cooled sufficiently so that neutral hydrogen could form, the mean free path of a CMB photon was extremely short. This occurred at a redshift of approximately 1100, when the universe was 300,000 years old, and is called the epoch of recombination. After this epoch, the universe became nearly transparent to CMB photons, which means that the CMB is a relatively unaltered picture of the universe at the time of recombination. Since the CMB photons were strongly coupled to the baryonic matter prior to recombination, the matter density fluctuations will produce fractional temperature fluctuations in the CMB, with a amplitude slightly less than the the fractional density fluctuations. In

⁴Prior to the three-year WMAP data, there was no evidence to suggest $n \neq 1$. However, the latest WMAP data shows that $n \simeq 0.95$, with $n < 1$ at a significance of approximately 3σ [132]. Additionally, the data slightly favor a running spectral index, rather than a simple power law [23, 132].

1967 Sachs and Wolfe predicted that the spectrum of the CMB will be flat at scales larger than a few degrees, if the primordial density fluctuations have the scale free spectrum given by Harrison and Zel'dovich [120]. These temperature anisotropies were finally detected in 1992 by the COBE experiment, with $\Delta T/T \simeq 10^{-5}$ on angular scales larger than seven degrees [90].

However, the amplitude of the CMB temperature fluctuations was expected to peak at an angular scale of approximately one degree, since photons separated by more than $\simeq 1$ degree would not have been able to interact prior to recombination. The first signs of this peak at an angular multipole of $\ell \simeq 200$ were detected by MAT/TOCO in 1999 [95], and later confirmed in 2000 by MAXIMA [61] and BOOMERANG [39]⁵. Then, in 2002, BOOMERANG [98] and DASI [60] were the first to detect the series of acoustic peaks in the CMB arising at smaller angular scales at multiples of the fundamental frequency at $\ell \simeq 200$. At even smaller scales, corresponding to $\ell \gtrsim 1000$, the CMB temperature fluctuations are averaged out by the finite length of the recombination epoch. This effect was first described in 1968 by Joseph Silk [130], and was detected by the Cosmic Background Imager (CBI) experiment in 2003 [129].

At angular multipoles above $\ell \simeq 2500$, corresponding to angular scales of less than a few arcminutes, there is thought to be a dramatic shift in the cause of the CMB anisotropies. While the CMB anisotropies on larger scales have not been significantly altered since the epoch of recombination, the vast majority of the anisotropies at these smaller scales have been imprinted on the CMB by the interaction between CMB photons and baryonic matter, specifically hot electrons in the intra-cluster medium. This effect was first described by Rashid Sunyaev and Yakov Zel'dovich in 1972 [139], and it produces anisotropies that do not have a thermal spectrum. To date, there have been tentative detections of the Sunyaev-Zel'dovich effect (SZE)-induced CMB anisotropies at 30 GHz by BIMA [37,38] and CBI [88], and a marginal detection at 150 GHz by ACBAR [78,79].

Clearly, the big bang model coupled with primordial density fluctuations has been successful in predicting a wide range of observed data. However, the big bang theory has no explanation for why the CMB is isotropic to one part in 100,000 on large scales that were not causally connected at the time of recombination. Since particles on these scales could

⁵WMAP has now measured this peak, with an uncertainty limited only by cosmic variance [63]. See Figure 1.4.

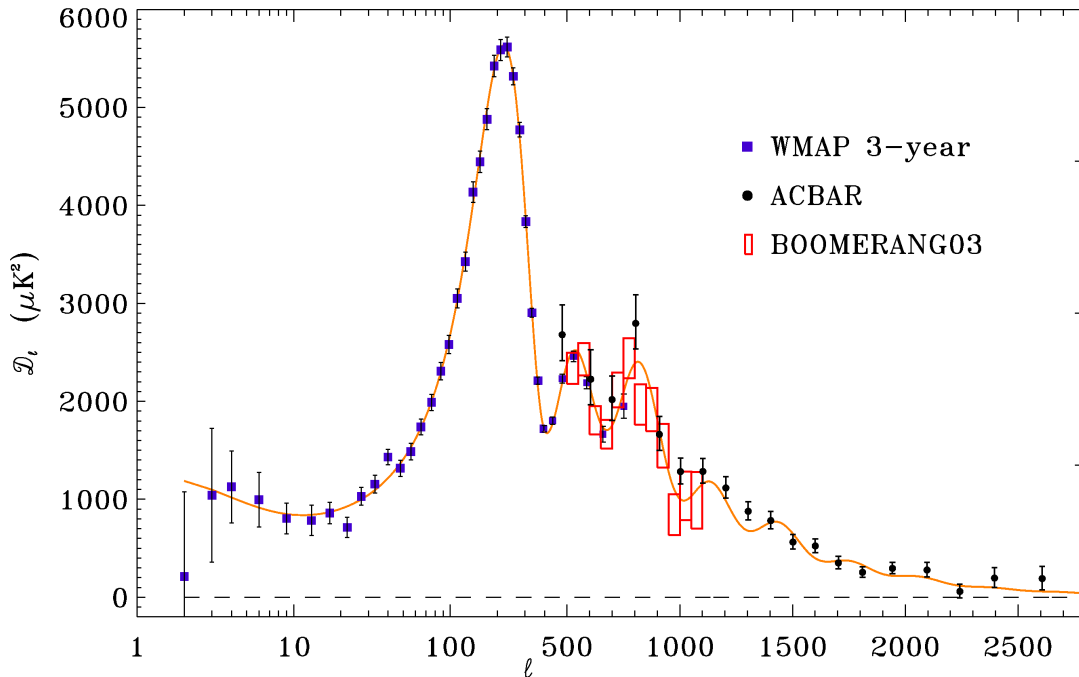


Figure 1.4: Current measurements of the CMB power spectrum, including data from the WMAP three-year release [63], the 2003 flight of BOOMERANG [69], and ACBAR [78]. Figure taken from Kuo, et al. [78].

not have interacted prior to recombination, there is no reason that they should be at the same temperature. Additionally, the matter/energy density, Ω , of the current universe is extremely close to the critical density, $\Omega = 1$.⁶ Since deviations from the critical density grow quickly as the universe evolves, this means that Ω must have been very finely tuned to a value of one in the early universe. Again, there is no reason why the matter/energy density of the early universe should be so close to the critical density. A solution to both of these problems was proposed by Alan Guth in 1981 [58]. In his theory, which is a modification of the standard big bang theory, the universe underwent an exponential expansion, or inflation, early in its history. Prior to inflation, the entire observable universe would have been causally connected, and the inflationary process would produce a nearly flat universe. Therefore, inflation accounts for the homogeneity of the universe on large scales, as well as the fact that the universe is flat or nearly flat. However, although inflation resolves the shortcomings of the standard big bang theory, there is still no direct observational evidence

⁶The critical density is the amount of matter/energy required in the absence of a cosmological constant to slow the expansion of the universe indefinitely without the universe re-collapsing. Additionally, the geometry of the universe will be flat (i.e., Euclidean) if $\Omega = 1$. $\Omega > 1$ will yield a closed or spherical universe, and $\Omega < 1$ will yield an open or hyperbolic universe.

supporting the theory of inflation.

Additionally, a complete model of the universe needs to describe the types of matter/energy that compose our universe. Initially, there was no reason to think that the universe contained anything other than baryonic matter. But, in 1933 Fritz Zwicky determined that the dynamics of the Coma cluster could only be accounted for if the majority of the mass in the cluster was a non-visible form of matter, or dark matter [163]. However, it was not until the mid 1970s, when observations of galaxies showed that their dynamics at large radii are also dominated by dark matter, that Zwicky's idea was widely accepted [113,149]. Several theories for dark matter were proposed, including baryonic dark matter, hot dark matter (HDM), and cold dark matter (CDM)⁷. Current observational evidence from the CMB and large scale structure show that the majority of the dark matter must be cold dark matter, and that the density of dark matter is approximately four to five times the density of baryonic matter in the universe [30, 132, 144]. Unfortunately, it is still unclear what particle(s) compose this cold dark matter. Additionally, in 1998, observations of distant supernovae showed that the expansion of the universe is accelerating [111]. Therefore, the universe contains some form of dark energy that has a negative pressure, and behaves similar to Einstein's cosmological constant, Λ . Recent CMB observations, combined with supernovae data, show that approximately 75% of matter/energy in the universe is dark energy [8, 112, 132].

1.2 Our Current Understanding of the Universe

Based on current observational data of big bang nucleosynthesis (BBN) [137], supernovae [8, 112], large scale structure (LSS) [30,144], and the cosmic microwave background (CMB) [78, 86, 132], a single model with several free parameters has emerged as the only viable theory of the universe. The model is based on general relativity, the big bang theory, a spectrum of primordial density fluctuations, and a period of inflation in the early universe. In its simplest form, this model predicts a flat universe composed of baryonic matter, cold dark matter, and a cosmological constant, with primordial density fluctuations described by a power law. The only parameters required to fit this model to the best observational data are: Ω_b , the density of baryonic matter relative to the critical density; Ω_m , the total matter density

⁷HDM is composed of relativistic massive particles like the neutrino, and CDM is composed of non-relativistic massive particles.

relative to the critical density; n_s , the spectral index of the primordial density fluctuations; $h \times 100 \text{ km sec}^{-1} \text{ Mpc}^{-1}$, the present day expansion rate of the universe; σ_8 , the amplitude of the density fluctuations; and τ , the optical depth to reionization⁸. Although additional parameters are not required to fit the data, the fit can be improved by including: Ω_Λ , the density of an unknown dark energy relative to the critical density; w , the equation of state of the dark energy; f_ν , the dark matter neutrino mass fraction; M_ν , the sum of the neutrino masses; α , running in n_s ; r , the ratio of tensor to scalar perturbations at $k = 0.002/\text{Mpc}$; and $\Delta_{\mathcal{R}}^2$, the amplitude of curvature perturbations as free parameters.

Regardless of the exact model chosen, several conclusions can be drawn about our universe. First, our universe is flat or nearly flat, and approximately 75% of the matter/energy is in the form of some dark energy that behaves similar to a cosmological constant. The remainder of the universe is composed of baryonic matter and dark matter, with approximately five times more dark matter than baryonic matter. Additionally, most of the dark matter is some form of cold dark matter, but a small ($\lesssim 5\%$) fraction is hot dark matter in the form of neutrinos. Finally, the spectrum of initial density perturbations appears to be slightly less than one, which is consistent with inflation.

The next logical step in verifying the standard cosmological model is to directly confirm the theory of inflation. Currently, this effort is focused on detecting the B-mode polarization signal in the CMB, which is produced by gravitational waves formed during inflation [70]. Several experiments are currently, or will soon begin, looking for this B-mode signal, including BICEP [157], Planck [145] PolarBeaR [105], Spider [133], and Clover [142]. Additionally, there is a large effort to understand the properties of dark matter and dark energy. These forms of matter/energy constitute more than 95% of our universe, yet little is known about either of them. In addition to the large number of observational experiments aimed at learning more about dark matter and dark energy, there are also some experiments attempting to directly detect dark matter particles (e.g., [4, 54]). Finally, a general goal of most cosmological observations is to improve the precision, or provide an independent confirmation, of the measured values of the cosmological parameters.

⁸Note that this simple model does include dark energy in the form of a cosmological constant. However, since the total energy density of the universe is equal to the critical density in this model, the density of the dark energy is constrained unambiguously by the values of Ω_b and Ω_m .

1.3 The Sunyaev-Zel'dovich Effect and Cosmology

One independent observational approach to learn more about the structure of the universe involves the SZE. SZE observations have been used to determine the value of the Hubble parameter without relying on the standard distance ladder approach [20, 107, 148], and can be used to constrain the values of σ_8 , Ω_m , Ω_Λ , and w . Additionally, the SZE is a powerful tool for understanding the largest bound objects in the universe, clusters of galaxies, at any redshift. For reference, excellent reviews of the SZE and its relevance to cosmology are given by Birkinshaw [15], Carlstrom et al. [26], and Carlstrom et al. [25].

1.3.1 Background

The thermal SZE⁹ involves the inverse Compton scattering of CMB photons with a distribution of hot electrons, causing a net increase in the energy of the photons [139]. Since the background CMB is redshifted along with the SZE-induced distortion, the relative amplitude of the distortion, $\Delta T_{CMB}/T_{CMB}$ is independent of redshift. On average, each scattering event increases the energy of the photon by $k_B T_e/m_e c^2$, where k_B is Boltzmann's constant, T_e is the average temperature of an electron, m_e is the electron mass, and c^2 is the speed of light [25]. In general, the SZE is mentioned in regards to a cluster of galaxies, since the intra-cluster medium (ICM) is filled with a diffuse plasma of electrons at temperatures of 10^7 to 10^8 K. Even in the most massive clusters, $\lesssim 1\%$ of the CMB photons that pass through the center of the cluster will be scattered [25], so the SZE will only produce a slight distortion to the CMB spectrum.

The distortion caused by the SZE is proportional to the Comptonization y parameter, which is a measure of the integral of the electron pressure along the line of sight and is described by

$$y = \frac{\sigma_T}{m_e c^2} \int dl n_e k_B T_e = \frac{\sigma_T}{m_e c^2} \int dl p_e, \quad (1.3)$$

where σ_T is the Thomson cross section, n_e is the electron density, and p_e is the electron pressure. Since the scattering process conserves photon number, the thermal spectrum of the CMB is distorted by the SZE; there is a negative temperature shift at low frequency and a positive temperature shift at high frequency. The cross-over point where there is no distortion of the CMB occurs at approximately 218 GHz. See Figure 1.5. Therefore, the

⁹Unless stated otherwise, SZE refers to the thermal SZE.

spectral dependence of the SZE is required in order to determine the fractional temperature shift induced in the CMB, and is given by

$$f(x) = x \frac{e^x + 1}{e^x - 1} - 4, \quad (1.4)$$

where $x = h\nu/k_B T_{CMB}$, h is Planck's constant, ν is the frequency, and $T_{CMB} = 2.73$ K is the temperature of the CMB. Combining Equations 1.3 and 1.4 the temperature shift caused by the SZE, ΔT_{CMB} , is

$$\frac{\Delta T_{CMB}}{T_{CMB}} = f(x)y. \quad (1.5)$$

Alternatively, the SZE distortion can be expressed as a change in the surface brightness of the CMB, ΔB_ν , with

$$\Delta B_\nu = \Delta T_{CMB} \left. \frac{dB_\nu}{dT} \right|_{T=T_{CMB}}. \quad (1.6)$$

Plots of the temperature distortion and surface brightness distortion caused by the SZE are given in Figure 1.6.

Additionally, since $k_B T_e / m_e c^2 \simeq 1/100$, treating the electrons classically leads to slight errors in the determination of ΔT_{CMB} . Including the relativistic effects results in a modification of $f(x)$ by $\delta(x, T_e)$, with

$$f_{rel}(x) = f(x)(1 + \delta(x, T_e)). \quad (1.7)$$

A good analytic approximation of $\delta(x, T_e)$ is given by Itoh, et al. [67]. The relative magnitude of these corrections depends on frequency, and can become significant near the null. However, the corrections are typically of order a few percent [25].

The kinetic SZE will also distort the CMB spectrum, and is due to a Doppler shift in the scattered CMB photons caused by the peculiar velocity of the cluster. Ironically, the distortion caused by the kinetic SZE has a thermal spectrum, in contrast to the non-thermal spectral distortion caused by the thermal SZE. The magnitude of the kinetic SZE is given by

$$\frac{\Delta T_{CMB}}{T_{CMB}} = - \left(\frac{v_{pec}}{c} \right) \int dl \sigma_T n_e, \quad (1.8)$$

where v_{pec} is the peculiar velocity of the cluster along the line of sight. For a realistic massive cluster, the kinetic SZE distortion is much smaller than the thermal SZE distortion, except

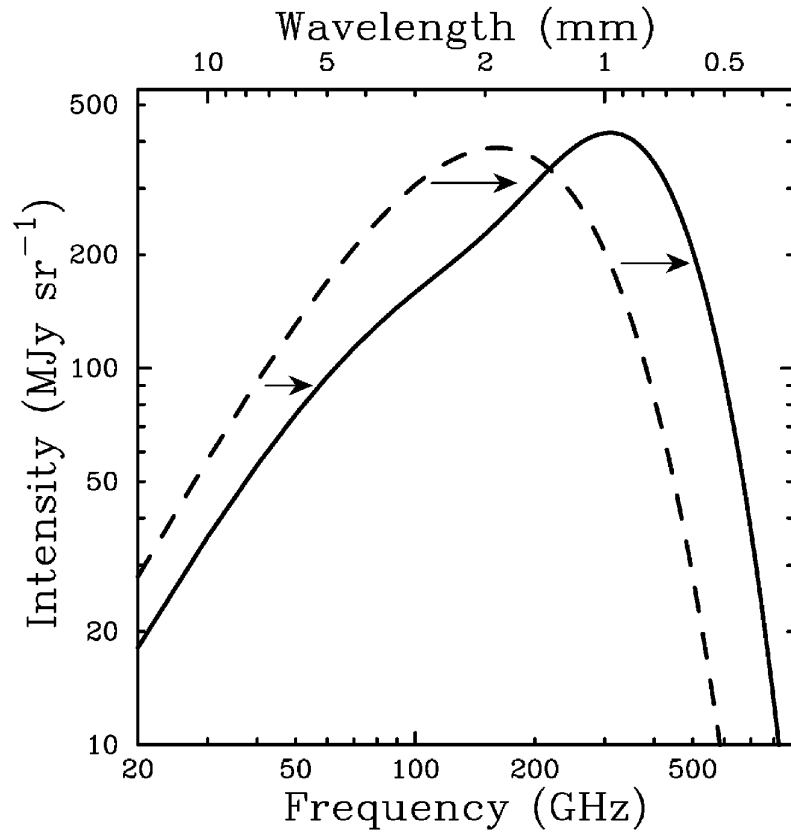


Figure 1.5: The spectral shift caused by the SZE. The undistorted thermal CMB spectrum is shown as a dashed line, and the SZE distorted CMB spectrum is shown as a solid line. A cluster approximately 1000 times more massive than a typical cluster was used in the calculation to increase the contrast. Figure taken from Carlstrom, et al. [25].

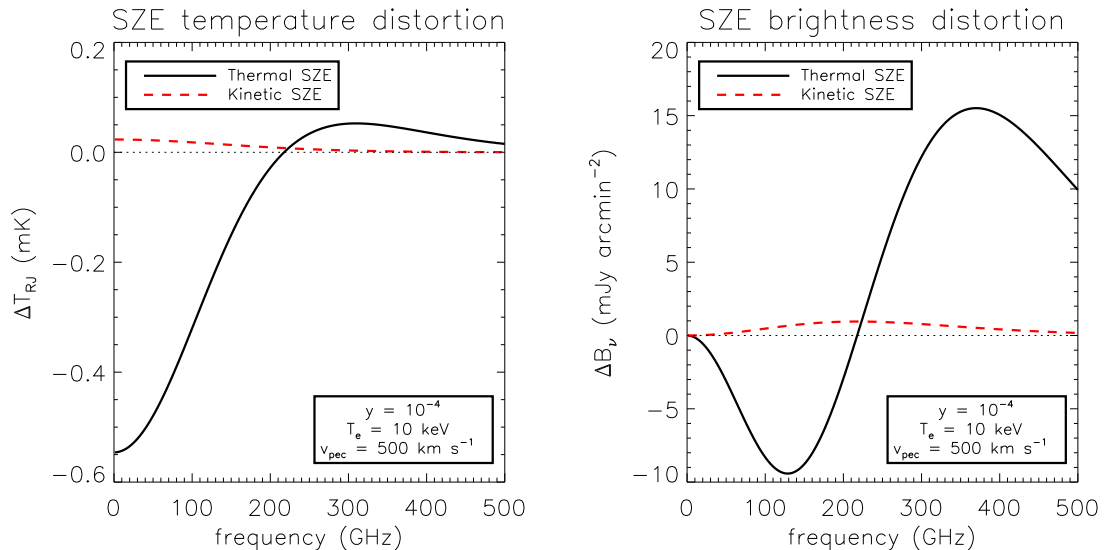


Figure 1.6: The thermal and kinetic SZE distortions of the CMB caused by a typical massive cluster with $y = 10^{-4}$, $k_B T_e = 10^4$ keV, and $v_{pec} = 500$ km/s. The solid black curve represents the thermal SZE, and the dashed red curve represents the kinetic SZE. The plot on the left shows the Rayleigh-Jeans temperature of the SZE, and the plot on the right shows the surface brightness of the SZE.

near the null in the thermal SZE. See Figure 1.6.

1.3.2 Applications

The SZE can be exploited in several ways to learn more about the properties of our universe. First, the thermal SZE signal, when combined with X-ray data, can be used to determine the Hubble constant, H_0 . SZE data can also be used to determine the baryonic mass fraction in the cluster, f_B , which is an extremely useful parameter for understanding the physics of clusters. The evolution of f_B as a function of redshift can also be used to place constraints on Ω_m and Ω_Λ . Additionally, kinetic SZE measurements are the only known way to determine large-scale peculiar velocities at high redshift. Finally, large surveys for the SZE can be used to constrain Ω_m , Ω_Λ , w , and σ_8 .

Thermal bremsstrahlung radiation is produced in clusters, and can be observed as an X-ray surface brightness given by

$$S_X = \frac{1}{4\pi(1+z)^3} \int dl n_e^2 \Lambda_e, \quad (1.9)$$

where z is the redshift to the cluster, n_e is the electron density, and Λ_e is the X-ray spectral

emission of the ICM [15]. Since the X-ray signal is proportional to the density of the ICM squared, while the SZE signal is proportional to the density of the ICM, the two measurements can be combined to estimate the physical scale of the cluster along the line of sight¹⁰. If we assume the cluster is spherically symmetric, the scale of the cluster along the line of sight will be equal to the angular scale of the cluster, $D_A\theta_c$, where D_A is the angular diameter distance and θ_c is the observed angular scale of the cluster. Although clusters are not in general spherically symmetric, numerical simulations have shown that there is no systematic bias in the SZE/X-ray estimation of the cluster scale when averaged over a large sample of clusters [138]. If we combine the assumption of spherical symmetry with Equations 1.5 and 1.9, then the angular diameter distance of the cluster is given by

$$D_A \propto \frac{1}{\theta_c} \left(\frac{\Delta T_{CMB}^2 \Lambda_e}{S_X T_e^2} \right), \quad (1.10)$$

which can be used to estimate the value of the Hubble constant since D_A is inversely proportional to H_0 .

The SZE signal is proportional to the number density of electrons in the ICM multiplied by the temperature of the electrons. Therefore, if the temperature is known, the SZE signal can be used to determine the amount of baryonic matter in the ICM. Additionally, the total mass of the cluster can be determined using weak or strong lensing data, or from knowledge of the distribution and temperature of the electrons under the assumption that the cluster is in hydrostatic equilibrium. Combining these measurements of the baryonic mass in the ICM and the total mass of the cluster gives an estimate of the baryonic mass fraction, f_B , for the cluster. However, f_B cannot be directly compared to the universal baryon mass fraction, Ω_b/Ω_m , because some baryons ($\simeq 15\%$) are lost during the cluster formation process, and some baryons within the cluster ($\simeq 10\%$) are contained in stars instead of the ICM. The exact relation between f_B and Ω_b/Ω_m is not well understood, but the value of f_B does provide a good test of the validity of cluster simulations [43]. Fortunately, the evolution of f_B as a function of redshift does not depend on the ratio of f_B to the universal baryon mass fraction, and can be used to constrain the values of Ω_m and Ω_Λ [122].

Since the magnitude of the kinetic SZE is proportional to the peculiar velocity of the

¹⁰This estimate relies on the assumption that the ICM is fairly uniform (i.e., $\langle n_e^2 \rangle \simeq \langle n_e \rangle^2$). If the ICM is significantly clumpy, then the length scale of the cluster along the line of sight will be underestimated by a factor of $\langle n_e^2 \rangle / \langle n_e \rangle^2$ [25].

cluster, measurements of the kinetic SZE provide a method to constrain velocity fields on large scales at high redshifts. These velocity fields provide a probe of gravitation perturbations to the otherwise uniform expansion of the universe [26]. Unfortunately, the kinetic SZE signal has the same spectrum as the background CMB, so it is difficult to distinguish from CMB anisotropies. Additionally, the kinetic SZE is much smaller in magnitude than the thermal SZE, except near the thermal null at 218 GHz. Therefore, it is unlikely that an accurate measurement of the peculiar velocity can be made for a single cluster, although it should be possible to determine large-scale peculiar velocities by averaging over many clusters [25].

Large, untargeted surveys for the SZE also provide a method to constrain cosmological parameters. Since the SZE signal is roughly proportional to the total mass of a cluster, and the surface brightness of the SZE signal is independent of the cluster redshift, the SZE offers an ideal tool to conduct a mass limited survey to high redshift¹¹. Such a survey is an excellent way to constrain Ω_m , since the formation history of large scale structure is sensitive to the density of matter in the universe. SZE number counts can also be used to constrain the values of Ω_Λ , w , and σ_8 [25]. See Figure 1.7. Additionally, unresolved objects in SZE surveys will produce anisotropies in the CMB that are expected to dominate the CMB power spectrum at small angular scales corresponding to angular multipoles above $\ell \simeq 2500$. The overall normalization of these SZE-induced CMB anisotropies is extremely sensitive to σ_8 , and can be used to constrain the value of this cosmological parameter [73]. See Figure 1.7.

Although the SZE provides a great tool for understanding the properties of our universe, it does present some observational and theoretical challenges. First, the signal is extremely small, with $\Delta T_{CMB} \lesssim 1$ mK for even the most massive clusters. Additionally, there is a significant amount of contamination from radio point sources at low frequencies ($\nu \lesssim 150$ GHz), and a significant amount of contamination from dusty submillimeter sources at high frequencies ($\nu \gtrsim 150$ GHz). Also, since clusters are dense, collapsed objects, the physics that describe them are complex and nonlinear. Since analysis of observational SZE

¹¹In practice, the SZE surface brightness depends strongly on the cluster core radius and density, and is not a good characterization of the total cluster mass. The total integrated flux of the cluster does provide a good measurement of the mass of the cluster, but it is not independent of redshift due to the factor of $1/D_A^2$. However, this angular diameter distance factor is largely canceled out by the evolution of the cluster virial temperature with redshift, since clusters that form earlier in the universe will be denser and hotter. The net result is a mass selection function that varies by less than a factor of two for redshifts between $z \simeq 0.1$ and $z \simeq 3.0$ [25].

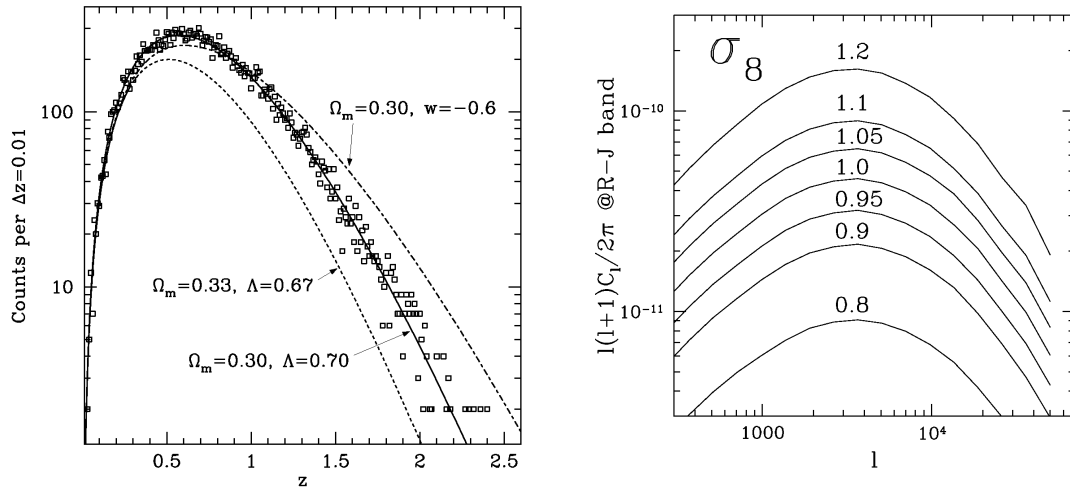


Figure 1.7: Examples of the dependence of two SZE observables as a function of some of the cosmological parameters. The figure on the left shows the number of clusters per redshift bin expected for a 4000-square-degree South Pole Telescope (SPT) survey with idealized sensitivity for three different sets of cosmological parameters. The boxes represent appropriate data points for such a survey. The figure was created by Gilbert Holder and was taken from Ruhl, et al. [116]. The figure on the right shows the SZE-induced CMB power spectrum as a function of σ_8 . The normalization of the power spectrum scales roughly as σ_8^7 , making it an extremely sensitive probe of this cosmological parameter. Figure taken from Komatsu and Seljak [73].

data generally relies on modeling the cluster profile and evolution, a detailed understanding of cluster physics is critical to properly interpret SZE data. Finally, large dishes or interferometers are required to achieve the angular resolution necessary to observe the SZE, which means ground-based observatories are the only practical way to collect SZE data. Consequently, the observations are subject to noise caused by variations in emission from the atmosphere and ground.

1.3.3 Current Observational Status

To date, images of forty-six clusters have been used to estimate the value of H_0 . Thirty-eight of these clusters have been imaged by the OVRO and/or BIMA interferometers at 30 GHz with a synthesized beam of $\gtrsim 1$ arcminute, seven have been imaged at 30 GHz with a synthesized beam of $\simeq 5$ arcminutes by the CBI interferometer, and one was imaged at 15 GHz with a $\gtrsim 2$ arcminute synthesized beam using the Ryle telescope [20,123,148]¹². The OVRO/BIMA data was compared to X-ray observations made with Chandra, (Figure 1.8) while the CBI images relied on X-ray data collected by ROSAT, ASCA, and BeppoSAX. The OVRO/BIMA observations produce a measurement of $H_0 = 76.9_{-8.7}^{+10.7}$ km s⁻¹ Mpc⁻¹, with the uncertainties dominated by systematics in the X-ray temperature calibration and the SZE flux calibration¹³.

The thirty-eight clusters observed with OVRO/BIMA have also been used to calculate the baryonic mass fraction, f_B , in the ICM gas [81]. Similar results were obtained for three different cluster profile models, with $f_B = 0.12_{-25\%}^{+\simeq 10\%}$, which is consistent with baryon fractions determined from X-ray observations of the same clusters. Combining the SZE and X-ray data yields an estimate of the ratio of f_B to the universal baryon fraction, with $f_B/(\Omega_b/\Omega_m) = 0.68_{-0.16}^{+0.10}$. This ratio is consistent with the results of cluster simulations that include radiative cooling and star formation. Additionally, the evolution of f_B as a function of redshift was used to estimate the value of Ω_m for a flat universe with a cosmological constant. The results are consistent with the WMAP value of Ω_m , and inconsistent with a matter-dominated universe ($\Omega_m = 1$).

The spectrum of the SZE signal has been measured in three frequency bands for eleven

¹²Additionally, one other cluster has been imaged with the Ryle telescope, and one cluster has been imaged at a high signal-to-noise ratio by the Arcminute Microkelvin Imager at 15 GHz [6,32].

¹³For comparison, the Hubble Space Telescope (HST) Key Project determined $H_0 = 72 \pm 8$ km s⁻¹ Mpc⁻¹ [47].

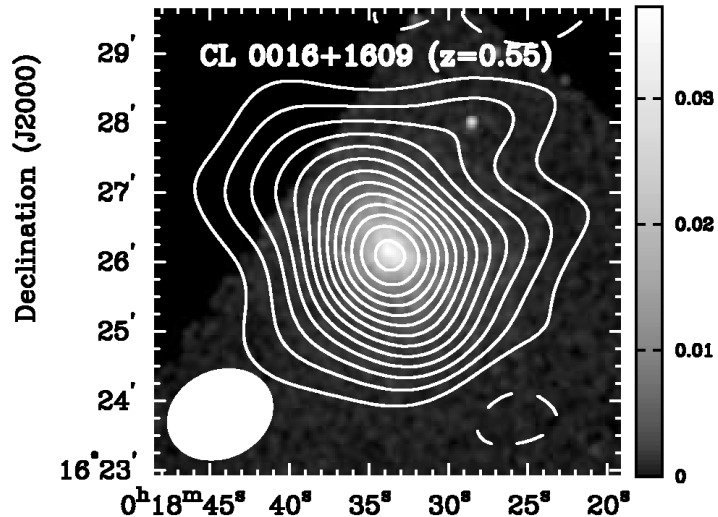


Figure 1.8: SZE decrement contours measured by OVRO/BIMA overlaid on the X-ray image produced by Chandra for CL0016+1609. The SZE contours correspond to $+1, -1, -2, -3, -4, \dots$ times the RMS noise in the image. The X-ray image shows the background subtracted surface brightness in the 0.7 - 7 keV band in units of counts per 1.97 arcsecond pixel. The full-width half-maximum of the synthesized OVRO/BIMA beam is overlaid in the lower left corner. Figure taken from [20].

clusters by the SuZIE II experiment [11, 12]¹⁴. SuZIE II observed with bands centered at 145, 221, and 355 GHz to measure the thermal SZE decrement, null, and increment, respectively. Combining the data from these bands allows the thermal SZE signal to be distinguished from the kinetic SZE. The kinetic SZE data was used to determine the peculiar velocities of the clusters, and set a 95% confidence level upper limit of 1410 km/s for the bulk flow of the universe at redshifts of $0.2 \lesssim z \lesssim 0.5$ [12]¹⁵. See Figure 1.9.

To date, there have been no detections of previously unknown clusters using the SZE. However, three experiments that recently began collecting data, APEX-SZ, ACT, and SPT, should each detect a large number of new clusters [7, 74, 116]. APEX-SZ and SPT plan surveys to a noise level of approximately $10 \mu K_{CMB}$ per arcminute size pixel over 200 and 4000 square degrees, respectively, and ACT plans to survey 200 square degrees to a noise level of around $2 \mu K_{CMB}$ per 1.7 arcminute pixel. At these sensitivities, APEX-SZ and ACT would detect of order 1000 clusters, and SPT would detect several thousand clusters. Additionally, several experiments have conducted SZE surveys that have produced marginal

¹⁴The SuZIE group has measured the SZE signal in fifteen clusters, but only eleven of the clusters were measured with enough sensitivity in the high-frequency channels to determine a peculiar velocity [11].

¹⁵This upper limit is based on the peculiar velocities determined from the six clusters described in 2003 by Benson, et al. [12].

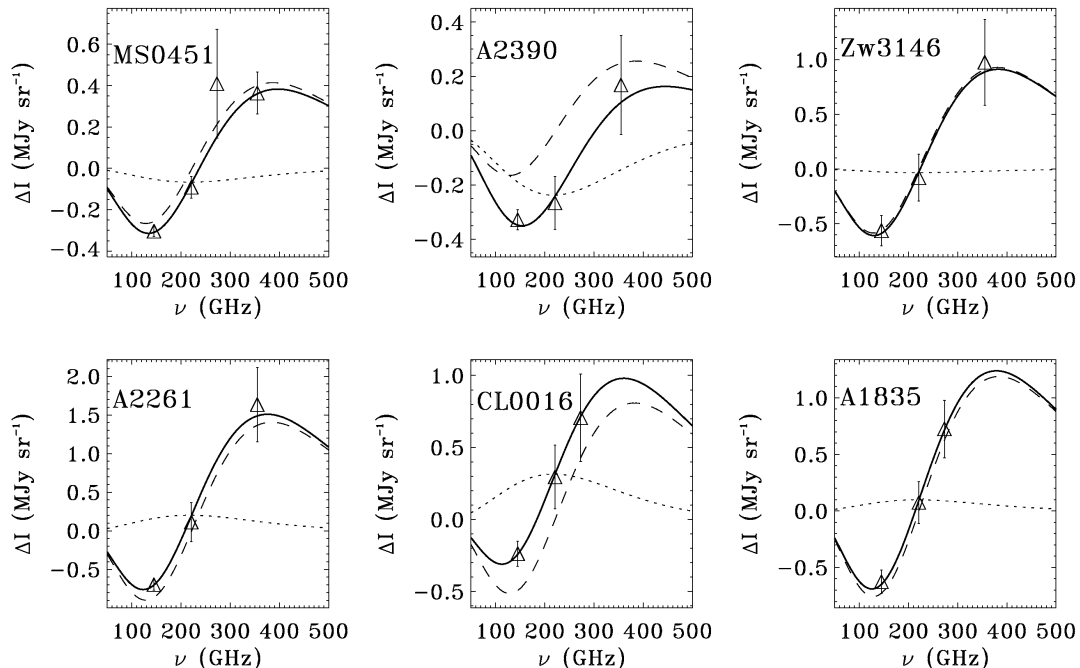


Figure 1.9: Spectra of six clusters observed by SuZIE II. The dashed curve is the best fit thermal SZE spectrum, the dotted curve is the best fit kinetic SZE spectrum, and the solid curve is the best fit total SZE spectrum. Figure taken from Benson, et al. [12].

detections of the SZE induced anisotropies in the CMB. At 30 GHz CBI has measured an excess CMB power between $\ell = 2000$ and $\ell = 3500$ at a significance of 3.1σ [88]. ACBAR, at 150 GHz and $2000 < \ell < 3000$, has also measured an excess power of $51 \pm 42 \mu\text{K}_{CMB}^2$ [78]. Finally, at 30 GHz, BIMA/OVRO has measured a CMB anisotropy of $220_{-120}^{+140} \mu\text{K}_{CMB}^2$ at an angular multipole of $\ell = 5237$ [37]. These marginal anisotropy detections have been used to constrain cosmological parameters; the CBI data is consistent with $\sigma_8 \simeq 1$ [21], and the BIMA/OVRO data measure $\sigma_8 = 1.03_{-0.29}^{+0.20}$ [37]. The upcoming APEX-SZ, ACT, and SPT experiments should measure the SZE-induced CMB anisotropies to high precision, and will be able to place tight constraints on σ_8 and Ω_m [116].

1.3.4 Summary

Although the theory for the SZE was developed in the early 1970s, the observational sensitivity required to detect the SZE signal was not achieved until the 1990s. Since then, SZE observations have been used to place meaningful constraints on several cosmological parameters, although these constraints are still inferior to those made with other observa-

tional techniques. However, the next generation of SZE experiments promises to improve the uncertainty on measurements of Ω_m , Ω_Λ , w , and σ_8 .

Chapter 2 The Bolocam Instrument

2.1 Overview

Bolocam, along with MAMBO, SCUBA, and SHARC II, represents the first generation of millimeter/submillimeter cameras with $\gtrsim 100$ background-limited detectors [41, 64, 77]. The Bolocam receiver consists of 144 Si_3N_4 micro-mesh bolometers. The camera can be operated non-simultaneously at 140, 220, or 275 GHz (2.1, 1.4, or 1.1 mm), where each band has a fractional bandwidth of $\sim 20\%$. With an instantaneous field of view much larger than the size of an individual detector beam, Bolocam is well suited for observations requiring wide angular coverage, including the blank field surveys for galaxy clusters described in this thesis [49–51, 59].

When I joined the Bolocam collaboration in late 2002 the instrument was in a highly refined state, and several engineering observations had already been made at the CSO. The first set of science data was collected in January 2003, and Bolocam was commissioned as a facility instrument at the CSO in late 2003. I participated in the final commissioning of Bolocam, including: measuring the optical transmission spectrum of each bolometer in the system, diagnosing and correcting the large optical load originating inside the dewar, upgrading the electronics cables, and making slight modifications to the 4 K stage to reduce the liquid helium consumption of the system. Additionally, I have assisted with several of the minor upgrades and maintenance that Bolocam has required since being commissioned at the CSO.

2.2 Cryogenics

The cryogenic system was designed to optimize the sensitivity of Bolocam, which requires 1) cooling the bolometers to $\lesssim 270$ mK to maximize their sensitivity and 2) cooling the junction gate field-effect transistors (JFETs), which are used to read out the bolometer signals, to $\simeq 135$ K in order to optimize their noise performance.

2.2.1 Refrigerator

We utilized a three-stage (^4He , ^3He , ^3He), closed-cycle sorption refrigerator in order to achieve the first goal of cooling the bolometers to $\lesssim 270$ mK. See Figure 2.1. This refrigerator was custom built for Bolocam by Chase Cryogenics, and has an ultra-cold (UC) stage which operates at 250 mK and an inter-cooler (IC) stage which operates at 360 mK. Prior to cycling, the helium in each stage of the refrigerator is absorbed in charcoal. Each stage is operated by heating the charcoal to desorb the helium that is condensed in a still, followed by cooling the charcoal with a gas gap heat switch to create a pump on the helium. This pump reduces the vapor pressure of the liquid helium, which reduces the temperature of the liquid. The ^4He stage is operated first, followed by the IC ^3He stage, and then the UC ^3He stage. The ^4He stage relies on the 4K LHe bath as a condensation point for the helium being desorbed by the charcoal, and the IC and UC stages each rely on the ^4He stage as a condensation point. This complicated design was utilized to allow operation from a LHe bath at ambient pressure. More details of the operation of the refrigerator can be found in two papers by Bhatia, et al. [13,14]. It takes approximately two hours to cycle the refrigerator, and the hold time is slightly more than 24 hours. The IC stage is used to thermally buffer the UC stage from the helium bath by intercepting the mechanical supports from the UC stage along with the bolometer and thermometry wiring. Thin, cylindrical vespel columns are used to mechanically support the IC stage from the helium bath, and to support the UC stage from the IC stage.

2.2.2 Dewar

The Bolocam dewar contains a 16 L liquid helium (LHe) reservoir which creates a 4 K stage, and a 16 L liquid nitrogen (LN_2) reservoir which creates a 77 K stage. See Figure 2.2. The hold time is approximately 24 hours for the LHe, and about 48 hours for the LN_2 . Bolocam uses JFETs as part of the read-out electronics chain, and these need to be operated at $\simeq 135$ K to minimize the voltage noise they produce. The JFETs are housed in an aluminum enclosure set off from the 4 K stage by G10 supports. The inside of the enclosure is blackened to help prevent radiation from the warm JFETs from escaping and being absorbed by the UC stage. Additionally, a long cylindrical rod that runs through the center of the LHe bath is used to thermally link the JFETs with the 77 K bath. In the steady state, the JFETs

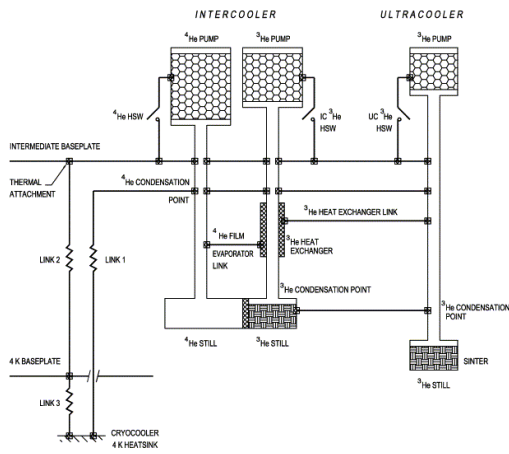


Figure 2.1: The diagram on the left is a simple schematic of the three-stage sorption refrigerator used in Bolocam. Figure taken from Bhatia et al [13]. The image on the right is a picture of the refrigerator installed in the Bolocam dewar.

operate between 125 - 130 K due to the energy they dissipate, so a heater was added to the assembly to allow them to operate at 135 K.

2.3 Detectors

2.3.1 Overview

Bolocam's detector array consists of 151 micro-mesh spider-web bolometers with neutron-transmutation-doped germanium (NTD) thermistors [18, 93], divided among six hexants. See Figure 2.3. Seven of the detectors are not read out, and six of them are not coupled with the optics¹, (i.e., dark), leaving 138 optical detectors. Of those 138 detectors, 114 are operational. The majority of the 24 non-operational detectors show an open circuit when measured at the array bond pads. Microscopic inspection of these detectors revealed that the photo-lithographed wires are functional, so the problem is thought to be in the NTD bump bonds. Additionally, a large number of the bad detectors are in a single hexant where there is a known mask error that makes open circuits more likely. The current version of the array has been in use since January 2003, and is the fourth array produced for Bolocam. In previous versions, problems with the photo-lithography or NTD chip bonding stages caused lower yields. These problems have been almost completely resolved, and the current array has only one bolometer with a broken web and one detector without an NTD chip.

¹The six dark bolometers are used to help characterize the electronics noise of the system.

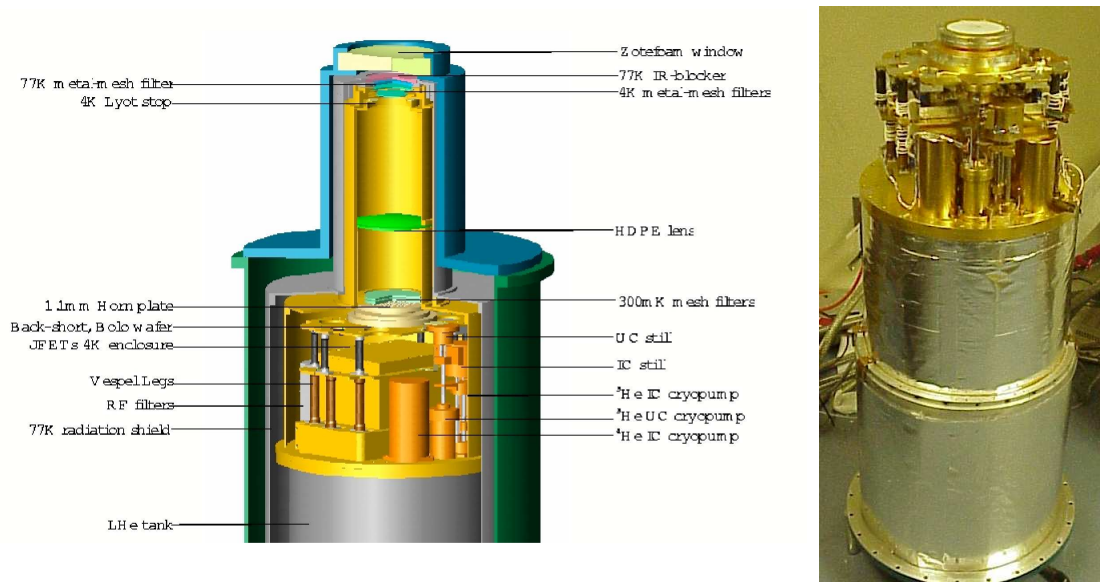


Figure 2.2: Left: a three-dimensional image of the Bolocam dewar created by Philippe Rossinot. Right: a picture of the Bolocam dewar with the 300 K, 77 K, and 4 K shields removed.

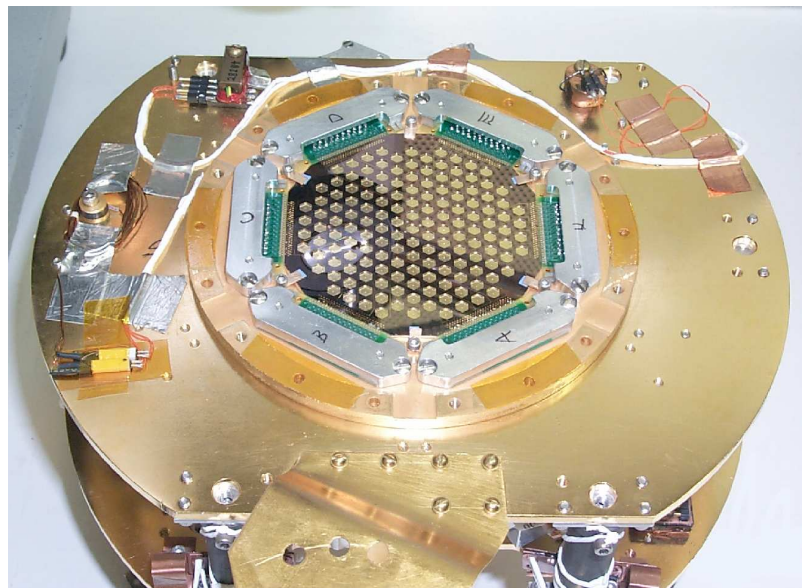


Figure 2.3: A photograph of the Bolocam detector array mounted on the ultra-cold stage outside the Bolocam dewar.

2.3.2 Characterization

The model we have used to describe the thermal and electrical properties of the NTD-Ge based bolometers contains four parameters. The temperature versus resistance relation for the thermistor is described by the parameters R_0 and Δ , with

$$R_b(T_b) = R_0 e^{\sqrt{\Delta/T_b}}. \quad (2.1)$$

R_b is the resistance of the bolometer, T_b is the temperature of the bolometer, and R_0 and Δ are influenced by the neutron doping concentration. The power flow through the thermal link between the bolometer and the low-temperature bath is described by the parameters g and α , with

$$P = g(T_b^\alpha - T_s^\alpha). \quad (2.2)$$

P is the total power deposited on the bolometer due to Joule heating and optical power, and T_s is the temperature of the bath, which is maintained by the UC stage. Typically, we are interested in the temperature change of the bolometer when there is a slight change in the total power, which is described by the thermal conductance,

$$G(T_b) = dP/dT_b = g\alpha T_b^{\alpha-1}, \quad (2.3)$$

and can be rewritten as

$$G(T_b) = G_0 (T_b/T_0)^\beta, \quad (2.4)$$

where G_0 is the thermal conductance at a bolometer temperature of T_0 and $\beta = \alpha - 1$.² The width and thickness of the material used for metalization of the web largely determines the values of g and α , which are used to tune G_0 for the expected bath temperature and background loading.

It is not possible to optimize G_0 for all three Bolocam observing bands, so we have chosen the value of G_0 that is a good compromise among the bands. Using data from the three prototype arrays built for Bolocam, we had a good idea what values of R_0 , α , and Δ to expect. Additionally, the optical efficiency and electronics noise have been measured, and we knew what the typical atmospheric opacities at the Caltech Submillimeter Observatory

²We define G_0 at a bolometer temperature of 300 mK.

(CSO) are. After assuming an optical load of 30 K from the optics outside the dewar, we calculated how Bolocam would perform with different values of G_0 .³ We determined that $G_0 \simeq 150$ pW/K would give mapping speeds within 20% of optimal for both the 140 GHz and 275 GHz bands, and had the fourth and final array fabricated with this design value of G_0 . Unfortunately, after the array was built an error in the calculation was found, and the best value of G_0 was found to be $\simeq 100$ pW/K. See Figure 2.4. However, the loading from the optics outside the dewar is actually $\simeq 75$ K or 3.5 pW at 2.1 mm. This means that the optimal value of G_0 for the 2.1 mm band is larger than our calculated value. The end result is that $G_0 \simeq 150$ pW/K is close to optimal given the measured amount of optical loading.

To determine the parameters for the Bolocam bolometers, we analyzed IV curves⁴ at various base temperatures. There are several ways to analyze these IV curves to determine the bolometer parameters, and following is the method used by Bolocam. First, if the bolometer is not exposed to optical power, then the total power deposited in the bolometer is exclusively due to Joule heating. These dark IV curves are taken at several different bath temperatures, and then converted to $P(R_b)$ curves. Differencing these $P(R_b)$ curves at a given value of R_b , and therefore T_b , results in

$$\Delta P = g(T_{s1}^\alpha - T_{s2}^\alpha), \quad (2.5)$$

which can then be used to determine g and α . Once g and α are known, the $P(R_b)$ curves can be converted to $T_b(R_b)$ curves, which are then converted to $T_b^{-1/2}(\log R_b)$ curves. These curves should be linear, which can be seen by rewriting Equation 2.1 as

$$T_b^{-1/2} = \Delta^{-1/2}(\log R_b - \log R_0). \quad (2.6)$$

The curves at several different bath temperatures were then combined, and a single linear fit was determined for the data which yielded the values of R_0 and Δ . After characterizing the bolometers, we found that they all perform close to the design values. The measured values are: $G_0 = 173 \pm 9$ pW/K, $\alpha = 2.49 \pm 0.09$, $R_0 = 179 \pm 61 \Omega$, and $\Delta = 35 \pm 1$ K.⁵

³For a single-moded system observing a blackbody in the Raleigh-Jeans limit, the power received from the blackbody is proportional to its temperature. Therefore it is common practice to quote optical loading power in units of temperature instead of power. 30 K corresponds to approximately 1.5 pW of power absorbed by the detector at 2.1 mm and 7.0 pW at 1.1 mm.

⁴IV curves involve varying the current applied across the bolometer while recording the voltage across the bolometer.

⁵Note that the uncertainties give the variations from one bolometer to the next. The measurement errors

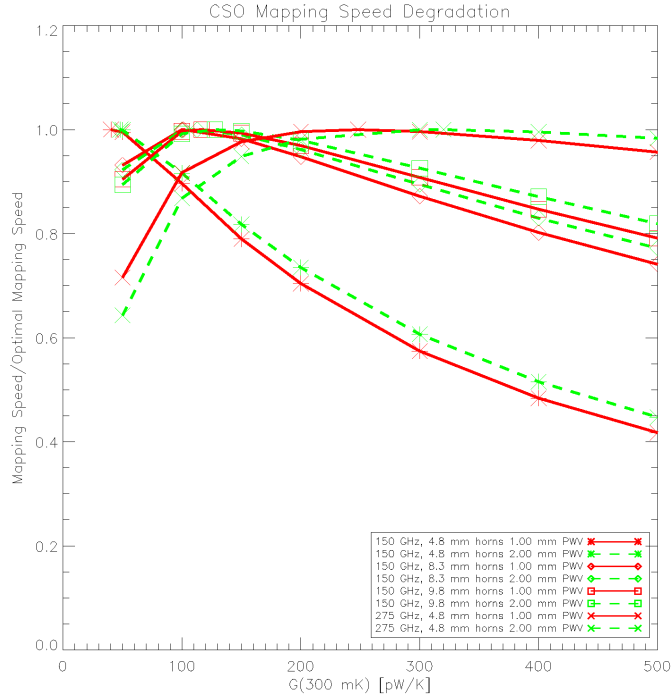


Figure 2.4: The ratio of mapping speed (in arcminutes²/Jy/sec) to the optimal mapping speed for the possible Bolocam configurations as a function of the bolometer thermal conductance, G_0 . The red curves represent 1.00 mm of precipitable water vapor, and the green curves represent 2.00 mm of precipitable water. Three possible configurations for observations at 140 GHz are shown, along with the configuration for 100 GHz. These curves are based on 30 K of loading from the telescope, and indicate a good choice of G_0 is 100 pW/K. However, the loading from the telescope is actually $\simeq 75$ K at 2.1 mm, which would shift the 2.1 mm curve to larger values of G_0 . This means the optimal value of G_0 is close to 150 pW/K, similar to what the bolometers were designed for. Figure taken from Golwala [53].

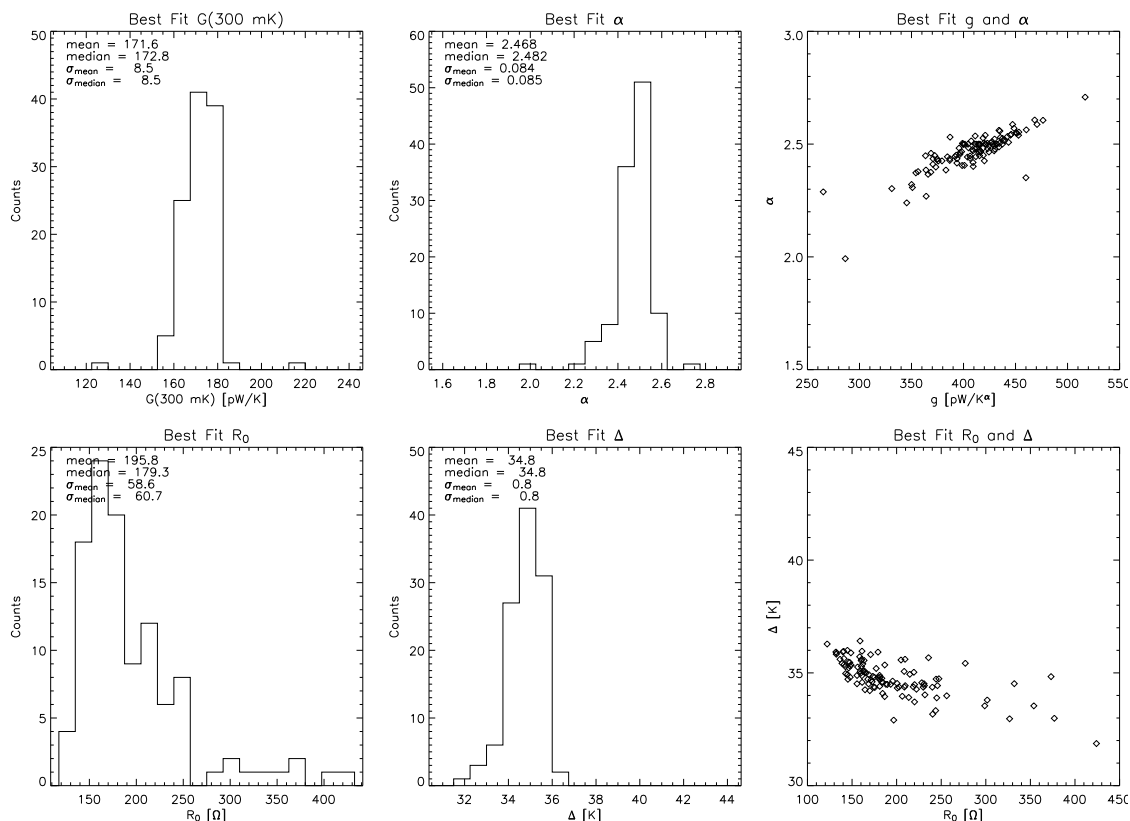


Figure 2.5: The measured bolometer parameters for all of the bolometers in the Bolocam focal plane. The plots on the left show histograms of the four parameters G_0 , α , R_0 , and Δ . The plots on the right show the degeneracies between g and α , and between R_0 and Δ . These degeneracies make it difficult to constrain the values of g and R_0 , although G_0 is well constrained.

Note that there are degeneracies between g and α , and between R_0 and Δ , that make it difficult to constrain the values of g and R_0 . However, the value of G_0 is well constrained. See Figure 2.5.

2.4 Electronics

The purpose of the electronic system is to digitally record the bolometer resistance without adding any noise. In practice, this is difficult because the bolometer is a high-impedance device operated at very low currents, and slight movements of the wires results in a noticeable amount of signal pickup. Additionally, the electrical system must be stable at low frequency because we are interested in signals on time scales that correspond to a few seconds given

are negligible in comparison. Therefore, when we model the bolometer response we use the measured value for each bolometer, rather than the averages quoted above.

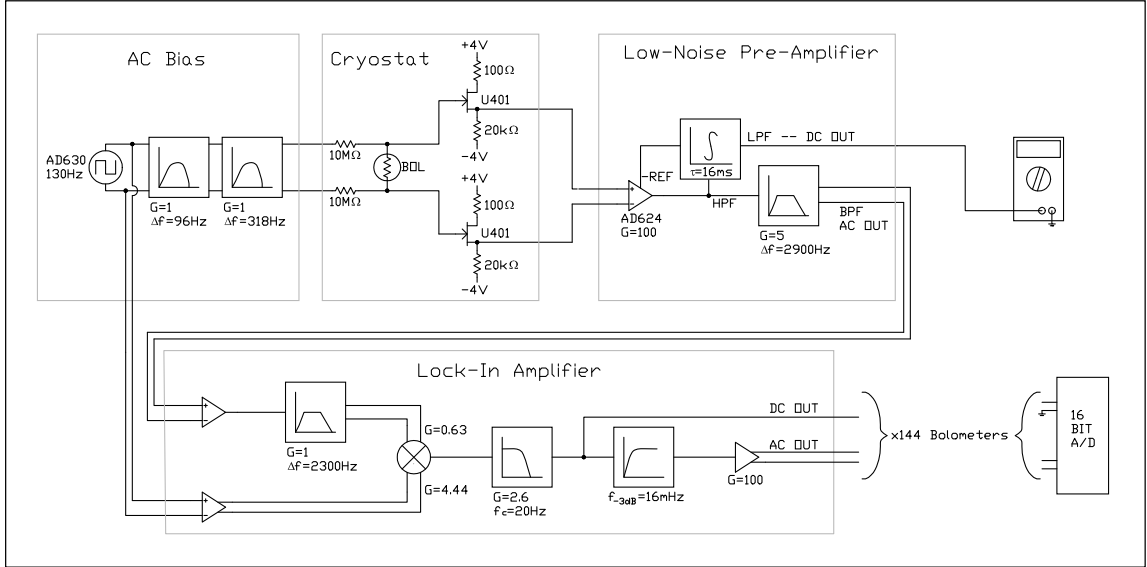


Figure 2.6: A simplified schematic of the Bolocam electronics made by Glenn Laurent. The overall gain of the AC output is 82933 at $f = 0$ Hz, and the overall gain of the DC output is 821 at $f = 0$ Hz.

our typical scan speeds.

2.4.1 Design

Bolocam utilizes the AC-biased bolometer-read-out electronics originally developed for the BOOMERANG experiment [33]. Two $10\text{ M}\Omega$ resistors are placed in series with each bolometer, converting the voltage bias into a pseudo-current bias. Therefore, the voltage across the bolometer provides a measurement of the bolometer resistance. Additionally, the bias voltage for every bolometer is supplied by a common circuit which is stable to a few parts per million above 10 mHz. The bolometers are biased using a 130 Hz sine wave produced by bandpass filtering a square wave. 130 Hz was chosen for the following reasons. First, since the bolometers have a thermal time constant of $\tau \simeq 10$ ms, the bias has to be above $\simeq 50$ Hz so that the bolometers see an effectively constant bias power. Additionally, the bias

frequency must be below $\simeq 500$ Hz to prevent phase shifts and attenuation from capacitive shunting from the RC time constant of the bolometer circuit (a few $M\Omega$ and several tens of pF). Finally, microphonic response resonant frequencies must be avoided; these resonances were determined by attaching audio speakers to the Bolocam dewar, then monitoring the signal output while doing a scanned frequency drive.

On the output side, the bolometers are buffered using a differential, unity-gain, source-follower circuit consisting of a pair of JFETs mounted near the bolometer array. The voltage on either side of the bolometer is fed into one of the JFETs in the pair, which are matched to have a minimal difference in offset voltage. The JFETs present the same signal with a lower output impedance, which significantly lowers the system's susceptibility to microphonic pickup, electromagnetic interference, and RC rolloff. Following the JFETs, the differential signal from each bolometer exits the dewar directly into an RF-tight enclosure mounted on the outside of the dewar. See Figure 2.7. Once inside this enclosure, the signals are amplified by a factor of 100 and then filtered with a band pass centered on the bias frequency⁶. The band pass filter has a gain of 4.98, so the overall amplification factor is approximately 500.

Following amplification, the differential bolometer signals leave the RF-tight enclosure via shielded twisted-pair cables to be demodulated by a square-wave using a set of analog lockin circuits. These lockins are located in a separate electronics rack, and another band pass filter centered at the bias frequency is applied to the differential signals prior to demodulation. The demodulated signal is then amplified by 2.6 and low-pass filtered by two two-pole Butterworth filters, each with a time constant corresponding to $\simeq 21$ Hz, in preparation for digitization at 50 Hz. This signal is then split, with one version digitized as the low-gain DC output (DC bolometer voltage). The DC bolometer voltage corresponds to the amplitude of the bias signal or carrier wave, and provides a measurement of the quiescent bolometer voltage⁷. The digitizer is composed of a set of National Instruments SCXI-1100 multiplexer banks with differential inputs coupled to a single National Instruments PCI-6034E Analog-to-Digital PCI card. The dynamic range of the A/D card is 16-bit, which is much coarser than the resolution of the analog signal, which is around one part per million.

⁶Prior to filtering, the signal is split, and a low-pass filter is applied to the second version of the signal. This low-pass filtered signal is output for instrument characterization.

⁷Actually, the DC bolometer voltage does not measure the true bolometer resistance due to phase shifts between the demodulation signal and the bolometer signal, along with imperfections in the demodulation.

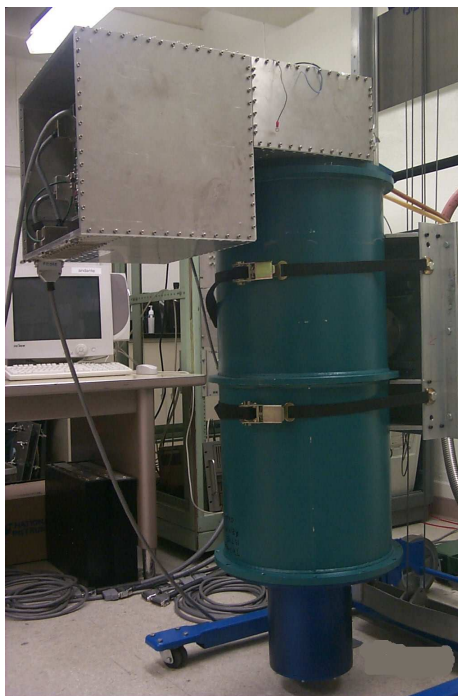


Figure 2.7: Photograph of the Bolocam dewar in the lab at Caltech. Note the large RF-tight enclosure on top of the dewar, which contains the first stage amplifiers.

Since the majority of the bolometer signal is a DC offset, the second version of the split signal is high-pass filtered by a single pole filter with a time constant corresponding to $\simeq 16$ mHz, and amplified by a factor of 100. This second signal is digitized as the high-gain AC output (AC bolometer voltage). Thanks to the removal of the DC offset, the AC bolometer voltage is not bit-noise limited.

With regard to the electronics, the 144 bolometers are split into six hexants, with 24 bolometers being read out by each hexant⁸. Along with the bolometer signals, the bias voltage that enters the dewar is also recorded for each hexant. This bias voltage is demodulated and amplified using the same electronics, and the corresponding DC bias voltage and AC bias voltage values are digitized. Additionally, the outputs from several thermometers are digitized along with other housekeeping signals. The read-out electronics for these thermometry signals is completely separate from the lockin electronics used for the bolometer and bias signals, and consists mainly of DC-biased diodes and DC-biased germanium resistance thermometers (GRTs). LabVIEW software is used to store all of the

⁸There are 151 bolometers in the focal plane, but seven bolometers are not read out. This is because the standard micro-D connectors used for the cables to transmit the bolometer signals only contain 51 pins. Since two pins are required to transmit the bias voltage applied to the hexant, the differential signal can only be read out from 24 bolometers.

data after digitization, which totals approximately one GB per night.

2.5 Optics

The Bolocam optical system was designed to couple the bolometers to the telescope at the CSO. Additionally, the system needs to define the spectral bandpass appropriate for each observing band, which is a fractional bandpass of approximately 20%.

2.5.1 Physical Components

Each bolometer is housed within its own integrating cavity, formed by a frontshort plate and a backshort plate. See Figure 2.8. The walls of the cavity are largely absent, due to the silicon substrate that the silicon nitride micromesh absorber for each bolometer is etched into. The 2.1 mm backshort plate is made from gold-plated aluminum, while the 1.1 mm backshort plate is made from gold-plated invar⁹. Although the bolometer array is the same for all three of the bands at which Bolocam can observe, the height of this integrating cavity can be adjusted to maximize the photon absorption efficiency at each wavelength [51]. Each bolometer is coupled to a single waveguide and feed horn, which are all machined into a single piece of gold-plated aluminum (horn-plate); a different horn-plate is used for each observing frequency. See Figure 2.9. The waveguide serves as a high-pass filter on the incoming photons, and defines the low-frequency edge of each band. Limited by the 5 mm spacing between bolometers, the opening aperture diameter of the feed horns is 4.8 mm. Since the incoming geometrical optics ray bundle is $f/2.8$, these openings correspond to $1.5 (f/\#)\lambda$, $1.2 (f/\#)\lambda$, and $0.7 (f/\#)\lambda$ for the 1.1 mm, 1.4 mm, and 2.1 mm bands, respectively¹⁰. Note that the opening diameter of the feed horns, and consequently the spacing between bolometers, was chosen as a compromise so that the focal plane is not significantly over or under sampled for any of the three observing bands.

The optical window at the outside of the dewar is made from Zotefoam PPA30, a nitrogen-expanded polypropylene foam with a closed cell structure, that is part of the 300 K vacuum enclosure of the dewar [118]. Inside this window is a Lyot stop, which is thermally linked to the 4 K stage, that truncates the beams from the feed horns so that

⁹Since the backshorts are pedestals that stick up into the bolometers, thermal contraction is a potentially major problem for the shorter 1.1 mm cavities. Therefore, to reduce the thermal contraction of the plate, the 1.1 mm backshorts were made from invar.

¹⁰The beams produced by the 26 mm thick horn plate are $f/5.0$ at 1.1 mm and $f/2.7$ at 2.1 mm.

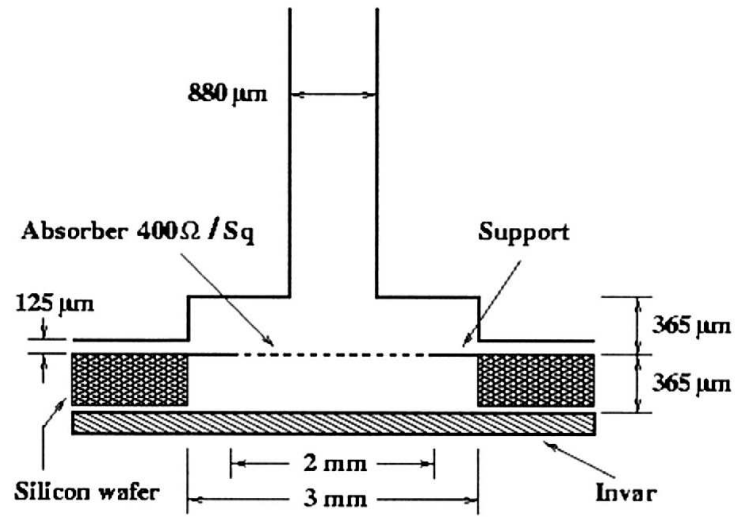


Figure 2.8: Profile of the integrating cavity used for each of the 144 Bolocam bolometers. This schematic shows the geometry for 1.4 mm observations. Note that the cavity is circularly symmetric about the axis of the waveguide. Figure taken from Glenn, et al. [51].

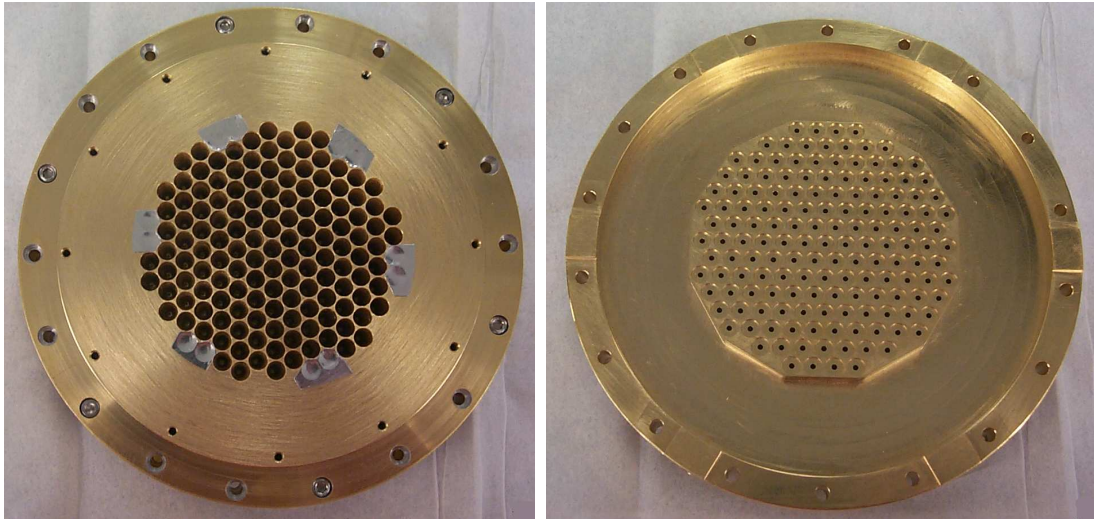


Figure 2.9: Left: a photon's-eye view of the horn-plate used for 2.1 mm observations. Right: the view from the bolometer of the same horn-plate.

they will slightly under-illuminate the primary mirror. The inside surfaces of the Lyot stop are covered in carbon lampblack mixed with epoxy¹¹, and these surfaces couple to 45% of the 1.1 mm beam, and 80% of the 2.1 mm beam. The last component in the optical system before the incoming photons couple to the feed horns is a double-parabolic high-density polyethylene (HDPE) lens that converts the incoming geometrical optics ray bundle from $f/7.4$ to $f/2.8$. The lens has circular anti-reflection grooves cut to a depth of $\lambda/4$ in its surface, so a different lens is required for each observing band. Additionally, this lens removes most of the field curvature.

Located between the Bolocam dewar and the CSO telescope is a large optics box which is located on-axis at the Cassagrain focus of the telescope and serves as a mounting point for Bolocam. See Figures 2.10 and 2.11. There is a rotator located at this mounting point that allows the Bolocam dewar to rotate about its axis, which is aligned with the telescope optical axis. From the Bolocam dewar, the first component in the optics box is an off-axis elliptical mirror which converts the beams from $f/7.4$ to $f/12.4$. Additionally, the ellipsoidal mirror, along with the cold HDPE lens, optimizes the image quality over the entire Bolocam focal plane [128]. The optics box also contains two parallel flat mirrors between the elliptical mirror and the telescope secondary mirror, which fold the beam to make the optics box sufficiently compact to be practical. A view of the entire Bolocam optical system, including the telescope, is given in Figure 2.12.

Additionally, the optical system contains a series of capacitive/inductive multi-layered copper mesh grids which act as low-pass filters on the incoming photos. Layered HDPE serves as the substrate for these grids. All of these filters were supplied by the group led by Peter Ade in Cardiff [1]. The filters define the high-frequency edge of each band, along with reducing the thermal photon load on the cold stages inside the dewar. The cutoff frequencies of the filters are chosen such that the harmonic leaks of one filter are reflected by another. A total of six filters are used, one linked to the 77 K stage, two linked to the 4 K stage, and three connected directly to the 250 mK UC stage. Three of these filters have gore-tex anti-reflection coatings, and the final filter at 250 mK is used to define the band edge. The details of these filters are given in Table 2.1.

¹¹This mixture of carbon lampblack and epoxy creates a very good blackbody at millimeter wavelengths [17].

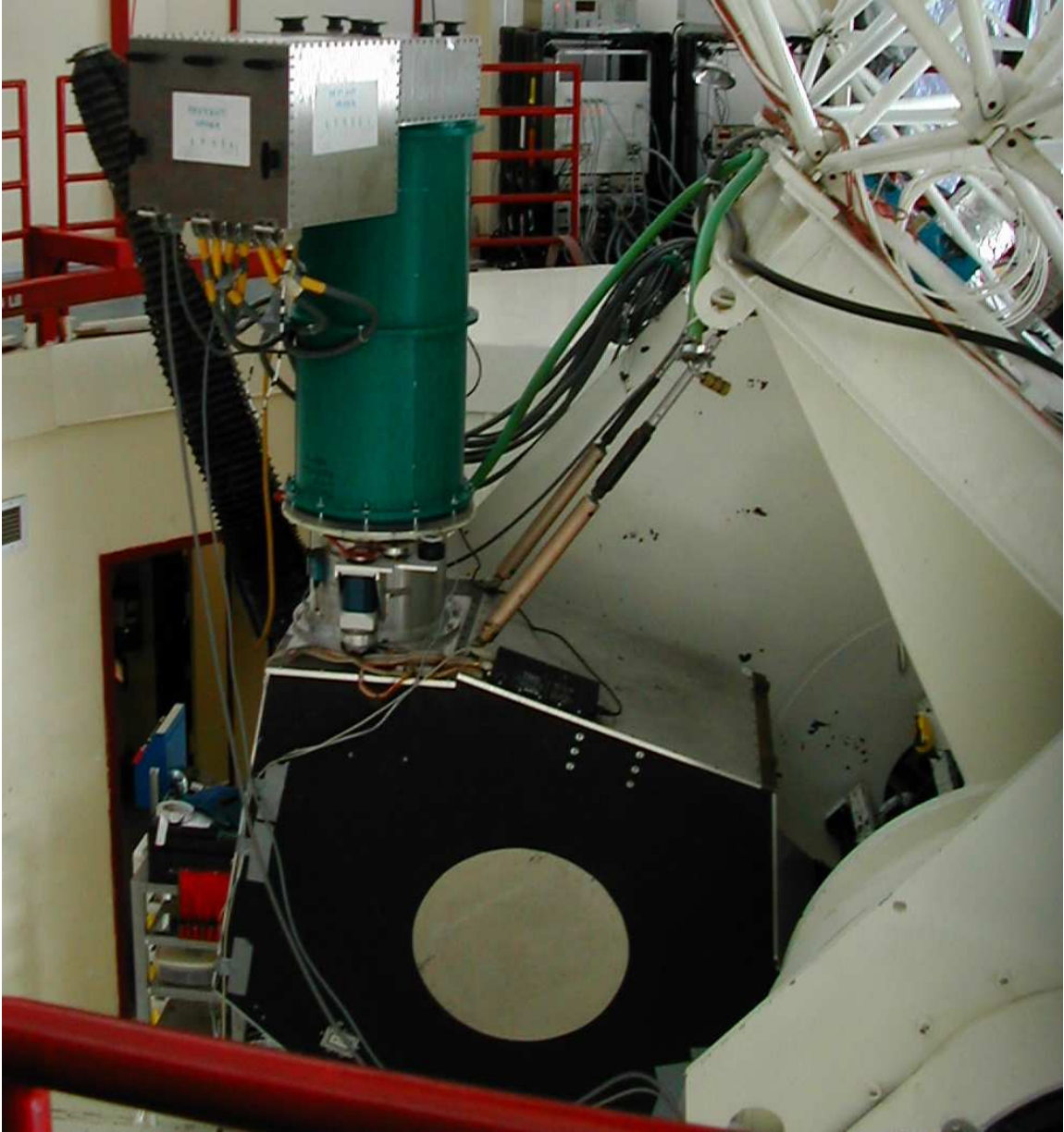


Figure 2.10: An image of Bolocam mounted on the optics box at the CSO. Bolocam is the green cylinder in the upper left of the picture, with a rectangular aluminum RF-tight electronics enclosure on top. Behind Bolocam is a black sleeve covering the elevation drive of the telescope. The Bolocam optics box is located near the bottom of the photo, with a black side panel. This optics box not only couples Bolocam to the telescope optics, but also provides a mechanical mounting point for the dewar. Note that only the back half of the optics box is visible in this photo.

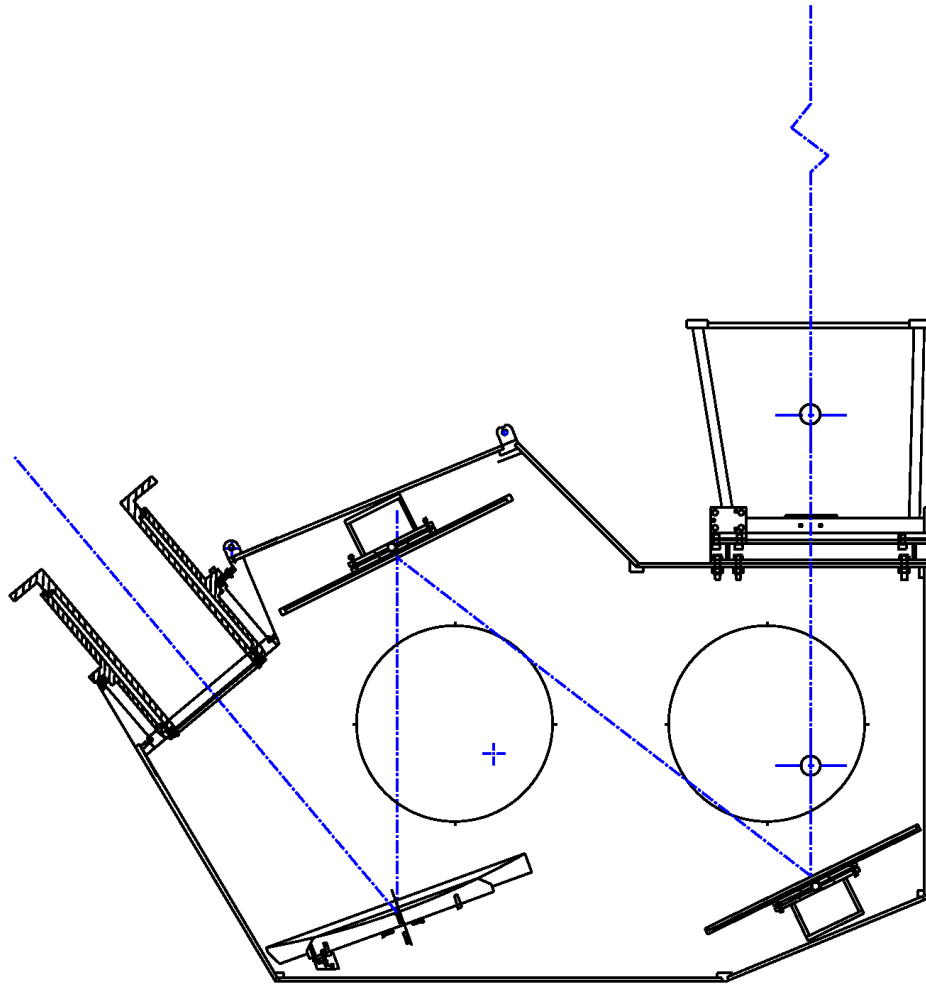


Figure 2.11: A schematic of the Bolocam optics box. The mount point to the telescope is on the upper right of the box, and the mount point for the Bolocam dewar is on the upper left of the box. The blue line traces the optical axis of the system. The two flat mirrors can be seen towards the lower right and upper left of the box, and the elliptical mirror is towards the lower left of the box. Figure created by Sunil Golwala.

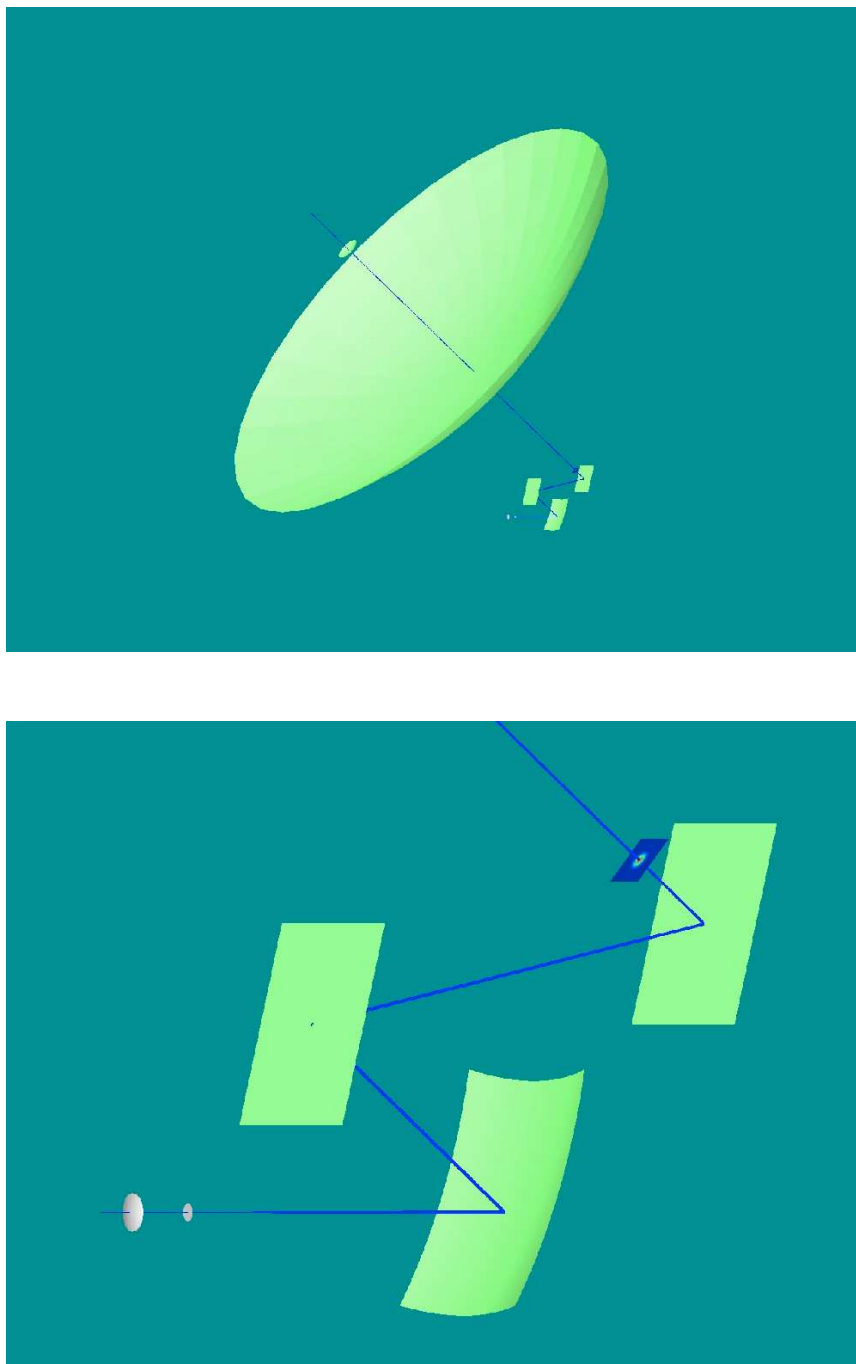


Figure 2.12: Three-dimensional scaled representations of the Bolocam optical system. The top image shows the entire system, with the primary mirror as the dominant feature in the image. The bottom image zooms in on the lower right section of the top image, and shows the two flat mirrors and elliptical tertiary, along with the lens and focal plane inside the dewar.

2.1 mm configuration

Position	cutoff ν	AR coating	serial #
77 K	420 GHz	none	B286
4 K	255 GHz	gore-tex	B131
4 K	420 GHz	gore-tex	B283
250 mK	255 GHz	gore-tex	B159
250 mK	233 GHz	none	C195
250 mK	150 GHz	none	B309

1.1 mm configuration

Position	cutoff ν	AR coating	serial #
77 K	540 GHz	PTFE	B445
4 K	420 GHz	none	B286
4 K	420 GHz	gore-tex	B283
250 mK	420 GHz	PTFE	B430
250 mK	360 GHz	PTFE	B161
250 mK	300 GHz	PTFE	B411

Table 2.1: The six optical filters used for 1.1 mm and 2.1 mm observations. The cutoff frequencies are chosen such that the harmonic leaks of one filter are absorbed by another filter.

2.5.2 Measured Performance

We used a Fourier transform spectrometer (FTS) to characterize the spectral bandpass of the filter/feed horn system. The FTS is a Michelson interferometer, with a movable mirror that smoothly varies the path length on one arm of the interferometer. The Fourier transform of the resulting interferogram recorded by the detector gives the spectral transmission of the Bolocam optical system. Each detector was analyzed separately, but the resulting spectra, $\Theta(\nu)$, are similar for all of the detectors. From these spectra, we calculated an effective bandwidth¹² according to

$$\Delta\nu = \int d\nu\Theta(\nu), \quad (2.7)$$

and an effective band center from

$$\nu_0 = \int \nu d\nu\Theta(\nu)/\Delta\nu. \quad (2.8)$$

¹²The absolute normalization of the $\Theta(\nu)$ is not known, so the peak of $\Theta(\nu)$ was normalized to one. This convention affects the bandwidth we calculate, but it does not alter the calculated band center.

For the 1.1 mm observing band, $\nu_0 = 268 \pm 1$ GHz and $\Delta\nu = 45 \pm 3$ GHz. For the 2.1 mm observing band, $\nu_0 = 143 \pm 2$ GHz and $\Delta\nu = 21 \pm 2$ GHz.¹³ See Figure 2.13 and Table 2.2.

The measured optical efficiency of Bolocam was determined from IV load-curves. The load-curves were taken at a constant bath temperature, while varying the incident optical power using a hot (300 K) blackbody and a cold (77 K) blackbody. Using Equation 2.2, we take the difference between the hot and cold load-curves at a given value of R_b (and therefore T_b). The result is

$$P_{hot} - P_{cold} = 0, \quad (2.9)$$

since the bath temperature, T_s , is the same for both load-curves. The total power (P) can be expressed as the sum of the electrical (P_e) and incident optical power (Q), so that

$$P_{e,cold} - P_{e,hot} = Q_{hot} - Q_{cold}. \quad (2.10)$$

Next, we determine the expected values of Q_{hot} and Q_{cold} . The two blackbodies are positioned just outside the dewar window, and they are oversized to ensure that they are beam-filling¹⁴. Therefore, for 100% optical efficiency, the expected optical power is

$$Q_{exp} = \int d\nu \lambda^2 \Theta(\nu) B_\nu(\nu, T), \quad (2.11)$$

where λ^2 is the throughput for a single-moded system [76], and $B_\nu(\nu, T)$ is the Planck function for the surface brightness of a blackbody at temperature T . Both observing bands, for both blackbodies, are well within the Rayleigh-Jeans limit, so we can approximate the Planck function as

$$B_\nu(\nu, T) = 2k_B T (\nu/c)^2, \quad (2.12)$$

where k_B is Boltzmann's constant. Using Equation 2.7, we can rewrite the expected optical power as

$$Q_{exp} = 2k_B T \Delta\nu. \quad (2.13)$$

The optical efficiency, η , is defined as the ratio of the measured optical power to the expected optical power. However, since the detector is exposed to optical power from

¹³Note the the uncertainties given for the band centers and bandwidths indicate the bolometer-to-bolometer variations rather than a measurement uncertainty.

¹⁴An object is beam-filling if it produces all of the optical power incident on the detector.

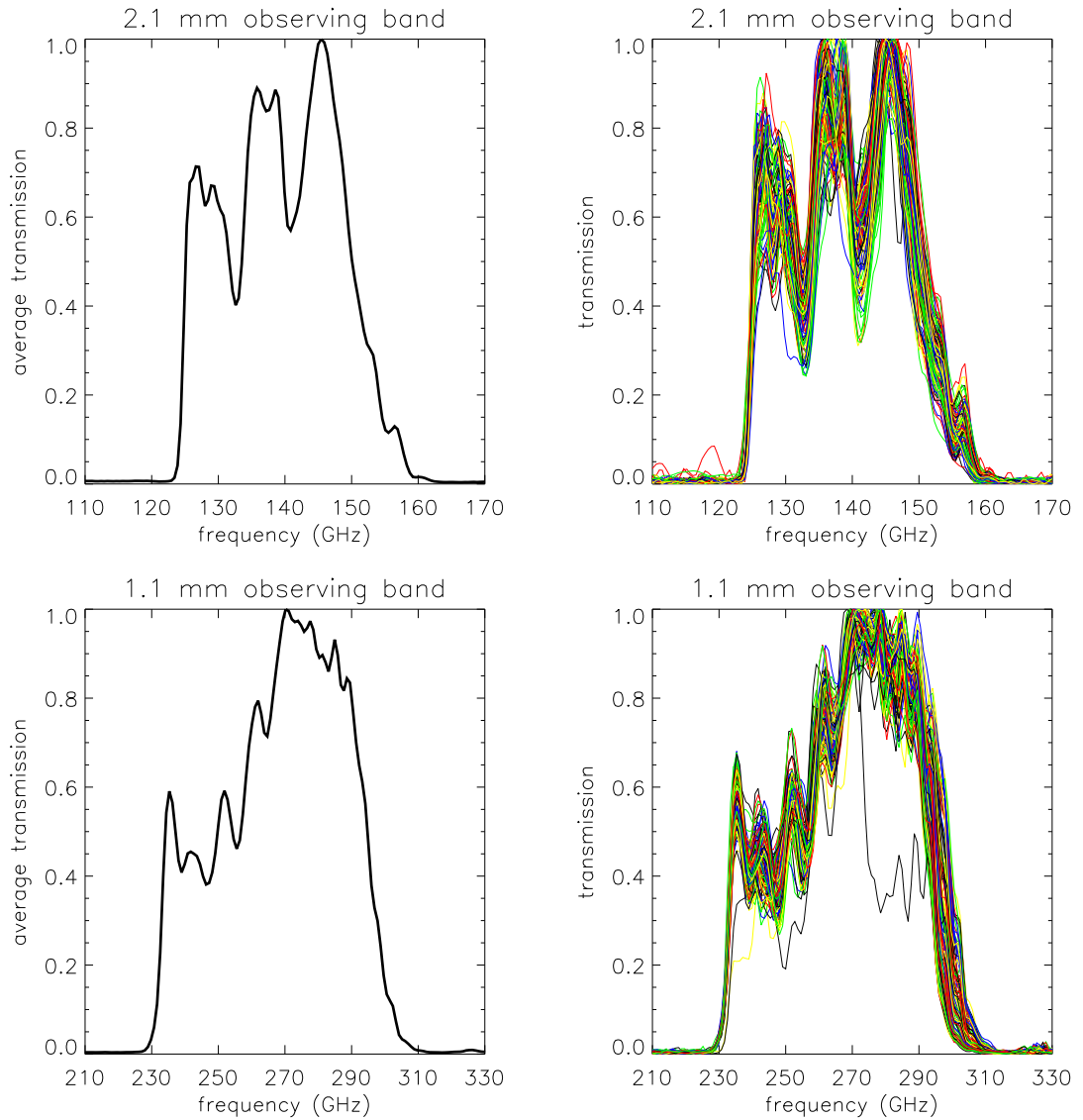


Figure 2.13: The top row shows the transmission spectra for the 2.1 mm observing band, and the bottom row shows the transmission spectra for the 1.1 mm observing band. The plots on the left have been averaged over all of the bolometers, and the plots on the right show the individual bolometer spectra. Each spectrum has been peak normalized to one.

parameter	2.1 mm observing band		1.1 mm observing band	
	value	RMS deviations	value	RMS deviations
band center (ν_0)	143 GHz	2 GHz	268 GHz	1 GHz
band width ($\Delta\nu$)	21 GHz	2 GHz	45 GHz	3 GHz
optical efficiency (η)	8%	1%	19%	1%
optical eff (dQ/dT_{RJ})	0.047 pW/K	0.003 pW/K	0.23 pW/K	0.01 pW/K

Table 2.2: A summary of the measured optical properties of the Bolocam instrument. In all cases the RMS deviations indicate the spread of values from one detector to another, rather than a measurement uncertainty.

emission inside the dewar, it is better to consider the difference in optical power between the hot and cold blackbody. Using Equation 2.10 and Equation 2.13 we find

$$\eta = \frac{Q_{hot} - Q_{cold}}{2k_B\Delta\nu(T_{hot} - T_{cold})}. \quad (2.14)$$

The measured optical efficiency for the 2.1 mm observing band is 8%, while the measured optical efficiency of the 1.1 mm band is 19%. See Figure 2.14 and Table 2.2. A larger amount of coupling to the Lyot stop (80% at 2.1 mm compared to 45% at 1.1 mm) is the reason for the lower efficiency at 2.1 mm. Alternatively, η can be multiplied by $2k_B\Delta\nu$ to give dQ/dT_{RJ} , which is the optical efficiency in terms of pW per K. For the 2.1 mm band the median value of dQ/dT_{RJ} is 0.047 pW/K, and for the 1.1 mm band the median value of dQ/dT_{RJ} is 0.23 pW/K. See Figure 2.14 and Table 2.2.

To date, no reliable measurements of the optical efficiency of the optics outside the dewar have been made. The best way to conduct this measurement would be with observations of bright astronomical point sources with known fluxes, since the physical dimensions of the telescope are too large to use beam-filling blackbodies in an analogous way to the measurements described above. However, these objects would need to be observed while the bolometers are DC biased to apply the same IV loadcurve analysis to determine the optical efficiency, and the sensitivity of the bolometers is severely degraded when they are DC biased. Bolocam would probably still be sensitive enough to detect Jupiter or Mars, but we have not observed either of these objects while DC biasing the bolometers. These objects have been observed numerous times while AC biasing the bolometers, but unfortunately it is difficult to determine the bolometer resistance while AC biasing because of the properties of the demodulation electronics¹⁵. However, simulations with Zemax show that all of the

¹⁵First, the bias voltage is not a perfect sine wave. So, the square wave used for demodulation couples

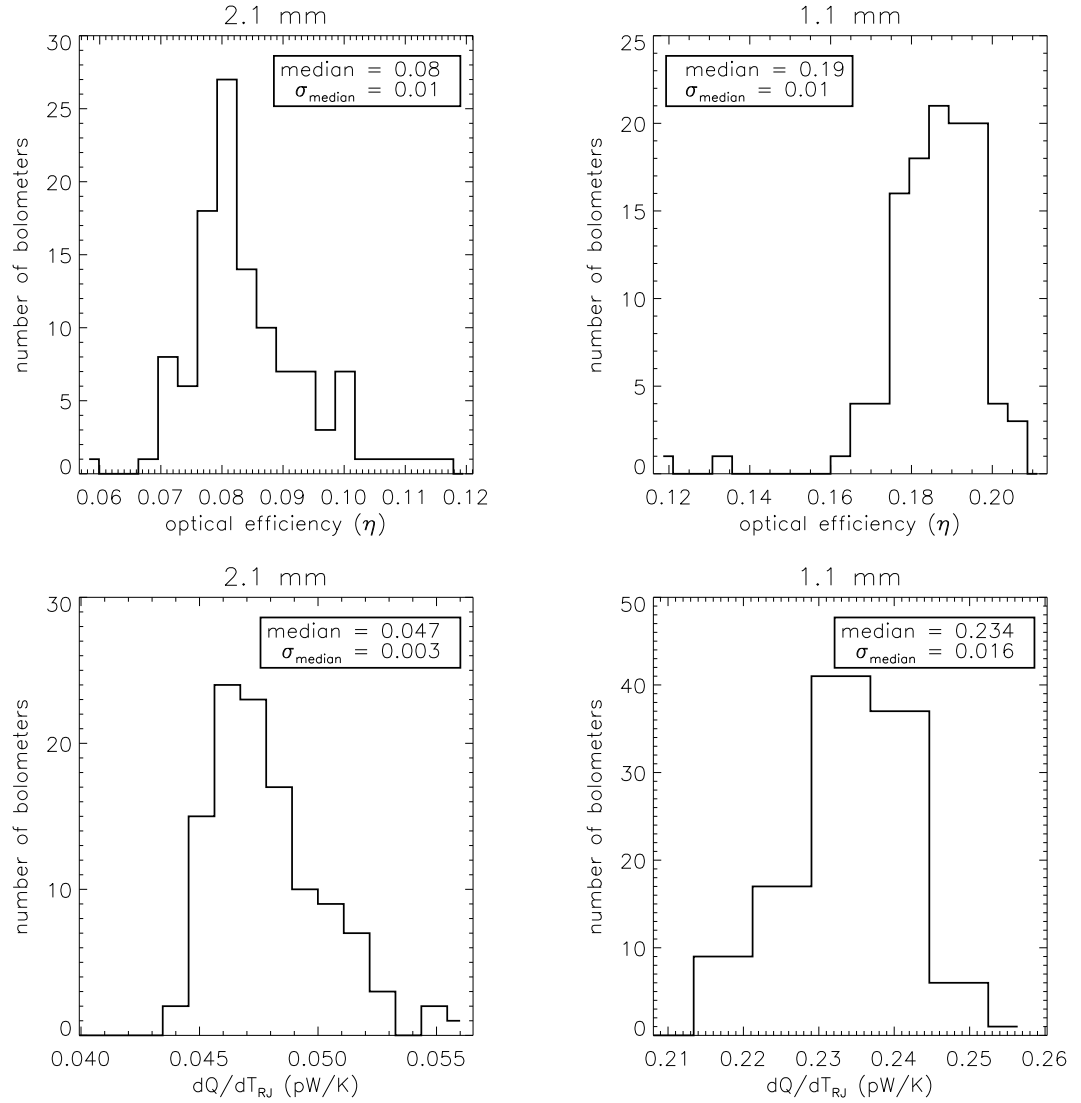


Figure 2.14: The measured optical efficiency of every working detector in the Bolocam focal plane. In the top row the histogram on the left shows the efficiency for the 2.1 mm optics, while the histogram on the right shows the efficiency for the 1.1 mm optics. In the bottom row the histograms show the optical efficiency in terms of pW per K for each band.

optics are considerably larger than the beam, indicating that very little power will be lost due to spillover. Additionally, the surface roughness of the CSO telescope corresponds to an RMS of $25\ \mu\text{m}$, which means the optical efficiency at 2.1 mm should be extremely good ($\simeq 98\%$ according to Ruze scattering theory [119])¹⁶.

Measurements of the Bolocam beam profiles have been made at several locations in the optics, and agree well with the predictions made by Zemax. By analyzing the system in a time-reverse sense¹⁷, the illumination of the primary mirror is defined by the truncated beam produced by the Lyot stop, since the optics produce an image of the primary mirror at the Lyot stop. The Lyot stop causes diffraction, and the finite size of the mirrors outside the dewar prevents all of the diffracted rays from being recovered and reconverged, which causes blurring. This blurring is predicted by Zemax, and has been confirmed by several measurements. See Figure 2.15. Fortunately, the beam profiles in the far-field of the telescope are relatively unaffected by this blurring because they are the Fourier transforms of the primary mirror illumination. The sharp truncation by the Lyot stop produces some ringing in the far-field beams, making them more Airy-like than Gaussian; which can be seen in high-resolution images of the far-field beams (see Figure 3.17). Overall, the optical system has performed close to expectations.

with frequencies other than the true bias frequency. Also, the presence of harmonics in the signal arriving at the demodulator makes the square-wave demodulation difficult to interpret. Additionally, the stray capacitance of the bolometer circuit produces an RC time constant that is non-negligible compared to the bias frequency. This time constant will cause a phase shift between the bolometer voltage and the bias signal used to demodulate the signal. Therefore, the bolometer voltage cannot be easily converted to a bolometer resistance when Bolocam is AC biased.

¹⁶There is now some concern that the imperfect alignment of the primary mirror panels might affect our optical efficiency. We did not use the CSO's dish surface optimization system (DSOS) during our observations, since we did not want to alter our optical system and it was thought that the DSOS would only make a noticeable difference at much higher frequencies. However, recent evidence shows that the DSOS can make a significant difference at frequencies as low as 350 GHz, fairly close to our observing band at 143 GHz [84].

¹⁷A time-reverse sense assumes that the detector emits photons that are absorbed by the source, rather than vice versa.

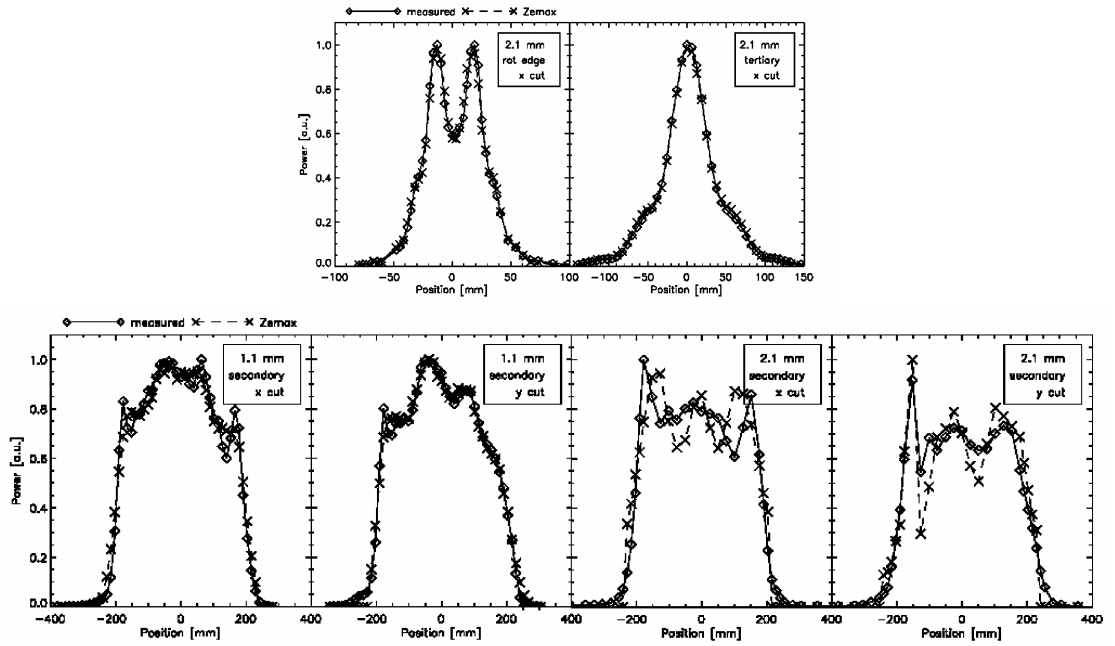


Figure 2.15: The profile of the Bolocam beam at various points in the optics. The plots in the top row show the one-dimensional profile of the beam for a detector approximately half-way between the center of the array and the edge. The plots in the bottom row show the one-dimensional profile of the beam for a detector near the edge of the array. The upper left plot was based on a measurement made approximately 280 mm outside the dewar window, while the upper right plot was based on a measurement made at the surface of the ellipsoidal tertiary mirror. The two lower left plots are based on measurements made at the secondary mirror with 1.1 mm optics, while the two lower right plots are based on measurements made at the secondary mirror with 2.1 mm optics. The measured values have been overlaid on the predicted values from Zemax simulations. Figure taken from Glenn, et al. [49].

Chapter 3 Observations and Performance

3.1 Observing Site

Bolocam was designed to be mounted on the CSO, and all of the astronomical data collected with Bolocam has been at the CSO. One of the premier submillimeter observatories in the world, the CSO is located near the summit of Mauna Kea on the Big Island of Hawaii, at an elevation of just over 4000 m.

3.1.1 Telescope

The CSO has an on-axis Cassagrain telescope, with a 10.4 m diameter Leighton radio dish as the primary mirror. Hexagonal panels have been used to construct the primary mirror. The secondary mirror is capable of chop throws of up to nine arcminutes in amplitude, although we held the secondary fixed at its nominal position for all of our observations. Equipped with an alt/az mount, the telescope can observe over the full range of 360 degrees in azimuth, and it can cover elevation angles between 1.5 and 86 degrees. However, the majority of our observations were made at elevations between 40 and 70 degrees. The telescope can raster scan at any alt/az angle or any RA/dec angle at speeds of several arcminutes per second. Even at high scan speeds the deviations from an exact raster are typically a couple of arcseconds or less, and these deviations are recorded to allow for correction when processing the data.

3.1.2 Typical Conditions

Precipitable water vapor in the atmosphere is generally the limiting factor in the sensitivity of broadband, ground-based, millimeter-wave observations. Consequently, the premier sites for these observations, which include Mauna Kea, Atacama, and the South Pole, are extremely dry. The CSO maintains a narrow-band, heterodyne τ -meter that measures the optical depth at 225 GHz (τ_{225}) [27]. Since τ_{225} is a monotonically increasing function of the column depth of precipitable water vapor in the atmosphere, these τ_{225} measurements can be used to quantify how dry the atmosphere above Mauna Kea is. Historically, the median

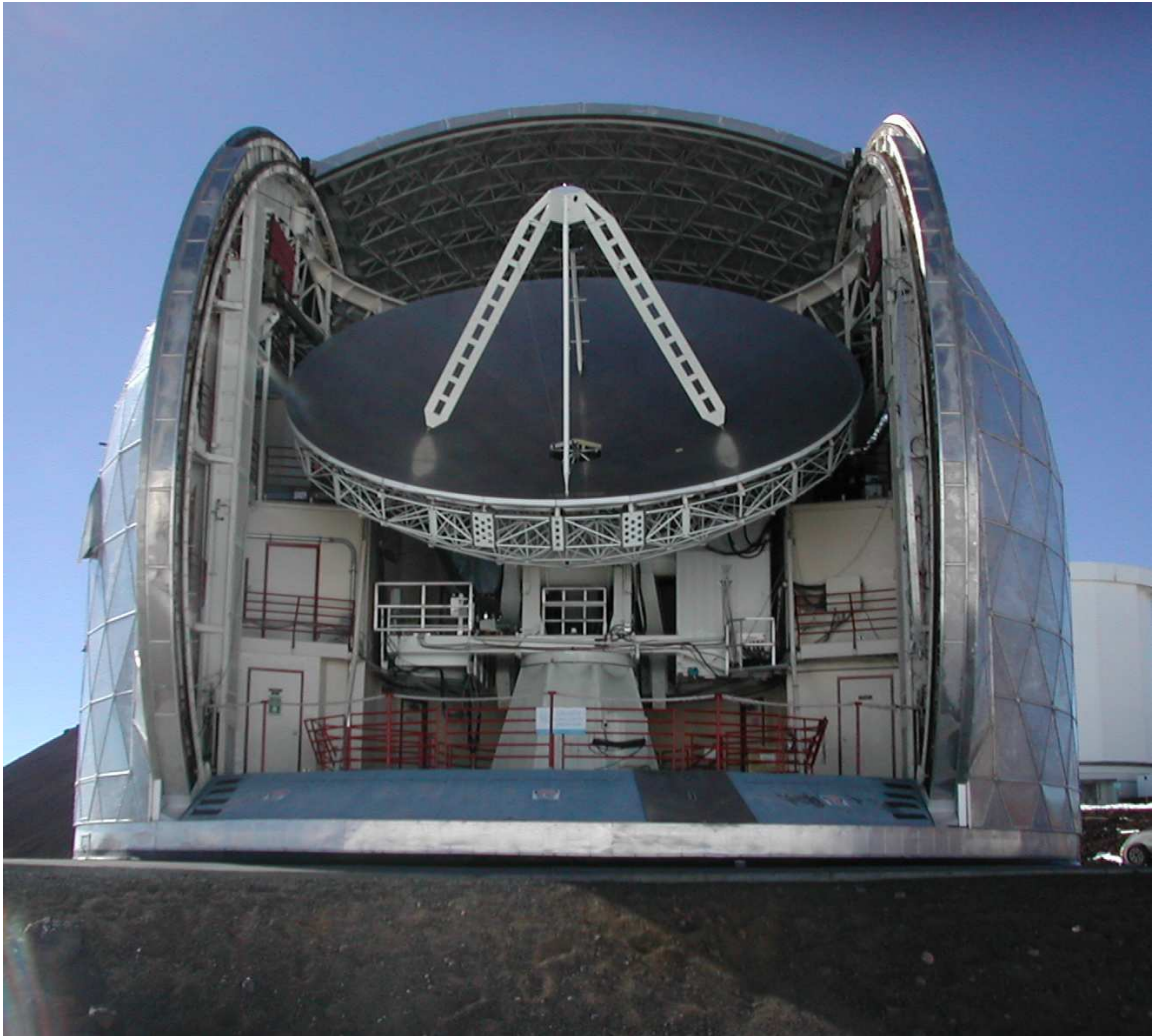


Figure 3.1: The Caltech Submillimeter Observatory

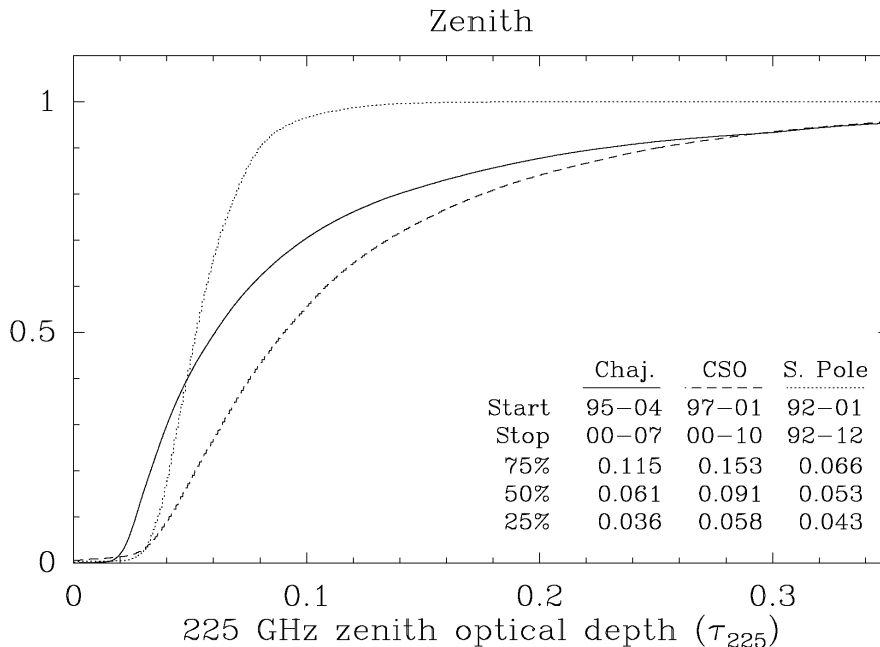


Figure 3.2: The cumulative distribution of τ_{225} at Atacama (Chajnantor), Mauna Kea, and the South Pole. Figure taken from Radford and Chamberlin [106].

value of τ_{225} is 0.091, with the 25% and 75% centiles at $\tau_{225} = 0.058$ and 0.153. Using the Pardo atmospheric model, the corresponding column depths of precipitable water vapor at the 25%, 50%, and 75% centiles are 1.00, 1.68, and 2.92 mm, respectively [34, 101]. For comparison, the median value of τ_{225} at Atacama is 0.061, while the median value at the south pole is around 0.053 [80, 104, 106, 136]. See Figure 3.2. These median column depths of precipitable water produce very low atmospheric zenith optical depths near the Bolocam band center at $\simeq 143$ GHz. Specifically, using the Pardo atmospheric model to extrapolate to 143 GHz, the median zenith optical depths are $\tau_{143} = 0.027$, 0.030, and 0.041 for the South Pole, Atacama, and Mauna Kea, respectively [34, 101].

3.1.3 Actual Conditions

We were granted two separate blocks of time from the CSO to make the observations discussed in this thesis; the first block was from October 30, 2003 to December 8, 2003 and the second block went from October 29, 2004 to December 6, 2004. After accounting for time spent observing calibration sources and other observing inefficiencies, we had approximately eight hours of potential on-source time per night. With a possible 320 hours on-source in

year	total hours	diagnostics	hardware	high-frequency	bad weather	on-source
2003	320	24	36	32	88	140
2004	312	8	48	16	100	140

Table 3.1: Breakdown of how our time was allocated during the two observing runs. Total hours refers to the time granted to us by the CSO, diagnostics refers to the time spent aligning the Bolocam and telescope optics and analyzing observing strategies, hardware refers to time spent working on Bolocam hardware, high-frequency refers to time where τ was exceptionally low and the CSO was used for observations at frequencies above 300 GHz, bad weather refers to time when the weather was too poor to observe, and on-source refers to the time spent observing our science targets.

2003 and 312 hours on-source in 2004, we spent approximately 140 hours on-source during each observing run. In each case, approximately half of the lost time was due to bad weather. Additionally, one night at the start of each run was devoted to aligning the optical system, and two nights at the start of the 2003 run were used to analyze various scan strategies¹. We also devoted approximately three and one half nights during the 2003 run to fixing problems with the electronics that generate the bias voltages for Bolocam, and we lost six nights in 2004 while changing the horn-plate. Finally, the CSO multiplexes between low-frequency ($\lesssim 300$ GHz) and high-frequency ($\gtrsim 300$ GHz) observations, granting nights with exceptionally low τ to the high-frequency programs. We lost four nights in 2003 and two nights in 2004 to high-frequency observations. See Table 3.1.

As mentioned in Section 3.1.2, the 25%, 50%, and 75% centiles of τ_{225} are 0.058, 0.091, and 0.153. Considering only the time spent on-source, the conditions we observed in both 2003 and 2004 were fairly close to these historical averages. However, the on-source time does not account for the time when τ_{225} is exceptionally low, or for the time when the weather is too bad for us to observe. A simplistic correction would be to set $\tau_{225} = 0.00$ for all the of the nights the telescope was used by high-frequency programs, and to set $\tau_{225} = 0.30$, the highest τ_{225} we will typically observe in, for all of the bad weather nights. These simplistic corrections make it appear that the conditions we experienced were much worse than the historical averages, but these simplistic corrections are somewhat flawed. For example, several of the bad weather days were caused by high winds or high relative humidity at the surface, and not by high values of τ_{225} . Therefore, the weather we experienced was probably a little worse than the historical averages, but not significantly worse, as indicated

¹The weather was not very good during these two nights, so the resulting degradation in sensitivity in the science fields due to the lost integration time was minimal.

by our simplistic correction. See Figure 3.3.

3.2 Observing Strategy

In order to maximize our sensitivity to the SZE, we 1) selected science fields that have a minimal amount of contamination from astronomical sources and that have already been observed at other wavelengths and 2) developed a strategy to map these science fields in a way that balances observing efficiency and instantaneous sensitivity in the optimal way.

3.2.1 Science Fields

First, we selected fields with low dust emission, to ensure that we observed a clean region of the sky. Additionally, we looked for fields with X-ray and optical coverage, which will enable us to determine the validity and redshift of cluster candidates, and allow us to study more of the cluster astrophysics. Finally, we decided to split our time between two separate fields instead of trying to observe a single field for the entire night. This allows us to observe the fields only when they are above an elevation of $\simeq 40$ degrees, since the atmospheric opacity and pointing stability tend to degrade rapidly at lower elevations.

During the first half of each night we observed a 0.5 deg^2 region centered at 02h18m00s, -5d00m00s, which coincides with the Subaru/XMM Deep Survey (SXDS or SDS1). This field has approximately 400 ksec of XMM-Newton EPIC X-ray imaging, coverage at optical and near IR wavelengths by Subaru and the CFHT Legacy Survey, IR coverage by the UK Infrared Deep Sky Survey Ultra-Deep Survey and the SWIRE Legacy Survey, submillimeter coverage from the SCUBA Half Degree Extragalactic Survey (SHADES), and $12 \mu\text{Jy}$ RMS data from the VLA. The dust emission in this field is only a few times larger than the best available regions in the whole sky, indicated by a $100 \mu\text{m}$ surface brightness of 1.17 MJy/sr [124].

During the second half of each night we observed a 0.5 deg^2 region centered on the Lynx field at 08h49m12s, +44d50m24s. This field has 150 ksec of XMM/Newton EPIC observations, and it contains three high redshift ($z > 1$) clusters that have been studied at X-ray and optical/IR wavelengths [135, 150]². Additionally, the dust emission in the field is

²The mass of the hottest X-ray cluster is approximately $4 \times 10^{14} M_{\odot}$. A cluster of this mass would produce a peak signal of $\lesssim 100 \mu\text{K}_{CMB}$ at 143 GHz, which is less than or comparable to the RMS per beam in our final map of Lynx. Therefore, we cannot resolve any of the known clusters.

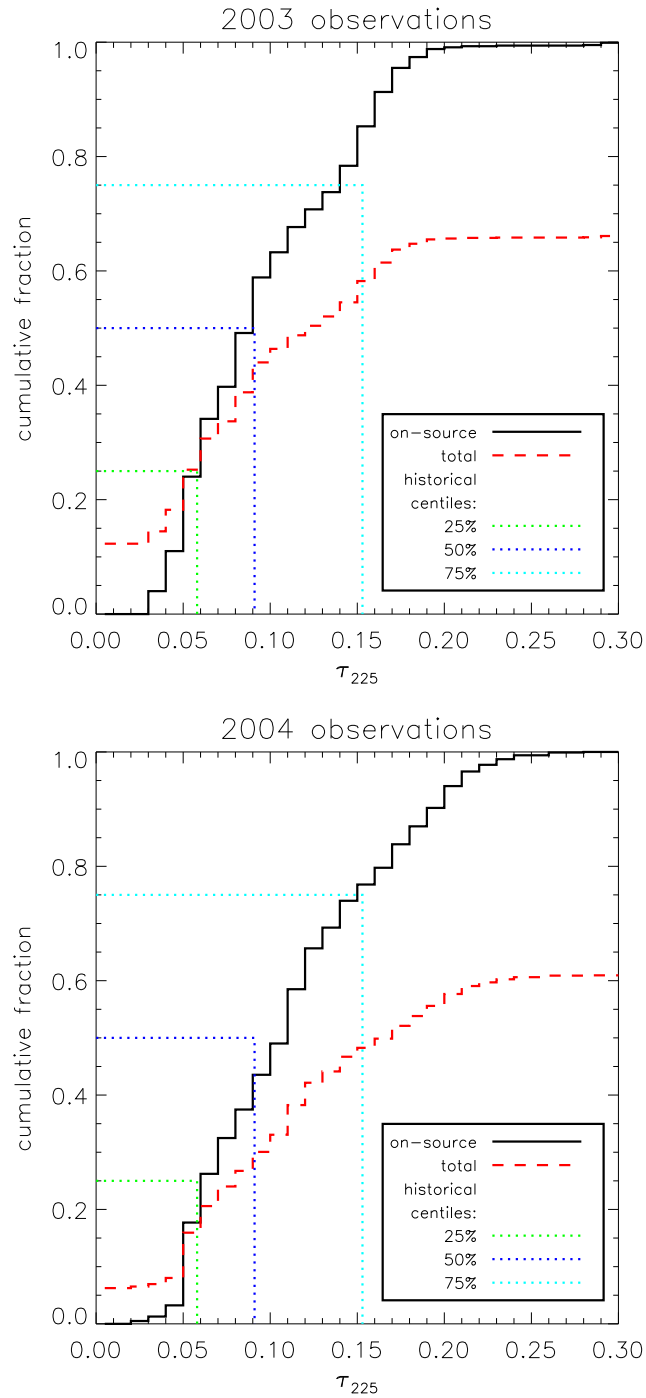


Figure 3.3: Cumulative distribution of τ_{225} for both observing runs. The historical 25%, 50%, and 75% centiles are shown on each plot, and our on-source time corresponds well with these averages (solid black line). However, after considering time when we could not observe due to bad weather, or when high-frequency programs observed in exceptionally good weather, it appears that the conditions during our runs were much worse than the historical averages (dashed red line). But, it should be noted that some of the bad weather time was caused by high winds or surface humidity, and not high values of τ_{225} .

very low, with a $100\ \mu\text{m}$ surface brightness of $1.33\ \text{MJy/sr}$.

3.2.2 Scan Pattern

Two nights at the start of the 2003 run were used to analyze different scan strategies which could be implemented to map the science fields. Prior to these studies, we had already decided to map the fields by raster scanning across them, stepping in the direction perpendicular to the scan, then raster scanning across the field in the opposite direction of the previous scan. This process is repeated until we have stepped across the entire field. With the geometry of the Bolocam focal plane, the most uniform coverage is obtained when the step size between scans is 162 arcseconds, so we maintained this step size during all of our tests. Additionally, the angle of the focal plane remained fixed for all of our tests because the rotator was not operable at the time³. Finally, we did not make any observations while chopping the secondary mirror of the telescope because it would reduce the amount of on-source time during an observation by a factor of two. Chopping would also remove signals with scales similar to the chop throw, and we wanted to achieve maximum fidelity on large scales. Additionally, the data is difficult to analyze because there is a chop-synchronous signal due to the receiver seeing the optics differently as a function of the throw⁴.

From our test observations, we found that the angle of the raster scan relative to the alt/az coordinate system had no effect on the noise level of the data. Therefore, we decided to scan parallel to either the RA or dec axis, which would allow us to map the science fields to a uniform depth in the most efficient way. Next, we found that the sensitivity of the Bolocam detectors is independent of how quickly the telescope turns around between scans⁵, so we had the telescope turn around as quickly as possible (approximately 9.5 seconds from the end of one scan to the start of the next). Finally, we varied the angular speed of the scans. Scanning more quickly broadens the profile of the Bolocam beams in frequency space, which

³The rotator was also not operable for the 2004 observing run. It would have been possible to rotate the dewar by hand for the test observations, but that would not have been practical for general observations. Since the rotation angle of the dewar is fixed in alt/az coordinates while the scan direction is parallel to RA or dec, the relative angle of the dewar to the scan direction changes continuously throughout the night. Therefore, even if the optimal rotation angle of the dewar was determined, we could only configure the system to be near that angle for a short amount of time each night.

⁴For single detector cameras, chopping is the only way to separate the atmospheric signal from the astronomical signal, but this is not the case with Bolocam. All of the beams from the $\gtrsim 100$ detectors overlap to a high degree through the atmosphere, so the majority of the atmospheric signal is common to all of the detectors and can be removed without chopping.

⁵Therefore, we can conclude that the microphonic, or any other, pickup from the accelerations in the turnarounds is negligible.

scan speed	sensitivity	time on-source	effective sensitivity
30	8.6 mK _{CMB} √sec	91%	9.0 mK _{CMB} √sec
60	6.1 mK _{CMB} √sec	84%	6.6 mK _{CMB} √sec
120	5.7 mK _{CMB} √sec	72%	6.7 mK _{CMB} √sec
240	4.0 mK _{CMB} √sec	57%	5.3 mK _{CMB} √sec

Table 3.2: Beam-smoothed point-source sensitivities achieved when scanning at various speeds during test observations prior to the 2003 observing run. The effective sensitivities shown in the far right column are obtained by dividing the sensitivity by the square root of the fraction of time spent on-source. Based on these results, all science observations were made while scanning at 240 arcseconds/sec.

means a larger amount of the astronomical signal will be separable from the atmospheric fluctuations at low frequency. See Figure 3.4. However, scanning at higher speeds results in less time on-source, since the relative fraction of time spent turning around between scans is larger⁶. In the end, we found that scanning at 240 arcseconds/sec was the optimal combination of instantaneous sensitivity and time spent on-source. See Table 3.2.

Our goal was to obtain maps with fairly uniform coverage over a square region with sides of approximately 40 arcminutes. To achieve uniform coverage over a region that size requires scanning the telescope over a square region with 50 arcminute sides. Therefore, each scan across this region takes 12.5 seconds, and 20 scans are required to map the entire field. Including turnaround time between scans, this means that a complete observation of the field is made in approximately 8 minutes.

3.3 Contrasts Between 2003 and 2004

Although very little changed between the 2003 observing run and the 2004 observing run, there was one important difference. In 2004 Bolocam was plagued by a large amount of noise from an unidentified source, but the most likely cause was poor grounding somewhere in the system. This noise is not common to all the detectors, and the only way to effectively remove it is with adaptive principle component analysis (PCA). Unfortunately, adaptive PCA also removes bright sources from the data, including all of the sources we use for calibrating Bolocam. The result is a slight, but noticeable, degradation in the instrument characterization that is described in Sections 3.4, 3.5, and 3.6 for the 2004 data. Section 4.4

⁶The CSO was not designed to scan this quickly. If it was equipped with an optimized motor drive, instead of simple ramps, then the CSO would probably be able to turnaround more quickly without making the accelerations worse.

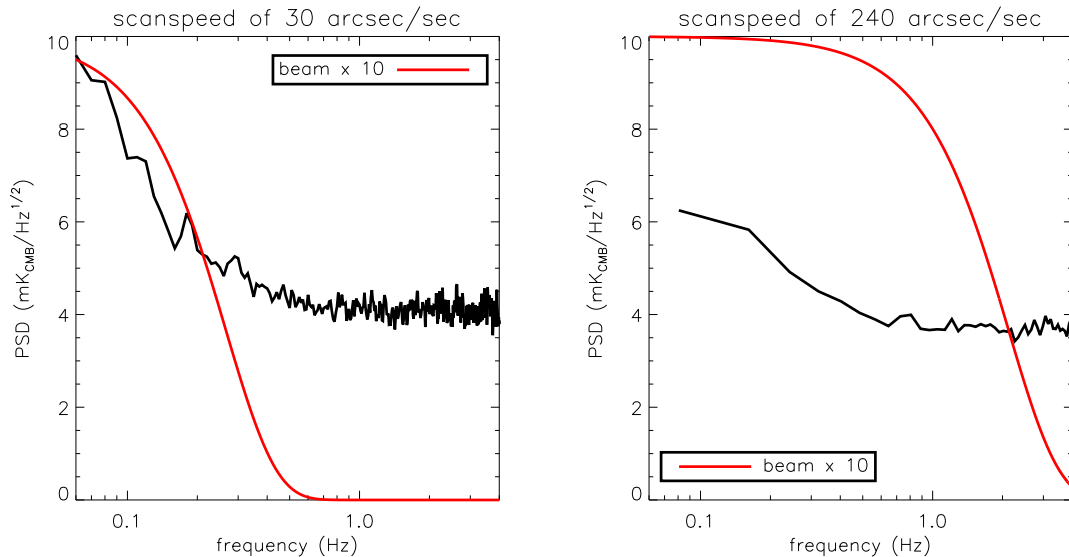


Figure 3.4: Results for two observations made during our study of various scan speeds prior to the 2003 observing run. The plot on the left shows an observation taken while scanning at 30 arcseconds/sec, and the plot on the right shows an observation taken while scanning at 240 arcseconds/sec. The power spectral density (PSD) of the time-ordered data is nearly identical for each observation, but the profile of the beam is dramatically different (in both cases the beam is normalized to have a peak height of 10). A much larger percentage of the power from a point source is above the $1/f$ knee when scanning at 240 arcseconds/sec.

contains more details about this noise.

3.4 Pointing Reconstruction

In order to find the conversion between the coordinates reported by the telescope and the actual location of each detector’s beam, we made observations of bright sources with known positions. We first determined the location of the beam from each detector relative to the array center, and then calculated the offset between the array center and the telescope coordinates.

3.4.1 Relative Beam Offsets

Approximately once every other night we made a fifteen minute observation of Uranus or Neptune. These planets are bright enough to appear at high signal-to-noise in a map made from a single bolometer, so they can be used to determine the position of each detector relative to the array center. Since Bolocam was held at a fixed angle in the

alt/az coordinate system for each observing run (2003 and 2004), each bolometer views the optics in the same way for the entire run and the coordinates on the sky in alt/az units remain fixed. Therefore, we combined the data from all the planet observations to determine the average position of each beam on the sky. See Figure 3.5. The uncertainties on these average positions were ~ 1 arcsecond for each observing run, which is negligible when compared to the 60 arcsecond full-width at half-maximum (FWHM) of a Bolocam beam. We found no evidence for a systematic difference in the beam positions derived from any single observation to the average beam position found from all the observations. This indicates that the optical system was very stable over the entire observing run, including a wide range of telescope elevation angles.

In order to better understand our optical system we first tried to model the observed beam positions using the Seidel aberration coefficients. The best fit of the Seidel coefficients produces a $\chi^2/DOF \sim 5000$, clearly not a good fit. Next, we tried to fit the optical system using the Zernike polynomials. Unfortunately, even with a seventh-order Zernike polynomial we still ended up with $\chi^2/DOF \sim 5000$. The lack of convergence of these polynomials is likely due to minor misalignments in the optical system [155]. However, these misalignments do not measurably affect the beam shapes, so they do not reduce the angular resolution of the system. Additionally, the actual location of each beam center is well characterized, so the poor fit produced by simple models of the optical system does not degrade the performance of Bolocam.

3.4.2 Developing a Model of the Array Center Location

We observed a bright source with a known position near the science field for approximately ten minutes once every two hours. Three different sources were used for the SDS1 field (0106+013, 0113-118, and 0336-019), and two different sources were used for the Lynx field (0804+499 and 0923+392). Each source was observed for five minutes while scanning parallel to RA, then for five minutes scanning parallel to dec (analogous to how the science fields were observed).

To determine if there is a systematic difference between observations made in these two scan directions, we examined the difference in the centroided position of the source for the map made from the RA scans and the map made from the dec scans for each ten-minute-long observation. Since we observed five sources, each with a centroid difference in

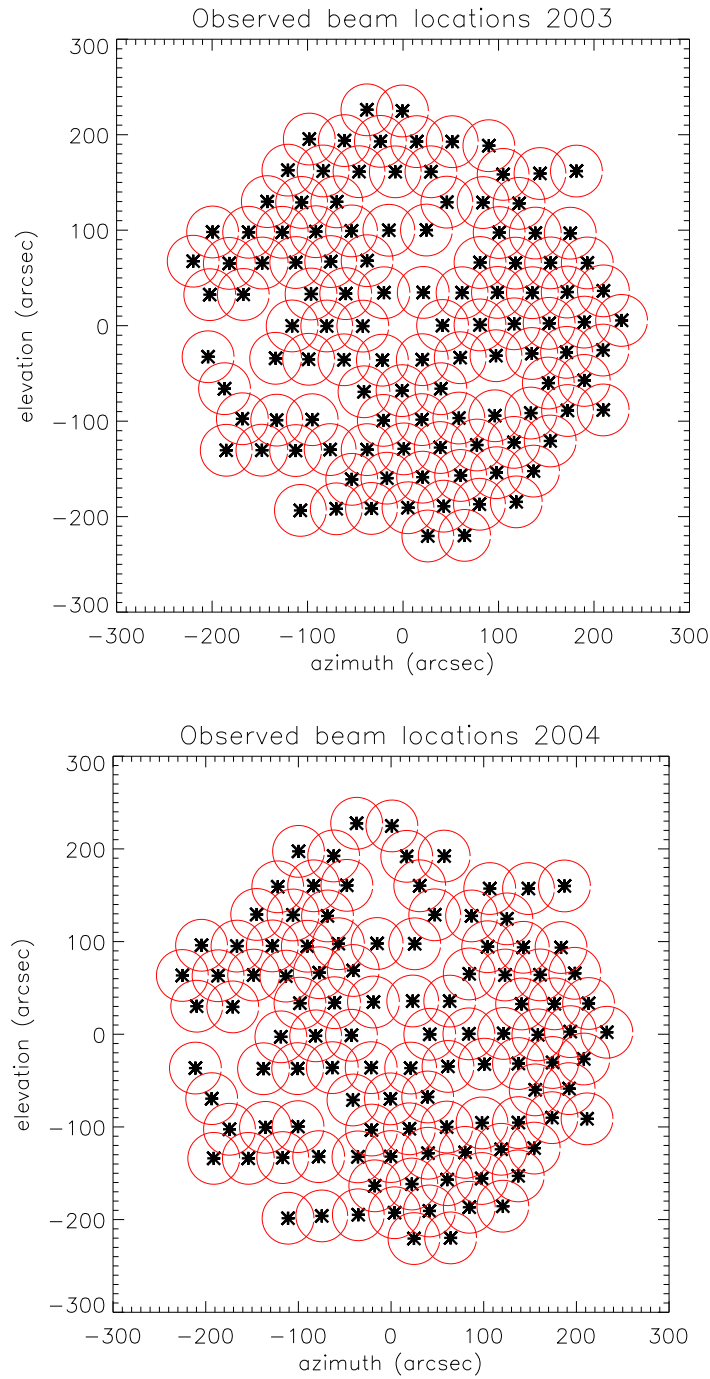


Figure 3.5: Location of the beam center of every working detector relative to the center of the array. The red rings around each beam center represent the approximate FWHM of the beam. The top plot shows the beam locations during the observing run in 2003, and the bottom plot represents the locations during the observing run in 2004.

source	0106+013	0113-118	0336-019	0804+499	0923+392
measured flux (Jy)	1.30 ± 0.09	0.87 ± 0.07	0.97 ± 0.07	0.33 ± 0.02	$2.76 \pm .15$
2003 centroiding error (arcsec)	2.85	3.64	3.32	4.20	2.13
2004 centroiding error (arcsec)	16.35	8.79	10.06	9.30	4.60

Table 3.3: Measured uncertainty in the centroided location for each of the five bright sources used for pointing calibration. There is a large degradation in the centroiding errors for the 2004 data, but the errors average down when constructing the pointing model. The end result is that the uncertainty in the 2004 pointing model is only about 15% worse than the uncertainty in the 2003 pointing model.

two orthogonal directions, there are a total of ten independent data sets to consider. For each set, the mean and standard deviation on the mean were calculated, and the mean was consistent with zero for all ten of the data sets⁷. Therefore, there is no systematic pointing offset between observations taken while scanning parallel to RA and those taken while scanning parallel to dec.

These distributions were then used to determine the uncertainty in the centroided position for each source. We found that there is no pointing difference between maps made from RA scans and those made from dec scans, and it is unlikely there is any significant change in the telescope over a ten minute period. Therefore, the difference of the centroided position in the map made from RA scans and the centroided position in the map made from dec scans is likely to be caused by measurement uncertainty on the centroid location. So, the uncertainty in the centroid for each source is calculated from the distribution of these centroid offsets. See Table 3.3. As expected, the centroiding error for the five sources is inversely proportional to the flux of the source.

Next, the pointing data was broken up into three distinct subsets corresponding to the azimuthal position of the telescope: SDS1 was observed between azimuth angles of 90 and 270 (in the south), while Lynx was observed between azimuth angles of -90 and 90 (in the north), and also between azimuth angles of 270 and 360.⁸ Most of the Lynx data was taken between an azimuth angle of -90 to 90, so the third subset of data is considerably smaller than the first two (about 1/5 the size). Note that the slewing limits of the telescope are

⁷Specifically, five data sets are within 1σ of zero, eight data sets are within 2σ of zero, and all ten data sets are within 2.3σ of zero.

⁸Azimuth angles between -90 and 0 are reached by slewing the telescope from the north, while azimuth angles between 270 and 360 are reached by slewing the telescope from the west. We found a slight difference in the pointing between the two sets, so we chose to treat them as distinct.

roughly equal to azimuth angles of -90 to 360. Each of these subsets was found to produce a slightly different pointing offset model.

There is a correlation between the elevation angle of the telescope and the pointing offset for each of these subsets. We attempted to model this correlation with several low order polynomials, but we ended up using a quadratic fit of elevation versus pointing offset because the residual scatter of the data does not improve significantly when going to a higher order fit. See Figure 3.6. We then looked for a correlation between telescope azimuth angle and the residual offset, and we concluded there is no correlation for the following reasons: 1) the Pearson's correlation coefficient indicated there is only a $\sim 50\%$ chance of any correlation between telescope azimuth angle and pointing offset and 2) the residual RMS deviations of the data were not noticeably improved after removing a fit of azimuth versus pointing offset (i.e., the fit did not improve our pointing model). Therefore, a simple quadratic fit of telescope elevation angle versus pointing offset served as our only pointing model. Plots of this final model can be found in Figure 3.7.

Finally, we tested to see if the pointing improves/degrades as a function of time of day. To test for any changes over the course of the night we binned up the residual scatter of the pointing data after removal of the quadratic fit as a function of universal time. See Figure 3.8. This data shows that there is no change in the quality of our pointing over the course of the night.

3.4.3 Uncertainties in the Pointing Model

The pointing uncertainty is a measure of how far away our model is from where the telescope was truly pointing during an observation⁹. To determine the uncertainty in our pointing model, σ_{ptg} , we analyzed the RMS deviations in the pointing data after the pointing model is removed. The RMS deviations are due to the uncertainty in the centroided position of each source, σ_{cen} ; they are also due to fluctuations in the telescope, errors in the reported position of the telescope, changes in the Bolocam optics, etc. (i.e., RMS deviations = $\sigma_{tot} = \sqrt{\sigma_{cen}^2 + \sigma_{ptg}^2}$). σ_{tot} was calculated for each source, for each of the three subsets based on telescope azimuth, along with the uncertainty on σ_{tot} , $\sigma_{\sigma_{tot}}$. We could then determine $\sigma_{ptg} = \sqrt{\sigma_{tot}^2 - \sigma_{cen}^2}$ and $\sigma_{\sigma_{ptg}} = \frac{\sigma_{tot}^2 \sigma_{\sigma_{tot}}^2 + \sigma_{cen}^2 \sigma_{\sigma_{cen}}^2}{\sigma_{ptg}^2}$ for each source in each subset.

⁹The pointing uncertainty is not to be confused with the pointing offset, which measures the difference between the coordinates reported by the telescope and where the telescope was actually pointing. Our pointing model is an attempt to determine this pointing offset.

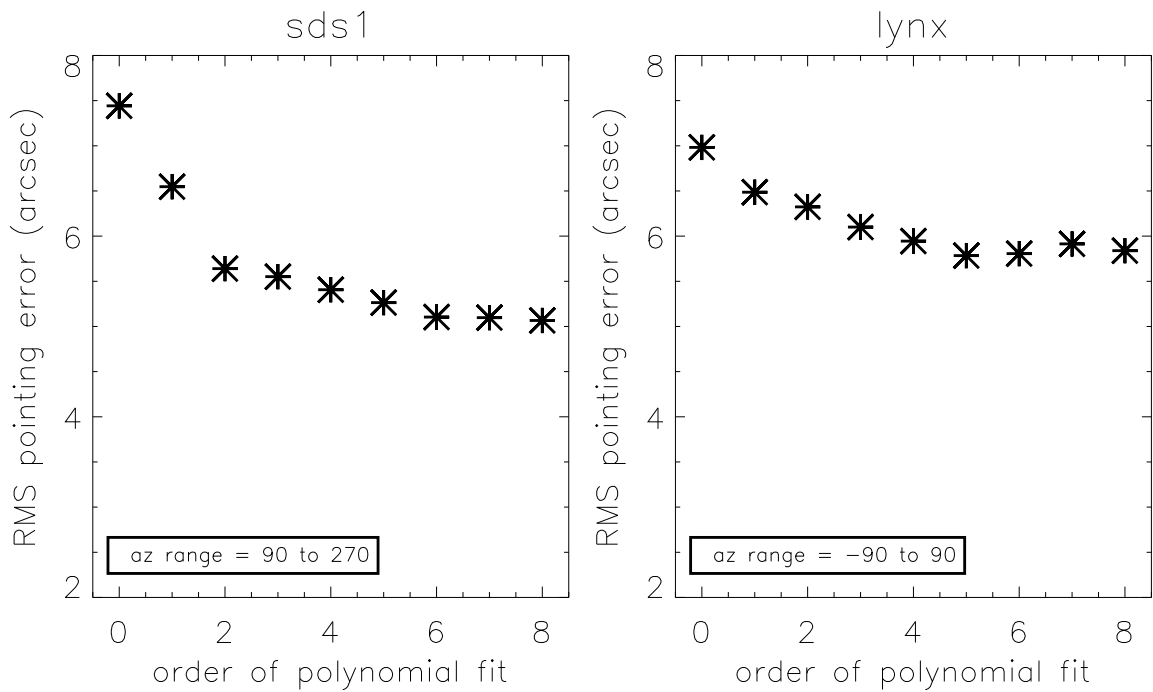


Figure 3.6: Each plot shows the residual scatter in the pointing data after removal of a n^{th} -order polynomial fit of telescope elevation angle vs. pointing offset. n was varied between 0 and 8, and $n = 2$ was chosen as the best compromise between residual pointing error and a physically reasonable fit. The plot on the left shows the 2003 pointing data for SDS1 and the plot on the right shows the 2003 pointing data for Lynx taken between azimuth of -90 to 90.

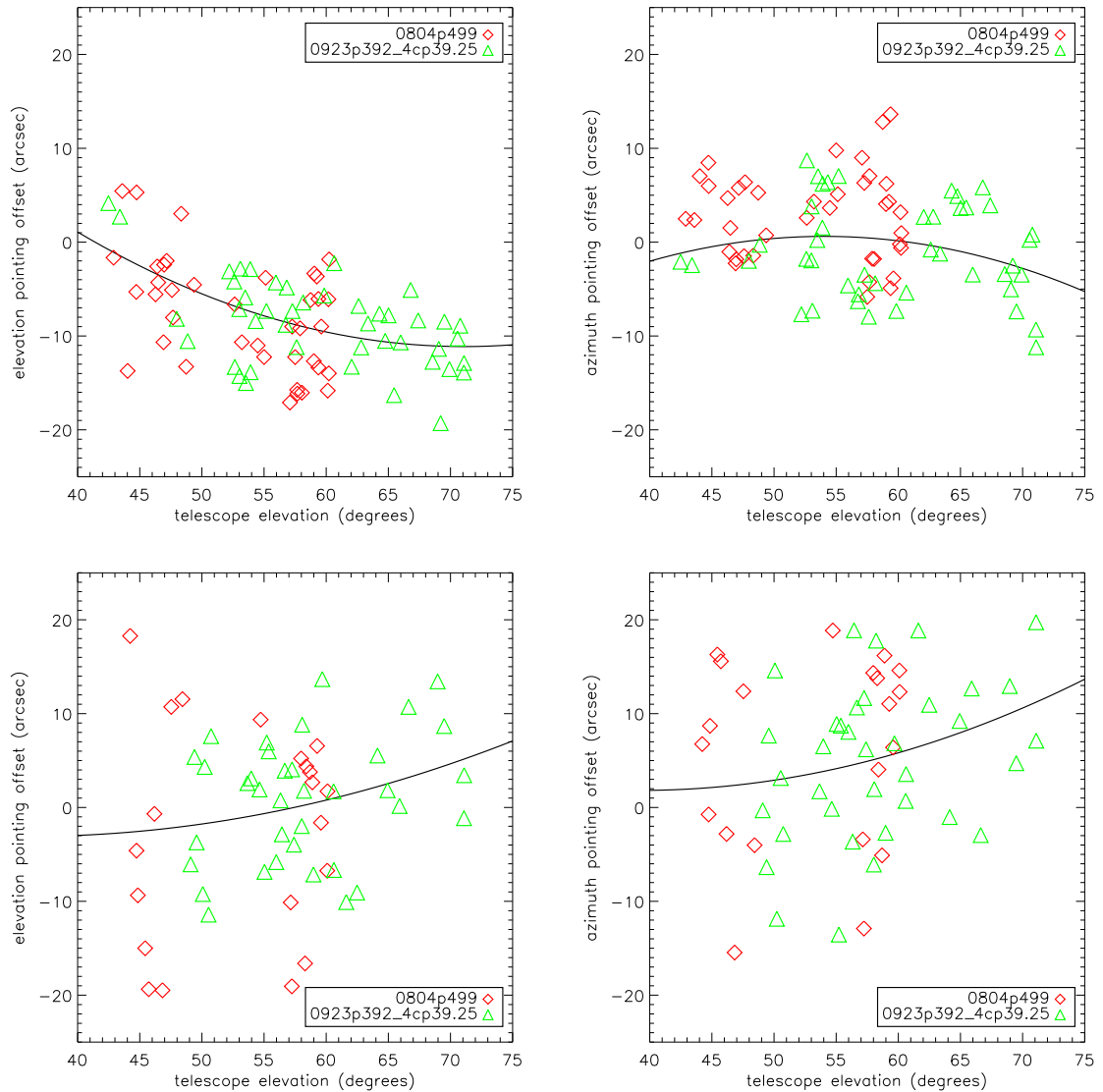


Figure 3.7: All of the raw pointing data for Lynx at azimuth angles between -90 and 90 degrees. The top row is data from 2003, and the bottom row is data from 2004. The pointing model (quadratic fit) is overlaid. Similar models were fit to the SDS1 pointing data and the Lynx data at azimuth angles between 270 and 360 degrees. Note that the scatter is slightly larger in 2004 due to increased noise in the data during that observing run.

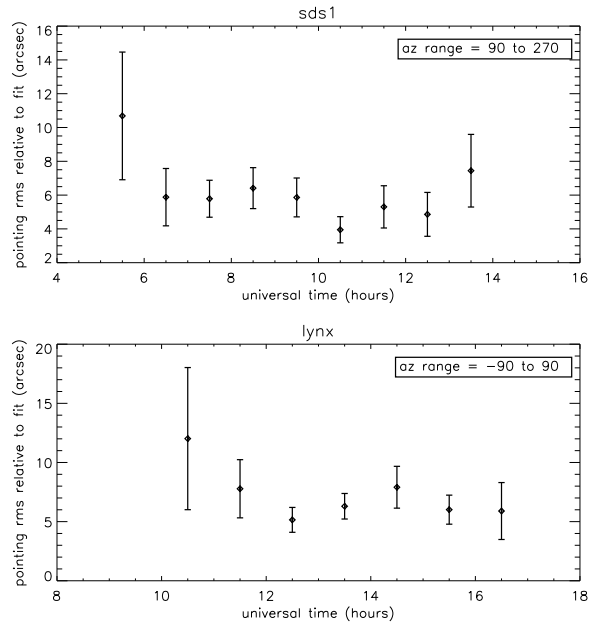


Figure 3.8: Residual pointing RMS (after removal of a quadratic fit versus telescope elevation) is shown as a function of time of day for the 2003 data. There does not appear to be any degradation/improvement in the pointing over the course of the night.

The next step was to determine σ_{ptg} for each of the subsets by taking the weighted mean over the pointing sources contained within that subset, since there is no evidence that σ_{ptg} is different for the different sources we observed. Finally, σ_{ptg} for the entire set of data was calculated, again taking the weighted mean over the three subsets since there is no evidence for a difference in σ_{ptg} between these subsets. The results are summarized in Table 3.4 and Figure 3.9. In the end, we determined that the uncertainty on our pointing model is just under 5 arcseconds in 2003 and just less than 6 arcseconds in 2004. This 5 - 6 arcsecond uncertainty is minor compared to the 60 arcsecond FWHM of a Bolocam beam¹⁰.

3.5 Flux Calibration

Our flux calibration is based on observations of Uranus and Neptune, which have fluxes known to $\simeq 6\%$ in our band, and the uncertainty in our final calibration is dominated by this 6% uncertainty in the fluxes of the planets. We observed one of these planets for approximately fifteen minutes every other night. Additionally, we made several observations

¹⁰To be specific, the 5 - 6 arcsecond uncertainty in the pointing model results in a $\lesssim 1\%$ reduction in the peak signal from a point source.

2003 data

subset	pointing source	1σ pointing error, σ_{ptg}
SDS1	0106+013	4.95 ± 0.67 arcsec
	0113-118	4.01 ± 1.01 arcsec
	0336-019	5.12 ± 0.92 arcsec
	all data	4.79 ± 0.48 arcsec
Lynx ($270 \leq AZ \leq 360$)	0804+499	0.81 ± 4.71 arcsec
	0923+392	4.13 ± 1.30 arcsec
	all data	3.90 ± 1.25 arcsec
Lynx ($-90 \leq AZ \leq 90$)	0804+499	4.80 ± 0.96 arcsec
	0923+392	5.42 ± 0.64 arcsec
	all data	5.23 ± 0.53 arcsec
all data	all data	4.91 ± 0.34 arcsec

2004 data

subset	pointing source	1σ pointing error, σ_{ptg}
SDS1	0106+013	10.49 ± 8.96 arcsec
	0113-118	6.65 ± 3.94 arcsec
	0336-019	7.00 ± 3.90 arcsec
	all data	7.14 ± 2.64 arcsec
Lynx ($270 \leq AZ \leq 360$)	0804+499	7.20 ± 1.99 arcsec
	0923+392	7.24 ± 1.75 arcsec
	all data	7.22 ± 1.31 arcsec
Lynx ($-90 \leq AZ \leq 90$)	0804+499	7.36 ± 2.47 arcsec
	0923+392	4.69 ± 1.00 arcsec
	all data	5.06 ± 0.92 arcsec
all data	all data	5.88 ± 0.73 arcsec

Table 3.4: Summary of the 1σ pointing error of the model fit to the data (σ_{ptg}) for the 2003 observing run (top) and the 2004 observing run (bottom).

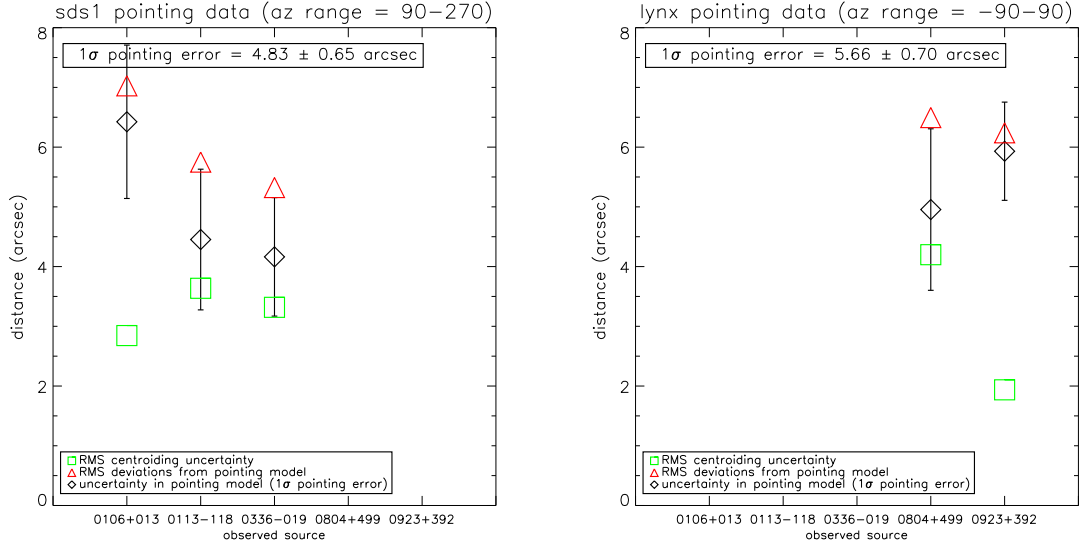


Figure 3.9: Summary of the uncertainty of the 2003 pointing model for each pointing source in two of the three subsets that the data was divided into based on telescope azimuth angle. Note that there is no statistically significant difference in the 1σ pointing error of the model for different sources or different subsets.

of NGC2071IR and 0923+392, which were used as secondary calibrators.

3.5.1 Overall Theory

Before discussing flux calibration it is useful to determine the expected voltage recorded by a bolometer for a given astronomical signal. Consider a nearly ideal point source (much smaller than the detector beam), described by a surface brightness, $B_\nu(\nu)$,¹¹ and a total solid angle Ω .¹² The voltage recorded by detector i will then be

$$V_i = s_i g_i \eta_i \eta_{i,atm} A_{i,tel} \int d\nu \Theta_i(\nu) \eta_{i,tel}(\nu) \Theta_{i,atm}(\nu) \Omega B_\nu(\nu) \quad (3.1)$$

where s_i is the responsivity of the detector in V/W, g_i is the gain in the electronics, η_i is the optical efficiency of the detector, $\eta_{i,atm}$ is the transmission of the atmosphere at our band center of ~ 143 GHz, $\eta_{i,tel}(\nu)$ is the optical efficiency of the telescope, $A_{i,tel}$ is the

¹¹The surface brightness can be described by an effective Rayleigh-Jeans temperature, with $B_\nu(\nu) = 2k_B T(\nu)/\lambda^2$, where k_B is Boltzmann's constant, $T(\nu)$ is the effective temperature of the source, and $\lambda = c/\nu$ is wavelength.

¹²Our calibration is based on observations of the planets, which have a constant surface brightness. However, the angular size of a given planet varies in a known way because the distance between the Earth and the planet changes as the two objects orbit the sun.

effective area of the telescope in m^2 ,¹³ $\Theta_i(\nu)$ is the normalized transmission of the Bolocam optical system for the detector, $\Theta_{i,atm}(\nu)$ is the transmission of the atmosphere (normalized to unity at our band center). Since we have no way to measure $\eta_{i,tel}(\nu)$, we are forced to make the approximation $\eta_{i,tel}(\nu) \simeq \eta_{i,tel}$. However, this approximation should be fairly good for the relatively small fractional bandwidth of the Bolocam optics. The detector beams also overlap to a high degree when passing through the atmosphere, so we will assume $\Theta_{i,atm}(\nu) = \Theta_{atm}(\nu)$. This leaves us with

$$V_i \simeq s_i g_i \eta_i \eta_{i,atm} A_{i,tel} \eta_{i,tel} \Omega \int d\nu \Theta_i(\nu) \Theta_{atm}(\nu) B_\nu(\nu). \quad (3.2)$$

However, it is more useful to rewrite Equation 3.2 as

$$V_i \simeq \frac{\chi_i \Omega}{(\Delta\nu_{atm})_i} \int d\nu \Theta_i(\nu) \Theta_{atm}(\nu) B_\nu(\nu) \quad (3.3)$$

where $\chi_i = s_i g_i \eta_i \eta_{i,atm} A_{i,tel} \eta_{i,tel} (\Delta\nu_{atm})_i$ is the flux calibration of the detector (in V/Jy), and $(\Delta\nu_{atm})_i = \int d\nu \Theta_i(\nu) \Theta_{atm}(\nu)$ is the effective bandwidth of the detector including the effects of the atmosphere. Similarly, it is possible to determine the voltage induced in a detector from fluctuations in the thermal emission from the atmosphere by

$$V_i = \frac{\chi_i}{A_{i,tel} (\Delta\nu_{atm})_i} \int d\nu \Theta_i(\nu) \lambda^2 \frac{2k_B \delta\varepsilon_{atm}(\nu) T_{atm}}{\lambda^2}, \quad (3.4)$$

where λ^2 takes the place of $A_{i,tel} \Omega$ for a beam-filling source such as the atmosphere, $\delta\varepsilon_{atm}(\nu)$ is a fluctuation in the emissivity of the atmosphere, and T_{atm} is the effective RJ temperature of the atmosphere. The fluctuations in $\varepsilon_{atm}(\nu)$ are caused primarily by changes in the column depth of precipitable water vapor, d_{pw} . So,

$$\delta\varepsilon_{atm}(\nu) \simeq \frac{\partial\varepsilon_{atm}(\nu)}{\partial d_{pw}} \delta d_{pw}. \quad (3.5)$$

Note that $\delta\varepsilon_{atm}(\nu)$ is also a weak function of d_{pw} . However, since d_{pw} is difficult to measure on short time scales we set $\delta\varepsilon_{atm}(\nu, d_{pw}) = \delta\varepsilon_{atm}(\nu, d_{pw} = 1.5 \text{ mm})$ because the median

¹³ $A_{i,tel}$ is not well defined because we do not have a simple top-hat illumination of the primary mirror. If $A_{i,tel}$ is set equal to the size of the primary mirror, then the normalization of $\eta_{i,tel}(\nu)$ will be artificially low because the primary is under illuminated. Alternatively, $A_{i,tel}$ can be set equal to λ^2/Ω_{beam} , and $\eta_{i,tel}(\nu)$ will only describe the efficiency losses due to poor reflectivity or scattering. Therefore, there is a degeneracy between $A_{i,tel}$ and the normalization of $\eta_{i,tel}(\nu)$. However, this degeneracy does not affect the flux calibration determined for our data.

value of d_{pw} when we are observing on Mauna Kea is ~ 1.5 mm. So, for fluctuations in thermal emission from the atmosphere we have

$$V_i \simeq \frac{\chi_i 2k_B T_{atm}}{A_{i,tel}(\Delta\nu_{atm})_i} \int d\nu \Theta_i(\nu) \frac{\partial \varepsilon_{atm}(\nu)}{\partial d_{pw}} \delta d_{pw}. \quad (3.6)$$

From Equation 3.4 we can measure the absolute calibration, $\bar{\chi} = \frac{1}{n_{bolos}} \sum_{i=1}^{n_{bolos}} \chi_i$, using observations of point sources with known fluxes (i.e., the planets), with

$$\bar{\chi} = \frac{1}{n_{bolos} \Omega} \sum_{i=1}^{n_{bolos}} \frac{V_i(\Delta\nu_{atm})_i}{\int d\nu \Theta_i(\nu) \Theta_{atm}(\nu) B_\nu(\nu)}. \quad (3.7)$$

The relative calibration, $\chi_i/\bar{\chi}$, can be calculated from point source observations using

$$\chi_i/\bar{\chi} = \left(\frac{V_i(\Delta\nu_{atm})_i}{\int d\nu \Theta_i(\nu) \Theta_{atm}(\nu) B_\nu(\nu)} \right) / \left(\frac{1}{n_{bolos}} \sum_{i=1}^{n_{bolos}} \frac{V_i(\Delta\nu_{atm})_i}{\int d\nu \Theta_i(\nu) \Theta_{atm}(\nu) B_\nu(\nu)} \right), \quad (3.8)$$

and from the science field observations according to

$$\chi_i/\bar{\chi} = \left(\frac{V_i(\Delta\nu_{atm})_i}{\int d\nu \Theta_i(\nu) \frac{\partial \varepsilon_{atm}(\nu)}{\partial d_{pw}} \delta d_{pw}} \right) / \left(\frac{1}{n_{bolos}} \sum_{i=1}^{n_{bolos}} \frac{V_i(\Delta\nu_{atm})_i}{\int d\nu \Theta_i(\nu) \frac{\partial \varepsilon_{atm}(\nu)}{\partial d_{pw}} \delta d_{pw}} \right). \quad (3.9)$$

Note that the science fields cannot be used to determine the absolute calibration because it is difficult to determine T_{atm} , and $\partial \varepsilon_{atm}(\nu)/\partial d_{pw}$ is determined from an imperfect atmospheric model. In Equation 3.9 we have assumed that $A_{i,tel}$ is the same for every bolometer. This assumption is reasonable since Ω_{beam} is the same for every bolometer within our measurement errors (see Section 3.6.3), and $A_{tel} = \lambda^2/\Omega_{beam}$.

The DC output of the lockin amplifiers provides a continuous measurement of the operating resistance of each bolometer. If the total thermal emission from the atmosphere, $\eta_{i,atm} T_{atm}$, increases, then the optical loading on the bolometer will go up and the bolometer resistance will decrease. Therefore, the median lockin DC output taken over all bolometers for a single observation is a monotonically decreasing function of $\eta_{i,atm}$ for a fixed value of T_{atm} . Additionally, the responsivity of the bolometer, s_i , decreases monotonically as the bolometer resistance decreases. Therefore, the flux calibration, χ_i , which is proportional to the product of $\eta_{i,atm}$ and s_i , is expected to be a monotonic function of the bolometer resistance. Consequently, we have empirically determined the flux calibration as a function

of the lockin DC output.

Six different flux calibrations were needed for the 2003 data set. The base temperature of the bolometers was changed on November 4, 2003, and the bias voltage applied to the bolometers was changed on November 5, 8 (twice), and 10, 2003. These bias voltage changes were not intentional, and were caused by an instability in the electronics used to generate our bias signal. Each of the changes listed above caused a change in the responsivity of the bolometers, so a different flux calibration is needed after each change. Note that for the first five data sets mentioned above, the lockin DC output changed by less than one or two percent over all the observations included in that set (since the data for each set is from one or two nights), so we did not fit the calibration versus median lockin DC output. However, the last 2003 data set had lockin DC output voltages that varied by up to $\simeq 10\%$, so we did fit the calibration versus median lockin DC output for this set.

3.5.2 Relative Calibration of the Detectors

For the 2004 data set, the increased noise prevented us from determining the relative calibration of the detectors. Therefore, we set the relative calibration of every detector equal to one for the 2004 data. This will not bias our results, but means that the 2004 data will not be co-added in the optimal way. However, since the relative calibration of all the detectors is fairly close to one, the resulting degradation will be small.

The relative calibration for the 2003 data was determined using the $\simeq 1000$ separate observations of the two science fields, Lynx and SDS1. Of these $\simeq 1000$ observations, approximately 800 were taken after the last calibration change on November 10. Since these observations covered regions of the sky with negligible amounts of astronomical flux, the fluctuations in thermal emission from the atmosphere are the dominant source of the AC signal recorded by each bolometer. Additionally, this signal should be the only one that is correlated among all the bolometers since the beams from all bolometers overlap to a high degree when passing through the atmosphere. Therefore, this signal should be the same in each bolometer, weighted by the responsivity of that bolometer. So, by determining how correlated the data from each bolometer is with this common signal, it is possible to determine the relative responsivity (calibration) of each bolometer¹⁴.

¹⁴Although none of the bolometer signals will be 100% correlated with the common mode signal, the ratio of the correlation for each bolometer signal to the average correlation of all the bolometer signals is the only quantity needed to determine the relative flux calibration. This is described mathematically in

Let the bolometer time-streams for a given observation be represented by d_{in} where i is the bolometer number ranging between 0 and n_{bolos} , and n is the sample number. First, we calculate a template describing the fluctuations in thermal emission from the atmosphere, a_n , with

$$a_n = \frac{1}{n_{bolos}} \sum_{i=1}^{i=n_{bolos}} d_{in}. \quad (3.10)$$

The correlation coefficient, c_i , is then determined from

$$c_i = \frac{\sum_n \tilde{a}_n d_{in}}{\sum_n \tilde{a}_n^2}, \quad (3.11)$$

where $\tilde{a}_n = a_n - \bar{a}$, and \bar{a} is the mean of a_n . However, it is more useful to work in terms of

$$\tilde{c}_i^{sky} = c_i \frac{(\Delta\nu_{atm})_i}{\int d\nu \Theta_i(\nu) \frac{\partial \varepsilon_{atm}(\nu)}{\partial d_{pw}}}. \quad (3.12)$$

From Equation 3.6, we see that

$$\chi_i \propto \frac{V_i (\Delta\nu_{atm})_i}{\int d\nu \Theta_i(\nu) \frac{\partial \varepsilon_{atm}(\nu)}{\partial d_{pw}}}. \quad (3.13)$$

Combining Equations 3.12 and 3.13 we have

$$\frac{\tilde{c}_i^{sky}}{\chi_i} = \frac{c_i}{V_i}. \quad (3.14)$$

Since the correlation coefficient for each bolometer, c_i , is proportional to the voltage induced by the common mode atmospheric signal, V_i , this means that $\tilde{c}_i^{sky} \propto \chi_i$. Consequently, the relative calibration is equal to

$$\frac{\chi_i}{\bar{\chi}} = \frac{\tilde{c}_i^{sky}}{\frac{1}{n_{bolos}} \sum_{i=1}^{n_{bolos}} \tilde{c}_i^{sky}}. \quad (3.15)$$

After determining the relative calibration for each working bolometer for each science field observation, we then calculated the best fit relative calibration for each bolometer for each of the six data sets (this best fit was a simple mean for the first five data sets, and a polynomial fit versus median lockin DC output for the last data set). See Figure 3.10

Equation 3.15.

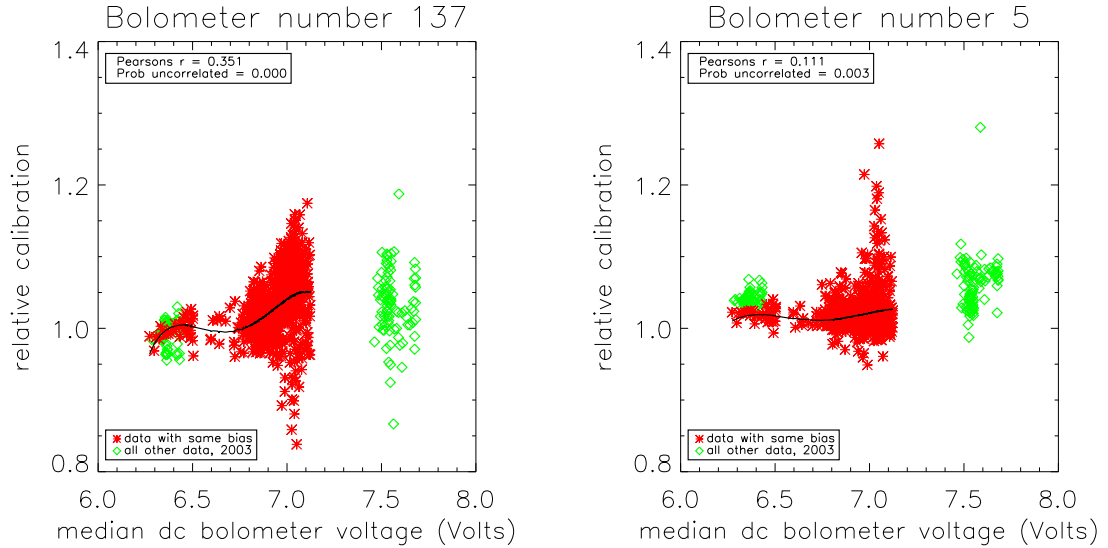


Figure 3.10: Each plot shows the relative calibration for each science field observation taken after November 10, 2003 in red (80% of the total data), and the other 2003 science field observations in green. Note that the data in green spans five different calibration sets of data, and are all in a different calibration set from the data in red. Overlaid is a fit of relative calibration versus median lockin DC output for the red data set. The plot on the left shows a bolometer with a relative calibration that is a strong function of the median lockin DC output, while the plot on the right shows a bolometer with a nearly flat relative calibration.

for typical plots of relative calibration versus median lockin DC output. Every bolometer produced a relative calibration between 0.74 and 1.31, and the standard deviation of the relative calibrations is .08 (so most bolometers have a relative calibration within $\sim 10\%$ of 1.00). The average (over bolometers) uncertainty on the relative calibration for each data set is shown in Table 3.5

Additionally, it is possible to determine the relative calibration from observations of bright point sources. The problem is that the source has to be bright enough to be seen by an individual bolometer in a single observation, which is true only for Uranus and Neptune

average statistical uncertainty on relative calibration for each calibration data set					
031102 ob1	031104 ob1	031105 ob1	031108 ob1	031108 ob70	031110 ob1
to	to	to	to	to	to
031103 ob40	031104 ob17	031107 ob42	031108 ob69	031109 ob70	031208 ob77
0.16%	1.23%	0.75%	0.76%	1.24%	0.12%

Table 3.5: The average statistical uncertainty on the relative calibration for each bolometer for each of the six calibration data sets.

among the sources we observed. So, we used each observation of these planets to determine a relative calibration for each bolometer¹⁵.

To start, we used a peak normalized¹⁶ map made from co-adding all bolometers and all observations of Uranus and Neptune to serve as a template for the shape of our beam. Then, we determined the peak signal voltage, V_i , for maps made of each bolometer's signal for each of the planet observations by fitting the map to the peak normalized beam shape template. Next, we computed

$$\chi_i = V_i \frac{(\Delta\nu_{atm})_i \Omega}{\int d\nu \Theta_i(\nu) \Theta_{atm}(\nu) \nu^2 T(\nu)} \quad (3.16)$$

using Equation 3.3, where $\Theta_{atm}(\nu)$ is the atmospheric transmission at $d_{pw} = 1.5$ mm [34]. It is then trivial to compute the relative calibration, $\chi_i/\bar{\chi}$. Recall that the overall normalization of the emissivity of the atmosphere is accounted for by fitting the calibration versus the median lockin DC output signal. Therefore, since the shape of $\Theta_{atm}(\nu)$ is relatively constant over the range of d_{pw} we observe in, it is adequate to use the value of $\Theta_{atm}(\nu)$ at d_{pw} of 1.5 mm. These relative calibration values were then compared to those derived from the science field observations, and the two sets of values agree well. See Figure 3.11.

3.5.3 Absolute Calibration

First, single-observation maps co-added over all bolometers (weighted by the relative calibrations found above) were made of all the observations of Uranus, Neptune, 0923+392, and NGC2071IR¹⁷. Since we did not have enough observations of Uranus and Neptune to adequately determine the shape of the calibration versus lockin DC output, we used 0923+392 and NGC2071IR as secondary calibrators. These two sources are known to have minimal variations in emitted flux as a function of time, so they are well suited to be used

¹⁵Note that there are a factor of $\simeq 100$ fewer observations of the planets than of the science fields, so the calibration derived from the planet observations will not be as precise as the calibration derived from the science field observations.

¹⁶The maps were peak normalized by fitting them to our beam profile pixelated at the same resolution as the map. This means that the value of the central pixel is $\simeq 0.95$, which is the expected value for the center pixel of a 60 arcsecond FWHM Gaussian beam normalized to 1 and pixelated at 20 arcseconds. The maps are made at this relatively coarse pixelization because of the lack of data in single observation maps made from a single bolometer, where some map pixels contain no data even with 20 arcsecond pixels.

¹⁷Mars was also observed, but there were inconsistencies in the beam profile produced by these observations. See Section 3.6.2. Therefore, the Mars observations were discarded.

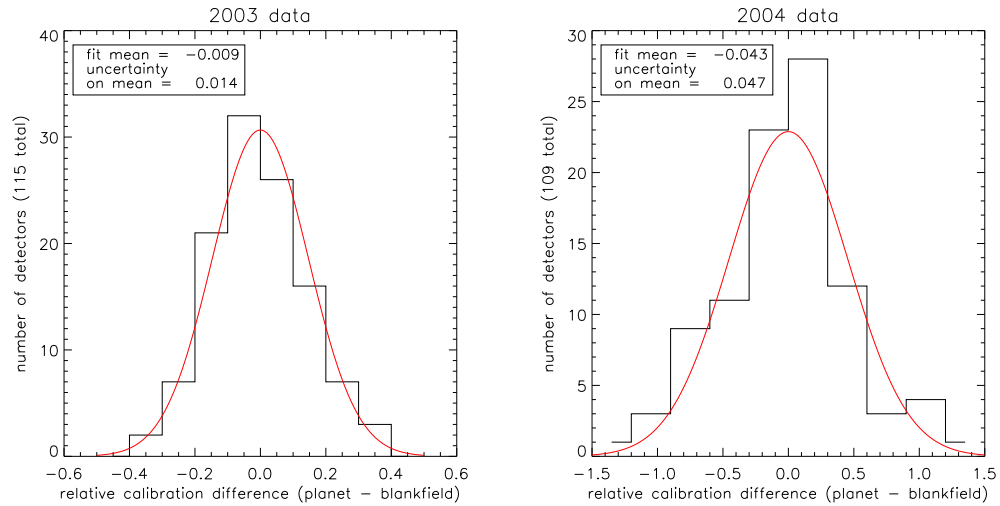


Figure 3.11: The plot on the left shows the difference between the relative calibration derived from the observations of Uranus and Neptune and the relative calibration derived from the observations of science fields for one of the data sets for 2003. The plot on the right shows the same values for the 2004 data, except that the relative calibration is assumed to be one for every detector in 2004 because noise prevented us from determining the relative calibration from the science field observations. In both cases, the relative calibration determined from the planet observations is consistent with the relative calibration determined from the science field observations. The wide distribution of relative calibration values determined from the planets is due to the relatively small number of observations made of the planets ($\lesssim 20$ each observing season).

for flux calibration [102, 121]¹⁸. Note that we did not use any of the published fluxes for 0923+392 or NGC2071IR, rather the fluxes were left as free parameters and they were used to determine the shape of the calibration curve versus lockin DC output.

Next, we determined the peak signal voltage by fitting each map to a peak normalized beam profile. Then, we used the peak signal voltage and median lockin DC output from each observation to determine the fit parameters in the following function

$$V_j(V_{DC}) = F_j(\alpha_1 + \alpha_2 V_{DC}), \quad (3.17)$$

where F_j is equal to the flux of the j^{th} source (known for Uranus and Neptune, left as a free parameter for NGC2071IR and 0923+392), and α_1 and α_2 free parameters. The planet fluxes were calculated from

$$F_j = \frac{2\Omega k_B}{c^2 n_{bolos}} \sum_{i=1}^{n_{bolos}} \left(\frac{1}{(\Delta\nu_{atm})_i} \int d\nu \Theta_i(\nu) \Theta_{atm}(\nu) \nu^2 T_j(\nu) \right), \quad (3.18)$$

where $\Theta_{atm}(\nu)$ is calculated at 1.5 mm of precipitable water vapor, and $\Theta_i(\nu)$ was measured with a Fourier transform spectrometer, $T_j(\nu)$ is effective Raleigh-Jeans temperature of the planet given in Griffin and Orton [57] or Orton et al. [100], and Ω is solid angle of the planet calculated from the James Clerk Maxwell Telescope (JCMT) website [68]. See Figure 3.12. Note that for the five data sets prior to the one beginning on November 10, 2003 we have set $\alpha_2 = 0$ since the range of V_{DC} values sampled is too small to produce a valid fit. Since the measurement error of the peak voltage for each source is difficult to determine from the algorithm that calculates the peak height, a first attempt to fit the free parameters assumes that the measurement errors are uniform for all sources. Next, using the residuals from the initial fit for each source, a measurement error is estimated for the peak voltage of each source and a new fit is computed weighting the data by these calculated errors¹⁹. This process of estimating errors and repeating the fit is continued until the values of the fit parameters remain constant within a given tolerance (1% in this case).

Up until now, all of the fit parameters have been calculated separately for each of the

¹⁸In our own data we found no evidence for variations in the emitted flux from these two sources as a function of time within each observing year. However, the observed flux of 0923+392 in 2004 is approximately 2σ (or 7%) lower than the observed flux in 2003, indicating it may be variable on long time scales.

¹⁹Note that since the errors are estimated based on the fit, it is not possible to determine the quality of the fit based on these errors. However, we are only interested in weighting the different observations correctly when determining the fit parameters, so this is not a problem.

six independent calibration data sets in 2003. However, the value of F_j should be the same for each set. Using the uncertainty on the calculated value of F_j for NGC2071IR and 0923+392 for each set, a weighted mean is calculated and used as the true flux for each of these sources. Finally, α_1 and α_2 are calculated one more time for each calibration set (while holding all the F_j fixed). Two examples of the final fits are given in Figure 3.13.

If we return to Equation 3.3 we see that

$$\bar{\chi}(V_{DC}) \simeq \frac{c^2(\Delta\nu_{atm})}{2\Omega k_B} \frac{V(V_{DC})}{\int d\nu \Theta(\nu) \Theta_{atm}(\nu) \nu^2 T(\nu)}. \quad (3.19)$$

Combining Equations 3.19 and 3.18 yields $\bar{\chi}(V_{DC}) = V(V_{DC})/F_j = \alpha_1 + \alpha_2 V_{DC}$, which gives the absolute flux calibration. For reference, the absolute calibration ranges from around 12 mV/Jy up to around 24 mV/Jy over the range of DC levels recorded during the 2003 observing run, and between 9 mV/Jy up to 15 mV/Jy during the 2004 observing run. The reason for such a large difference between the calibration of the two runs is a change in the normalization convention within the analysis software, rather than a fundamental change in the Bolocam instrument²⁰.

3.5.4 Uncertainty in the Flux Calibration

First, the temperature profiles of Uranus and Neptune were derived by Griffin and Orton using Mars as an absolute calibrator [57]. To determine the surface brightness of Mars at millimeter wavelengths, Griffin and Orton used the model developed by Wright based on observations made at far infrared wavelengths [153], along with the logarithmic interpolation to longer wavelengths described by Griffin, et al. [56]. The estimated uncertainty on this interpolated model is approximately 5% [153]²¹. Second, the uncertainties on the temperature profiles of Uranus and Neptune are estimated to be less than 1.5% relative to

²⁰The Bolocam software normalizes the calibration to the bolometer with the largest relative calibration. For the 2003 data the most sensitive bolometer had a relative calibration approximately 30% higher than the average relative calibration. However, in 2004 the relative calibration of all of the bolometers was set to one. Therefore, the absolute flux calibration in 2003 will be artificially inflated by a factor of approximately 1.3 compared to the absolute flux calibration determined for the 2004 data.

²¹There is also a brightness model based on a physical model of the dielectric properties of the Martian surface that was developed by Rudy [114,115]. This model was constrained by measurements at centimeter wavelengths, and also needs to be extrapolated to millimeter wavelengths. Griffin and Orton, along with Goldin, et al., compared the results of these two models at millimeter wavelengths, and found that they agree within their estimated uncertainties [52,57]. Based on the comparison of these two models, Griffin and Orton conclude the the uncertainty in the Martian brightness based on the Wright model is 5%.

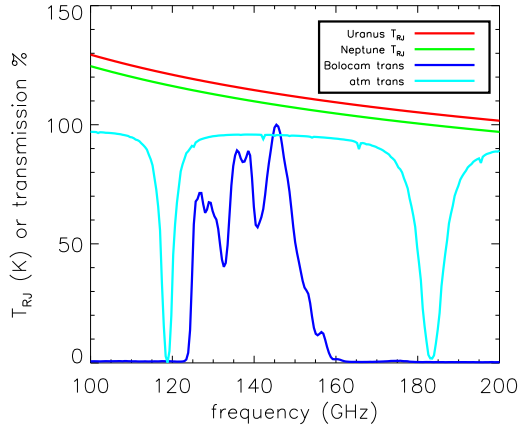


Figure 3.12: The red and green curves show the RJ temperature of Uranus and Neptune, respectively, versus frequency. The dark blue curve shows the transmission, measured by FTS, of the Bolocam filters/horns/window/lens/etc., normalized to a maximum value of 100%. The light blue curve shows the transmission of the atmosphere at 2.1 mm of precipitable water [34].

Mars [57]²². Additionally, the observations of Uranus and Neptune were taken with a precipitable water vapor of 1.5 ± 0.5 mm, which results in a calibration uncertainty of $\sim 1.4\%$. Finally, the error inferred by the scatter of our measurements results in calibration uncertainties between 0.6% and 3.0% for each of the data sets. These results are summarized in Table 3.6.

3.5.5 Derived Source Fluxes

We observed five different sources to use for pointing calibration: 0923+392 along with 0106+013, 0113-118, 0336-019, and 0804+499²³. Also, we observed NGC2071IR for use as a secondary flux calibrator. Using the flux calibration described earlier we were able to derive a flux for each of these sources, which is given in Table 3.7. It should be noted that the effective band center of our detectors is ~ 143 GHz = 2.1 mm, and the effective bandwidth is ~ 21 GHz.

²²Griffin and Orton find that the uncertainty is 1.7 K for both their Uranus and Neptune models. Since the temperature of these planets in our band is approximately 115 K, this translates to an uncertainty of $\simeq 1.5\%$.

²³Other than 0923+392, none of these sources have been shown to emit a (nearly) constant amount of flux as a function of time (i.e., they are or could be variable). Therefore, they were not used when computing the flux calibration. However, an estimate of the average flux of each source during the course of our observations has been determined.

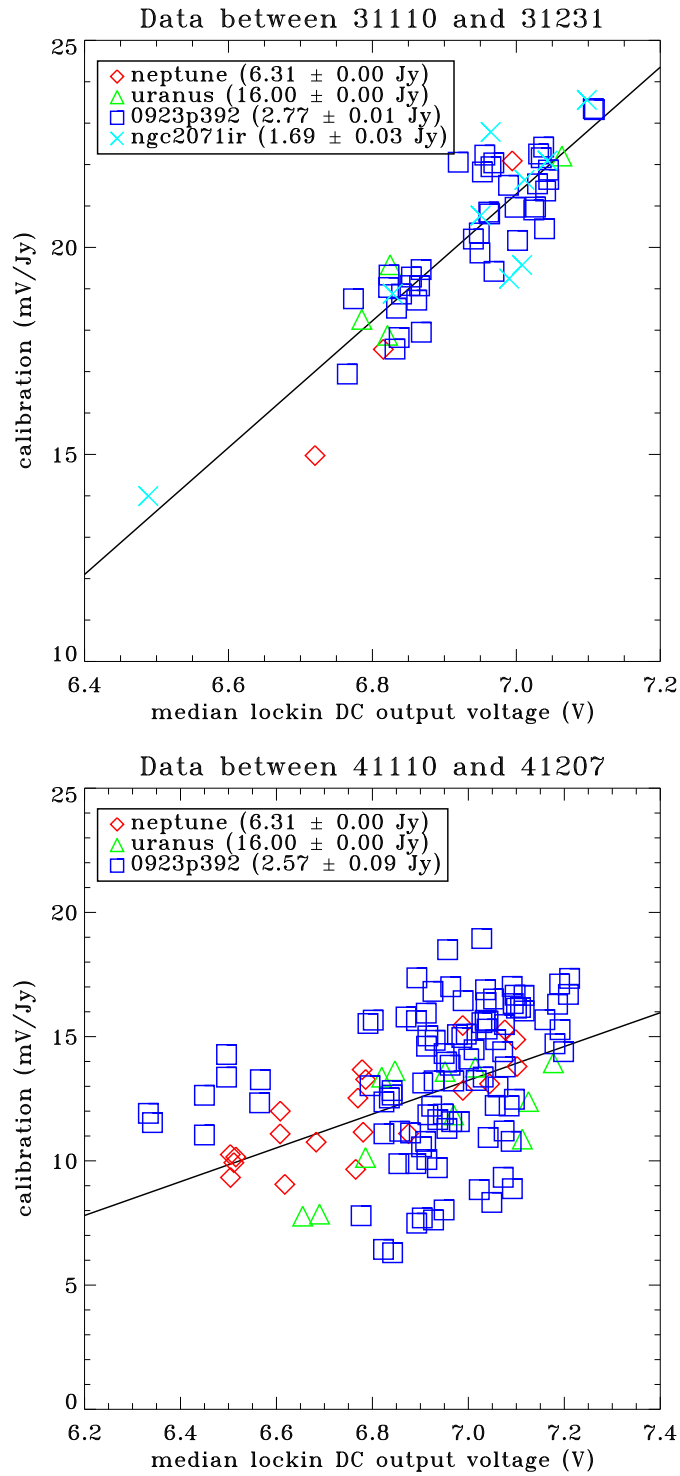


Figure 3.13: Flux calibration for one of the six calibration data sets from 2003 (top), and for the 2004 data set (bottom). The linear fit of calibration versus median lockin DC output is overlaid on each plot. The reason the calibration for the 2004 data appears to be $\simeq 30\%$ lower than the 2003 data is because of a change in normalization convention within the analysis software between the two observing runs.

uncertainty in the flux calibration				
cause of uncertainty	2003/11/02	2003/11/04	2003/11/05	2003/11/08
	to 2003/11/03	to 2003/11/04	to 2003/11/07	to 2003/11/08
Mars	5.0%	5.0%	5.0%	5.0%
Neptune/ Uranus range of atmospheric opacity	1.5%	1.5%	1.5%	1.5%
measurement	1.4%	1.4%	1.4%	1.4%
total	2.8%	3.0%	3.0%	2.5%
	6.1%	6.2%	6.2%	6.0%

uncertainty in the flux calibration			
cause of uncertainty	2003/11/08	2003/11/10	2004/11/10
	to 2003/11/09	to 2003/12/08	to 2004/12/06
Mars	5.0%	5.0%	5.0%
Neptune/ Uranus range of atmospheric opacity	1.5%	1.5%	1.5%
measurement	1.4%	1.4%	1.4%
total	1.5%	0.6%	1.5%
	5.6%	5.4%	5.6%

Table 3.6: Description of the flux calibration uncertainties for each of the six calibration data sets for 2003 and the single data set for 2004. The overall uncertainty on the calibration for every set is $\simeq 6\%$, dominated by the uncertainty in the flux of Mars.

Derived source fluxes from 2003 (in Jy)						
	NGC2071IR	0106+013	0113-118	0336-019	0804+499	0923+392
observed flux	1.69	1.30	0.87	0.97	0.33	2.77
measurement uncertainty	0.03	0.04	0.04	0.04	0.02	0.01
normalization uncertainty	0.10	0.08	0.05	0.06	0.02	0.15
total uncertainty	0.10	0.09	0.07	0.07	0.02	0.15

Derived source fluxes from 2004 (in Jy)						
	NGC2071IR	0106+013	0113-118	0336-019	0804+499	0923+392
observed flux	-	0.55	0.66	0.71	0.77	2.57
measurement uncertainty	-	0.11	0.07	0.08	0.06	0.09
normalization uncertainty	-	0.03	0.04	0.04	0.05	0.14
total uncertainty	-	0.11	0.08	0.09	0.08	0.17

Overall Results (in Jy)						
total	1.69 ± 0.10	Variable	Variable	Variable	Variable	2.76 ± 0.15
published flux	1.5 ± 0.2 @2 mm, [121]	-	-	-	-	3.2 ± 0.4 @2 mm, [48]

Table 3.7: Derived flux for several bright sources observed with Bolocam. The measurement uncertainty is due to the scatter of the measured values and the normalization uncertainty is due to published uncertainties in the flux of Uranus and Neptune, along with changes in the atmospheric opacity between observations of these planets. No attempt has been made to determine how much of the measurement uncertainty is due to variability in the emitted source flux. The bottom table gives the derived flux using the data from both observing seasons, except for the sources which appear to be variable.

3.6 Beam Profiles

Since our maps are inherently smoothed based on the profile of the Bolocam beams, it is important to understand their shapes. The beam profile will also determine what filter should be applied to the maps to optimize the peak of any potential clusters. Additionally, our flux calibration is based on observations of point sources, so we end up with maps with units of flux density. However, since the CMB or SZE signal we are looking for is a surface brightness or temperature, we need to know the area of our beam in solid angle to convert our maps to surface brightness units. Therefore, any error in our determination of the beam area will show up as a surface brightness or temperature calibration error.

3.6.1 Overview

The map of a point source will produce an exact replica of the beam shape²⁴. Observations were made of Mars (in 2003), Neptune, and Uranus in order to calculate beam areas, which were chosen because they were the brightest sources available during the observing runs. All three sources are not true point sources, and had semi-diameters during the observations of 5.2, 8.0, 1.1, and 1.8 arcseconds, respectively [68]. Note that the semi-diameter of Mars changed dramatically during our observations of it in 2003. To determine how non-point-like the planets are for our beams the following simulation was run. The time-stream of a Gaussian beam with a 60 arcsecond FWHM²⁵ was convolved with a top hat of the same diameter as the planet. An area was then calculated by mapping the resulting time-stream into a 1-dimensional map, revolving the map about its center to generate a 2-dimensional map, then integrating the peak-normalized map. The results of this calculation are given in Table 3.8. Uranus and Neptune were nearly ideal point sources, so no correction is needed. However, Mars requires a correction which changes for each observation, since the excess area due to the size of Mars varies by a non-negligible amount during the course of the observing run.

The beam areas are calculated from a map of the planet that is peak normalized to one, in order to make the calculation independent of source flux. To normalize our maps of the

²⁴A true point source can be represented by a delta function, with all of its flux originating at a single point in the sky. So, scanning past a point source is equivalent to convolving the beam with a delta function, which is equal to the beam.

²⁵Bolocam was designed to have beams with a FWHM of 60 arcseconds, so Gaussians of this size were used in several places to simulate a Bolocam beam. In the end, we found the profile of the Bolocam beams to be very close to this Gaussian approximation, justifying its use in simulations.

Planet	Date	Semi-Diameter	Beam Area	Excess Area	Percent Change
Pt. Src.	-	0.0	4070	0	0 %
Mars	11/01/2003	8.0	4180	120	2.9 %
Mars	12/08/2003	5.2	4120	60	1.4 %
Neptune	-	1.1	4070	0	0 %
Uranus	-	1.8	4070	0	0 %

Table 3.8: All semi-diameters are given in arcseconds and all beam areas are given in arcseconds².

planets we first calculated the values of the central nine pixels for a simulated Gaussian beam with a FWHM of 60 arcseconds.²⁶ Each pixel in the simulation is a 20 arcsecond square, just like in our real maps, and the beam is centered on the central pixel. Because of pixelization, the center pixel has a value of 0.95, not 1.0. The values of these central nine pixels are relatively unchanged for FWHMs within a couple arcseconds of the assumed value of 60, making this simulation robust to small differences between the real beam profiles and the assumed profile. Next, the average ratio between these simulated values and the values of the central nine pixels in the planet map is used to normalize the map. The planet map has been centered, but the RMS pointing uncertainty for a single bolometer for a single observation of one of these planets is $\simeq 5$ arcseconds. This pointing uncertainty results in the beam area computed from the planet maps to be systematically high by about 4%.²⁷

Due to the geometry of the optical system no two bolometers will necessarily produce the same beam area, which means the beam area must be calculated for each one separately. With this in mind, the beam area was calculated by co-adding the data from all the observations of a given planet for each bolometer. These maps were then peak normalized and integrated. The best way to quantify the uncertainty in the beam area is to calculate the beam area for a given bolometer for each observation; the RMS of these values can then be

²⁶The reason we normalize the beam based on these central nine pixels is that we cannot assume a priori that the beam profiles are Gaussian or that they are the same for every bolometer. Since there is not enough information to produce a high signal-to-noise measurement of the beam profile for each bolometer, we do not have a reliable profile to fit to. However, the central portion of the beam profile is well described by a Gaussian, which was used to normalize the beam based on the central nine pixels.

²⁷Because the maps are normalized based on the assumption that the source is centered, a pointing error makes the center of the map appear dimmer than it should. This is because the center of the map is located away from the peak of the source. The result is that the normalization is too large, and the peak amplitude of the source will be larger than one after applying the normalization. Therefore, the beam area calculated from this map will be larger than the beam area calculated from a map where the source peak is normalized exactly to one. However, the pointing errors average down when the data from a large number of observations or detectors is added together. In these maps the peak will be much closer to the center of the map, and the normalization error will be negligible even though the beam profile will be slightly broadened by the pointing errors. We have not attempted to correct for this broadening because the beam profile will be broadened during normal observations by the same effect.

planet	$\text{abs}(\mu) \leq 1\sigma$	$\text{abs}(\mu) \leq 2\sigma$	$\text{abs}(\mu) \leq 3\sigma$	$\text{abs}(\mu) \leq 4\sigma$	$\text{abs}(\mu) \leq 5\sigma$
Mars	4/35	12/35	18/35	23/35	27/35
Neptune	7/10	10/10	10/10	10/10	10/10
Uranus	5/10	9/10	10/10	10/10	10/10
Ideal Gaussian	0.68	0.95	1.00	1.00	1.00
Mars	0.11	0.34	0.51	0.66	0.77
Neptune	0.70	1.00	1.00	1.00	1.00
Uranus	0.50	0.90	1.00	1.00	1.00

Table 3.9: Results of self-consistency tests for the beam area data of each planet. For each planet the data was split into two sets with an equal number of observations in each set, then the test described in Section 3.6.2 was applied to these two sets of data. The data for Mars is not self consistent, indicating an underlying variation from one observation of Mars to the next. Therefore, the observations of Mars were discarded.

used to determine the uncertainty under the assumption that the beam area values follow a Gaussian distribution (this assumption is justified based on the data in Table 3.9). Unfortunately, 10 - 20% of the pixels in a map made from an individual bolometer for a single observation have no value (i.e., no data was taken while the detector was pointing within a given pixel). Therefore, the 115 working bolometers were divided into 28 groups of four bolometers and one group of three bolometers, where each group contains bolometers that are close to each other on the focal plane²⁸. The data from each group was then co-added into a map for each observation, and this data was used to calculate the uncertainty in the beam area for each bolometer and each planet, under the assumption that all bolometers in a given group have the same uncertainty on their beam area. Four different divisions of the bolometers into 29 groups were used, and an uncertainty on the beam area for each bolometer was calculated from the uncertainty in the beam area for each of the four groups that bolometer was placed in. These uncertainties were then used to compute the weighted mean of the beam area calculated from each planet, with the results given in Table 3.10.

3.6.2 Consistency Tests

It should be noted that the beam areas in Table 3.10 were calculated using only data from Uranus and Neptune. The data from Mars was not used because it was inconsistent with both the Uranus and Neptune data (see Figure 3.14), and it was not consistent from one observation of Mars to the next (see Table 3.9). Some possible explanations for the

²⁸Bolometers close to each other on the focal plane propagate through a similar optical path, and should therefore have a similar profile.

peak normalized beam areas and uncertainties in arcsec ²								
bolo	area		bolo	area		bolo	area	
0	4176	± 111	44	3985	± 179	95	4071	± 120
1	4159	± 134	46	3817	± 92	96	4202	± 107
2	4128	± 110	47	4008	± 86	100	3751	± 105
3	3933	± 137	48	4048	± 122	101	3999	± 93
5	4127	± 141	49	4031	± 90	102	3884	± 92
6	3955	± 134	50	3971	± 81	103	3958	± 123
7	4091	± 153	51	4016	± 80	106	4040	± 91
9	3957	± 151	52	3968	± 84	108	4027	± 141
10	3896	± 181	55	4006	± 108	109	3852	± 106
11	4185	± 139	57	3963	± 114	110	3982	± 106
12	3912	± 112	61	3995	± 92	112	4978	± 153
13	3897	± 104	62	3932	± 144	113	3957	± 142
14	3978	± 160	64	4054	± 97	114	3793	± 134
15	4236	± 182	65	4046	± 95	115	3724	± 121
16	4309	± 188	66	4050	± 100	116	3759	± 115
17	3903	± 102	67	3873	± 104	118	3777	± 115
18	3986	± 99	70	3855	± 100	119	3681	± 109
19	3802	± 104	72	4027	± 121	120	4212	± 116
20	3963	± 154	73	3979	± 123	121	4127	± 118
22	3878	± 110	74	3972	± 118	122	4136	± 128
24	3940	± 71	75	3997	± 118	123	4272	± 156
25	4967	± 55	76	4161	± 113	124	4175	± 126
26	4155	± 96	77	3930	± 106	125	3791	± 108
28	3849	± 79	78	3996	± 106	126	4081	± 163
29	4057	± 147	79	3922	± 103	127	4087	± 111
30	4291	± 85	80	3876	± 111	128	3861	± 126
31	3796	± 114	82	3878	± 86	129	3927	± 86
32	3945	± 109	83	3826	± 86	130	3944	± 151
33	4047	± 141	84	3875	± 74	131	4054	± 131
34	3937	± 164	85	3866	± 87	132	4013	± 126
35	3959	± 100	86	3920	± 107	133	3959	± 101
36	3804	± 119	87	3934	± 86	134	4050	± 103
37	4038	± 110	88	3851	± 82	135	3951	± 135
38	4111	± 167	89	4036	± 103	136	3797	± 106
39	4070	± 169	90	4082	± 111	137	3874	± 92
40	3963	± 156	91	3865	± 112	138	3829	± 89
41	3989	± 131	92	3805	± 93	140	3783	± 81
42	3863	± 111	94	4044	± 123	143	4250	± 103
43	3804	± 105						

Table 3.10: Beam area and associated uncertainty for each bolometer.

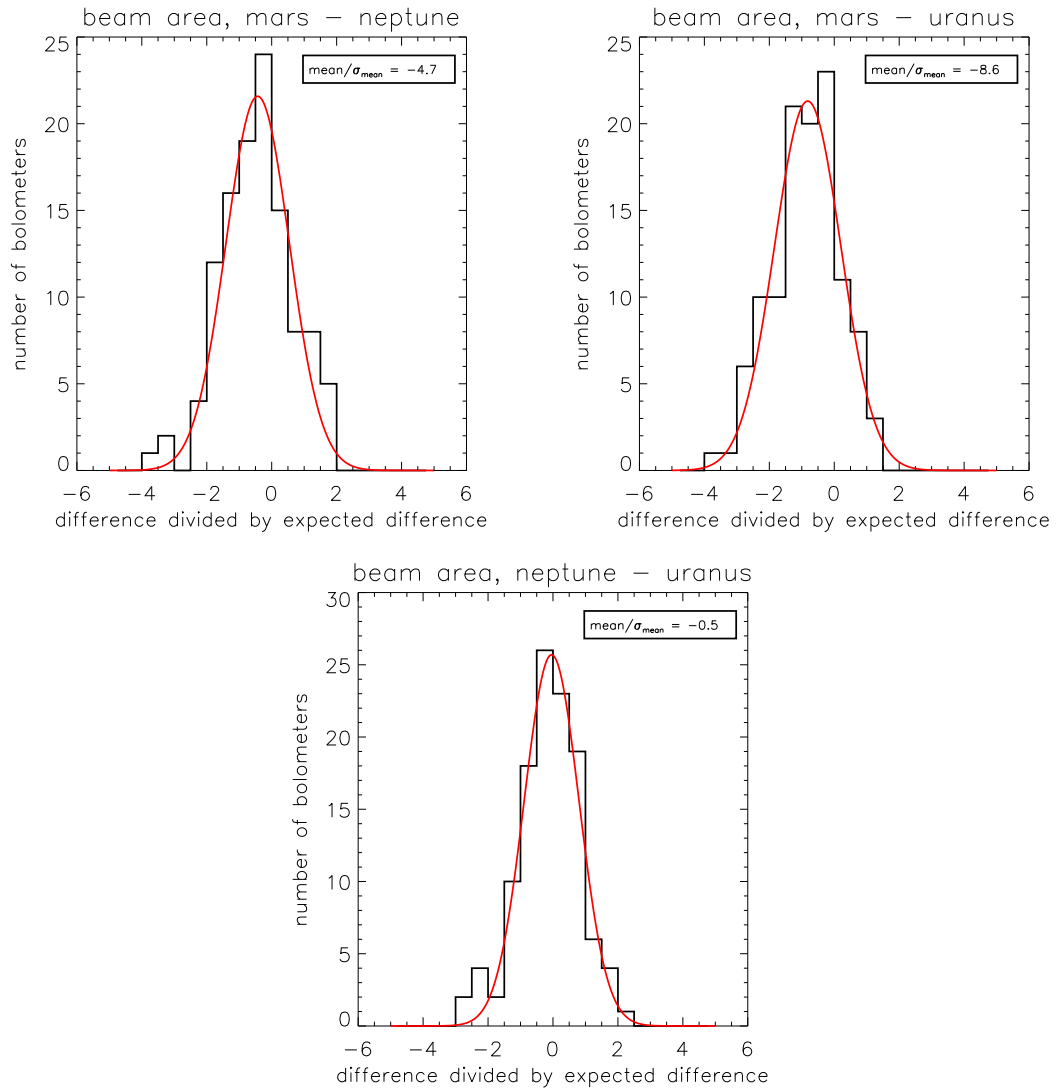


Figure 3.14: The data sets used in these histograms were generated as follows: 1) taking the difference in the average beam area determined for each bolometer from two different planets, 2) dividing this difference by the expected uncertainty in the difference. This data set should then have a sigma of 1 and a mean consistent with 0 if the beam areas from the two planets are the same. The data from Uranus and Neptune appear to be consistent, while the data from Mars is vastly different.

problems with the Mars data include: lockin DC output data had to be used for Mars because it was bright enough to saturate the amplifiers, the large signal produced by Mars might have pushed the bolometers to a point where the bolometer model is no longer valid, or the uniform brightness disk used to model the large size of Mars might not be valid. Unfortunately, we have not been able to determine the cause of the inconsistencies in the Mars data.

In order to test if the data for a given planet is self-consistent, the following analysis was performed. First, maps were made for each observation from co-adding the bolometers into the 29 groups described above. Next, beam areas were calculated from these maps, along with the standard deviation of the beam areas for each of the 29 groups for each planet. At this point we have a set of beam areas, $A_{i,j}^p$, along with uncertainties on these beam areas, σ_i^p , where i represents the group of bolometers, j represents the observation, and p represents that planet. The observations for each planet were then split into two equal-size, non-overlapping subsets, $\{j_1\}$ and $\{j_2\}$. Next, the average beam area, $\bar{A}_{i,\{j\}}^p$, for each of the 29 bolometer groups was calculated for each of the two subsets. These average beam areas were then differenced and divided by the expected uncertainty according to

$$x_i^p = \frac{\bar{A}_{i,\{j_1\}}^p - \bar{A}_{i,\{j_2\}}^p}{(\sqrt{2/n})\sigma_i^p}, \quad (3.20)$$

where n is the number of observations in each subset $\{j\}$. If the two subsets of data are consistent, then x_i^p should follow a standard normal distribution. The data for each planet was split into every possible combination of subsets, and the subsets for Uranus and Neptune showed that the observations of each of these planets are self consistent. However, the Mars subsets produce mean values of x_i^p that are clearly not consistent with 0, which means there is some variation from one observation of Mars to the next (see Table 3.9).

Additionally, tests were performed to see if there is a variation in the beam area from one bolometer to another (i.e., to determine if the beam area of each bolometer is the same to within the measurement precision). First, the RMS of the 115 beam areas found in Section 3.6.1 was calculated (σ_{BA}). Recall that the uncertainty for each beam area, σ_P , was found using the RMS calculated for each individual bolometer's beam area. If there is no variation in the beam area from one bolometer to the next then σ_{BA} should be consistent with the distribution of σ_P s. We find that σ_{BA} is somewhat larger than expected given

	measured σ	predicted σ (σ_P)	σ_{σ_P}	$\sqrt{\sigma_{meas}^2 - \sigma_P^2}$
single bolometers	124 arcsec ²	112 arcsec ²	22 arcsec ²	53 arcsec ²
groups of 4 bolos	78 arcsec ²	59 arcsec ²	8 arcsec ²	51 arcsec ²
groups of 6 bolos	48 arcsec ²	45 arcsec ²	6 arcsec ²	17 arcsec ²
groups of 8 bolos	70 arcsec ²	42 arcsec ²	4 arcsec ²	56 arcsec ²

Table 3.11: Actual σ of the distribution of beam areas compared to what is predicted by the uncertainty on each individual bolometer. If the beam area of each bolometer is the same then the measured sigma, (σ_{BA}), should be consistent with the distribution of σ_{PS} . The data for the first row is shown in Figure 3.15.

the distribution of σ_{PS} (see Table 3.11). Unfortunately, the fact that uncertainties add in quadrature means that σ_{BA} could be consistent with the σ_{PS} even if there is a large variation from bolometer to bolometer. To reduce the spread of the σ_{PS} , beam areas can be calculated using maps made from more than one bolometer, since σ_P is proportional to $1/\sqrt{N_{bolos}}$. The variation in beam area from one bolometer to the next is thought to be dominated by differences in the optical system based on bolometer location, so nearby bolometers should have similar beam areas, and this averaging should not reduce the systematic spread in the beam areas. With this in mind, beam areas were calculated for groups of 4, 6, and 8 nearby bolometers, with the results given in Table 3.11. These results allow for there to be a systematic variation in the beam area from one bolometer to the next of up to a few tens of arcseconds², but our measurement uncertainty on the beam areas prevents this variation from being adequately characterized. Note that in the end we have chosen to use the most conservative value for the uncertainty on the beam area, 124 arcseconds².

3.6.3 Results

Looking at the beam areas we determine from the individual bolometers, we find an area of 3968 ± 124 arcseconds². For a Gaussian beam, this corresponds to a FWHM of 59.2 ± 0.9 arcseconds, consistent with the expectation for Bolocam. Since there is no evidence for systematic variations in the beam profile from one bolometer to another, we will assume that all of the beam profiles are the same. Therefore, we co-added all bolometers over all observations of Uranus and Neptune to create the highest S/N measurement of our beam. See Figure 3.16. These co-added maps produce a beam profile with an area of 3949 arcseconds² for the 2003 data, and an area of 3923 arcseconds² for the 2004 data. The shape of the beam looks slightly more spread out in 2004 (See Figure 3.17), which is

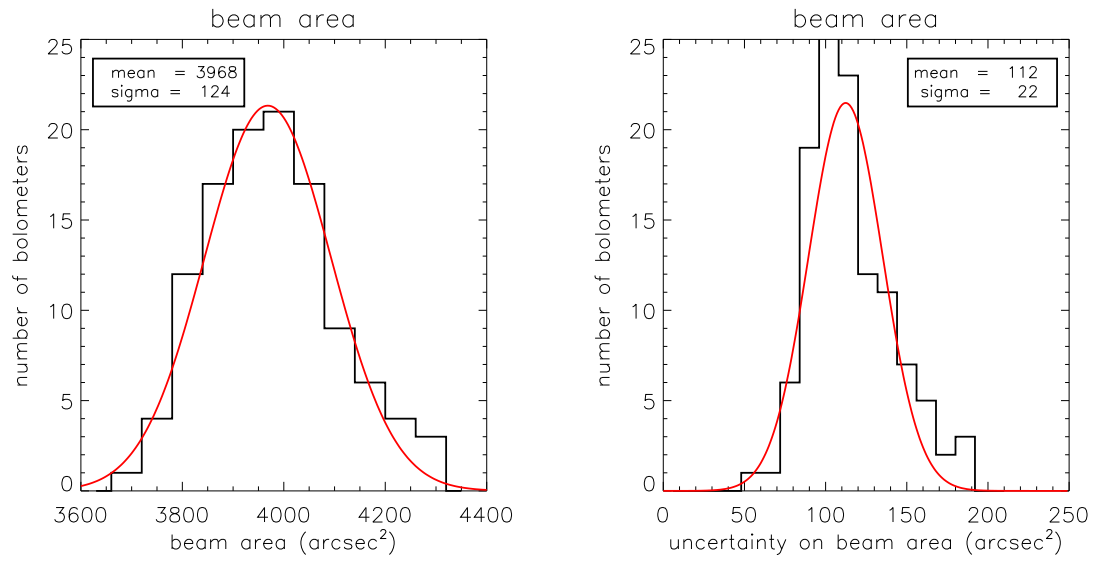


Figure 3.15: The histogram on the left shows the beam areas calculated for the 115 working bolometers, the histogram on the right shows the predicted uncertainties on these beam areas based on the RMS for an individual bolometer for an individual observation.

probably caused by the larger pointing uncertainty for that data.

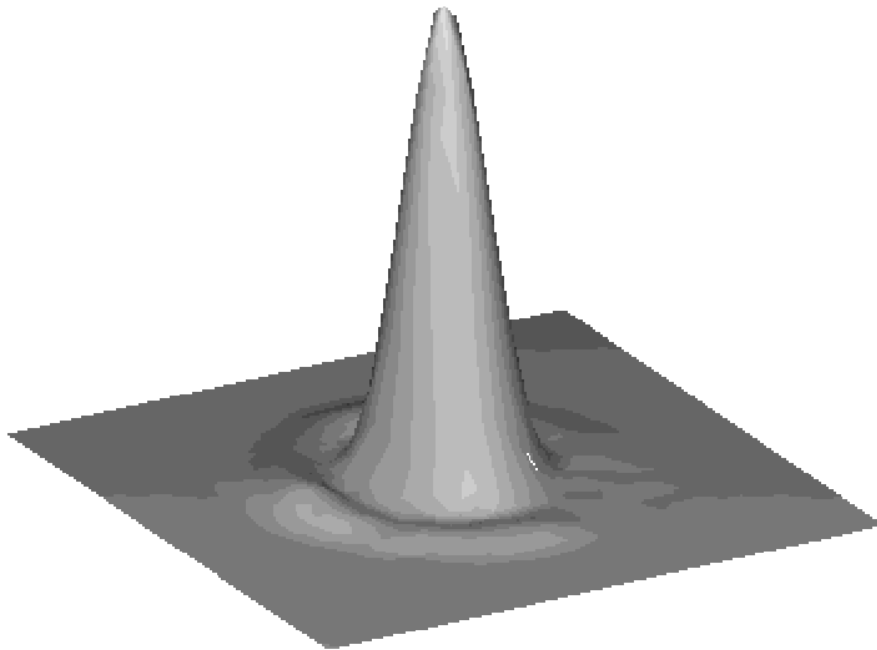


Figure 3.16: A surface plot of the Bolocam beam profile.

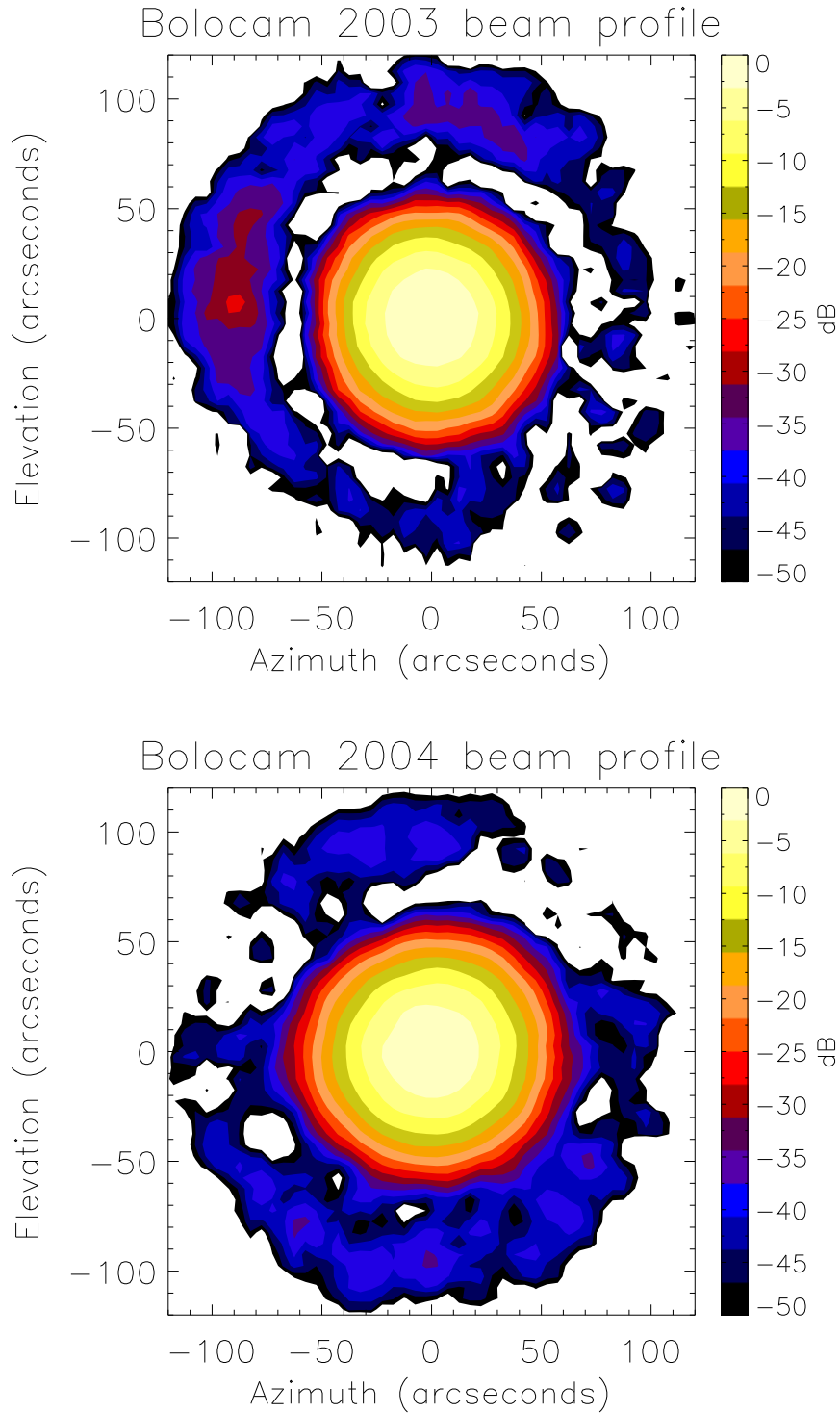


Figure 3.17: Contour plots of the Bolocam beam profile from the 2003 observing run (top) and the 2004 observing run (bottom). The scale on the right of each plot is in dB relative to the beam peak. The first Airy ring is visible, with an amplitude of $\lesssim 30$ dB relative to the beam peak.

Chapter 4 Noise

Numerous sources, both within and external to Bolocam, produce noise which hinders our ability to measure the astronomical sources we are looking for. Ideally, the dominant source of noise is the random arrival time of background photons, where the system is referred to as background noise limited (BLIP limited). At low frequencies Bolocam is not BLIP limited due to residual atmospheric fluctuations that cannot be removed. At high frequencies Bolocam is a factor of $\simeq 1.5$ above the BLIP limit due to instrumental noise.

4.1 Photon Noise

4.1.1 Theory

The Bolocam detectors are exposed to photons from numerous sources, most notably emission from surfaces inside the dewar, emission from the optics, and emission from the atmosphere. The vast majority of this emission is constant, and is easily removed from the data by the high-pass filter in the electronics. The number of photons emitted from a blackbody and absorbed by a bolometer per spatial mode per second per Hz of bandwidth is given by the Planck law

$$n_\gamma = \eta\epsilon/(e^{h\nu/k_B T} - 1) \quad (4.1)$$

where η is the efficiency of the Bolocam optics between the emission source and the bolometers, ϵ is the emissivity of the source, h is Planck's constant, ν is the frequency, k_B is Boltzmann's constant, and T is the temperature of the source. However, even for sources with constant emission, there will be fluctuations in n_γ . When the number of photons is small ($h\nu/k_B T \gg 1$), the fluctuations will obey Poisson statistics, with $\langle(\Delta n_\gamma)^2\rangle = n_\gamma$. But, when the number of photons is large ($h\nu/k_B T \ll 1$), the fluctuations will be dominated by the penchant for photons to bunch together because they are bosons. The Bose term fluctuations are described by $\langle(\Delta n_\gamma)^2\rangle = n_\gamma^2$ [110]. For Bolocam, the temperatures of the emitting surfaces range from 4 - 300 K, resulting in $h\nu/k_B T \lesssim 1$. Therefore, Bolocam falls in the regime where both the shot and Bose terms are important.

Next, we need to convert from fluctuations in the number of photons per mode per second

per Hz of bandwidth to fluctuations in the optical power received by the bolometer. If there are N spatial modes, each with two polarizations, then for an integration time of one second the mean square fluctuation in energy arriving at the bolometer is $\int d\nu 2Nh^2\nu^2\langle(\Delta n_\gamma)^2\rangle$, since the energy per photon is $h\nu$. The bandwidth for an integration time of one second is 1/2 Hz, so the mean square fluctuation in power per unit bandwidth at the bolometer is given by

$$NEP_{photon}^2 = 2 \int d\nu 2Nh^2\nu^2\langle(\Delta n_\gamma)^2\rangle, \quad (4.2)$$

where NEP_{photon}^2 has units of W^2/Hz . Alternatively, we can write the noise equivalent power as

$$NEP_{photon}^2 = 2 \int d\nu P_\nu h\nu + \int d\nu P_\nu^2/N \quad (4.3)$$

where $P_\nu = 2Nn_\gamma h\nu$ is the spectral power absorbed by the bolometer [110]. Since $h\nu/k_B T \lesssim 1$, the term $e^{h\nu/k_B T}$ in Equation 4.1 is reasonably well approximated as $1 + h\nu/k_B T$, which means that P_ν is fairly constant over the Bolocam observing band. We can then simplify Equation 4.3 as

$$NEP_{photon}^2 = 2Qh\nu_0 + Q^2/\Delta\nu = NEP_{shot}^2 + NEP_{Bose}^2, \quad (4.4)$$

where $Q = \int d\nu P_\nu$ is the total optical power, $\nu_0 = 143$ GHz is the Bolocam band center, and $\Delta\nu = 21$ GHz is the effective Bolocam band width¹.

4.1.2 Measured Values

The optical power deposited on the bolometers (optical loading) can be calculated using the IV load-curves described in Section 2.5.2. Equation 2.13 can be rewritten as

$$Q_{exp} = \eta 2k_B T \Delta\nu + Q_0 \quad (4.5)$$

¹In deriving Equation 4.4 we have also used the fact that Bolocam's optical system is single moded ($N = 1$). For Bolocam's cylindrical waveguides, the ratio between the cut-on frequencies of the two lowest propagation modes, TE₁₁ and TM₀₁, is approximately 1 to 1.3. Therefore, if the high-frequency cutoff defined by the metal mesh filters is less 1.3 times the low-frequency cutoff defined by the waveguide, then only one spatial mode can propagate through to the bolometer. This corresponds to a fractional band width, $\Delta\nu/\nu_0$ of approximately 0.26, which is much larger than the measured fractional band width of 0.15. Therefore, Bolocam operates as a single-moded optical system.

to include the measured optical efficiency from Equation 2.14 and the optical loading, Q_0 .² First, the load-curves taken with a source just outside the dewar window can be used to provide a measurement of the optical loading inside the dewar, Q_{dewar} . Originally, the Bolocam dewar was designed to operate with the LHe bath at atmospheric pressure. In this configuration, Q_{dewar} is approximately 2.4 pW, which corresponds to a blackbody temperature of 52 K using our measured dQ/dT_{RJ} of 0.047 pW/K.³ See Table 2.2 and Figure 2.14. However, if we pump on the LHe bath to maintain a pressure of ~ 10 torr, then Q_{dewar} drops to approximately 0.3 pW (6 K). See Figure 4.1. The reason for this large reduction in loading is not well understood, but it is thought to be a result of the bolometer coupling to multi-moded high-frequency radiation emitted by the inside of the snout that holds the cold lens and Lyot stop. Approximately 80% of the beam couples to the snout or the Lyot stop, which are at a temperature of 4.6 K when the LHe bath is at atmospheric pressure, and a temperature of 3.1 K when the LHe bath is at $\simeq 10$ torr. Therefore, the expected drop in optical loading should only be about 1.5 K (0.08 pW). But, since the high-frequency radiation from the lower portions of the snout will not be perpendicular to the plane of the copper mesh filters, the filters may not be effective at blocking it. The feed horns will couple to multiple modes of these high-energy photons, which could produce a substantial optical load. Because these photons are in the Wien part of the emission spectrum from the snout and Lyot stop, a small reduction in temperature results in a significant reduction in photons, which may be the reason for the dramatic reduction in optical loading when we pump on the LHe bath.

Additionally, the optical loading due to the Bolocam optics box can be measured using IV load-curves with Bolocam mounted on the optics box. The hot load is still a room temperature blackbody, but the night sky is used as the cold load. The CSO tipper tau measurements allow us to determine the emissivity of the atmosphere, which is multiplied by an average atmospheric temperature of 260 K to determine an effective temperature⁴. Typically, the effective atmospheric temperature is near 10 K, and the errors introduced

²Note that this equation assumes that the Rayleigh-Jeans limit holds, i.e., that $h\nu \ll k_B T$. This is true for the 2.1 mm observations made with Bolocam for blackbodies with a temperature $\gtrsim 10$ K.

³In the Rayleigh-Jeans limit, the optical power emitted by a blackbody is proportional to the temperature of the blackbody. Therefore, the optical loading is often referenced to a blackbody temperature instead of a power in pW.

⁴The average atmospheric temperature corresponds to the average temperature of the water vapor in the atmosphere; and is determined by assuming that the amount of water vapor in the atmosphere falls exponentially with height, and that the temperature of the atmosphere falls according to the adiabatic lapse rate [94].

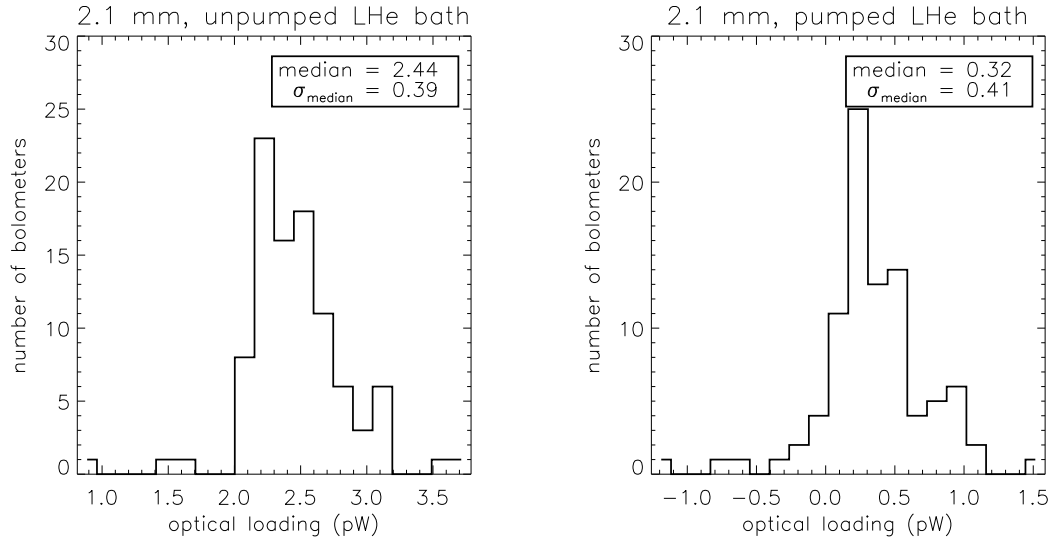


Figure 4.1: The measured optical loading from inside the dewar. The plot on the left shows the loading when the LHe bath is left at atmospheric pressure, and the plot on the right shows the loading when the bath is pumped down to a pressure of ~ 10 torr. It is unclear why there is such a large drop in loading while pumping on the LHe bath, but a likely suspect is coupling to multi-moded high-frequency radiation emitted from the Lyot stop. Note that the large spread in measured loading values is due to a combination of measurement uncertainty and imperfections in the bolometer model that arise because we are extrapolating from the measured Q for 77 K and 300 K loads down to the expected Q for no optical load outside of the dewar.

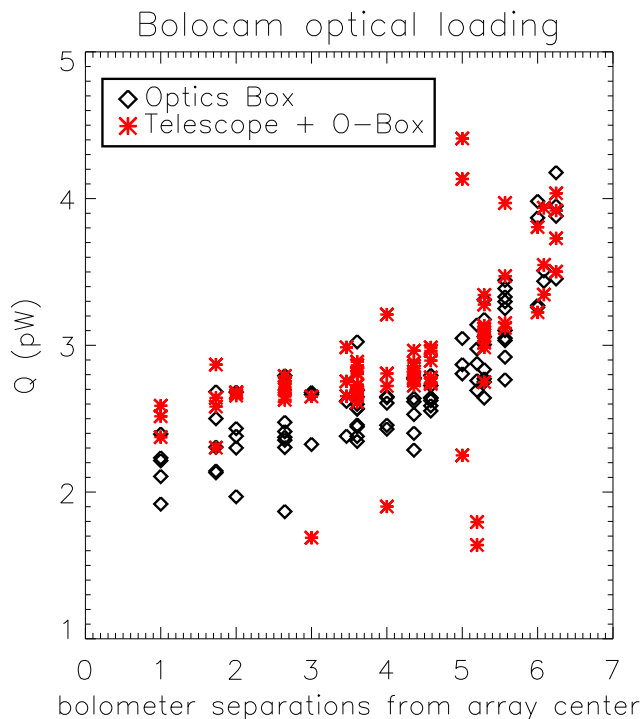


Figure 4.2: The black squares show the optical loading from the Bolocam optics box for each bolometer, as a function of the bolometer distance from the center of the focal plane. The red asterisks show the optical loading from the optics box and the telescope. Most of the loading in the optics box is from diffraction at the opening where the dewar attaches to the box and/or spillover of the beam at the elliptical mirror. Therefore, the loading for pixels farther from the array center is larger. The difference between the two values is used to infer the loading from the telescope, which is 0.3 ± 0.1 pW (6 ± 2 K).

by our method of determining an average atmospheric temperature should be of order 1 K. After subtracting Q_{dewar} , we find that the optical loading from the optics box is $Q_{obox} = 2.5 - 3.5$ pW, which translates to 55 - 75 K. The loading is smallest for the inner bolometers, and largest for the outer bolometers. See Figure 4.2. This optical load is much larger than expected for the optics box, and we have isolated the sources of this excess loading within the box. By using a 77 K blackbody to probe around the surfaces in the optics box, we found that the beams are hitting the edge of the opening to the optics box where the dewar is mounted. Additionally, the beams are spilling over the elliptical mirror inside the box. No modifications have been made to the optics box, mainly because the excess noise produced by the large optical load is sub-dominant to the noise from fluctuations in atmospheric emission.

We have also taken IV load-curves while Bolocam is mounted on the telescope. Although

source	optical power (Q)	comments
inside dewar	0.3 pW (6 K)	measured using IV load-curves
optics box	2.5-3.5 pW (50-70 K)	measured using IV load-curves, varies over array
telescope	$\simeq 0.3$ pW (6 K)	measured using IV load-curves
atmosphere	$\simeq 0.5$ pW (10 K)	estimated from $T_{atm} = 260$ K and 2 mm PWV
total	$\simeq 3.5$ - 4.5 pW (70-90 K)	$NEP_{photon} = 4.0 \times 10^{-17}$ W/ $\sqrt{\text{Hz}}$

Table 4.1: The optical loading contributions from various components in the Bolocam optics. The total optical loading of $\simeq 3.5 - 4.5$ pW produces a total noise equivalent power (NEP_{photon}) of around 4.0×10^{-17} W/ $\sqrt{\text{Hz}}$, with $NEP_{shot} \lesssim 3.0 \times 10^{-17}$ W/ $\sqrt{\text{Hz}}$ and $NEP_{Bose} \lesssim 3.0 \times 10^{-17}$ W/ $\sqrt{\text{Hz}}$.

it is impractical to put a room-temperature load in front of the primary mirror, the sky can be used as a cold load in the same way it was for IV load-curves taken on the optics box. By changing the elevation angle of the telescope, and therefore the optical depth of the atmosphere, it is possible to model the optical load from the atmosphere, which can then be subtracted. Finally, the known optical loading caused by the dewar and optics box is subtracted, and the optical loading caused by the telescope optics is the only remaining optical power on the detector. With this method, we find the optical loading from the telescope optics is 0.3 ± 0.1 pW, which translates to 6 ± 2 K. Since the telescope consists of two aluminum mirrors at a temperature of approximately 275 K, this corresponds to an emissivity of $\simeq 1$ % for the mirror surfaces. This is several times larger than the theoretical emissivity of $\simeq 0.2\%$, although even freshly polished aluminum surfaces tend to be a factor of $\simeq 2$ more emissive than the theoretical value at millimeter wavelengths [19]⁵.

A summary of the optical loading from various components in the Bolocam optics is given in Table 4.1. The total optical power deposited on the bolometers is $\simeq 3.5 - 4.5$ pW, which corresponds to 70 - 90 K, with most of this loading coming from the optics box. This corresponds to a photon noise of approximately 4.0×10^{-17} W/ $\sqrt{\text{Hz}}$, with approximately equal contributions from the shot and Bose terms.

⁵Small cracks between primary mirror panels, along with dust that collects on the mirror surface probably add to its emissivity.

4.2 Bolometer and Electronics Noise

4.2.1 Bolometer Noise

Since the bolometers operate at a non-zero temperature they are subject to Johnson noise, which is caused by the thermal agitation of electrons in a conductor. This noise has a flat frequency spectrum, with a Gaussian distribution of amplitudes. The RMS voltage fluctuations across the bolometer per unit square-root bandwidth are given by

$$V_{RMS} = \sqrt{4k_B T_b R_b}, \quad (4.6)$$

where k_B is Boltzmann's constant, T_b is the temperature of the bolometer, and R_b is the resistance of the bolometer. Under typical observing conditions, the current across the bolometer is approximately 0.8 nA and the bath temperature is $\simeq 235$ mK. These biasing conditions produce approximately optimal noise properties for the bolometers for typical observing conditions at 2.1 mm. Since the optical power is known to be around 4 pW, Equations 2.1 and 2.2, along with the measured bolometer parameters, can be used to solve for the typical bolometer temperature and operating resistance, which are $\simeq 300$ mK and $\simeq 3.0$ M Ω , respectively. Using Equation 4.6, these values produce RMS fluctuations around 7 nV/ $\sqrt{\text{Hz}}$ for the Bolocam bolometers. Additionally, the Johnson noise fluctuations described in Equation 4.6 can be converted to an equivalent noise in units of optical power received by the detector, by dividing by the electrical responsivity of the detector, s (in V/W), and multiplied by $\sqrt{2}$ to account for the noise appearing in both sidebands around the bias frequency, with

$$NEP_{Johnson} = \sqrt{8k_B T_b R_b} / |s|. \quad (4.7)$$

Since the phase of the responsivity is not important, the absolute value of s is used [110]. For Bolocam, $s \simeq -4.0 \times 10^8$ V/W,⁶ which means $NEP_{Johnson} \simeq 2.4 \times 10^{-17}$ W/ $\sqrt{\text{Hz}}$.

Another source of noise that is inherent to the bolometers is phonon noise, which is caused by fluctuations in the energy of the bolometer [110]. These fluctuations are caused

⁶The responsivity obtained from our measured flux calibration is approximately -3.0×10^8 V/W, approximately 25% lower in magnitude than the predicted value of -4.0×10^8 V/W. However, since we only digitize the real part of the signal output by the lockin electronics, the magnitude of this measured responsivity can only serve as a lower limit. This is because the finite stray capacitance of the bolometer circuit will put the bolometer signal out of phase with the bias reference signal, resulting in attenuation when the bolometer signal is demodulated by the lockin. For our 130 Hz bias frequency, and several M Ω bolometer resistance, a physically reasonable stray capacitance of $\simeq 100$ pF would cause the responsivity to appear 25% low.

because carriers that pass energy through the thermal link between the bolometer and the bath are quantized. Even if there is no net DC power flow between the bolometer and the bath, the noise will still appear because phonons flow back and forth through the thermal link to keep the bolometer temperature fixed. The power spectrum of the fluctuations is flat⁷, and is described by

$$NEP_{phonon} = \sqrt{4k_B T_b^2 G}, \quad (4.8)$$

where G is the thermal conductance given in Equation 2.3 [110]. For Bolocam, $NEP_{phonon} \simeq 2.1 \times 10^{-17} \text{ W}/\sqrt{\text{Hz}}$.

4.2.2 Electronics Noise

The electronics used to read out the bolometer signals also add noise. The spectrum of the room-temperature electronics has been measured, and the white-noise level is approximately $8 \text{ nV}/\sqrt{\text{Hz}}$, with a $1/f$ knee at less than 10 mHz. Additionally, we measured the power spectrum of the warm electronics plus the cold JFETs (i.e., all of the read-out electronics). This PSD also has a white spectrum down to at least 10 mHz, at a level of approximately $11 \text{ nV}/\sqrt{\text{Hz}}$. See Figure 4.3. Therefore, the cold JFETs also contribute approximately $8 \text{ nV}/\sqrt{\text{Hz}}$ of noise to the the electronics. The total noise contributed by the read-out electronics corresponds to an NEP of $\simeq 3 \times 10^{-17} \text{ W}/\sqrt{\text{Hz}}$.

Compared to similar instruments (e.g., ACBAR, with a noise level of $3 \text{ nV}/\sqrt{\text{Hz}}$), our electronics noise is not optimal [117]. There is a degradation of $\sqrt{2}$ due to our AC-biased read-out compared to ACBAR's DC-biased read-out, but our noise level is still a factor of two higher due to two separate design decisions. First, the original NJ132 JFET modules⁸ used for Bolocam failed after several thermal cycles due to a poor mechanical design. Once the problem was discovered there were no remaining NJ132s to replace the broken modules, and no funding to purchase new NJ132s, so available U401 dies were used to construct the final JFET modules even though they are known to be noisier than the NJ132s. Second, the original Bolocam design used INA103 low-noise amplifier chips. However, these chips were suspected of powering up in a strange state that dramatically heated the detectors and

⁷The bolometer has a finite time constant, and cannot respond to fluctuations on time scales that are short compared to this time constant. The result is that the power spectrum of the phonon noise is attenuated at high frequency, although the bolometer time constant is short enough that the power spectrum is flat in our signal band.

⁸ACBAR utilized NJ132 JFET modules.

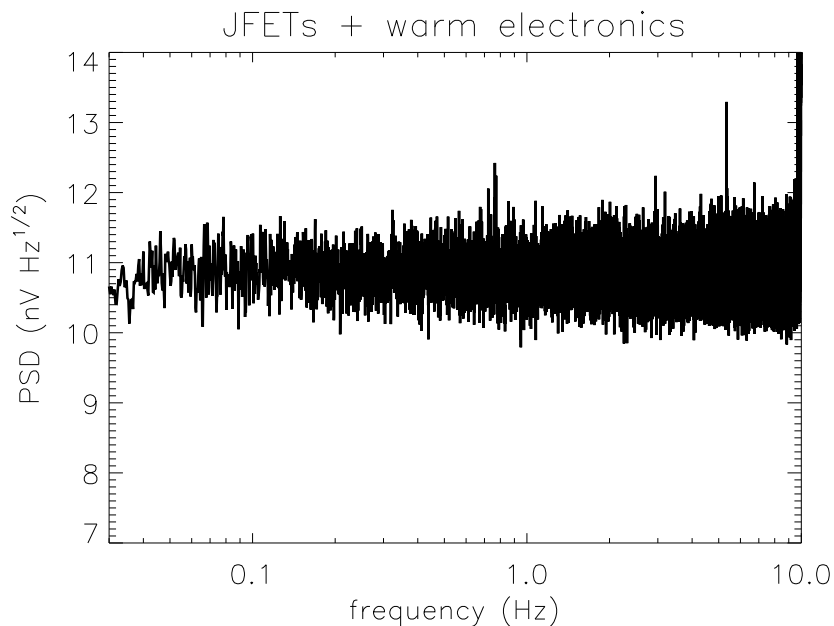


Figure 4.3: PSD showing the noise level of the room-temperature electronics and cold JFETs.

caused the refrigerator to fail. By the time the problem was traced to a simple design flaw in the circuit implementation of the INA103 chips, new boards had already been produced with AD624 chips which are a factor of $\simeq 4$ noisier than the INA103s. Unfortunately, since the AD624s are not pin-compatible with the INA103s, it was not possible to revert to the original chips.

Additionally, there are fluctuations in the bias voltage applied to the bolometers. We remove this noise by creating a template from the bias signal, correlating this template to the data from each bolometer, and then subtracting this template weighted by the correlation coefficient. On average, the signal removed has an NEP of approximately $1 - 4 \text{ nV}/\sqrt{\text{Hz}}$, which is almost negligible compared to the total NEP of $\simeq 25 \text{ nV}/\sqrt{\text{Hz}}$.

A summary of the optical, bolometer, and electronics noise is given in Table 4.2. A comparison between the total noise expected and the total noise recorded during an observation at the CSO is given in Figure 4.4. Note that the photon noise ($2.5 \text{ mK}_{CMB}/\sqrt{\text{Hz}}$) is comparable to the instrumental noise ($2.7 \text{ mK}_{CMB}/\sqrt{\text{Hz}}$), so Bolocam is not quite BLIP limited⁹. There is a degradation in our sensitivity due to the excess optical load from the optics box (3 pW compared to the expected 0.5 pW). If the loading from the optics

⁹However, although Bolocam is not BLIP limited, the sensitivity is limited by fluctuations in atmospheric emission rather than instrumental noise.

box was 0.5 pW, and the bolometers were fabricated with the optimal compromise G_0 of 100 pW/K for this loading, then the total noise would decrease from $3.7 \text{ mK}_{CMB}/\sqrt{\text{Hz}}$ to $1.9 \text{ mK}_{CMB}/\sqrt{\text{Hz}}$. However, Bolocam would still not be BLIP limited with photon noise equal to $1.1 \text{ mK}_{CMB}/\sqrt{\text{Hz}}$ and instrumental noise equal to $1.6 \text{ mK}_{CMB}/\sqrt{\text{Hz}}$. See Table 4.3.

This degradation from the BLIP limit is caused by several different factors. First, if we only observed at 2.1 mm, then we could fabricate the bolometers with the optimum value of $G_0 = 40 \text{ pW/K}$ for this band. With this thermal conductance the photon noise level would be $1.1 \text{ mK}_{CMB}/\sqrt{\text{Hz}}$ and the instrument noise level would be $1.3 \text{ mK}_{CMB}/\sqrt{\text{Hz}}$, which is closer to BLIP limited. Another factor that prevents us from achieving BLIP limited performance is the excess electronics noise described in Section 4.2.2. If our electronics noise was reduced by a factor of two then the photon noise level would be $1.1 \text{ mK}_{CMB}/\sqrt{\text{Hz}}$ and the instrument noise level would be $1.0 \text{ mK}_{CMB}/\sqrt{\text{Hz}}$, approximately BLIP limited.

Finally, our performance is degraded by the poor optical efficiency of the system at 2.1 mm. This poor optical efficiency is a result of the $0.7 (f/\#)\lambda$ spacing of the bolometers on the focal plane, which requires the use of small feed horns that couple a large amount of power to the Lyot stop. If the spacing was closer to $2 (f/\#)\lambda$, then the larger feed horns would increase the optical efficiency by a factor of almost three. With this increased optical efficiency, along with the improved electronics noise, we would be even closer to BLIP limited. The photon noise level would be $0.8 \text{ mK}_{CMB}/\sqrt{\text{Hz}}$ and the instrument noise level would be $0.5 \text{ mK}_{CMB}/\sqrt{\text{Hz}}$. See Table 4.3. To achieve this higher optical efficiency we would lose approximately 75% of our detectors because of the larger feed horns. The end result is that the overall sensitivity of the camera is similar to using all of the detectors with poor optical efficiency. Note that for the actual G_0 and electronics noise of Bolocam, the overall sensitivity of the camera is a little better with the smaller feed horns¹⁰.

Underlying all of these calculations is the fact that the BLIP limit in $\text{mK}/\sqrt{\text{Hz}}$ changes as a function of optical loading and optical efficiency. For comparison, the BLIP limit of ACBAR at 150 GHz is around $0.35 \text{ mK}/\sqrt{\text{Hz}}$, which is a factor of 2 better than our best case estimate of $0.8 \text{ mK}/\sqrt{\text{Hz}}$ [117]. ACBAR has a total optical load of 39 K, similar to what we would achieve if the optics box performed close to our expectations. However, the

¹⁰The excess correlations between bolometer time-streams discussed in Section 4.6.5 was not discovered until after the final observing run in 2004. Since the correlations are likely caused by the close spacing of the detectors, using the larger feed horns may have eliminated these correlations.

source	per-detector sensitivity					
	W/ $\sqrt{\text{Hz}}$	nV/ $\sqrt{\text{Hz}}$	mJy/ $\sqrt{\text{Hz}}$	mK _{RJ} / $\sqrt{\text{Hz}}$	mK _{CMB} / $\sqrt{\text{Hz}}$	SZE _y / $\sqrt{\text{Hz}}$
optical shot	2.8×10^{-17}	11	62	1.1	1.8	2.0×10^{-4}
optical Bose	2.8×10^{-17}	11	62	1.1	1.8	2.0×10^{-4}
bolo Johnson	2.4×10^{-17}	10	54	0.9	1.5	1.6×10^{-4}
bolo phonon	2.1×10^{-17}	8	47	0.8	1.3	1.4×10^{-4}
room-temp amp	2.0×10^{-17}	8	44	0.8	1.2	1.4×10^{-4}
JFET	2.0×10^{-17}	8	44	0.8	1.2	1.4×10^{-4}
total noise	5.8×10^{-17}	23	130	2.2	3.7	4.1×10^{-4}

Table 4.2: *NEPs* for Bolocam under standard observing conditions. The optical noise is calculated for a bolometer with average loading from the optics box for the median atmospheric opacity at the CSO. The value used for the typical total optical loading is 80 K. The Johnson and phonon noise are calculated for a bolometer with 80 K of optical loading using the parameters determined from the bolometer model, which are a bolometer temperature of 300 mK and a bolometer operating resistance of 3.0 M Ω . The room temperature amplifier and cold JFET noise have been measured in the lab. The responsivity, s , to convert from W to nV is -4.0×10^8 V/W. The conversion from nV to Jy is determined using the average flux calibration of $\simeq 15$ mV/Jy. Note that the mV in the flux calibration is post lockin, and has been amplified by a factor of 82933 relative to the voltage at the bolometer. All of the other conversion factors are given in Appendix A.

optical efficiency of ACBAR is 40%, approximately twice what we can achieve using the larger feed horns for detectors spaced at $2(f/\#\lambda)$.

4.3 Non-Optical Noise

Six bolometers on the Bolocam focal plane are left dark (i.e., they are surrounded by reflective surfaces that are at sub-Kelvin temperatures). We use the signals from these dark bolometers to create a template, which is then correlated with the time-stream from each standard bolometer and removed after applying the appropriate weighting factor. The dark bolometers have a white power spectrum, since they are shielded from the atmospheric emission. See Figure 4.5. Since the standard bolometer time-streams are dominated by fluctuations in atmospheric emission below $\simeq 0.5$ Hz, the dark and standard bolometer time-streams are high-pass filtered at 1 Hz before the correlation coefficients are calculated. The typical PSD of the weighted template that is removed from the data is a few nV/ $\sqrt{\text{Hz}}$, which can be compared to the typical time-stream NEP of $\simeq 25$ nV/ $\sqrt{\text{Hz}}$. Since each bolometer has its own amplifier and lockin electronics, the cause of this correlated noise between the dark and light bolometers is thought to be thermal fluctuations on the bolometer array. This noise was not included in the noise budget described in Table 4.2 because it can be

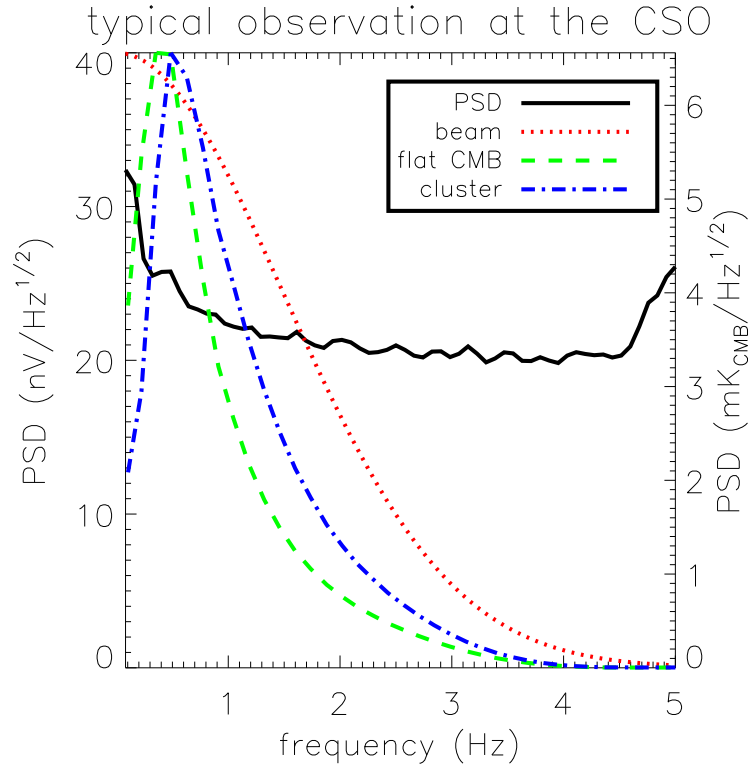


Figure 4.4: PSD from a typical observation made from the CSO. This PSD represents processed data, and the atmospheric noise has been removed in the optimal way. The excess noise at low frequency is caused by non-removable fluctuations in emission from the atmosphere, while the slight rise in the noise at high frequency is caused by the deconvolution of a 5 Hz anti-aliasing filter. The white noise level is approximately equal to expected noise level of $23 \text{ nV}/\sqrt{\text{Hz}}$ determined from the photon, bolometer, and electronics noise estimates. For reference, the profile of the Bolocam beam is shown as a red dotted line, and the profile of a flat band power CMB power spectrum multiplied by the transfer function of the beam and our atmospheric noise removal algorithm is shown as a green dashed line. Additionally, the profile of a massive cluster, based on the fit parameters for CL0016 given in Bonamente, et al., multiplied by the transfer function of the beam and our atmospheric noise removal algorithm is shown as a blue dot-dashed line [20].

source of noise	NET_{CMB} per detector mK_{CMB}/\sqrt{Hz}			
	observed o-box = 3 pW	compromise G_0 o-box = 0.5 pW	optimum G_0 o-box = 0.5 pW	optimum G_0 , o-box, elec noise, opt eff
optical shot	1.8	0.9	0.9	0.6
optical Bose	1.8	0.6	0.6	0.6
bolo Johnson	1.5	0.9	0.7	0.4
bolo phonon	1.3	0.8	0.6	0.3
room-temp amp	1.2	0.7	0.6	0.1
JFET	1.2	0.7	0.6	0.1
total noise	3.7	1.9	1.7	1.0

Table 4.3: A summary of our observed noise with 3 pW of optical load from the optics box (left column), the estimated noise given the predicted optical loading from the optics box of 0.5 pW (second column), the estimated noise given the predicted loading from the optics box and using a bolometer thermal conductance optimized for 2.1 mm (third column), and the estimated noise given the predicted optics box loading, an optimized 2.1 mm thermal conductance, improved electronics noise, and higher optical efficiency from larger feed horns (right column). Note that approximately 75% of the detectors are lost if larger feed horns are used, so the overall sensitivity of the camera does not improve as much as would be expected from the single detector noise level.

removed.

4.4 Extra Noise During the 2004 Observing Season

As mentioned in Section 3.3, there was excess noise in the data during the 2004 observing season. This noise was not correlated among all the bolometers, and could not be removed using our standard data processing techniques. See Figure 4.6. However, the noise is correlated between the bolometers in a way that allows us to remove most of it using adaptive PCA subtraction. The correlations are not well understood, and appear to change over time. A grounding problem is a possible explanation for this excess noise, but the exact cause is not known. This noise has not reappeared in any of the data collected after the fall 2004 observing run, indicating it was unique to how the instrument was set up for that run. Unfortunately, we were not examining the data closely enough to discover and correct this problem while we were still collecting data.

4.5 Atmospheric Noise: Theory

The dominant source of non-removable noise in Bolocam data is fluctuations in emission from the atmosphere. Since water vapor produces most of the emission at millimeter wave-

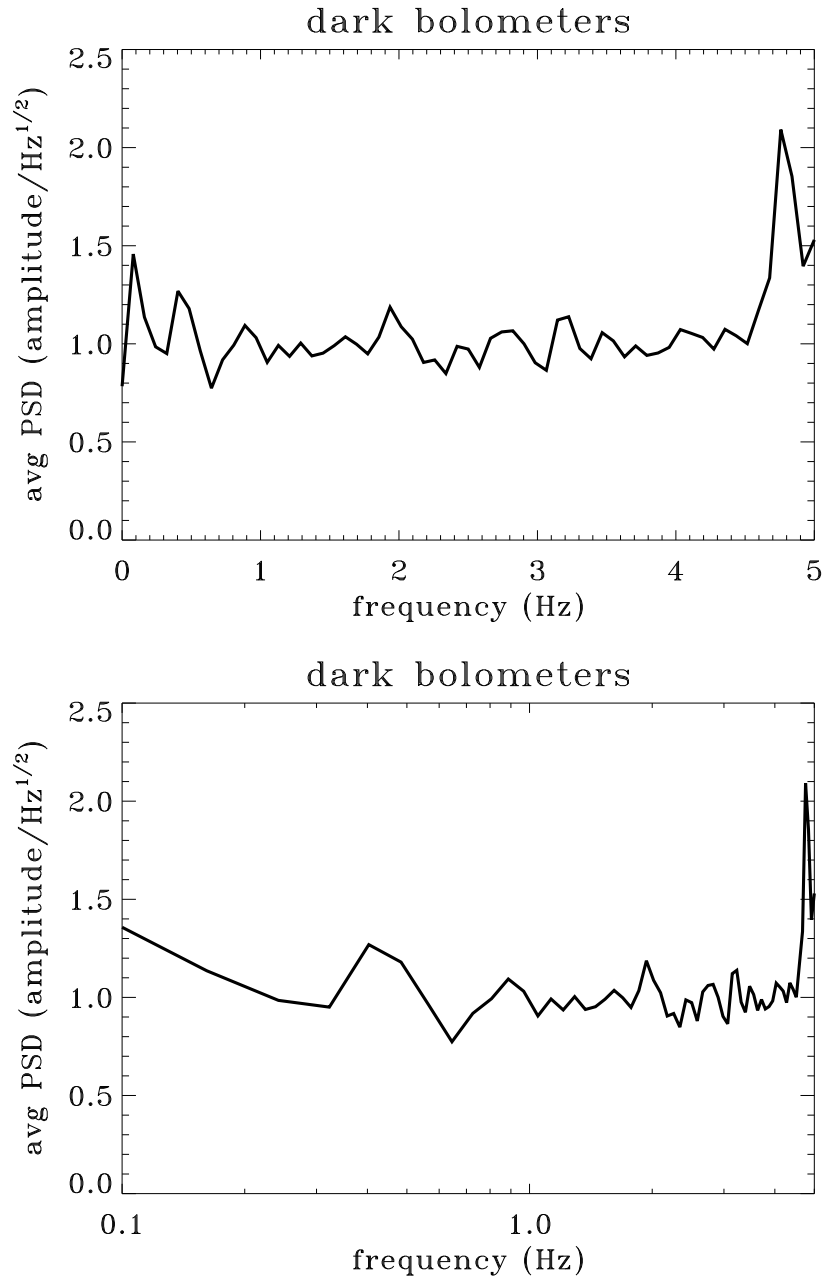


Figure 4.5: A typical PSD for the dark bolometers, averaged over all scans and all dark bolometers for a single ten-minute-long observation. The top plot shows the spectrum with a linear x-axis, and the bottom plot shows the spectrum with a logarithmic x-axis. The plots are made in arbitrary units of amplitude/ $\sqrt{\text{Hz}}$, since the responsivity of the dark bolometers is not known. Note that the power spectrum is white, except at high frequency where the effects of the anti-aliasing filter can be seen. In contrast, the normal bolometers have a $1/f$ -type power spectrum due to fluctuations in emission from the atmosphere.

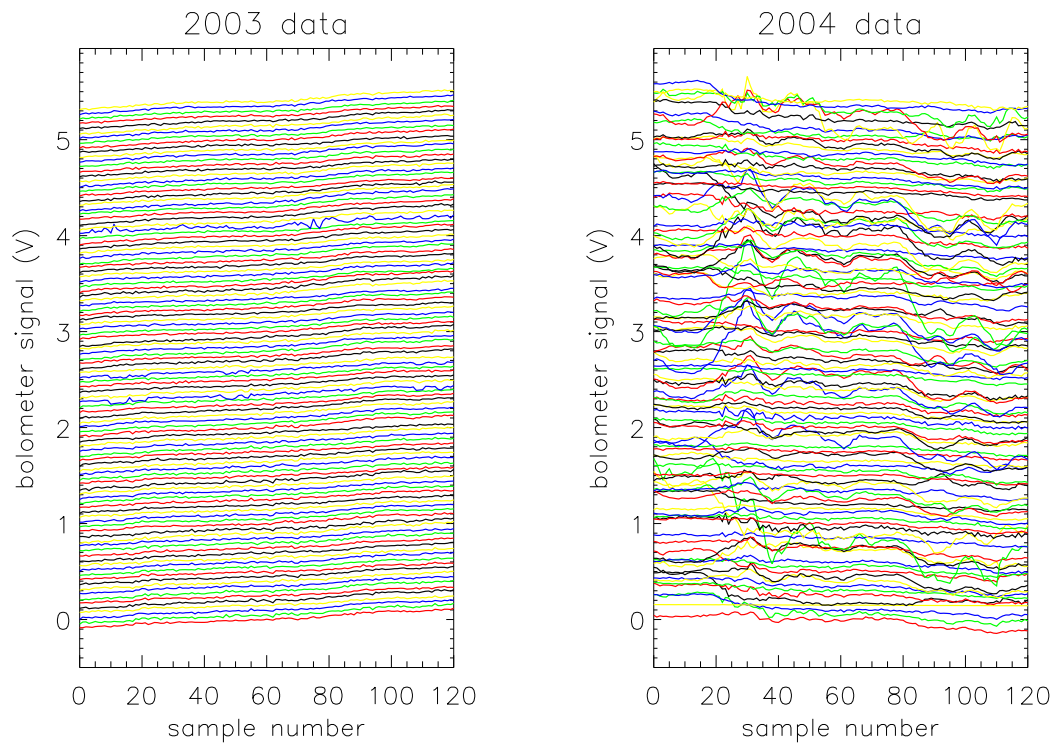


Figure 4.6: The plot on the left shows a typical set of bolometer time-streams taken in 2003, and the plot on the right shows a typical set of bolometer time-streams taken in 2004. In each plot, the time-stream from every working bolometer is plotted for the same 12.5 second long observation. The data for each bolometer was given a different DC offset to make them easier to view. In 2003 the majority of the noise is at low frequency and is common to every bolometer. This common mode low-frequency noise can also be seen in the 2004 data, but there is a lot of additional noise that is not common to all the bolometers.

lengths, these fluctuations are caused by variations in the column depth of precipitable water between Bolocam and the astronomical object of interest [28, 83, 89]¹¹. Bolocam was designed to have a high degree of overlap between the individual beams as they pass through the atmosphere, so most of the fluctuations in atmospheric emission show up as a common mode signal in all of the bolometers. However, the beams do diverge; the largest separation between beam centers increases by about 2.5 m per kilometer above the telescope. This divergence is small compared to the 10 m diameter of the the beams, but the result is that only $\simeq 90 - 95\%$ of the atmospheric fluctuations are common to all of the bolometers. Since the remaining noise from these fluctuations still dominates the data, we have attempted to model the variations in water vapor in the atmosphere. The goal of this modeling is to obtain a better understanding of the fluctuations, so that we can develop better schemes for their removal.

4.5.1 Kolmogorov/Thin-Screen Model

The Kolmogorov model of turbulence provides a good description of air movement in the atmosphere [72, 141]. According to the model, processes such as convection and wind shear inject energy into the atmosphere on large length scales, of order several kilometers [83, 154]. This energy is transferred to smaller scales by eddy currents, until it is dissipated by viscous forces at millimeter scales [83]. For a three-dimensional volume, the model predicts a power spectrum for the fluctuations from this turbulence that is proportional to $|\vec{q}|^{-11/3}$, where \vec{q} is a three-dimensional spatial frequency with units of 1/length. The same spectrum holds for particulates that are passively entrained in the atmosphere, such as water vapor [141].

For our analysis, we adopted the two-dimensional thin-screen model described by Lay and Halverson [83]. A schematic of this thin-screen model is given in Figure 4.7. This model assumes that the fluctuations in water vapor occur in a turbulent layer at a height h_{av} and a thickness Δh , where $h_{av} \gg \Delta h$. This layer is moved horizontally across the sky by wind at a velocity \vec{w} . Given these assumptions, the three-dimensional Kolmogorov power spectra

¹¹The column depth of oxygen in the atmosphere also produces a non-negligible amount of emission, a factor of a few less than the emission from water vapor under typical conditions at Mauna Kea. However, the oxygen in the atmosphere is well mixed, and therefore fluctuations in the emission are minimal. In contrast, the temperature of the atmosphere tends to be close to the condensation point of the water vapor, and causes the water vapor to be poorly mixed in the atmosphere. Therefore, there are in general significant fluctuations in the emission from water vapor [89].

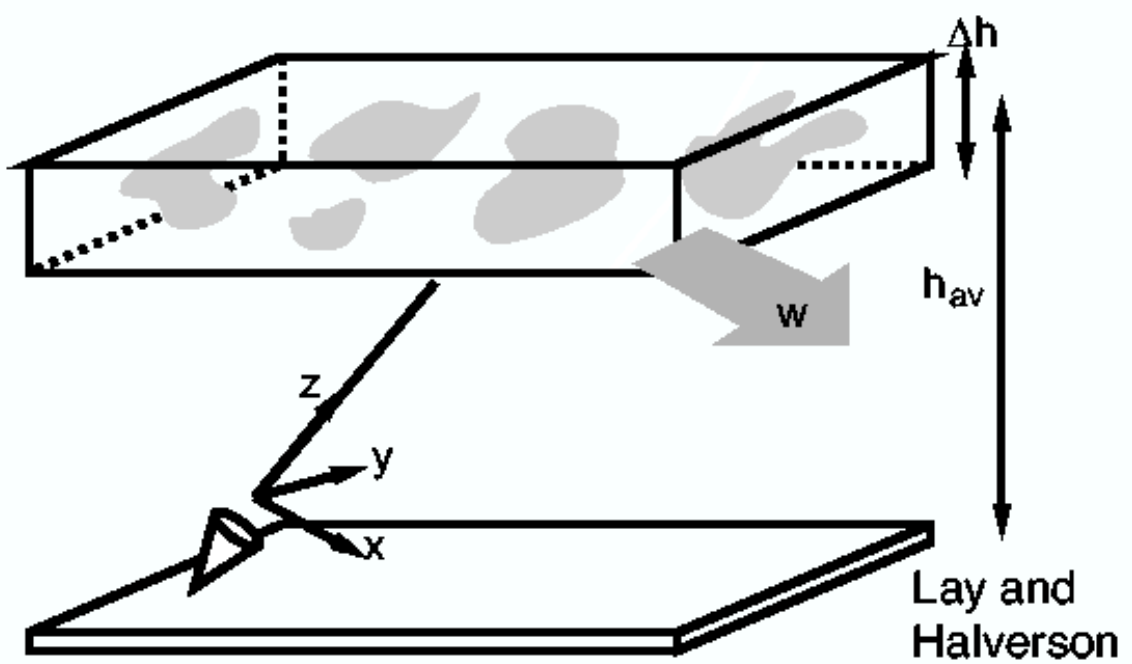


Figure 4.7: A schematic of the atmospheric model described by Lay and Halverson. The fluctuations in water vapor occur in a turbulent layer at a height of h_{av} and a thickness of Δh , where $h_{av} \gg \Delta h$. The turbulent layer is being moved by the wind, with a velocity \vec{w} . Figure taken from Lay and Halverson [83].

reduces to

$$P(\vec{\alpha}) = Ah_{av}^{5/3} \sin \epsilon^{-8/3} |\vec{\alpha}|^{-11/3}, \quad (4.9)$$

where A is a measure of the turbulent intensity, ϵ is the elevation angle of the telescope, and $\vec{\alpha}$ is the two-dimensional angular frequency with units of 1/radians.

4.5.2 Comparison to Data: Instantaneous Correlations

Equation 4.9 can be converted from a power spectrum in angular frequency space to a correlation function as a function of angular separation [24]. Since the power spectrum is azimuthally symmetric, we can write $P(\vec{\alpha})$ as $P(\alpha)$, where $\alpha = |\vec{\alpha}|$. This power spectrum will produce a correlation function according to

$$C(\theta) = 2\pi \int_0^\infty d\alpha \alpha P(\alpha) J_0(2\pi\alpha\theta), \quad (4.10)$$

where θ is the angular separation in radians and J_0 is the 0th-order Bessel function of the first kind¹². The correlation function produced by the integral in Equation 4.10 is an infinite series of hyper-geometric functions, which can be reduced to

$$C(\theta) = C_0 + C_1\theta^{\beta-2} + \mathcal{O}(\theta^2) \quad (4.11)$$

for small values of θ , where $\beta = 11/3$ for the Kolmogorov model we have adopted and C_0 and C_1 are functions of several of the physical parameters from the model. Note that C_1 is negative, because the correlation decreases with increasing angular separation. Without loss of generality, Equation 4.11 can be rewritten as

$$C(\theta) = C_0 + C_1\theta^{\gamma(\theta)}, \quad (4.12)$$

where $\gamma(\theta) = 5/3$ for $\theta \ll 1$. If atmospheric emission is the only signal in the time-stream, which is a reasonable approximation for Bolocam data, then $C_0 = 1$ and C_1 will be negative. However, Equation 4.11 is only valid for point-like beams, which is a poor assumption for Bolocam because the beam diameters are $\simeq 10$ m and the separations are of order 1 m. Since the far-field distance for Bolocam is $\simeq 50$ km at 2.1 mm, the beams can be well approximated by a top-hat function with a diameter of 10 m. With this assumption, we can numerically solve for the correlation as a function of angular separation, with the results shown in Figure 4.8. The result is that $\gamma(\theta)$ should be between 1.6 and 2.0 for any physically reasonable height of the turbulent layer.

To compare our data to this model, we calculated the relative correlation coefficient between the time-streams of every bolometer pair. A single correlation value for each pair was calculated for each 12.5-second-long scan made while observing one of the science fields, and then averaged over the twenty scans in one complete observation of the field¹³. Next, the correlations were binned according to the separation of the bolometer pair and fit to a function of the form

$$C(\theta) = C_0 + e^{a_0 + a_1 \log(\theta) + a_2 \log(\theta)^2}, \quad (4.13)$$

where C_0 , a_0 , a_1 , and a_2 are free parameters. This functional form was chosen because it

¹²In practice, the integral in Equation 4.10 diverges as $\alpha \rightarrow 0$, so a cutoff is made at α_{min} . This is physically reasonable because there is a maximum length scale for the turbulence.

¹³Since there is very little astronomical signal in the science fields, the atmospheric signal dominates the time-streams.

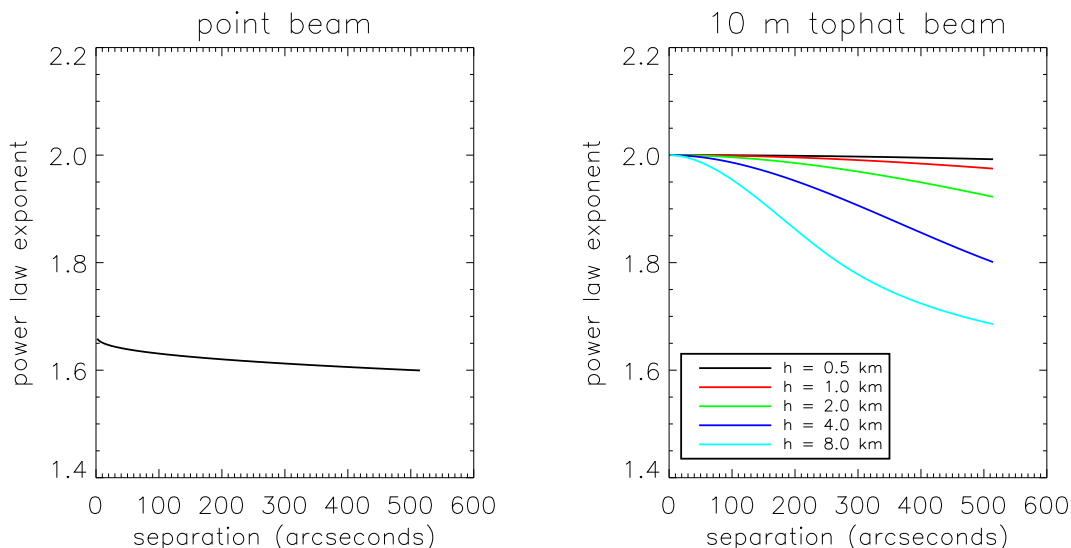


Figure 4.8: Plots of the exponent, $\gamma(\theta)$ from Equation 4.12, as function of angular separation. The plot on the left shows $\gamma(\theta)$ for a point-like beam, which goes to $5/3$ at small separations as expected from Equation 4.11. The plot on the right shows $\gamma(\theta)$ for a 10 m top-hat beam for several potential heights of the turbulent layer. As the turbulent layer gets higher and the separation gets larger, $\gamma(\theta)$ approaches the point-like beam approximation as expected. For reference, the diameter of the Bolocam focal plane is approximately 500 arcseconds. Note that in all cases the $\gamma(\theta)$ is between 1.6 and 2.0.

is a simple way to represent a running power law. Some examples of the data with a fit overlaid are given in Figure 4.9. We calculated a fit for all $\simeq 1000$ observations made in 2003, and approximately 400 of the observations produced a physically reasonable fit with $C_0 \leq 1$. Of these 400 observations, approximately 50 produced a reasonable fit without a running power law (i.e., $a_2 = 0$). The average power law index for the observations fit with a running model is $\gamma(\theta) = 1.0$, while the average fit for the observations without running is $\gamma(\theta) = 1.6$. A summary is given in Figure 4.10. In general, we found that observations made in good weather (i.e., less atmospheric noise) are more likely to produce a good fit to the model than observations made in bad weather.

Additionally, the same analysis was applied to data collected with Bolocam at 1.1 mm in early 2004. Approximately half of the observations were well fit by the model in Equation 4.13, including approximately 15% of the observations that are fit by a model without running. The average value of $\gamma(\theta)$ for the fits with running is 1.4, and the average value of $\gamma(\theta)$ for the fits without running is 1.7. It is not clear why the model works better for the 1.1 mm data than the 2.1 mm data, but the increased atmospheric opacity at 1.1 mm,

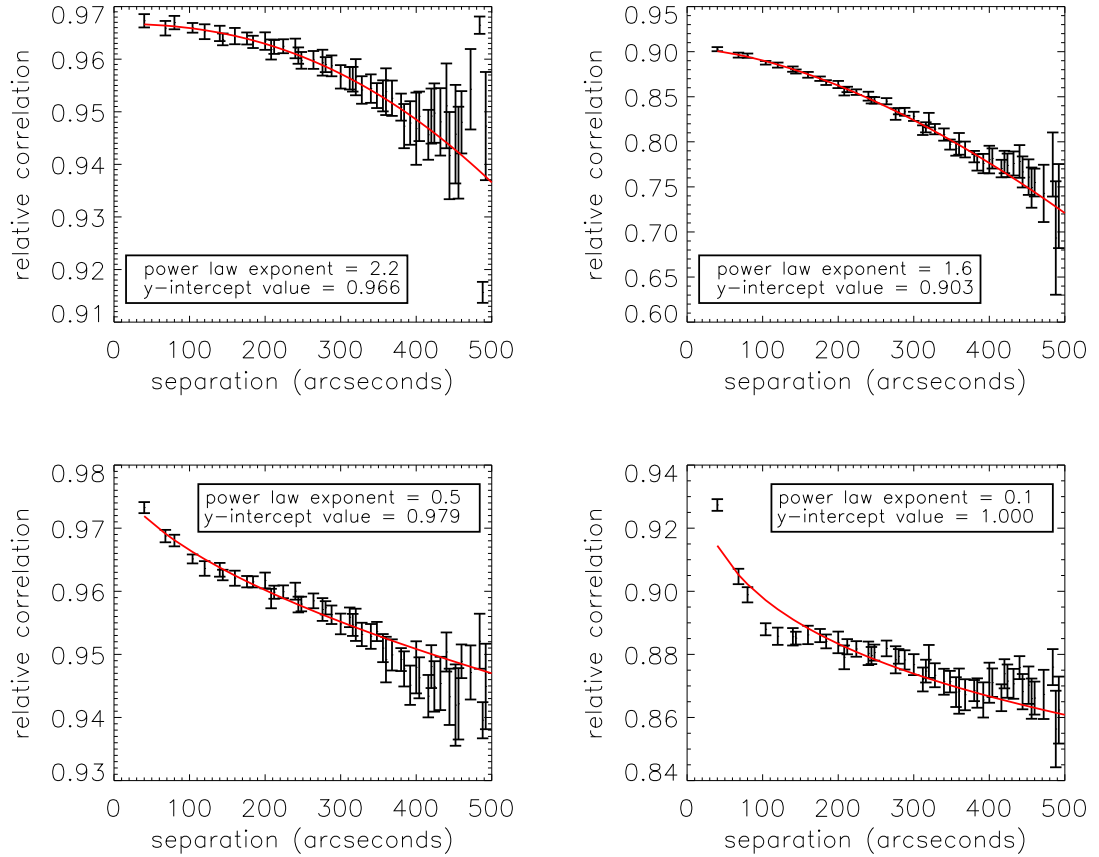


Figure 4.9: Relative correlation of the time-streams of all bolometer pairs for a single eight-minute-long observation of a science field. The correlations have been binned according to the separation between the bolometer pair. Overlaid in red is a fit of the running power law given in Equation 4.13. The legend in each plot gives the average value of the power law exponent, along with the y-intercept, C_0 . If the time-streams contained only atmospheric signal, then C_0 would equal one. The power law exponent is expected to be between 1.6 and 2.0, if the atmosphere is well approximated by the Kolmogorov turbulence model and the thin-screen approximation. The bottom right plot shows an observation that is not well described by the model, due to an excess correlation at small separations.

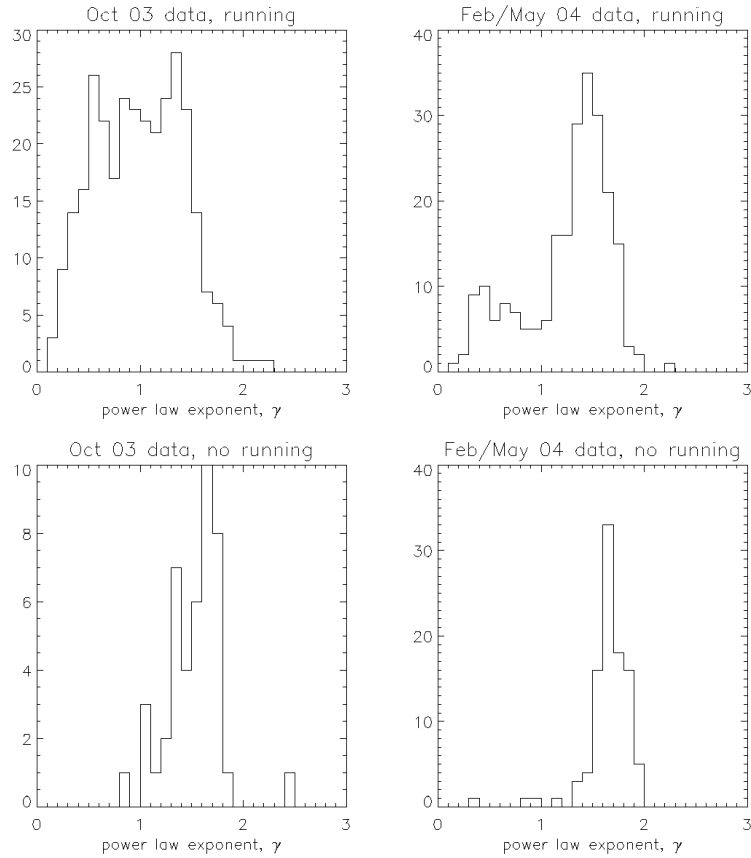


Figure 4.10: Histograms of the average fitted value of $\gamma(\theta)$ from Equation 4.12 for individual observations. The plots on the left show 2.1 mm data from 2003, and the plots on the right show 1.1 mm data from 2004. The top row of plots shows observations where a running value of $\gamma(\theta)$ produced the best fit, and the bottom row of plots shows observations where a fixed value of $\gamma(\theta)$ produced the best fit. $\gamma(\theta)$ is expected to run, and have a value between 1.6 and 2.0.

which produces more emission from the atmosphere, might play a role.

4.5.3 Comparison to Data: Time-Lagged Correlations

Another component in the model described by Lay and Halverson is the wind velocity, \vec{w} . If the wind velocity is assumed to be constant, and the spatial structure of the turbulent layer is static, then detectors aligned with the wind velocity will see the same atmospheric emission, but at different times [28]. Making reasonable assumptions for the wind speed (10 m/s) and height of the turbulent layer (1 km) yields an angular speed of approximately 30 arcminutes/sec for the layer. Since the diameter of the Bolocam focal plane is 8 arcminutes, the wind velocity and spatial structures only need to be constant for a fraction

of a second to make our assumption valid. To look for these time-lagged correlations we computed the relative cross power spectrum between every pair of bolometers. The details of this calculation are given in Appendix C, and it is important to note the cross spectra referred to in this section have units of V^2/Hz , not $V/\sqrt{\text{Hz}}$.

If two bolometers see the same signal at different times, then the cross PSD of these bolometers will have a phase angle described by

$$\tan^{-1}(xPSD) = \Theta_f = 2\pi f \Delta t \quad (4.14)$$

where f is the frequency in Hz and Δt is the time difference (in sec) between the signal recorded by the two bolometers. Therefore, the slope of a linear fit to Θ_f versus f will be proportional to Δt . If the simple atmospheric model we have assumed is correct, then $\Delta t/s_{pair}$ should be a sinusoidally varying function of the relative angle between the bolometer pair (θ_{pair}), where s_{pair} is the distance between the two bolometers. Analogous to the time-instantaneous model, approximately half of the observations were well fit by the time-lagged model. Some examples of $2\pi\Delta t/s_{pair}$ versus θ_{pair} are given in Figure 4.11. The data from the observation taken on November 10, 2003 in relatively good weather (i.e., less atmospheric noise) shows very good agreement with a sinusoid, which indicates that the simple model is close to reality. However, the data from December 7, 2003, when the weather was relatively poor, is clearly not sinusoidally varying. In general, the model appears to work better in good weather than in bad weather.

Using the data that is accurately described by the time-lagged model, we were able to determine the angular speed of the wind. Most of the speeds we inferred were between 10 and 40 arcminutes/second, in good agreement with what we expect for a reasonable wind speed and turbulent height. As an example, the amplitude of the sin wave for the plot on the left of Figure 4.11 is $0.22 = 2\pi\Delta t$, so $\Delta t = 0.035$ seconds for bolometers that are adjacent to each other¹⁴. This gives an angular velocity of 20 arcminutes/second, which corresponds to a wind velocity of about 10 km/hr at a height of 500 m, or a wind velocity of about 20 km/hr at a height of 1 km.

¹⁴Adjacent bolometers are approximately 40 arcseconds apart.

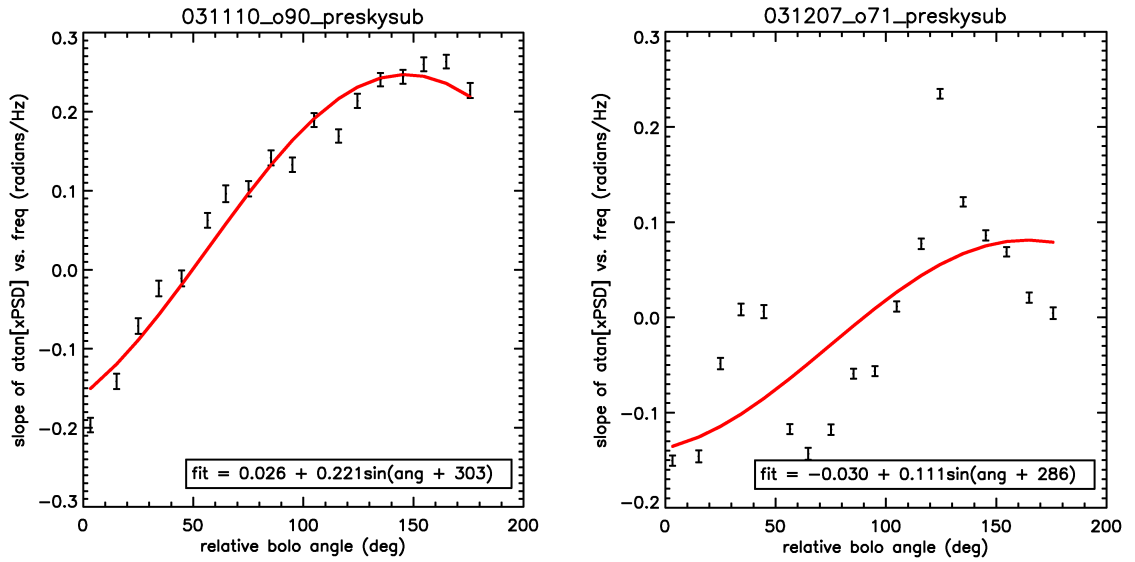


Figure 4.11: Plots of the slope of Θ_f/s_{pair} versus frequency for all bolometer pairs and all scans of a given observation. This slope is binned according to θ_{pair} , and a sinusoidal fit is overlaid in red. The fit is based only on frequencies where the atmospheric noise is the dominant signal, which is usually $f \lesssim .5$ Hz. The plot on the left comes from an observation taken on November 10, 2003, in good weather and the plot on the right comes from an observation taken on December 7, 2003, in bad weather. In general, the data collected in good weather is well fit by the model, while data collected in bad weather is not.

4.5.4 Comparison to Data: Summary

In summary, the time-lagged atmospheric model described in this section appears to describe approximately half of the data, which is similar to how well the time-instantaneous atmospheric model described our data. It is not clear why these models only work half of the time, but the models could fail because: 1) $\Delta h / h_{\text{av}} \simeq 1$ due to the turbulent layer being thick or close to the ground, or 2) there is more than one turbulent layer or a varying angular wind velocity within a single layer.

4.6 Atmospheric Noise: Removal

We have tried several methods to remove the signal produced by fluctuations in the atmosphere (atmospheric noise), since this is by far the largest noise signal in the Bolocam data. To start, the beams from each individual bolometer were designed to overlap to a high degree when passing through the atmosphere, so that most of the atmospheric noise will be a common mode signal that can be removed. Unfortunately, even after removing this common mode signal, atmospheric noise is the dominant source of noise in Bolocam data. More of the atmospheric noise can be removed using the different methods described in this section, but the remaining data are still significantly contaminated by atmospheric noise.

The adaptive PCA algorithm described in Section 4.6.4 was developed for Bolocam by Sunil Golwala, Glenn Laurent, Douglas Haig, Christian Reichardt, and other members of the Bolocam team prior to my work with atmospheric noise. I have not modified the algorithm that they developed. Additionally, the average template algorithm described in Section 4.6.1 was developed by the Bolocam team prior to my work, but I have made several modifications to improve this routine.

4.6.1 Average Template Subtraction

The most basic method for removing atmospheric noise is to subtract the signal that is common to all of the bolometers. Initially, a template is constructed according to

$$T_n = \frac{\sum_{i=1}^{i=N_b} c_i d_{in}}{\sum_{i=1}^{i=N_b} c_i} \quad (4.15)$$

where n is the sample number, N_b is the number of bolometers, c_i is the relative responsivity of bolometer i , d_{in} is the signal recorded by bolometer i at sample number n , and T_n is the template. A separate template is computed for each 12.5-second-long scan. After the template is computed, it is correlated with the signal from each bolometer to determine the correlation coefficient, with

$$\tilde{c}_i = \frac{\sum_{j=1}^{N_s} T_n d_{in}}{\sum_{j=1}^{N_s} T_n^2}. \quad (4.16)$$

\tilde{c}_i is the correlation coefficient of bolometer i and N_s is the number of samples in the 12.5-second-long scan¹⁵. Next, the c_i in Equation 4.15 are set equal to the values of \tilde{c}_i found from Equation 4.16, and a new template is computed. The process is repeated until the values of c_i stabilize. We generally iterate until the average fractional change in the c_i s is less than 1×10^{-8} , which usually takes five to ten iterations. If the c_i s fail to converge after 100 iterations, then the scan is discarded from the data. This algorithm generally removes around 90% of the atmospheric noise, as shown in Figures 4.12 and 4.13.

Even in the limit that the atmospheric noise is perfectly correlated between bolometers, and the template is a perfect reproduction of this atmospheric signal, the instrumental noise will still cause a statistical uncertainty in the c_i s we determine. Since the instrumental noise is white, with a PSD of $\simeq 4 \text{ mK}_{CMB}/\sqrt{\text{Hz}}$, this translates to a time-stream RMS of around 9 mK_{CMB} for our 5 Hz of bandwidth. Since each scan that we correlate to the atmospheric template has approximately 60 independent time samples, this means that the statistical variations in c_i caused by the instrumental noise will produce an RMS of around 1 mK_{CMB} in the time-stream. Since the atmospheric template is not white, this will not produce a flat noise level of $\simeq 0.5 \text{ mK}_{CMB}/\sqrt{\text{Hz}}$. Instead, the noise level is approximately $0.2 \text{ mK}_{CMB}/\sqrt{\text{Hz}}$ at high frequency and around $1 - 2 \text{ mK}_{CMB}/\sqrt{\text{Hz}}$ at low frequency. Still, even at low frequency, this residual noise is almost negligible when added in quadrature with the instrumental noise.

¹⁵The best fit correlation coefficients change from one scan to the next, typically by a couple percent. It is not clear what causes these fluctuations in the correlation coefficients, but there is a noticeable improvement in the amount of noise removed from the data when the coefficients are floated for each scan, rather than fixing them for all twenty scans in the observation.

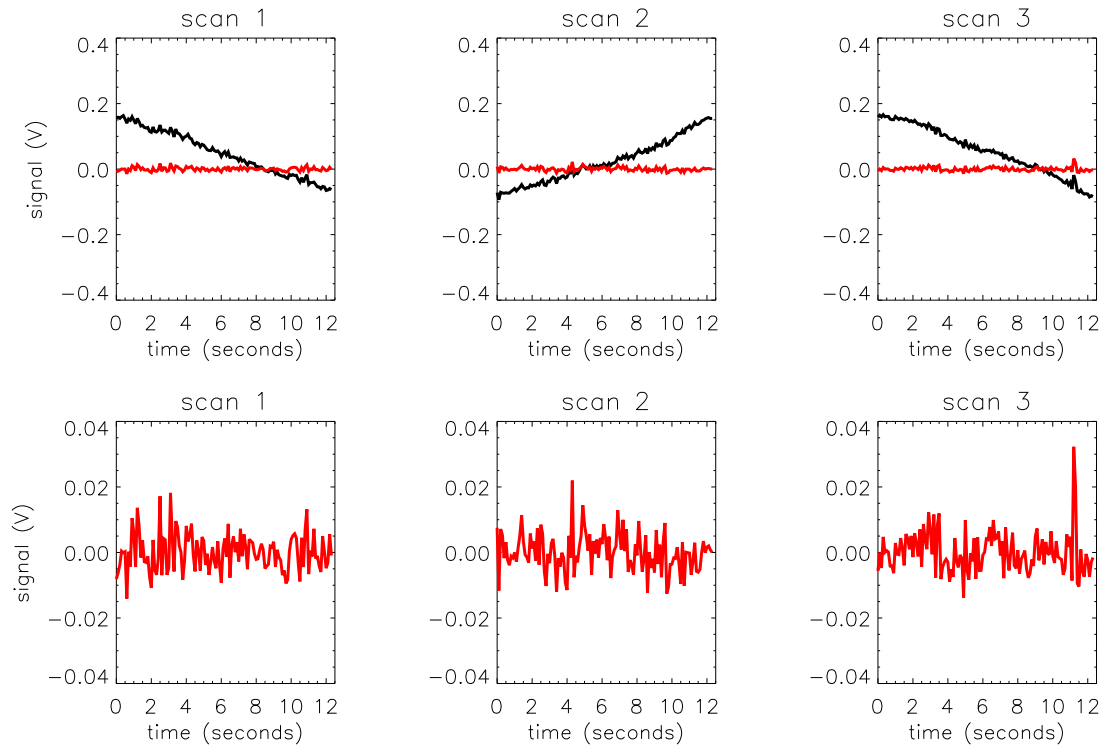


Figure 4.12: The top row of plots shows raw bolometer data in black. The data is dominated by a low-frequency drift caused by atmospheric noise. The red line shows the data after removing an average template. The bottom row of plots shows the same post-subtraction data, but the scale of the y-axis has been reduced by a factor of ten.

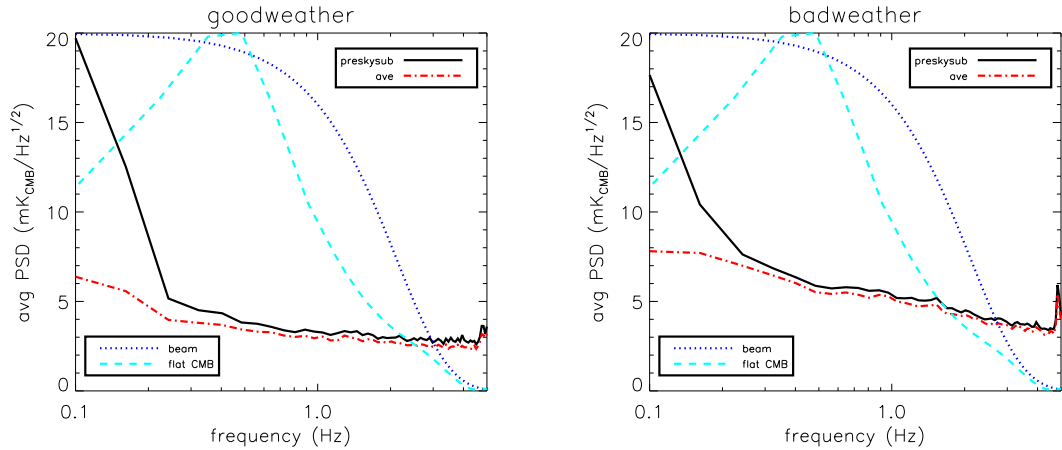


Figure 4.13: Plots of the time-stream PSDs averaged over all scans and all bolometers for a single observation. The black solid line shows the PSD prior to subtracting the atmospheric noise, and the red dot-dashed line shows the PSD after removing an average template of the atmosphere. Note the dramatic improvement at low frequency. The plot on the left shows data collected in relatively good weather on November 10, 2003, and the plot on the right shows data collected in relatively poor weather on December 7, 2003. Overlaid as a dark blue dotted line is the profile of the Bolocam beam, and overlaid as a light blue dashed line is the profile of a flat band power CMB power spectrum multiplied by the transfer function of the beam and our average template atmospheric noise removal algorithm. Note that in these plots, the PSD is reduced by a factor of $\simeq 50 - 75\%$ at low frequency after average subtraction, which appears to contradict the claim that average subtraction removes 90% of the atmospheric noise. However, there is a factor of $\simeq 10$ difference in the time-stream RMS calculated from the two PSDs, if frequencies below 100 mHz are included.

4.6.2 Wind Model

Since the atmospheric model described in Section 4.5.3 seemed promising, we attempted to improve our atmospheric noise removal algorithm by applying the appropriate time delay/advance to every bolometer prior to average subtraction. Since the fit in Section 4.5.3 gives the time delay/advance (Δt) as a function of the relative separation and angle between bolometer pairs, it is necessary to pick a reference point on the focal plane. We chose the center as our reference point (i.e., the location where $\Delta t = 0$), and then determined the angle and distance to each bolometer from this point. Next, Δt is determined for each bolometer using the sinusoidal fit for the slope of $2\pi\Delta t/s_{pair}$ versus Θ_{pair} . For example, the plot on the left in Figure 4.11 has a maximum at a relative bolometer angle of 147 degrees. With our convention for relative bolometer angle, this means the wind is coming from 147 degrees in the bolometer coordinate system. The amplitude of the sin wave is $0.22 = 2\pi\Delta t$, so $\Delta t = 0.035$ seconds for bolometers that are adjacent to each other.

For example, using the data described above, if a bolometer is located at 4.5 bolometer spacings from the center of the array, at an angle of 127 degrees, then that bolometer will see the atmospheric signal $0.035 \times 4.5 \times \cos(147 - 127) = .175$ seconds before a bolometer at the center of the array would. Since our processed data is sampled at 10 Hz, this corresponds to an advance of 1.75 samples. A linear interpolation is used to account for these fractional shifts. We applied the appropriate shift to the time-stream of each bolometer before performing average subtraction, but this did not seem to improve the data. See Figure 4.14. Additionally, the map made from data that was cleaned using this shift was extremely stripey and had a lot of $1/f$ noise. Therefore, we abandoned this atmospheric noise subtraction algorithm.

4.6.3 Higher-Order Template Subtraction

It is useful to think about what type of modes in the atmosphere will cause bolometers at different positions to see different signals, which is the reason subtraction of an average template does not remove all the atmospheric noise. Since the diameter of an individual beam within the atmosphere is of order 10 m, and the separation between beams within the first several km of the atmosphere is of order 1 m, average subtraction will not be able to remove variations in the atmosphere that occur on scales smaller than a few meters. But,

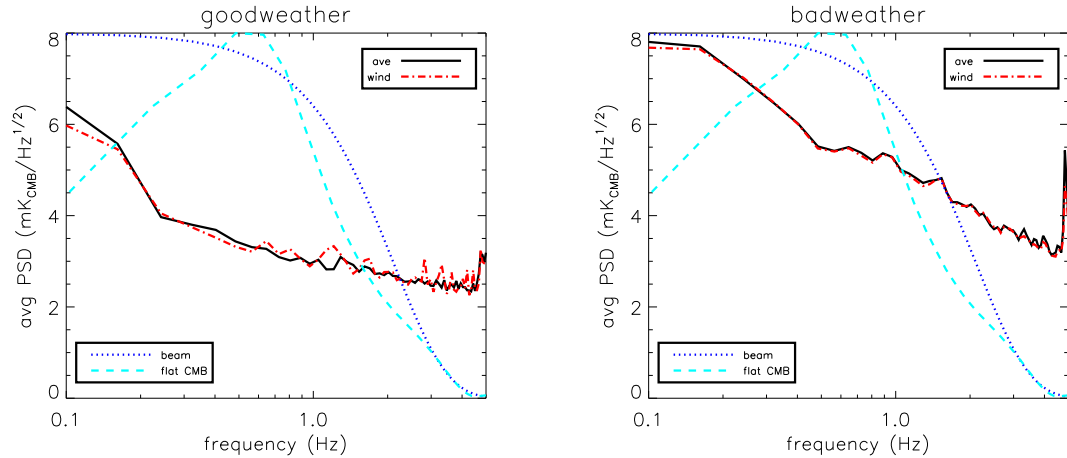


Figure 4.14: Plots of the time-stream PSDs averaged over all scans and all bolometers for a single observation. The plot on the left shows an observation taken in relatively good weather on November 10, 2003, and the plot on the right shows an observation taken in relatively poor weather on December 7, 2003. The solid black line is the PSD after removing atmospheric noise using an average template. The dot-dashed red line is the PSD after shifting the data to account for the wind velocity before removing an average template. In good weather there is an $\sim 10\%$ improvement in the noise at the lowest frequency, but in general the two methods produce similar results. Note that the wind velocity is determined from analyzing the cross power spectra between the bolometers, not from a direct measurement. Overlaid as a dark blue dotted line is the profile of the Bolocam beam, and overlaid as a light blue dashed line is the profile of a flat band power CMB power spectrum multiplied by the transfer function of the beam and our average template atmospheric noise removal algorithm.

the power spectrum of the atmosphere shows there is almost no variation in emission on these short scales. In general, most of the atmospheric noise in our time-stream data is below 0.1 Hz, and the atmospheric noise becomes negligible above 0.5 Hz. We found in Section 4.5.3 that the angular speed of the wind in the thin-layer model is approximately 20 arcminutes/sec, which means that most of the atmospheric noise occurs on scales larger than $\simeq 0.05$ radians and the noise becomes negligible on scales shorter than $\simeq 0.01$ radians. If we assume a reasonable height for the thin layer of water vapor, around 1 km, this implies that the atmospheric noise is negligible on scales $\lesssim 10$ m, and most of the noise occurs on scales $\gtrsim 100$ m. This means that the residual atmospheric noise signal that remains after processing the data with the average subtraction algorithm is not caused by atmospheric fluctuations on scales smaller than a few meters.

Consequently, the cause of variations in the atmospheric signal recorded by different bolometers must be fluctuations in atmospheric emission that occur on scales much larger than the projected size of the focal plane. This means that the variation in signal over the focal plane should resemble a low-order two-dimensional polynomial. Therefore, we decided to try removing a planar fit of atmospheric signal versus bolometer position, and also a two-dimensional quadratic fit of atmospheric signal versus bolometer position. This is similar to the method used by SHARC II to remove atmospheric noise [75].

The fit is carried out as follows. First, a template is created at each point in the time-streams by fitting a plane (or 2-D quadratic) to signal versus bolometer position in the focal plane. Appendix D.1 contains the details of how the template is constructed. This template is then iteratively correlated to each bolometer for each 12.5-second-long scan and removed, in the same way the average sky subtraction template is correlated. Compared to average sky subtraction, a slight reduction in noise, most noticeable at low frequencies, can be seen in the time-streams (see Figure 4.15). However, the difference in the noise level of a map made from co-adding all $\simeq 500$ 2003 observations of Lynx is significant (see Figure 4.16). The reason such a small change in the time-stream PSDs produces such a large change in the map PSDs is because planar and quadratic subtraction reduce the amount of correlation between the bolometer time-streams, especially among nearest neighbor bolometers. See Figure 4.20.

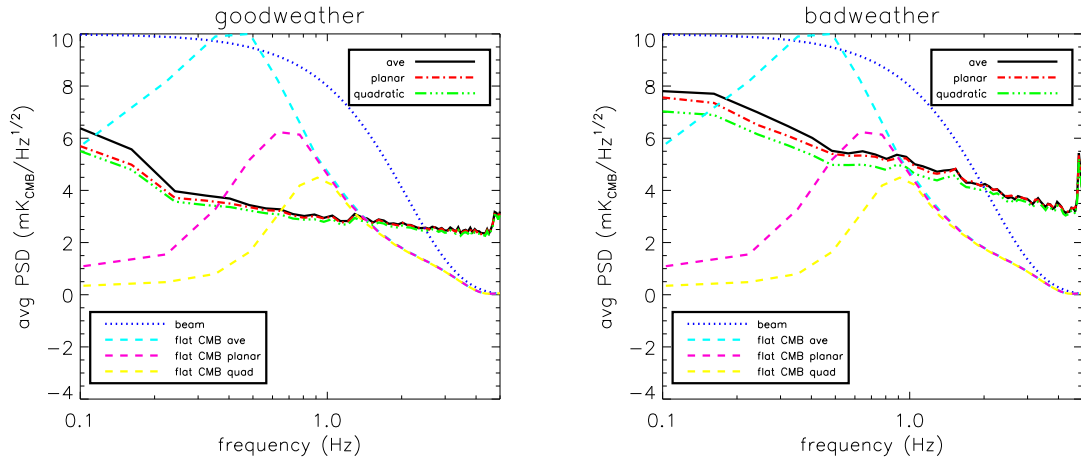


Figure 4.15: Plots of the PSD averaged over all scans and all bolometers for a single observation. The plot on the left shows an observation taken in good weather on November 10, 2003, and the plot on the right shows an observation taken in bad weather on December 7, 2003. The solid black line is the PSD after removing atmospheric noise using an average template. The dot-dashed red line is the PSD after removing a planar fit to signal versus bolometer position. The dot-dot-dot-dashed green line is the PSD after removing a 2-D quadratic fit to signal versus bolometer position. Overlaid as a dark blue dotted line is the profile of the Bolocam beam. Overlaid as a light blue/magenta/yellow dashed line is the profile of a flat band power CMB power spectrum multiplied by the transfer function of the beam and our average/planar/quadratic template atmospheric noise removal algorithm. Although the ratio of the PSD to the transfer function makes it appear that average subtraction is clearly the best method, these plots do not show the residual correlations between the bolometer time-streams. Quadratic and planar subtraction remove more of these correlations, which translates into a large reduction in the map-space noise, which can be seen in Figure 4.16.

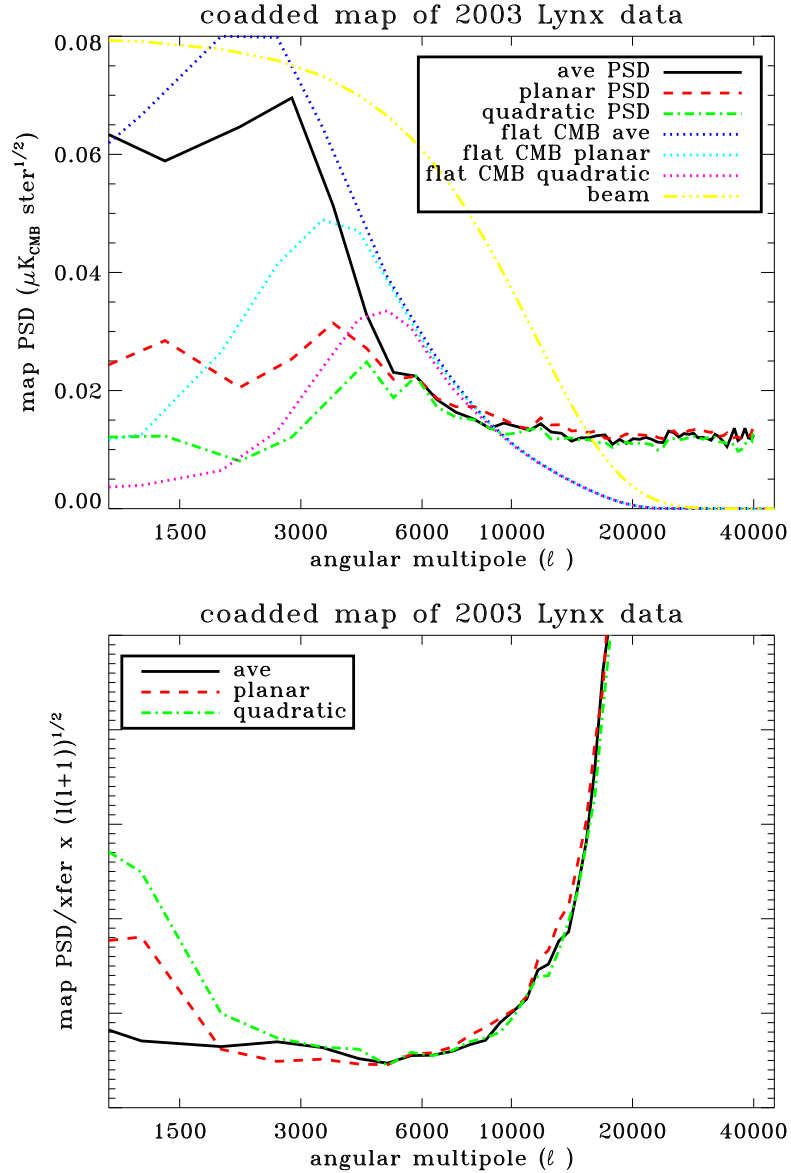


Figure 4.16: Plots of the map PSD for a map made from co-adding all $\simeq 500$ observations of Lynx taken in fall 2003. The PSDs have been azimuthally averaged to present a radial PSD. The solid black line represents data cleaned with average subtraction, the dashed red line represents data cleaned with planar subtraction, and the dot-dashed green line represents data cleaned with quadratic subtraction. Overlaid on the top plot with a dot-dot-dot-dashed line is the profile of the Bolocam beam. Overlaid on the top plot with a dotted dark blue/light blue/magenta line is the profile of a flat band power CMB power spectrum multiplied by the transfer function of the beam and our average/planar/quadratic atmospheric noise removal algorithm. The bottom plot shows the PSD for each atmospheric noise removal algorithm divided by the transfer function for that algorithm and multiplied by $\sqrt{\ell(\ell+1)}$, to show the relative sensitivity to a flat band power CMB power spectrum.

4.6.4 Adaptive Principal Component Analysis (PCA)

We have also used an adaptive PCA algorithm to remove atmospheric noise from Bolocam data [82, 96]. First, a square correlation matrix with dimensions equal to the number of bolometers is calculated from the time-streams for each scan. This matrix is then decomposed into orthogonal eigenvectors, and an eigenvalue is computed for each vector. Next, the distribution of eigenvalues is analyzed, and the large eigenvalues that are outliers are iteratively removed until no outliers remain. Finally, the remaining eigenvectors are transformed back into bolometer time-streams. More details of the algorithm are given in Appendix D.2.

Typically, adaptive PCA only removes one or two eigenvectors from the 2003 data. At high frequencies, adaptive PCA works slightly better than the quadratic method described in Section 4.6.3, but there is very little astronomical signal at these frequencies because of attenuation by the beam. In good weather, the results from adaptive PCA are comparable to the results from quadratic subtraction, but adaptive PCA performs much worse than quadratic subtraction in bad weather. See Figure 4.17. However, adaptive PCA attenuates more of the astronomical signal than quadratic subtraction¹⁶, so adaptive PCA was not used to remove atmospheric noise for the 2003 data.

In addition to removing signals that are correlated between all bolometers (e.g., atmospheric noise), adaptive PCA is also effective at removing signals that are correlated among a subset of bolometers. Specifically, adaptive PCA is able to remove most of the additional noise that Bolocam experienced during the 2004 observing season (see Section 4.4). For a typical observation in 2004, adaptive PCA will remove between 5 and 10 eigenvectors. Unfortunately, a large amount of astronomical signal is also removed when this many eigenvectors are subtracted, but adaptive PCA is the only effective method for removing this noise.

4.6.5 Nearest-Neighbor Bolometer Correlations

In general, all of the Bolocam observations taken in bad weather produce a large number of bolometer pairs with abnormally high correlations between their time-streams. Addi-

¹⁶For a dim point-like source, adaptive PCA removes approximately 19% of the flux, while quadratic subtraction only removes about 12% of the flux. For reference, average subtraction removes around 2% of the flux and planar subtraction removes approximately 6% of the flux. For a more diffuse source, like the CMB, quadratic subtraction actually attenuates a little more signal than adaptive PCA. However, quadratic subtraction is only used for observations taken in bad weather when processing for non point-like signals (e.g., the CMB), and in bad weather quadratic subtraction significantly outperforms adaptive PCA.

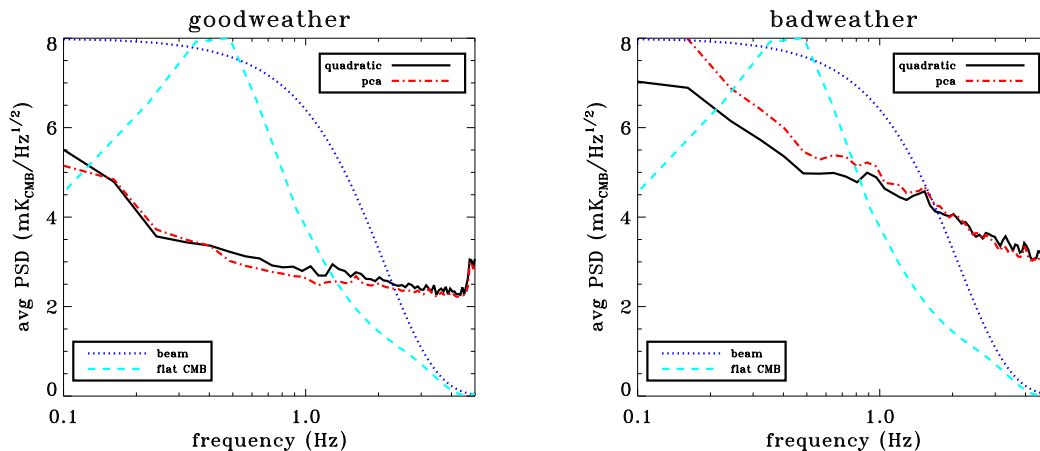


Figure 4.17: Plots of the PSD averaged over all scans and all bolometers for a single observation. The plot on the left shows an observation taken in good weather on November 10, 2003, and the plot on the right shows an observation taken in bad weather on December 7, 2003. The solid black line is the PSD after removing atmospheric noise using a quadratic fit to signal versus bolometer position. The dot-dashed red line is the PSD after using the adaptive PCA algorithm to remove atmospheric noise. Overlaid as a dark blue dotted line is the profile of the Bolocam beam, and overlaid as a light blue dashed line is the profile of a flat band power CMB power spectrum multiplied by the transfer function of the beam and our average template atmospheric noise removal algorithm.

tionally, the pairs with very large correlations in bad weather are almost always adjacent bolometers. See Figure 4.18. The reason for the high correlation among nearest neighbor bolometers is the small separation between them on the focal plane, since the horns are only 5 mm, or $0.7 (f/\#)\lambda$,¹⁷ on center from each other. Using the optical properties of the telescope and Bolocam optics, along with the geometry of the focal plane, we simulated the amount of correlation between nearest neighbor bolometers for a beam-filling source (like the atmosphere). The result is that approximately 53% of the power received by nearest neighbor bolometers is completely correlated. If the emission from the atmosphere was uniform, then this correlation would be removed by average subtraction since the signal would be correlated among all bolometers. However, since the emission from the atmosphere is not uniform, especially in bad weather, this excess correlation of nearest neighbors will not be completely removed by our sky subtraction algorithms. Although, in good weather most of the correlation can be removed with the planar or quadratic atmospheric noise removal algorithm. See Figure 4.19. A summary of the correlation between the nearest

¹⁷The value of $(f/\#)\lambda$ corresponds to the ratio between the opening diameter of the feed horn and the FWHM of Airy function describing the illumination pattern.

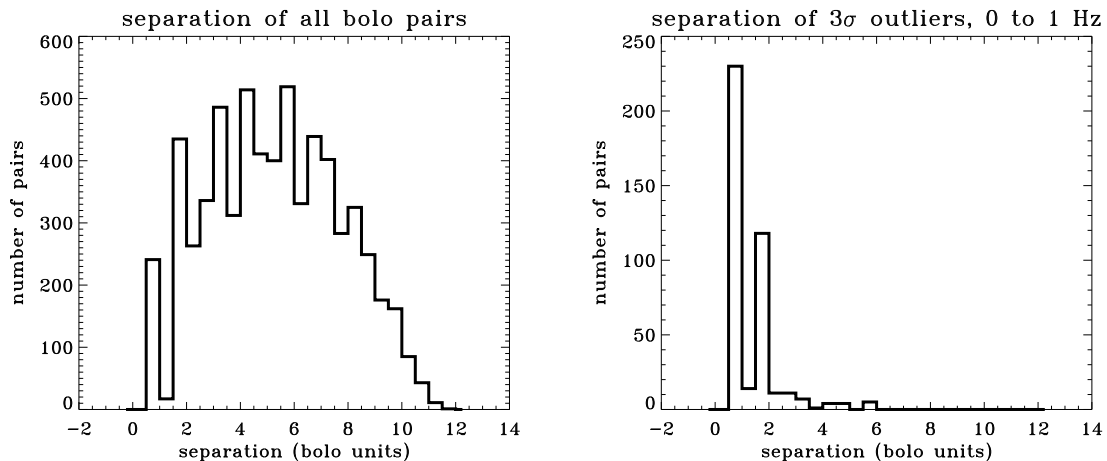


Figure 4.18: The histogram on the left shows the separation between all bolometer pairs. The histogram on the right shows the separation between bolometer pairs that have an abnormally high correlation between their time-streams. Note that most of the highly correlated pairs are close to each other. The bolometer pairs with abnormally high correlations are flagged if the absolute value of the cross PSD between the pair is more than 3σ from zero. Typically, these pairs are highly correlated at all temporal frequencies, but the effect is strongest at low frequency. Therefore, only the cross spectra below 1 Hz were used to determine which pairs are highly correlated. These histograms are made from an observation taken on December 7, 2003, and are typical of an observation made in bad weather.

neighbor bolometer pairs for all of the observations that were made in 2003 is given in Figures 4.20 and 4.21.

This noise is difficult to remove, because it is only correlated among bolometers that are close to each other on the focal plane. We have attempted to remove this noise by constructing localized templates using the data from a bolometer and the $\lesssim 10$ bolometers that are adjacent to it on the focal plane. We have removed these localized templates from the data both before and after applying our atmospheric noise removal algorithm to the data. Unfortunately, subtracting these templates from the data resulted in an unacceptable amount of signal attenuation, and not all of the locally correlated noise was removed.

4.7 Sensitivity Losses Due to Correlations and Atmospheric Noise

Ideally, the noise in our data would be uncorrelated between bolometers and have a white spectrum. This is approximately what we would expect if instrumental or photon noise was the dominant source of unwanted signal in our data time-streams. However, at low

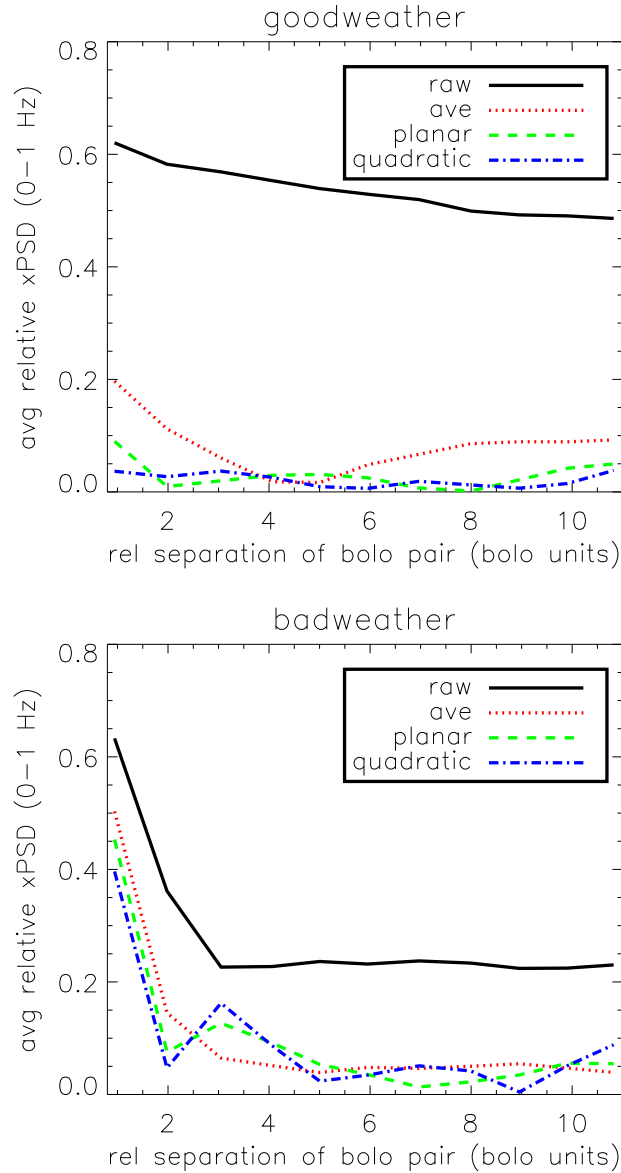


Figure 4.19: These plots show the relative cross PSD averaged over all scans and all frequencies below 1 Hz, then binned according to bolometer pair separation for a single observation. See Appendix C. The plot on the top shows data from an observation taken in good weather on November 10, 2003, and the plot on the bottom shows data taken in bad weather on December 7, 2003. Note that the excess correlation at small relative separations is essentially removed from the data in good weather using higher-order atmospheric noise removal algorithms. However, even after applying the quadratic algorithm, the correlations remain in the data collected in bad weather. The reason these plots show a lower correlation fraction compared to the plots in Figure 4.9 is because the relative xPSD has been averaged over all frequencies below 1 Hz. This means that all of the modes below 1 Hz are weighted equally, in contrast to correlations shown in Figure 4.9 which are dominated by the strong atmospheric signal at very low frequency.

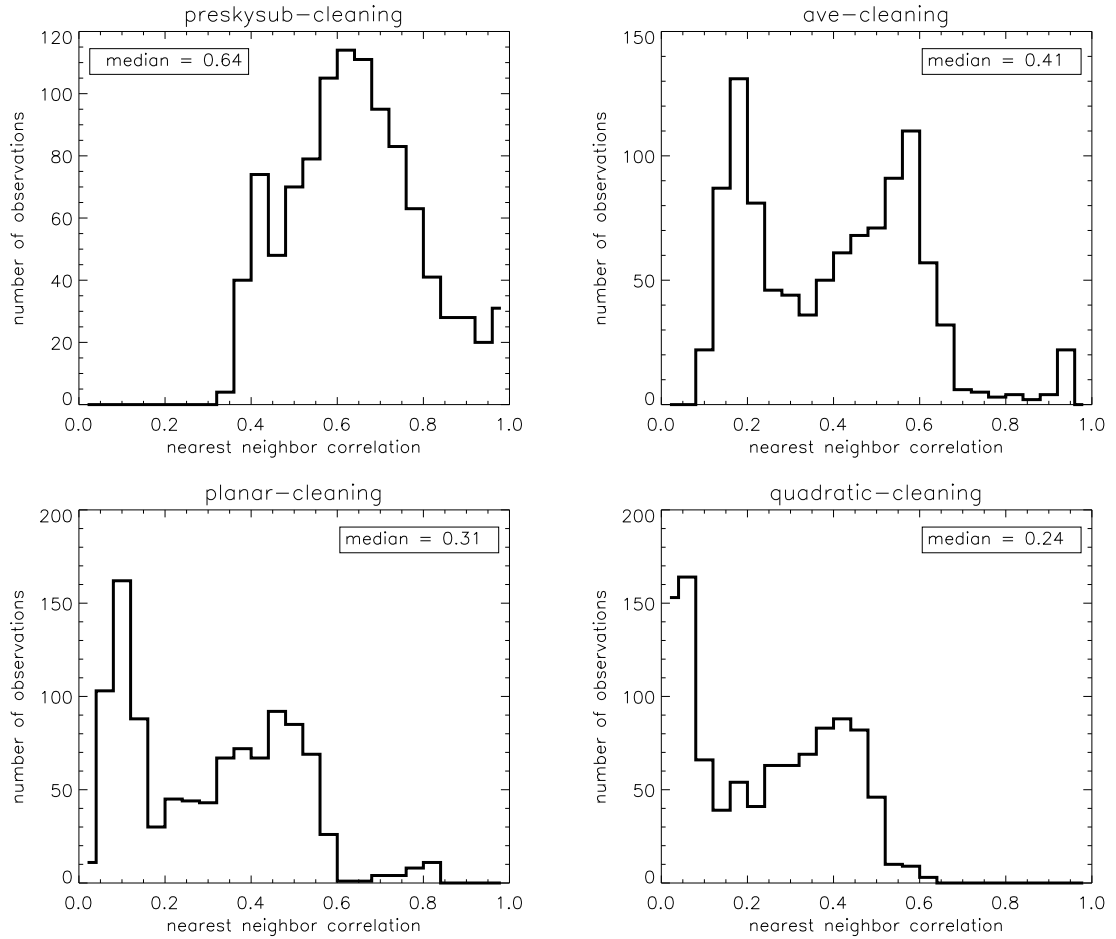


Figure 4.20: Histograms of the average relative correlation between nearest neighbor bolometer pairs over an entire observation. The histograms cover all of the data collected in 2003. Only data between 0 and 1 Hz was used to compute the correlation. The plot in the upper left shows data prior to removing the atmospheric noise, the plot in the upper right shows data after average subtraction, the lower left plot is data after planar subtraction, and the lower right plot is data after quadratic subtraction. Note the bimodality in the data after atmospheric noise subtraction. There is one group of observations with very little correlation between bolometer time-streams (good weather) and another group of observations with a relatively large amount of correlation between bolometer time-streams (bad weather).

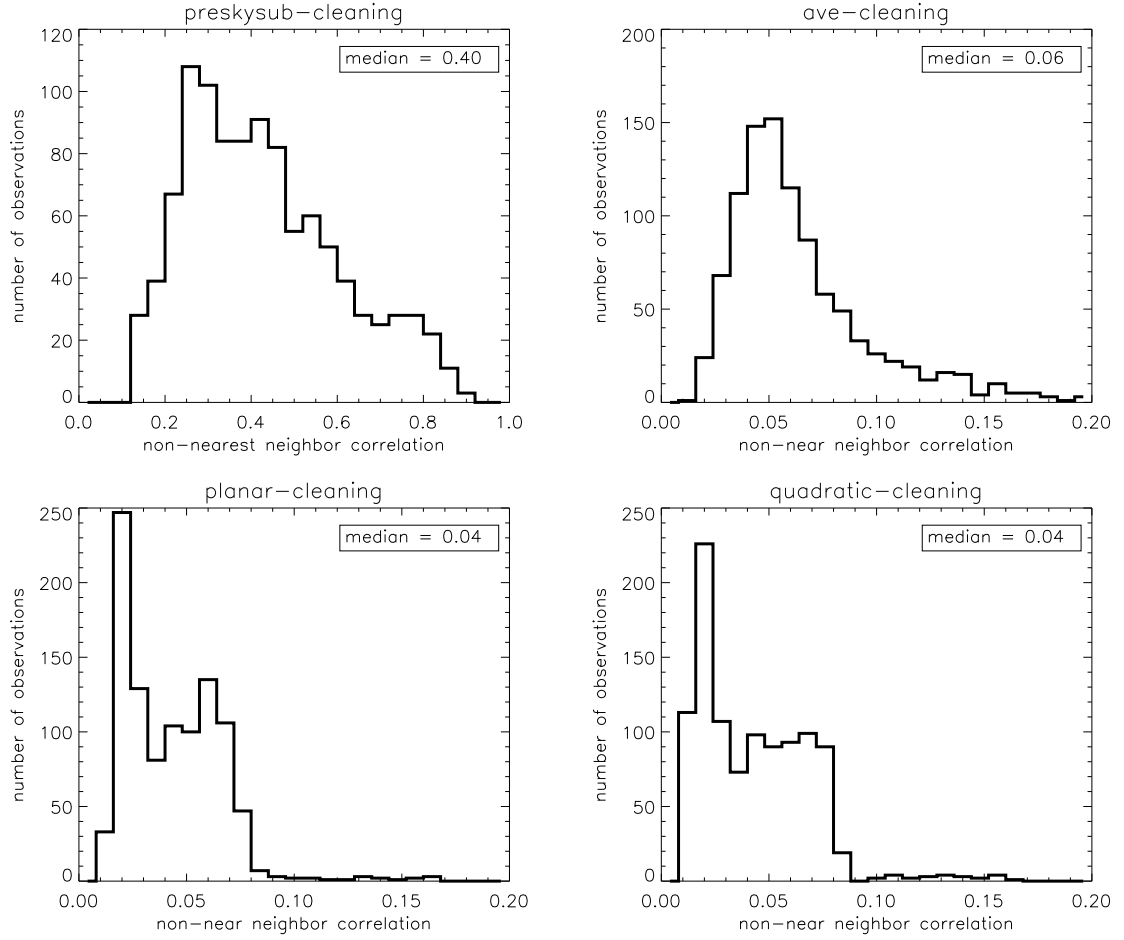


Figure 4.21: Histograms of the average relative correlation between all bolometer pairs that are not nearest neighbors over an entire observation. The histograms cover all of the data collected in 2003. Only data between 0 and 1 Hz was used to compute the correlation. The plot in the upper left shows data prior to removing the atmospheric noise, the plot in the upper right shows data after average subtraction, the lower left plot is data after planar subtraction, and the lower right plot is data after quadratic subtraction. Note that the scale of the x-axis is different for the plots on the bottom and top right, compared to the plot in the upper left and the plots in Figure 4.20.

frequencies our data is dominated by atmospheric noise which rises steeply with a $1/f$ -type spectrum. Additionally, the unremoved atmospheric noise produces correlations between the bolometer time-streams. The atmospheric noise also indirectly creates correlations among the bolometer time-streams due to our removal algorithms. This is because the atmospheric template is a superposition of all the bolometer data, so a small amount of signal from each bolometer is subtracted from the time-stream of every other bolometer when the template is subtracted from the data.

To determine the degradation in our sensitivity to measure a CMB anisotropy caused by these non-idealities in our data, we have created two sets of simulated time-streams. A different simulated data set was generated for each detector for each eight-minute-long observation, based on the measured PSD of each bolometer for each observation. One simulated data set contains randomly generated data with the same noise properties as our actual data, except the simulated data is completely uncorrelated between bolometers. The second set was generated using a flat noise spectrum (i.e., white noise), based on the white noise level observed in our actual data at high frequency. This simulated data set provides a best case scenario for Bolocam. For each simulation we generated data corresponding to all of the 2003 observations of Lynx, and the results are shown in Figure 4.22. Additionally, we made a map from our actual data after masking off 79 of the 115 working detectors. This data set includes 36 detectors, all of which are separated by more than $2(f/\#)\lambda$, allowing us to test if the time-stream correlations are isolated to near-neighbor detector pairs. The results from this data set are also shown in Figure 4.22.

At high spatial frequency ($\ell \gtrsim 10000$) the simulated data sets produce noise levels that are similar to our actual data, which implies that the correlations between detectors occur at low frequency and due to the atmospheric noise. However, both simulated data sets have a much lower noise level than our actual data at low spatial frequencies. To quantify the difference between the simulated data sets and our actual data set we have estimated the uncertainty in determining the amplitude of a flat CMB power spectrum using Equation F.13. Additionally, we estimated the uncertainty in determining the amplitude of a flat CMB power spectrum for the data set that contains our actual data for 36 detectors. This uncertainty was multiplied by $36/115$ to account for the degradation caused by masking off 79 detectors. The results are shown in Table 4.4. The simulated data indicate that our uncertainty on the amplitude of a flat CMB power spectrum would be improved by a factor

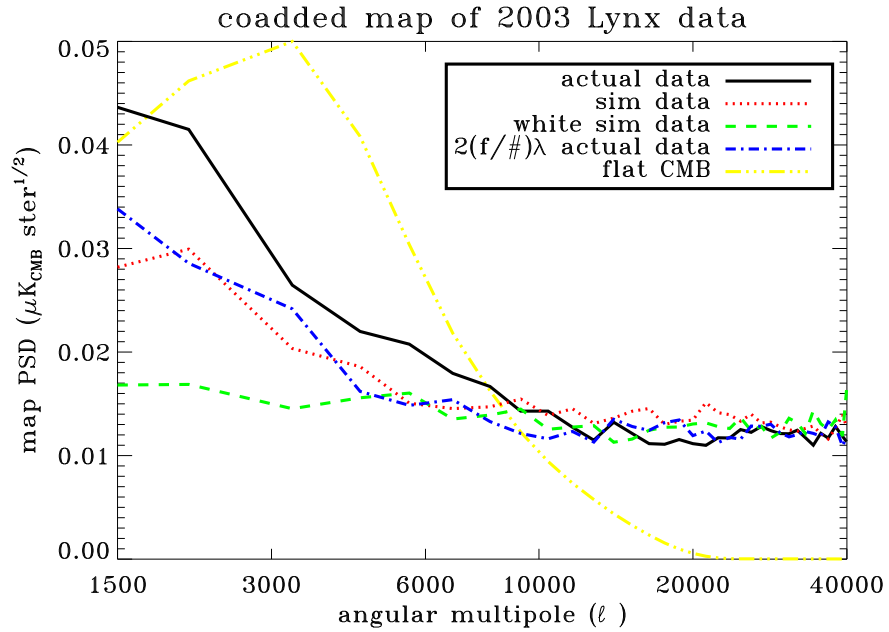


Figure 4.22: The solid black line shows the map PSD for all of the data collected for the Lynx field in 2003. The red dotted line shows the map PSD for simulated data generated from the noise spectrum of our actual time-streams, except that the simulated data are uncorrelated between detectors. The green dashed line shows the map PSD for uncorrelated simulated data that has a flat frequency spectrum and is based on the white noise level of our actual data. The blue dot-dashed line shows the map PSD for a map made from our actual data, after masking out some detectors so that the spacing between all detectors is at least at least $2(f/\#)\lambda$. This reduces the number of detectors from 115 to 36, but it discards the relatively correlated data between near neighbor detectors. Since this PSD overlaps with the uncorrelated simulated PSD, we can conclude that most of the correlations between detector time-streams occurs for near neighbor detectors. Note that this spectrum has been multiplied by $\sqrt{36/115}$ to account for the change in the number of detectors. Also shown as a yellow dot-dot-dashed line is a flat band power CMB spectrum multiplied by our transfer function.

Lynx 2003 data

data type	data spectrum	CMB amplitude uncertainty
actual data	actual data	$270 \mu\text{K}_{CMB}^2$
simulated	actual data	$170 \mu\text{K}_{CMB}^2$
simulated	white	$100 \mu\text{K}_{CMB}^2$
actual data, $2(f/\#)\lambda$	actual data	$170 (550) \mu\text{K}_{CMB}^2$

Table 4.4: The estimated uncertainty on measuring the amplitude of a flat CMB power spectrum using Equation F.13 for all of the 2003 Lynx observations. The four data sets include: our actual data, simulated data using our actual time-stream noise spectra, simulated data using our actual time-stream white noise level, and our actual data after masking off 79 of our 115 detectors so that the spacing between all detectors is at least $2(f/\#)\lambda$. For the two simulated data sets the bolometer time-streams are uncorrelated. The results for the second and fourth data sets are similar, after accounting for the reduction in detector number in the fourth set, indicating that the majority of the correlations between our detector time-streams are between near-neighbor detectors. The results show that our sensitivity to a CMB amplitude is reduced by a factor of $\lesssim 2$ due to these correlations, and by another factor of $\lesssim 2$ due to the $1/f$ -type spectrum of the residual atmospheric noise in our data.

of $\lesssim 2$ if the detector time-streams were uncorrelated, and by another factor of $\lesssim 2$ if the time-streams had a white spectrum instead of the $1/f$ -type spectrum due to the residual atmospheric noise. Additionally, after correcting for the loss of 79 detectors, the data set with 36 detectors produces a similar result to the simulated data set based on our actual noise spectra. This indicates that all of the correlations between our detector time-streams occur for near-neighbor bolometer pairs.

4.8 Atmospheric Noise as a Function of Atmospheric Opacity

Ironically, we found almost no correlation between the amount of water vapor in the atmosphere and the magnitude of the atmospheric noise in our data. We compared the value of the atmospheric opacity measured by the CSO tau-meter, which corresponds to the amount of water vapor, to both the point source sensitivity and RMS of our time-stream data, which are good proxies for the amount of atmospheric noise in our data. The results are shown in Figure 4.23, and look like a scatter plot. It is not clear why there is little or no correlation between the amount of water vapor in the atmosphere and the amount of atmospheric noise in our data. However, a possible explanation is that the clumpiness of the water vapor in the atmosphere is independent of the total amount of water vapor in the atmosphere.

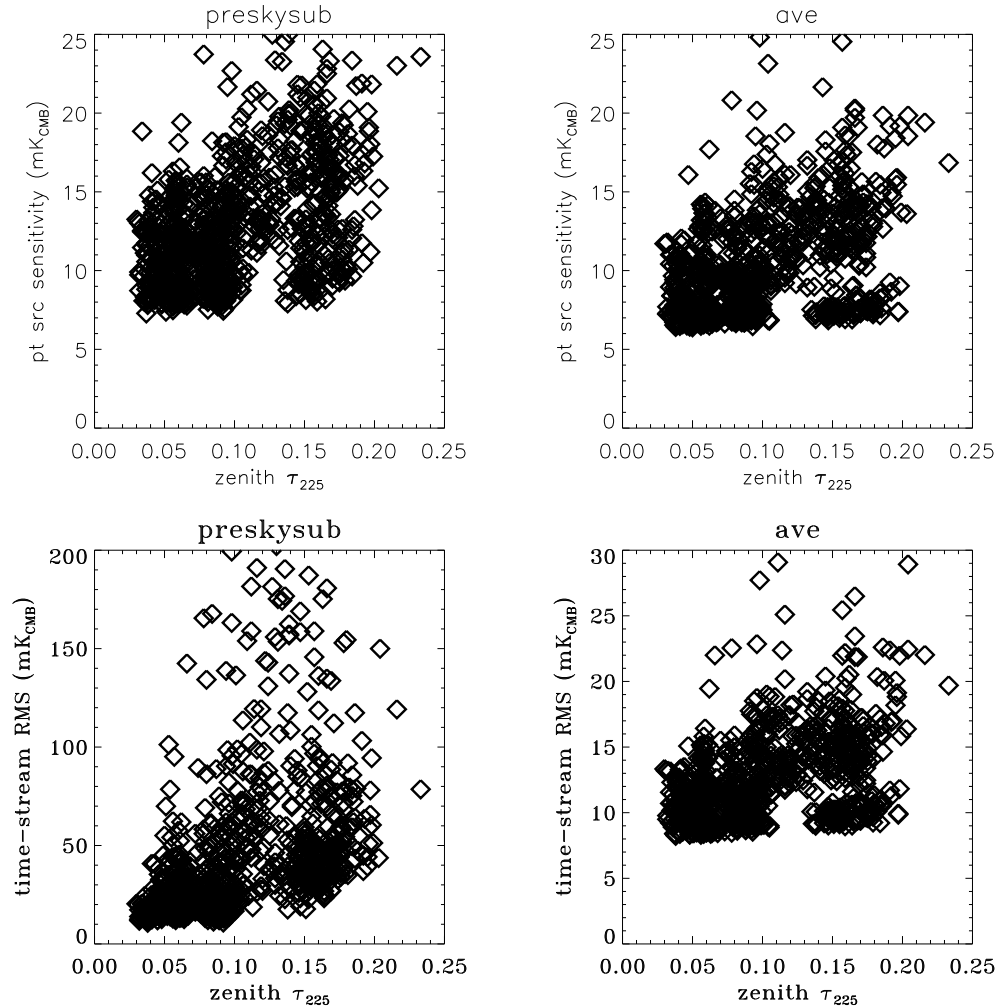


Figure 4.23: The top row of plots show the point source sensitivity of our time-stream data as a function of the zenith atmospheric opacity at 225 GHz measured by the CSO tau-meter. The bottom row of plots shows the time-stream RMS as a function of zenith atmospheric opacity at 225 GHz. The plots on the left show data prior to removing atmospheric noise, and the plots on the right show data after subtraction an average template. Both the point source sensitivity and time-stream RMS provide a measure of the amount of atmospheric noise in the data, so these plots indicate there is little or no correlation between the amount of atmospheric noise and the atmospheric opacity. It is not clear why the atmospheric noise is not well correlated with the atmospheric opacity, but a possible explanation is that the clumpiness of the water vapor is more important than the amount of water vapor. Note that the reason the point source sensitivity improves only moderately after removing an average atmospheric template is because a large fraction of the signal is at frequencies above the atmospheric noise. Unfortunately, this is not true for extended sources, such as the CMB.

4.9 Summary of Atmospheric Noise

After removing the common mode signal over Bolocam’s eight arcminute diameter focal plane, the residual signal from fluctuations in atmospheric emission is the dominant source of noise in our data at frequencies below a couple hundred mHz. This is true even in the best observing conditions at the CSO. We can remove more of the atmospheric noise by effectively subtracting the common mode signal on shorter length scales by allowing linear or quadratic variations over the focal plane, but the residual noise still dominates our data at low frequency. However, the trade off when subtracting the common signal on shorter length scales is that more astronomical signal is attenuated. Since only $\simeq 10\%$ of our observations were optimally processed using quadratic subtraction for a CMB spectrum, we can conclude that in almost all conditions the loss of astronomical signal is more important than the reduction in atmospheric noise achieved by subtracting the common mode signal on smaller spatial scales. Therefore, spatial subtraction of atmospheric noise on scales of several arcminutes will not allow BLIP limited performance below a couple hundred mHz for broadband 150 GHz receivers operating at the CSO.

However, this does not mean that BLIP limited performance is impossible from the CSO. SUZIE I.5 was able to achieve instrument limited performance¹⁸ down to 10 mHz at 150 GHz at the CSO by subtracting a combination of spatial and spectral common mode signals [92]. The initial subtraction of the spatial common mode signal is obtained from differencing detectors separated by $\simeq 4$ arcminutes, and removes the atmospheric noise to within a factor of two of the instrument noise level below a couple hundred mHz. However, SUZIE I.5 has three observing bands (1.1, 1.4, and 2.1 mm) per spatial pixel, which allows them to determine the correlated signal over a range of frequencies. The remaining atmospheric noise at low frequency can be removed down to the instrument noise level by subtracting this spectral common mode signal.

SUZIE II was able to employ a similar subtraction method, using observing bands at 0.85, 1.4, and 2.1 mm for each spatial pixel [10]. Additionally, SUZIE II has a much lower instrument noise level at 150 GHz compared to SUZIE I.5, within 50% of the BLIP limit. Similar to Bolocam, SUZIE II reaches the instrument noise level at frequencies above a couple hundred mHz by subtracting a spatial common mode signal. However, by

¹⁸For reference, SUZIE I.5’s BLIP limit is a factor of $\simeq 3$ below the instrument noise limit at 100 mHz and a factor of $\simeq 6$ below the instrument noise limit at 10 mHz.

subtracting the spectral common mode signal SUZIE II achieves instrument noise limited performance below 100 mHz, and is within a factor of 1.5 of the instrument noise limit at 10 mHz. Therefore, spectral subtraction of the atmospheric noise does provide a method to achieve BLIP, or nearly BLIP, limited performance from the CSO.

Chapter 5 Data Processing

To create a map from the bolometer time-streams recorded by our data acquisition system (DAS) computer requires a fair amount of processing. First, the DAS time-streams must be merged with time-streams recorded by the telescope computer. Next, the data is parsed and organized to make the bookkeeping as easy as possible. Then, the bolometer data is filtered and cleaned to remove systematic biases and maximize the signal-to-noise ratio. Finally, a map is created from the time-stream data after determining the optimal way to bin and add the different time-stream samples.

The routines to merge the telescope and bolometer data described in Section 5.1 were developed by the Bolocam team prior to my arrival. I have not made any modifications to these routines, other than the minor improvements to the data alignment that are described in Appendix B.2. Additionally, a full reduction pipeline was developed, largely by Glenn Laurent, Ben Knowles, and Samantha Edgington, to analyze the dusty galaxy surveys conducted with Bolocam in early 2003. This pipeline provided me with a large number of utilities and driver routines that I have made use of and/or adapted to create the software used to analyze the data described in this thesis.

5.1 Merging and Parsing the Data Time-Streams

Several data time-streams are digitized by the DAS computer at 50 Hz, including: AC bolometer voltages, DC bolometer voltage¹, bias monitor voltages, information about the rotator, an observation number, several thermometer signals, and a logic signal which transitions at the start and end of each scan. Additionally, several data streams are digitized by the telescope computer at 100 Hz, including: the position of the telescope, the position and name of the observed astronomical source, ambient weather information, the location of the secondary mirror, and the same logic signal which transitions at the start and end of each scan. The first step in merging the time-streams from these two computers is to down-sample the telescope data to 50 Hz. Since all of the information recorded by the tele-

¹Recall from Section 2.4 that the DC bolometer voltage is the bolometer signal after demodulation by the lockin electronics. The AC bolometer voltage is the same signal, after a high-pass filter is applied.

scope is slowly varying on time scales of tens of milliseconds, this down-sampling is trivial. Once the telescope computer data are down-sampled, we merge it with the DAS computer data into a single netCDF file².

Next, it is useful to parse this data into files that contain a single observation using the observation number recorded by the DAS computer. Each single observation contains a set of scans that completely map the astronomical field or object, and they are typically around ten minutes in length. Separating these observations into individual files makes bookkeeping much easier because each netCDF file can be grouped according to the source or field that was observed. Additionally, this parsed data is easy to work with because it contains a relatively small number of time-stream samples.

Note that aligning the DAS computer and telescope computer time-streams is non-trivial, since the two computer clocks drift relative to each other. The drift is relatively slow, so by synchronizing the two clocks at the start of each night we can ensure that they are within $\simeq 1$ second of each other for the entire night. As long as the two clocks are aligned within $\simeq 10$ seconds, the logic signal which transitions at the start and end of each scan, which is digitized by both computers, can be used for high-precision alignment of the two sets of time-streams. More details of this synchronization process are given in Appendix B.2. Additionally, the individual DAS computer time-streams are slightly misaligned due to the finite sampling rate of the multiplexer. This issue is correctable, and is discussed in detail in Appendix B.1.

5.2 Filtering and Down-Sampling

Once the initial merging and parsing of the data is complete, we begin the process of refining the data. Before filtering and down-sampling³ the data we Fourier transform the time-stream from the entire observation for each bolometer⁴. Next, we remove the effects of the

²Network Common Data Form (netCDF) is a set of machine-independent software libraries that can be used to store and access array-oriented scientific data. See the netCDF website at <http://www.unidata.ucar.edu/software/netcdf/>.

³We down-sample the data to remove noise due to 60 Hz pickup that is at frequencies above our signal band. See the detailed explanation below.

⁴Each observation contains several tens of thousands of samples for each bolometer, making the Fourier transform a computationally intensive operation. To reduce the computation time, we reduce the number of samples at the start and end of each observation, such that the total number of samples is divisible by 2^n , where $n \geq 6$. For the fast Fourier transform algorithm we use, the run time is roughly proportional to the number of elements times the sum of the prime factorization of the number of elements. Therefore, by ensuring that the number of samples is divisible by $2^{n \geq 6}$, the run time can be reduced by a factor of up to

filtering applied by the lockin electronics by dividing the transformed data by the effective lockin filter. See Figure 5.1 for profiles of the lockin filters. At this point we multiply the transformed bolometer time-stream by an anti-aliasing filter prior to transforming the data back to time space and down-sampling it by a factor of five. This filter is given by

$$\mathcal{F} = \frac{1}{1 + 10(f/f_N)^3}, \quad (5.1)$$

where f is the frequency in Hz and f_N is the Nyquist frequency of the data after it is down-sampled, equal to 5 Hz. An ideal anti-aliasing filter would attenuate all of the signal above f_N , but still be slowly varying so that it does not produce ringing in the time domain. In practice there is always a trade off between high-frequency attenuation and ringing, and the filter in Equation 5.1 proved to be the best combination of good attenuation and minimal ringing for our bolometer time-streams.

Several factors influenced our decision to down-sample the data from 50 Hz to 10 Hz. First, the half-width at half-maximum (HWHM) of a Bolocam beam in frequency space is about 1.75 Hz.⁵ Therefore, very little astronomical signal is found at frequencies above a few Hz. However, there is a lot of noise above a few Hz, due primarily to 60 Hz pickup. See Figure 5.2. By down-sampling we can eliminate almost all of this noise caused by 60 Hz pickup, yet the amount of astronomical signal attenuation is negligible⁶. After the data is down-sampled, it is Fourier transformed again and divided by the filter in Equation 5.1 to remove any artifacts caused by the filter. Finally, the data is transformed back to time space, and we are left with bolometer time-streams that are sampled at 10 Hz and are free from any filtering effects.

5.3 Noise Removal

The next step in the data processing involves removing several types of correlated noise from the data. First, the emission from the atmosphere changes as a function of telescope elevation angle due to the changing path length through the atmosphere. The path length

⁵ $2^6 = 64$. Since there are some extra samples in each observation prior to the first scan and after the last scan, this reduction in the total number of samples does not eliminate any of the on-source data.

⁵The scan speed of 240 arcseconds/sec can be used to convert the beam profile in physical space, where the FWHM is 60 arcseconds, to frequency space.

⁶Adaptive PCA is also effective at removing this 60 Hz pickup noise, but it also attenuates a large amount of astronomical signal in the process.

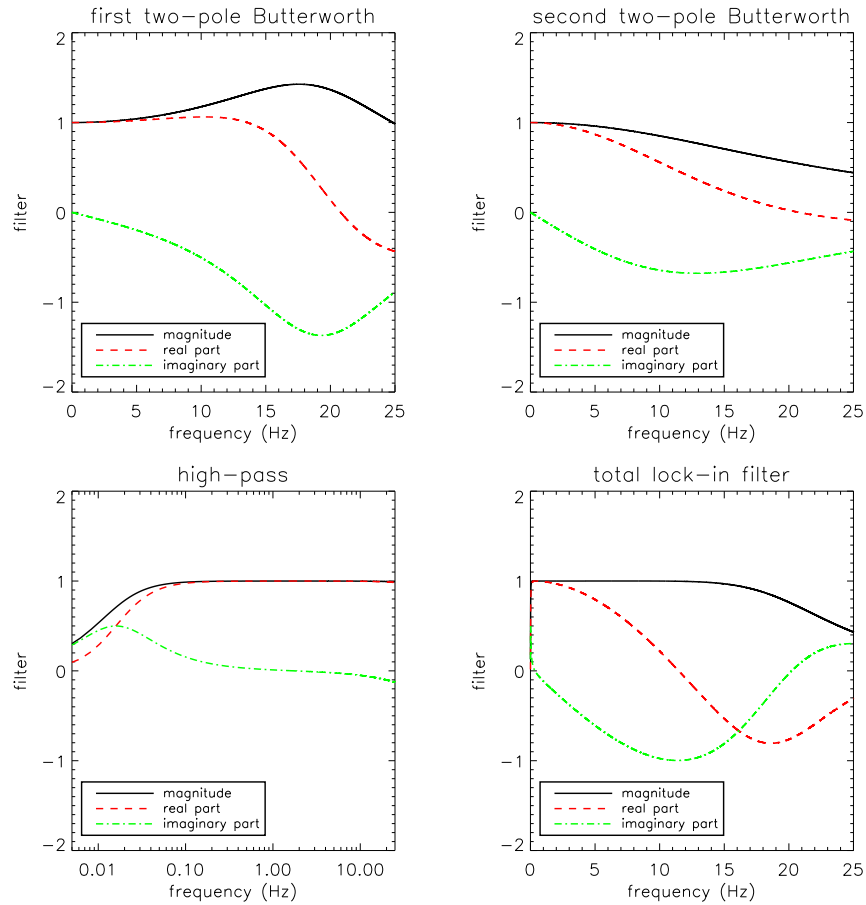


Figure 5.1: Profiles of the filters applied by the lockin electronics. In each plot, the solid black line shows the absolute value of the filter, the dashed red line shows the real part of the filter, and the dot-dashed green line shows the imaginary part of the filter. Clockwise from the top left, the plots show: 1) the first of two two-pole Butterworth filters, 2) the second two-pole Butterworth filter, 3) the single-pole high-pass filter, and 4) the total effective filter applied by the lockin electronics. Note that the plot of the high-pass filter has a logarithmic x-axis.

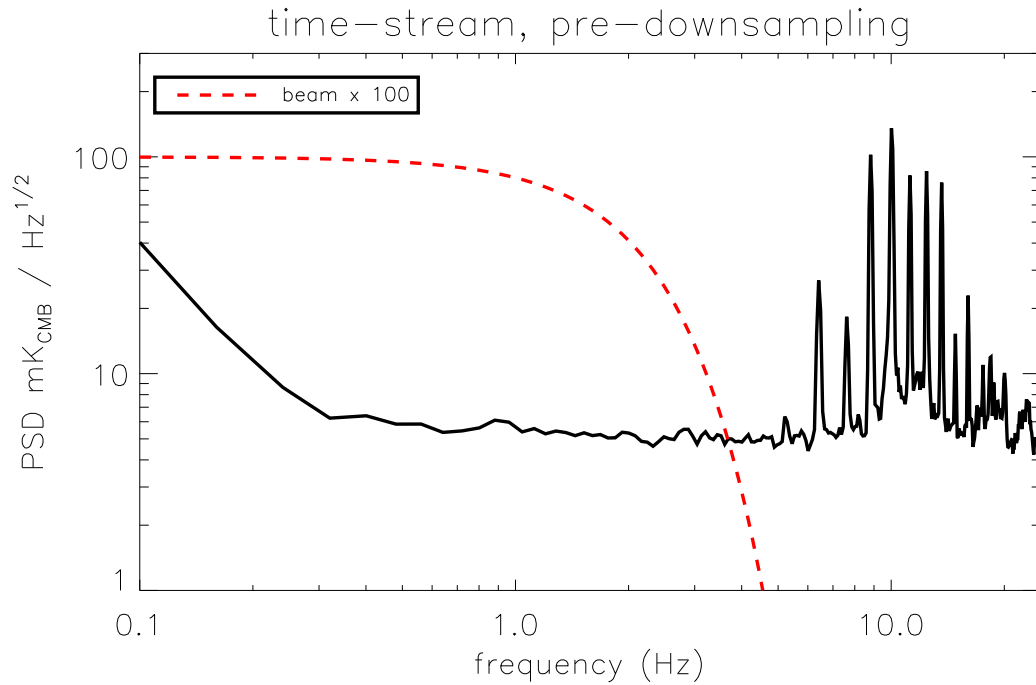


Figure 5.2: A pre-down-sampled time-stream PSD showing 60 Hz pickup at frequencies above $\simeq 10$ Hz. Some of these 60 Hz lines are larger in amplitude than the low-frequency atmospheric noise. Overlaid as a red dashed line is the beam profile multiplied by a factor of 100, showing that very little astronomical signal will be present above a few Hz. Note that the time-stream PSD represents data before removing any atmospheric noise.

through the atmosphere relative to the zenith path length is called the airmass, A , and is described by

$$A = 1/\sin(\epsilon), \quad (5.2)$$

where ϵ is the elevation angle. For a typical observation the range of elevation angles is approximately one degree, which corresponds to a change in airmass between 0.005 and 0.060 for elevation angles between 75 and 30 degrees.⁷ To remove this elevation-dependent signal we calculate a linear fit of bolometer voltage versus airmass. Since the bolometer data is high-pass filtered on scales of $\simeq 10$ seconds, the airmass must also be filtered in a similar way before calculating the fit coefficients. In practice, this is accomplished by building the fit up from each 12.5-second-long scan within the observation after subtracting the mean from the airmass for the scan. This process yields one set of linear fit coefficients for each bolometer for the entire observation, which is used to create a template that is removed from the bolometer time-streams.

Next, we remove a template that is created from the bias voltage monitors from the bolometer time-streams. Details of this process are given in Section 4.2.2. A template created from the dark bolometer signals is also removed from the bolometer time-streams, as described in Section 4.3. Finally, and most importantly, we remove a template describing the fluctuations in emission from the atmosphere (i.e., the atmospheric noise). Several algorithms for removing atmospheric noise are described in Section 4.6. The type of atmospheric noise removal algorithm applied to the data depends on the type of observation, as described below.

5.3.1 Observations of Bright Point-Like Sources

Since these observations are used to calibrate the profile of the Bolocam beams and to determine the flux calibration of our data, we want to minimize the amount of astronomical signal that we attenuate while removing the atmospheric noise. Therefore, prior to calculating an atmospheric noise template we mask off all of the data that is within 2 arcminutes of the source⁸. For any given time-stream sample, no more than $\simeq 40$ bolometer signals are masked off, so a good atmospheric template can still be constructed at every sample. This

⁷For reference, a change of 0.06 in airmass corresponds to a change of approximately 0.5 K of optical loading from the atmosphere, or a change in surface brightness of a little less than 1 K_{CMB} .

⁸For a true point source the signal relative to the peak is approximately 1×10^{-5} at a distance of 2 arcminutes from the center. So, to a good approximation, all of the signal from the source is masked off.

template is then subtracted from every sample, including the ones that were masked out. For the 2003 data, a desourcing version of average sky subtraction was used. For the 2004 data, a desourcing version of adaptive PCA sky subtraction was used.

5.3.2 Observations of Science Fields

None of the bolometer data samples are masked out prior to removing the atmospheric noise from the science field observations, since we do not have any information about the location or profile of the astronomical signal. Additionally, the amplitude of the astronomical signal is much smaller than the amplitude of the atmospheric noise, so masking off samples would not significantly alter the template. For the 2003 data, three different atmospheric noise removal algorithms were applied to each observation: average, planar, and quadratic sky subtraction. Therefore, three different files are generated for each observation. A figure of merit is calculated for each of the three files for each observation, based on the noise level of the data and the expected astronomical signal shape⁹. For each observation, the file with the best figure of merit value will be the one used to create the final map of the data. In general, observations made in poor weather and observations of compact astronomical sources are optimally cleaned by the more aggressive algorithms (planar or quadratic sky subtraction), while observations made in good weather and observations of extended astronomical sources are optimally cleaned by the more benign algorithms (average or planar sky subtraction). For the 2004 data, all of the observations are cleaned with adaptive PCA sky subtraction, since the average/planar/quadratic sky subtraction algorithms are unable to remove the excess noise present during that year's observations.

5.4 Map Making

5.4.1 Least Squares Map Making Theory

The astronomical signals we are looking for can be thought of as two-dimensional objects, which can be represented by a map with finite pixelization. For simplicity, this two-dimensional map can be thought of as a vector, \vec{m} . This map is stored in the bolometer time-streams, \vec{d} , according to

$$\vec{d} = \mathbf{p}\vec{m} + \vec{n}, \quad (5.3)$$

⁹This figure of merit is described in more detail in Section 5.6.

where \mathbf{p} is a matrix containing the pointing information and \vec{n} is noise. Since \vec{m} is what we are fundamentally interested in obtaining, we need to find a solution to Equation 5.3 that yields the optimum unbiased estimate of \vec{m} given \vec{d} . There are several methods that can be used to estimate \vec{m} [143], including the commonly used least squares method described below [97].

Solving the least squares problem for Equation 5.3 requires minimizing

$$\chi^2 = (\vec{d} - \mathbf{p}\vec{m})^T \mathbf{w}(\vec{d} - \mathbf{p}\vec{m}), \quad (5.4)$$

where \mathbf{w} is the inverse of the time-stream noise covariance matrix, $\langle \vec{n}\vec{n}^T \rangle^{-1}$. The estimator for \vec{m} derived from Equation 5.4 is

$$\vec{m}' = \mathbf{c}\mathbf{p}^T \mathbf{w}\vec{d}, \quad (5.5)$$

where $\mathbf{c} = (\mathbf{p}^T \mathbf{w}\mathbf{p})^{-1}$ is the map-space noise covariance matrix. If the time-stream noise, \vec{n} , has a white spectrum then the various terms in Equation 5.5 are easy to understand because \mathbf{w} and \mathbf{c} are both diagonal. \mathbf{w} is the inverse of the time-stream noise variance, and applies the appropriate weight to each sample in the time-stream. \mathbf{p}^T then bins the data time-stream into a map, and \mathbf{c} corrects for the fact that \mathbf{p}^T sums all of the data in a single map bin instead of averaging it. The general idea is the same for non-white time-stream noise, but \mathbf{w} will mix time samples and \mathbf{c} will mix map pixels.

If the time-stream noise is stationary then the time-stream noise covariance matrix can be diagonalized by applying the Fourier transform operator, \mathbf{F} [2,97]. For stationary noise, any element of the inverse time-stream noise covariance matrix can be described by

$$\mathbf{w}(t_1, t_2) = \langle n(\vec{t}_1)n(\vec{t}_2)^T \rangle^{-1} = \mathbf{w}(\Delta t), \quad (5.6)$$

where t_1 and t_2 are any two time samples separated by Δt . The corresponding elements of the Fourier transform of the inverse covariance matrix, $\mathbf{W} = \mathbf{F}\mathbf{w}\mathbf{F}^{-1}$, can be written as

$$\mathbf{W}(f_1, f_2) = \mathbf{W}(f_1)\delta_{f_1, f_2}, \quad (5.7)$$

where δ_{f_1, f_2} represents a Kronecker delta and f is frequency in Hz. The diagonal elements

of \mathbf{W} are equal to $1/(\text{PSD} \cdot \text{df})$, where PSD is the power spectrum and df is the frequency resolution of the time-stream. The delta function ensures that all of the off-diagonal elements are equal to zero. Returning to Equation 5.5, the estimate for \vec{m} can be rewritten as

$$\vec{m}' = ((\mathbf{p}^T \mathbf{F}^{-1})(\mathbf{F} \mathbf{w} \mathbf{F}^{-1})(\mathbf{F} \mathbf{p}))^{-1} (\mathbf{p}^T \mathbf{F}^{-1})(\mathbf{F} \mathbf{w} \mathbf{F}^{-1})(\mathbf{F} \vec{d}), \quad (5.8)$$

using the fact that $\mathbf{F}^{-1} \mathbf{F} = 1$. Finally, taking the Fourier transform of the various terms in Equation 5.8 yields

$$\vec{m}' = (\mathbf{P}^T \mathbf{W} \mathbf{P})^{-1} \mathbf{P}^T \mathbf{W} \vec{D} \quad (5.9)$$

as an alternate expression to estimate the value of \vec{m} . Note that $\mathbf{c} = (\mathbf{p}^T \mathbf{w} \mathbf{p})^{-1} = (\mathbf{P}^T \mathbf{W} \mathbf{P})^{-1}$ does not in general simplify as a result of Fourier transforming.

5.4.2 The Bolocam Algorithm: Theory

The science field maps produced by Bolocam each contain $n_p \simeq 20000$ pixels, and an extremely large matrix must be inverted to calculate \mathbf{c} since $\mathbf{P}^T \mathbf{W} \mathbf{P} = \mathbf{p}^T \mathbf{w} \mathbf{p}$ has dimensions of $n_p \times n_p$. Storing a matrix this size requires approximately 1 GB of memory, and the inversion takes a prohibitive amount of computation time. Therefore, we developed an algorithm to approximate \vec{m}' by exploiting the simplicity of our scan pattern, which involved raster scanning parallel to either the RA or dec axis.

To illustrate this simplification, consider the map made from a single bolometer for a single scan within an observation. This scan will produce a one-dimensional map at a single dec value (for an RA scan) or a single RA value (for a dec scan). Each data point in the time-stream is separated by 24 arcseconds in map-space since our data is sampled at 10 Hz and the telescope scans at 240 arcseconds/sec. The maps are binned with 20 arcsecond pixels, so \mathbf{p}_s^T will map either one or zero time-stream samples to each map pixel¹⁰. Note that n_s , the number of time-stream samples, will be slightly less than n_p , the number of map-space pixels. Since \mathbf{p}_s^T has dimensions of $n_s \times n_p$, the sum of each row in \mathbf{p}_s^T is either one or zero and the sum of each column is one. Therefore, a simple transformation would allow us express \mathbf{p}_s^T as a square identity sub-matrix and rectangular sub-matrices of zeros. Consequently, we will make the approximation that $\mathbf{p}_s^T = 1$.¹¹ From Equation 5.5, this

¹⁰The subscript s will denote that a given matrix or vector corresponds to the data from a single scan.

¹¹This approximation is equivalent to ignoring the small number of map pixels which do not correspond to a time-stream sample. Alternatively, this approximation can be thought of as a reordering of the map-space

means that

$$\mathbf{c}_s = \mathbf{w}_s^{-1}, \quad (5.10)$$

and therefore $\vec{m}_s = \vec{d}_s$ for a single scan of time-stream data. If we Fourier transform Equation 5.10, then we find that

$$\mathbf{C}_s = \mathbf{W}_s^{-1}. \quad (5.11)$$

Since \mathbf{W}_s is diagonal, the inversion is trivial, and the result is that the Fourier transform of the map-space noise covariance matrix is diagonal with elements equal to the time-stream PSD*df.

The next step is to consider a map made from a single bolometer for an full observation, which contains twenty scans. We move the telescope in the orthogonal direction to the scan between scans by more than the size of a single map pixel, so we can still approximate $\mathbf{p}^T \approx 1$. Since it takes $\gtrsim 20$ seconds to go from the start of one scan to the start of the next scan¹², there will be almost no correlations between the data in one scan and the data in all the other scans because the time-stream data is high-pass filtered with a time constant corresponding to approximately 10 seconds. Therefore, the time-stream data and map-space data for different scans are independent. This means that the noise in map-space will be stationary, which means that the noise covariance matrix can be diagonalized by Fourier transforming it. The Fourier transform of the full-map noise covariance matrix, \mathbf{C} , can be visualized by noting that each diagonal element corresponds to a single map-space pixel (or equivalently, a single time-stream sample). So, this visualization of \mathbf{C} will be equal to the single scan time-stream PSD*df for rows of map-space pixels that are parallel to the scan direction, and will have a white spectrum for columns of map-space pixels that are perpendicular to the scan direction. Alternatively, since there is a one-to-one correspondence between time-stream samples and map-space pixels, this visualization of the diagonal elements of \mathbf{C} is equal to the full map-space PSD*df $_{\Omega}$, where df $_{\Omega}$ is the angular frequency resolution of the map.

At this point, we need to add together all of the individual observations to make a single map. Since we have shown that the map-space data is equivalent to the time-stream data for a single observation, the easiest way to co-add data from separate observations is to use

 pixels, so that all of the matrices in Equation 5.5 are block diagonal, and contain only one block of non-zero values.

¹²This includes the 12.5-second-long scan and the $\lesssim 10$ seconds of turnaround time between scans.

the single observation maps. Since the noise in separate observations is uncorrelated, the maps can be co-added according to

$$\vec{m} = \left(\sum_i \mathbf{c}_i^{-1} \right)^{-1} \sum_j \mathbf{c}_j^{-1} \vec{m}_j, \quad (5.12)$$

where the subscripts i and j refer to observation number. The easiest way to evaluate Equation 5.12 is to Fourier transform it, so that the noise covariance matrices are all diagonal. The result is

$$\vec{M} = \left(\sum_i \mathbf{C}_i^{-1} \right)^{-1} \sum_j \mathbf{C}_j^{-1} \vec{M}_j, \quad (5.13)$$

where \vec{M} is the Fourier transform of the map and \mathbf{C} is the Fourier transform of the noise covariance matrix, with diagonal elements equal to the PSD* df_Ω of the map. Since all of the \mathbf{C} s are diagonal, we can simplify Equation 5.13 to

$$M = \left(\sum_i \frac{1}{\mathcal{P}_i} \right)^{-1} \sum_j \frac{M_j}{\mathcal{P}_j}, \quad (5.14)$$

where M is the two-dimensional Fourier transform of the map and \mathcal{P} is the two-dimensional PSD of the noise in the map¹³.

Finally, to make a map using all of our data we need to consider every bolometer, not just a single detector. To properly weight the data from each bolometer prior to co-adding, we calculate the expected variance, $(\sigma_{pf})_i^2$, in measuring the peak flux of a point-like source from a single scan through the center of the source for bolometer i . This variance is calculated using the scan average time-stream PSD for each bolometer, $PSD_i(f)$, and the Fourier transform of the expected signal shape of a point source, $S(f)$, according to

$$(\sigma_{pf})_i^2 = \int df \frac{S(f)^2}{PSD_i(f)} \quad (5.15)$$

where f is temporal frequency. Then, the data from each bolometer is weighted by a factor proportional to $1/(\sigma_{pf})_i^2$ prior to co-adding it with data from other bolometers. This is the optimal way to co-add the data for point-like signals; it is nearly optimal for signals of any shape if the PSDs have similar profiles for every bolometer.

¹³ df_Ω is the same for every map, so the constant factor of df_Ω from the first sum in Equation 5.14 cancels the factor of $1/df_\Omega$ from the second sum in Equation 5.14.

However, due to atmospheric noise, along with our noise removal algorithms, there are correlations between the bolometers. But, all of these correlations are instantaneous in time and constant over the observation. Additionally, the relative positions of the bolometers do not change during the observation, so the map-space separation of the correlations does not change. If we also assume that the correlations between different bolometers are time-instantaneous and independent of time, then the Fourier transform of the time-stream noise covariance matrix will still be diagonal. The reason that this \mathbf{W}^{-1} is diagonal is because the correlations do not depend on the time-stream sample number of either bolometer, nor on the relative difference in time-stream samples for each bolometer. Since \mathbf{W}^{-1} is still diagonal, co-addition of the maps of individual observations can proceed according to Equation 5.14. Therefore, Equation 5.14 can be used as the algorithm to produce our final science field maps, with

$$M = \left(\sum_i \frac{1}{\mathcal{P}_i} \right)^{-1} \sum_j \frac{M_j}{\mathcal{P}_j},$$

where M is the Fourier transform of the full-data map, \mathcal{P}_i is the two-dimensional PSD (in μK_{CMB}^2 ster) of the noise in the map made from observation i , and M_i is the Fourier transform of the map made from observation i .

Note that we were forced to make several simplifying assumptions in order to develop Equation 5.14. We have assumed that the pointing matrix, \mathbf{p}^T , is equal to one. We have also assumed that the noise in our time-streams is stationary for each eight-minute-long observation. Additionally, we have assumed that the PSD of the correlations between bolometers is white, and that all of the correlations are time-instantaneous. Finally, we have assumed that the map coverage (i.e., the number of time-stream samples that are binned in each map-space pixel) is uniform, so that the Fourier transform of the map is a valid description of the time-stream data. Deviations from these assumptions will alter the map estimate we compute from the optimal least squares map estimate. But, these deviations only effect how each time-stream sample is weighted before it is mapped. This means our final map will have more noise compared to an optimal map, but it will not be biased in any way. In other words, since the map-making operation is linear, the resulting map will be unbiased no matter what weightings are used to co-add the data, as long as the weights are properly normalized.

5.4.3 The Bolocam Algorithm: Implementation

To start, we need to produce a map from the time-stream data for each eight-minute-long observation. As mentioned in Section 5.4.2, this is done by calculating the variance in measuring the peak flux of a point-like source under the assumption that the profile of the time-stream PSD is similar for every bolometer. To determine this variance, we calculate the PSD for each bolometer for each scan according to the formalism described in Appendix C. These spectra are then averaged over all twenty scans and all temporal frequencies for each bolometer, under the assumption that the noise properties do not change over the course of the observation. Then, we determine the expected shape of a point-like source using our measured beam profile and scan speed. Finally, Equation 5.15 is used to determine the variance in measuring the peak flux of a point-like source for each bolometer, which is inversely proportional to the weighting factor applied to the time-stream data for that bolometer.

At this point, we have individual observation maps for every observation, and we can make a map from all of the data using Equation 5.14. But, one of the main assumptions made in developing Equation 5.14 was that the map coverage is uniform for each observation. If this assumption fails, then the Fourier transform of the map is not a good description of the time-stream data. Fortunately, our scan strategy produced highly uniform coverage in the central region of the map, and this coverage falls rapidly to zero at the edges of the map. See Figure 5.3. If we restrict our map to a square region in the center, with sides of 42 arcminutes, then the fractional RMS variations in coverage for a single eight-minute-long observation are only about 8 - 9%.¹⁴ Since the coverage variations are minimal, we will assume that this square central region has uniform coverage, and therefore uniform noise properties. This assumption of uniform coverage allows us to directly compute the Fourier transform and noise properties of the map.

We now have a uniform coverage map for each observation, which can easily be Fourier transformed to produce the M_i s needed in Equation 5.14. But, we still need to determine the two-dimensional PSD of each single observation map. Due to residual correlations between bolometers we do not understand the noise properties of our data well enough to determine the map PSD from simulation, so we instead estimated the PSD by generating a large

¹⁴Discarding the data outside of this central region is equivalent to losing about 30% of the time-stream samples.

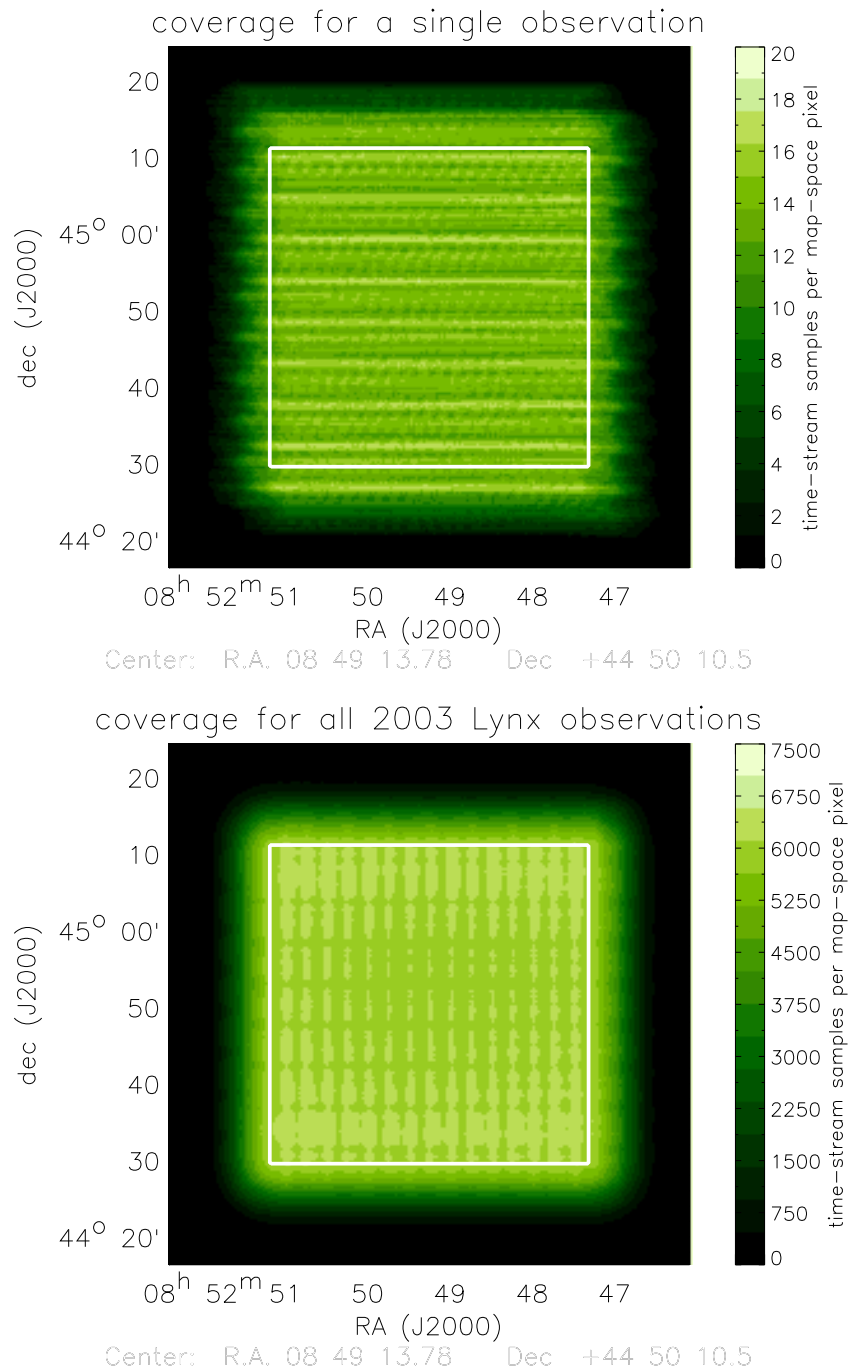


Figure 5.3: Map coverage, quantified by the number of time-stream samples that correspond to a particular map-space pixel. The top plot shows a single eight-minute-long observation made while scanning in the RA direction; the bottom plot shows the total of all $\simeq 500$ observations made of the Lynx field in 2003. The white square has sides of approximately 42 arcseconds and represents the region of the map defined to have uniform coverage. The RMS deviations in coverage within this region relative to the average coverage within the region are approximately 8 - 9% for a single observation and around 1.5% for the co-add of all observations.

number of jackknifed maps from our real data. In each jackknifed map, a different subset of the time-streams from half of the scans within each observation was multiplied by -1. This multiplication leaves the noise properties of the map unchanged¹⁵, while allowing us to produce a large number of realizations for each map. Note that the residual atmospheric noise correlations are time-instantaneous, so they remain in the jackknifed realizations. We generated 100 realizations for each observation, and we set the true PSD for each observation equal to the average of the map-space PSD computed for each realization. See Equation 5.17. Examples of the PSDs we calculated are given in Figure 5.4. This method of determining the map-space PSDs assumes that the time-stream data from each scan is uncorrelated with the data from all other scans. We made the same assumption in developing our map making algorithm, and it is reasonable since the time between scans is larger than the cutoff of the high-pass filter we apply to the time-stream data. Additionally, the covariance of maps made for a single observation from alternate scans is negligible, supporting our assumption that individual scans are uncorrelated.

To determine the validity of the map-space PSDs we estimated from the jackknifed map realizations, we examined the distribution of PSD values for each realization. If the noise properties of the data are Gaussian, as we have assumed, then the PSD measured at any given Fourier map-space pixel will be drawn from

$$f(x_{i,\vec{\nu}}) = (1/\mathcal{P}_{\vec{\nu}})e^{(-x_{i,\vec{\nu}}/\mathcal{P}_{\vec{\nu}})}, \quad (5.16)$$

where $x_{i,\vec{\nu}}$ is the measured PSD for realization i at pixel $\vec{\nu}$, $\mathcal{P}_{\vec{\nu}}$ is the true PSD for pixel $\vec{\nu}$, and $f(x_{i,\vec{\nu}})$ is the probability density function of $x_{i,\vec{\nu}}$. See Appendix F for a derivation of $f(x_{i,\vec{\nu}})$. Note that $\vec{\nu}$ has units of spatial frequency (i.e., radians⁻¹), and describes a pixel in the spatial Fourier transform of the map. The true PSD is estimated from

$$\widehat{\mathcal{P}}_{\vec{\nu}} = \frac{1}{N_r} \sum_{i=1}^{i=N_r} x_{i,\vec{\nu}}, \quad (5.17)$$

¹⁵Each time-stream sample (and therefore each map-space pixel) can be expressed as the sum of two signals: 1) an astronomical signal and 2) a random noise signal that is drawn from the underlying distribution of the noise in the Bolocam system. The astronomical signal corresponding to a particular map-space pixel will be the same for any scan, and will disappear in the jackknife realizations when time-stream data from half of the scans is multiplied by -1. But, if the underlying distribution of the noise is Gaussian, then the distribution of signals it will produce is symmetric about 0. Therefore, the statistical properties of the noise will be unchanged when half of the data is multiplied by -1.

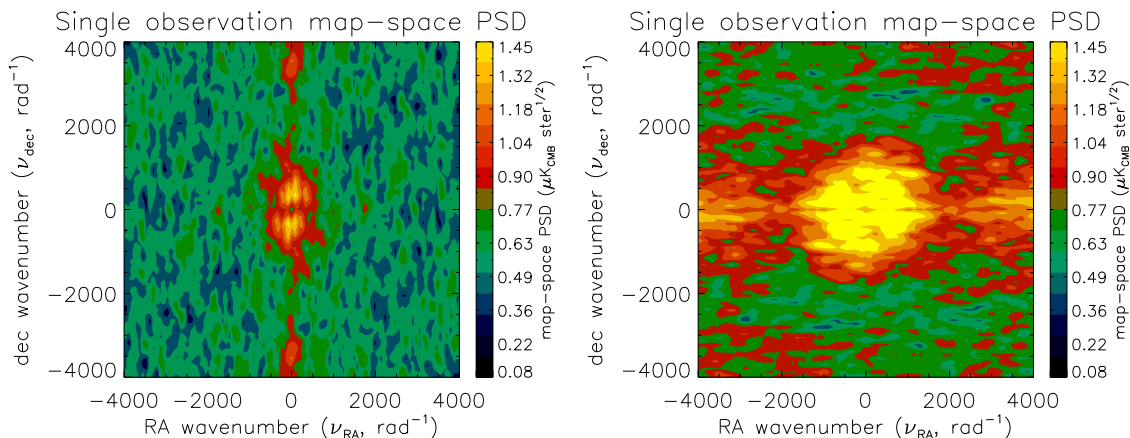


Figure 5.4: The map-space PSDs for single observations. The plot on the left shows the PSD for an observation made while scanning in the RA direction in good weather conditions. The plot on the right shows the PSD for an observation made while scanning in the dec direction in poor weather conditions. In each case, note that there is a stripe of increased noise at low frequency along the scan direction, due to time-stream noise with a $1/f$ spectrum.

where $N_r = 100$ is the number of realizations. To compare our measured PSDs to the probability density function (PDF) given in Equation 5.16, we created the dimensionless value

$$y_{i,\vec{\nu}} = \frac{x_{i,\vec{\nu}}}{\widehat{\mathcal{P}}_{\vec{\nu}}}, \quad (5.18)$$

with associated PDF

$$f'(y_{i,\vec{\nu}}) = e^{-y_{i,\vec{\nu}}}. \quad (5.19)$$

Then, we compared our measured values of $y_{i,\vec{\nu}}$ to the PDF in Equation 5.19. In general, we found that our measured $y_{i,\vec{\nu}}$ follow a distribution extremely close to $f'(y_{i,\vec{\nu}})$, except that the number of $y_{i,\vec{\nu}}$ with values near zero is slightly less than expected. See Figure 5.5. Therefore, the map-space PSDs estimated from the jackknife realizations should be a good estimate of the true map-space PSDs.

5.5 Transfer Functions

The transfer function describes the fraction of the astronomical signal that remains after processing, as a function of map-space Fourier mode. In order to determine the transfer

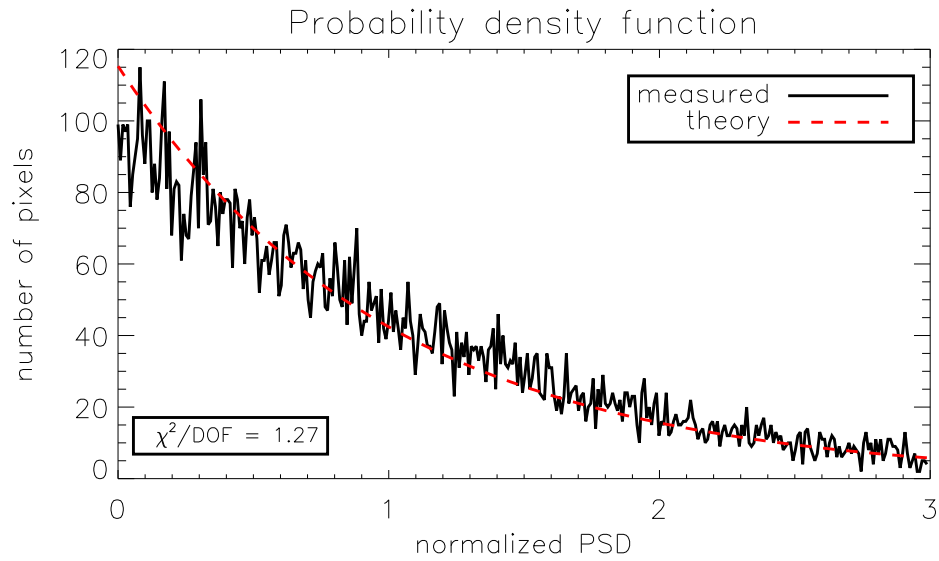


Figure 5.5: The measured probability density function for the map-space PSD of a single observation. This plot is typical of the distribution for all observations. The plot shows a histogram of the number of times that the value of the normalized PSD for a pixel, $y_{i,\vec{v}}$, takes a particular value. The solid black line is the measured data, and the dashed red line is the theoretical values for an ideal Gaussian distribution. There is a slight decrement in the number of $y_{i,\vec{v}}$ near zero, which results in a poor quality of fit ($\chi^2/\text{DOF} = 1.27$). However, the departures in the measured data from a Gaussian distribution are small.

function of our data processing algorithms, we first generate a simulated map of the expected astronomical signal. This map is then reverse mapped into a time-stream using the pointing information in a real observation. Next, this simulated time-stream is added to the real bolometer time-streams from the observation, and then processed and mapped in the standard way. A map made from data that did not have a simulated signal added to it is then subtracted from this map, producing a map with the simulated signal after processing. Finally, the PSD of this map is divided by the PSD of the original simulated signal map to determine how much of the signal remains. More details of this calculation are given in Appendix E.

This transfer function was computed for twenty randomly selected observations, ten taken while scanning parallel to RA and ten taken while scanning parallel to dec. Realizations of the expected CMB signal were used as the simulated signal. These realizations were generated in Fourier map-space assuming Gaussian fluctuations and a flat band power in $\mathcal{C}_\ell = C_\ell \ell(\ell+1)/2\pi$ of $50 \mu\text{K}_{CMB}^2$.¹⁶ For each observation, we averaged the transfer function obtained from 100 different CMB realizations to determine the average transfer function. We then compared the average transfer function for each of the ten observations taken with a similar scan pattern. The result is that the transfer functions were the same within our measurement uncertainty for all of the observations¹⁷. Therefore, we averaged the transfer function from all ten observations to produce a high signal-to-noise measurement for each cleaning method. See Figures 5.6 and 5.7.

Since all of the data processing is performed on the time-streams, the attenuation caused by the processing has a preferred orientation based on the scan strategy. The result is a transfer function that is not azimuthally symmetric, due to the large amount of attenuation at low frequencies parallel to the scan direction. Additionally, there is a lot of attenuation on scales larger than the Bolocam focal plane ($\simeq 500 \text{ radians}^{-1}$) due to the atmospheric noise removal algorithms. This occurs because these algorithms are designed to remove all time-instantaneous signals at each data sample, which is equivalent to subtracting any signals that vary slowly compared to the size of the focal plane.

¹⁶We chose to use $50 \mu\text{K}_{CMB}^2$ for the CMB signal because that is the best estimate for the amplitude at 150 GHz. However, in Appendix E we show that the transfer function does not depend on the amplitude of the astronomical signal.

¹⁷Additionally, the transfer functions from the observations made while scanning parallel to RA are equivalent to the transfer functions made while scanning parallel to dec, after a rotation of 90 degrees to account for the scan direction.

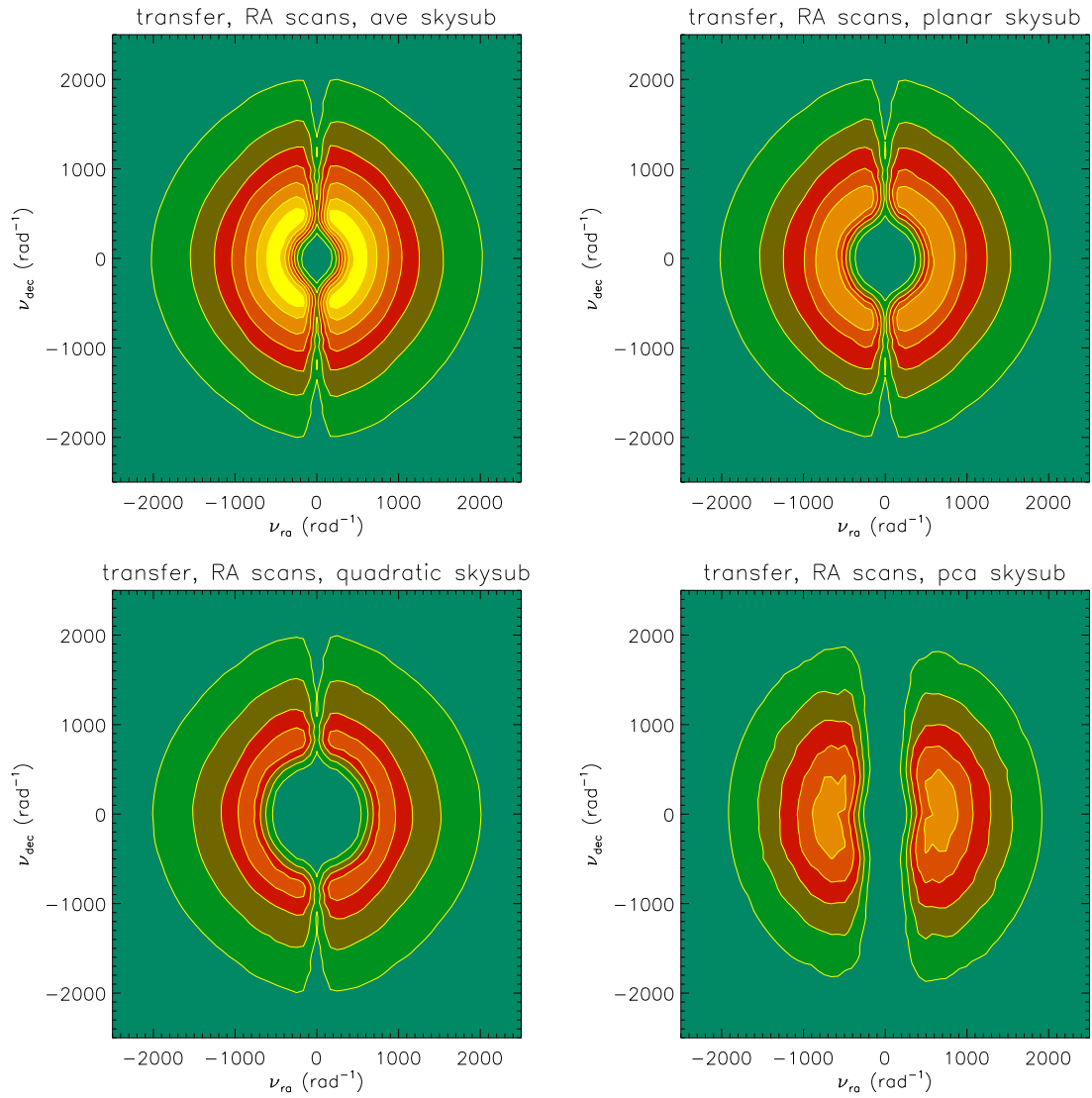


Figure 5.6: The transfer function for observations made while scanning parallel to RA. Clockwise from top left, the plots show the transfer function for average sky subtraction, planar sky subtraction, quadratic sky subtraction, and adaptive PCA sky subtraction. Each contour on the plots represents 0.1. Additionally, each transfer function has been multiplied by the effective transfer function of the beam, which attenuates the signal at high- $\vec{\nu}$. Note the large amount of attenuation at low frequencies along the scan direction, and at scales larger than the focal plane size of approximately 500 radians^{-1} .

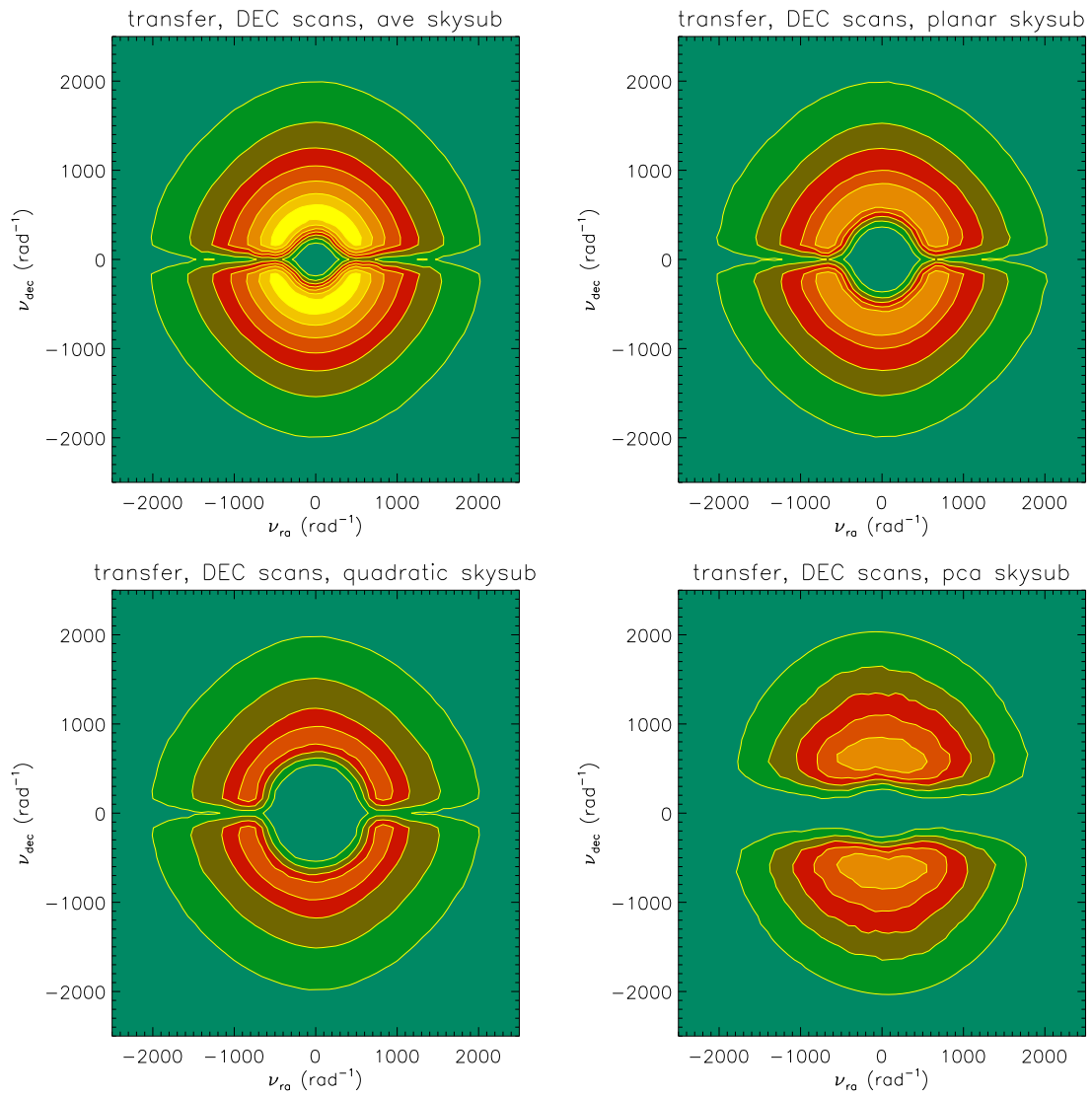


Figure 5.7: The transfer function for observations made while scanning parallel to dec. Clockwise from top left, the plots show the transfer function for average sky subtraction, planar sky subtraction, quadratic sky subtraction, and adaptive PCA sky subtraction. Each contour on the plots represents 0.1. Additionally, each transfer function has been multiplied by the effective transfer function of the beam, which attenuates the signal at high- $\vec{\nu}$. Note the large amount of attenuation at low frequencies along the scan direction, and at scales larger than the focal size of approximately 500 radians^{-1} .

In addition to the signal attenuation caused by the data processing, the Bolocam system also attenuates some of the astronomical signal. By scanning across the sky, we are effectively convolving any signal with the profile of a Bolocam beam; since the beams have a non-zero width, this convolution will act like a low-pass filter on all of the astronomical signals. This filter will be approximately symmetric because the Bolocam beam profiles have a high degree of rotational symmetry. Additionally, since the beams are nearly Gaussian, the filter will be approximately Gaussian with a HWHM of about $1000 \text{ radians}^{-1}$ (which is equivalent to a $\text{HWHM}_\ell \simeq 6000$ in angular multipole space). See Figures 5.6 and 5.7.

In order to quantify the amount of signal attenuation by each atmospheric noise removal algorithm, it is useful to determine the effective bandwidth of the transfer function. The effective bandwidth describes the range of angular multipoles defined by the transfer function, and can be used to convert an angular power, C_ℓ , to a map-space variance in μK_{CMB}^2 . In general, the effective bandwidth is calculated by integrating the transfer function over all angular multipoles. However, since the expected SZE power spectrum is approximately flat in C_ℓ , it is more useful to weight the transfer function by the expected signal spectrum of $1/\ell(\ell+1)$. This weighting will produce an effective logarithmic, rather than linear, bandwidth, and can be used to convert an angular power in C_ℓ to a map-space variance. This effective logarithmic bandwidth, BW_{eff} , is defined as

$$\text{BW}_{eff} = \int_{\vec{\nu}} d\vec{\nu} S_{\vec{\nu}} W_{\vec{\nu}} B_{\vec{\nu}}, \quad (5.20)$$

where $\vec{\nu}$ is the two-dimensional spatial frequency, $S_{\vec{\nu}}$ is the expected signal spectrum, $W_{\vec{\nu}}$ is the transfer function of the data processing (in amplitude squared), and $B_{\vec{\nu}}$ is the transfer function of the Bolocam beam (in amplitude squared). Since the expected CMB signal has a flat band power in C_ℓ ,

$$S_{\vec{\nu}} \propto \frac{1}{\ell(\ell+1)} \quad (5.21)$$

for $\ell = 2\pi|\vec{\nu}|$.¹⁸ Assuming this spectrum for $S_{\vec{\nu}}$, a symmetric top-hat window between $\ell = \ell_{min}$ and $\ell = \ell_{max}$ will produce a bandwidth approximately equal to

$$\text{BW}_{eff} \propto \log(\ell_{max}) - \log(\ell_{min}) = \Delta \log \ell. \quad (5.22)$$

¹⁸We have used the small-scale flat sky approximation, $\ell = 2\pi|\vec{\nu}|$.

sky subtraction	$\Delta \log(\ell)$
average	0.98
planar	0.58
quadratic	0.37
adaptive PCA	0.51

Table 5.1: The effective bandwidth of the transfer function for the four types of atmospheric noise removal algorithms.

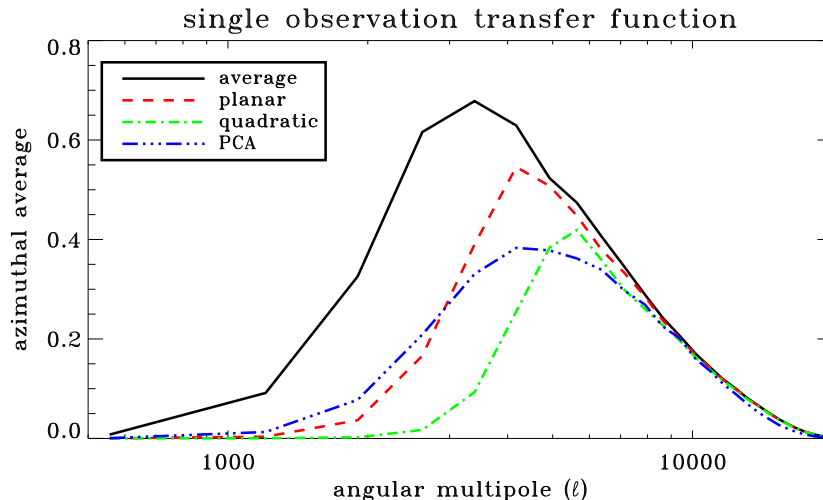


Figure 5.8: Azimuthally averaged transfer functions for a single observation for each of the four types of atmospheric noise removal algorithms.

Although the Bolocam transfer functions are highly non-symmetric, it is still useful to determine the effective $\Delta \log(\ell)$ for each of the atmospheric noise removal algorithms. See Table 5.1 and Figure 5.8.

5.6 Optimal Sky Subtraction

Each of the 2003 science field observations were processed with average, planar, and quadratic sky subtraction, creating three separate files for each observation. Quadratic subtraction removes the most atmospheric noise, while average subtraction retains the most astronomical signal, so there is an optimal sky subtraction algorithm for each observation based on the type of astronomical signal we are looking for. To determine which algorithm is optimal, we computed a figure of merit, FOM, for each subtraction method. Since the CMB signal appears as a variance in the map, the variance on the CMB signal will be proportional to the square of the map PSD divided by the transfer function of the experiment. This can

be seen in Equations F.12 and F.13. Therefore, the FOM is defined as the inverse of this variance on the CMB signal summed over all angular scales according to

$$\text{FOM} = \sum_{\vec{\nu}} \frac{S_{\vec{\nu}}^2 W_{\vec{\nu}}^2 B_{\vec{\nu}}^2}{\mathcal{P}_{\vec{\nu}}^2}, \quad (5.23)$$

where $\vec{\nu}$ is a two-dimensional spatial frequency with units of radians⁻¹, $S_{\vec{\nu}}$ is the expected CMB power spectrum, $W_{\vec{\nu}}$ is the transfer function of the data processing, $B_{\vec{\nu}}$ is the transfer function of the Bolocam beam, and $\mathcal{P}_{\vec{\nu}}$ is the PSD of the noise in the map. Note that we have included the $\simeq 5 - 6$ arcsecond uncertainty in our pointing model in $B_{\vec{\nu}}$, and this pointing uncertainty effectively broadens the beam. To be precise,

$$B_{\vec{\nu}} = \left(\mathbf{B}_{\vec{\nu}} e^{-|\vec{\nu}|^2/2\sigma_k^2} \right)^2, \quad (5.24)$$

where $\mathbf{B}_{\vec{\nu}}$ is the measured beam profile in Figure 3.17, and $\sigma_k = 1/2\pi\sigma_p$ for a pointing uncertainty of σ_p . For the CMB spectrum, we assumed a flat band power in \mathcal{C}_ℓ , so

$$S_{\vec{\nu}} = \frac{1}{\ell(\ell+1)} \quad (5.25)$$

for $\ell = 2\pi|\vec{\nu}|$. The figure of merit is inversely proportional to the variance in an estimate of the CMB amplitude (in μK_{CMB}^2), so it characterizes the signal-to-noise ratio of the map.

In the end, average subtraction was the optimal method for just over 50% of the observations, planar subtraction was the optimal method for just over 40% of the observations, and quadratic subtraction was the optimal method for just under 10% of the observations. See Table 5.2. In general, the amount of atmospheric noise in the data determines which subtraction algorithm is optimal. Therefore, for a given night where the conditions are similar for every observation, one algorithm is usually optimal for most of the observations. This effect can be seen in Figure 5.9, where the the FOM is plotted for every observation taken in 2003 for each science field. Note that quadratic subtraction is the optimal method only when the weather conditions are extremely poor. This is because the CMB spectrum falls quickly at high frequency, and the quadratic subtraction algorithm attenuates a large amount of signal at low frequency. For point-like sources, whose spectra are flatter, quadratic subtraction is often the optimal processing method.

science field	average	planar	quadratic
Lynx	256	211	48
SDS1	260	226	33

Table 5.2: The number of observations of each science field that were optimally processed by a given atmospheric noise removal algorithm.

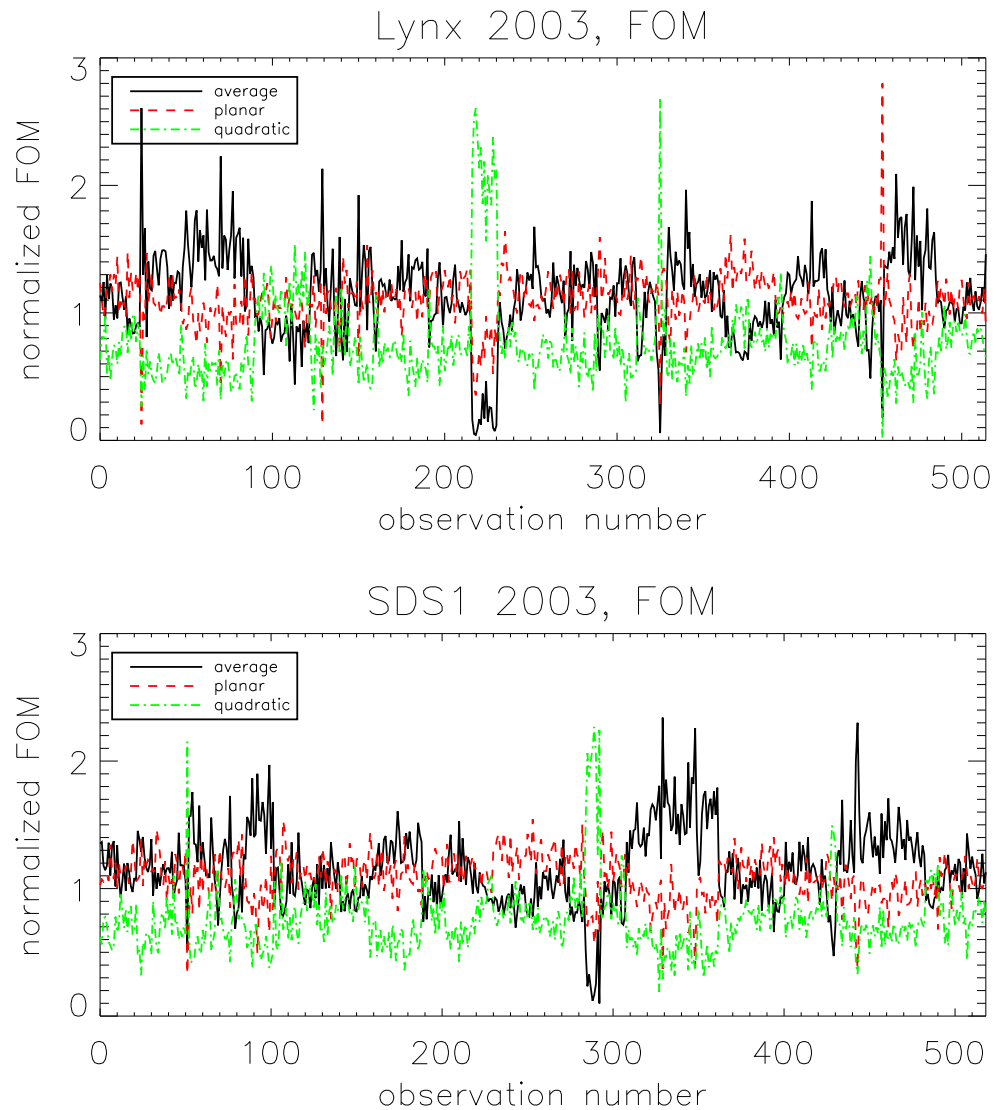


Figure 5.9: The figure of merit (FOM) for the three types of atmospheric noise removal algorithms for every observation made in 2003. The plot on the top shows observations of Lynx, while the plot on the bottom shows observations of SDS1. The x-axis is observation number, with the observations presented in chronological order.

5.7 Final Map Properties

Once the FOM is determined for each subtraction method for each observation, we can then produce a map of all of the data using the optimally processed map for each observation. To produce this final map, we need to make a slight modification to Equation 5.14 to account for the transfer function of the data processing and the Bolocam beam. We need to account for these effects because the transfer function depends on the scan direction and optimal sky subtraction algorithm for each observation. Therefore, the amount of astronomical signal in the map is in general different for each observation. To account for the amount of signal attenuation in each observation, the map PSD needs to be divided by the transfer function and the Fourier transform of the map needs to be divided by the square root of the transfer function. After making these modifications to Equation 5.14, we have

$$\mathcal{M} = \frac{\sum_i \left(\frac{M_i}{\sqrt{W_i B_i}} \right) \left(\frac{W_i B_i}{\mathcal{P}_i} \right)}{\sum_j \left(\frac{W_j B_j}{\mathcal{P}_j} \right)} \quad (5.26)$$

as the optimal map estimate, \mathcal{M} . W_i is the transfer function of the data processing for observation i , B_i is the Bolocam beam profile for observation i ,¹⁹ M_i is the Fourier transform of the map from observation i , and \mathcal{P}_i is the noise PSD for observation i . Note that the astronomical signal in \mathcal{M} will be equal to the true astronomical signal, because we have divided the Fourier transform of each single observation map, M_i , by the appropriate attenuation factor, $\sqrt{W_i B_i}$. However, for some pixels in Fourier space, W_i and/or B_i take on extremely small values, which means that some pixels in both the numerator and denominator of \mathcal{M} have extremely small values. Therefore, before taking the ratio of the numerator and denominator in Equation 5.26 we apply a regularizing factor, so that

$$M' = \sqrt{\mathcal{R}} \mathcal{M} = \frac{\frac{1}{\sqrt{\mathcal{R}}} \sum_i \left(\frac{M_i}{\sqrt{W_i B_i}} \right) \left(\frac{W_i B_i}{\mathcal{P}_i} \right)}{\frac{1}{\mathcal{R}} \sum_j \left(\frac{W_j B_j}{\mathcal{P}_j} \right)}, \quad (5.27)$$

for

$$\sqrt{\mathcal{R}} = \frac{\sum_i (\sqrt{W_i B_i}) \left(\frac{W_i B_i}{\mathcal{P}_i} \right)}{\sum_j \left(\frac{W_j B_j}{\mathcal{P}_j} \right)}. \quad (5.28)$$

¹⁹The beam profile is the same for every observation taken during a single observing season, but the beam is slightly different for the 2003 and 2004 observing seasons.

Although M' will be biased (i.e., it is not the Fourier transform of the true map of the sky), this bias is accounted for by the final transfer function we calculate in Section 5.7.2²⁰. Note that M' can be Fourier transformed back to map-space to produce a map m' , although m' will be biased.

5.7.1 Noise PSDs

Analogous to the case of a single observation, we used jackknifed realizations of our data to estimate the noise PSD of m' . In this case, each realization is generated by multiplying a randomly selected set of half the observations in m' by -1 . The map-space PSD from 1000 realizations were averaged to determine the best estimate of the noise PSD for each observing season for each science field, with the results shown in Figure 5.10. We also analyzed the distribution of individual realization PSDs to determine if the underlying probability distribution describing the noise is Gaussian. As in the single observation case, we computed a dimensionless PSD value according to Equation 5.18, and compared the distribution of these values to the PDF given in Equation 5.16. In general, the agreement is excellent, indicating the underlying noise distribution is Gaussian²¹. However, the Gaussian fits to the 2004 data are slightly worse than the fits to the 2003 data. Specifically, the probability of getting a worse χ^2 is 88%, 25%, 91%, and 2% for the 2003 Lynx field, 2003 SDS1 field, 2004 Lynx field, and 2004 SDS1 field, respectively. See Figure 5.11.

5.7.2 Astronomical Signal Attenuation

Now that the noise properties of the maps are well described, we need to determine the amount of astronomical signal attenuation due to data processing, the Bolocam beam, and the regularizing factor in Equation 5.27. Again, the method for calculating the transfer function of the data processing and regularizing factor is analogous to the method described in Section 5.5 for single observations. First, a simulated map of the expected CMB signal is

²⁰In Equations 5.27 and 5.28, $W_i B_i / \mathcal{P}_i$ acts as a weighting factor for each observation. Therefore, \mathcal{M} represents the weighted mean of the Fourier transform of each single observation map divided by the square root of the transfer function for that map, (M/\sqrt{WB}) . Similarly, \sqrt{R} represents the weighted mean of the square root of the transfer function for each observation, \sqrt{WB} . So, $M' = (\sqrt{WB})(M/\sqrt{WB})$, which reduces to the weighted mean of all the single observation map Fourier transforms, $M' \simeq \overline{M}$, in the limit that all of the single observation transfer functions, $W_i B_i$, are the same.

²¹The Hanning window we apply to each map prior to Fourier transforming could potentially alter the probability density function given in Equation 5.16. However, we have shown through simulations that the Hanning window does not noticeably alter $f(x_{i,\bar{v}})$.

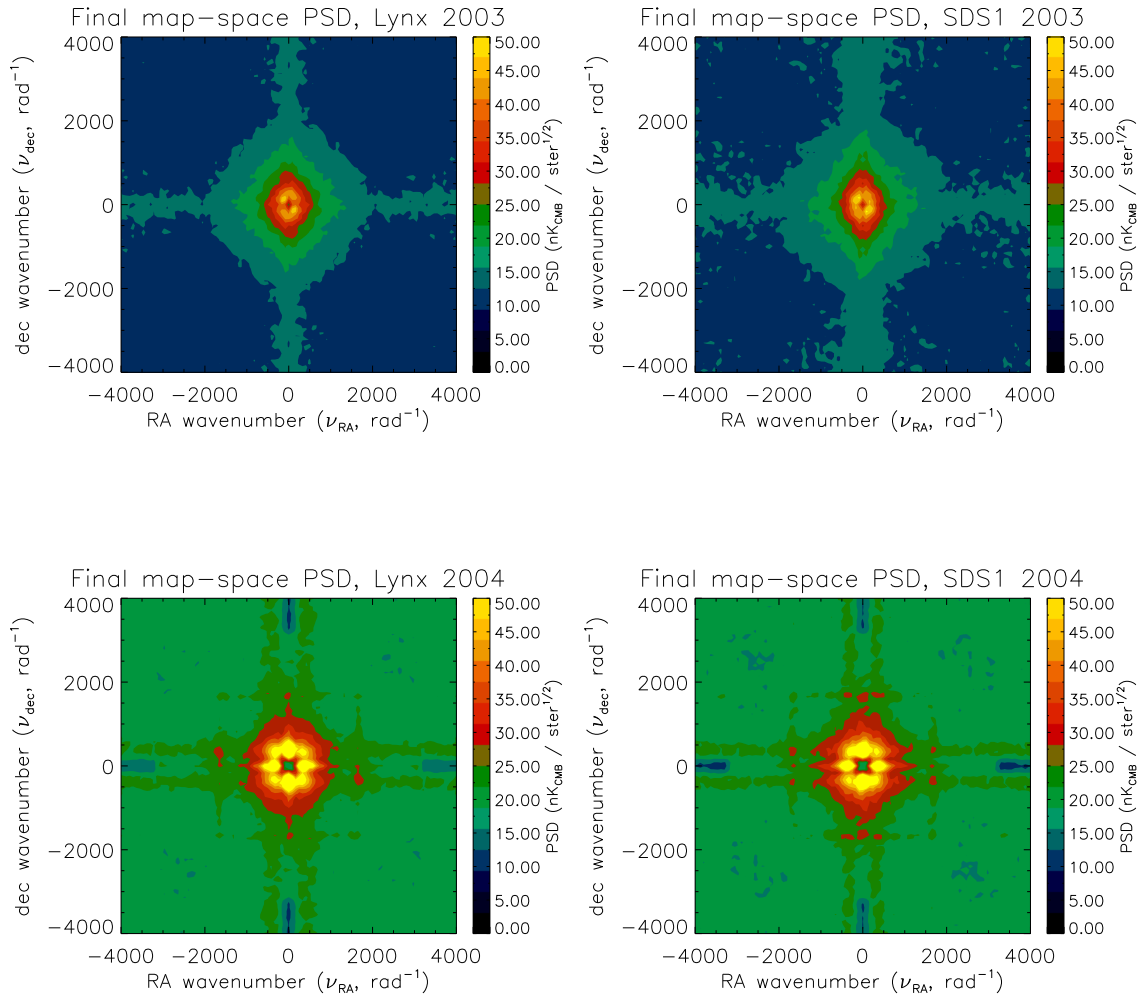


Figure 5.10: The map-space PSDs of the maps made from co-adding all observations for a given observing season. The plots in the top row are from 2003, and the plots in the bottom row are from 2004. The plots on the left are for the Lynx field, and the plots on the right are for the SDS1 field. Note that these PSDs have been calculated after applying the regularizing factor in Equation 5.27, so the profiles and surface brightness units are not, in general, physical. Additionally, the effects of the highly non-uniform transfer functions have not been included. Still, the PSDs do illustrate that there is excess noise at low frequency due to residual atmospheric noise, and they show an overall increase in noise level in the 2004 data compared to the 2003 data.

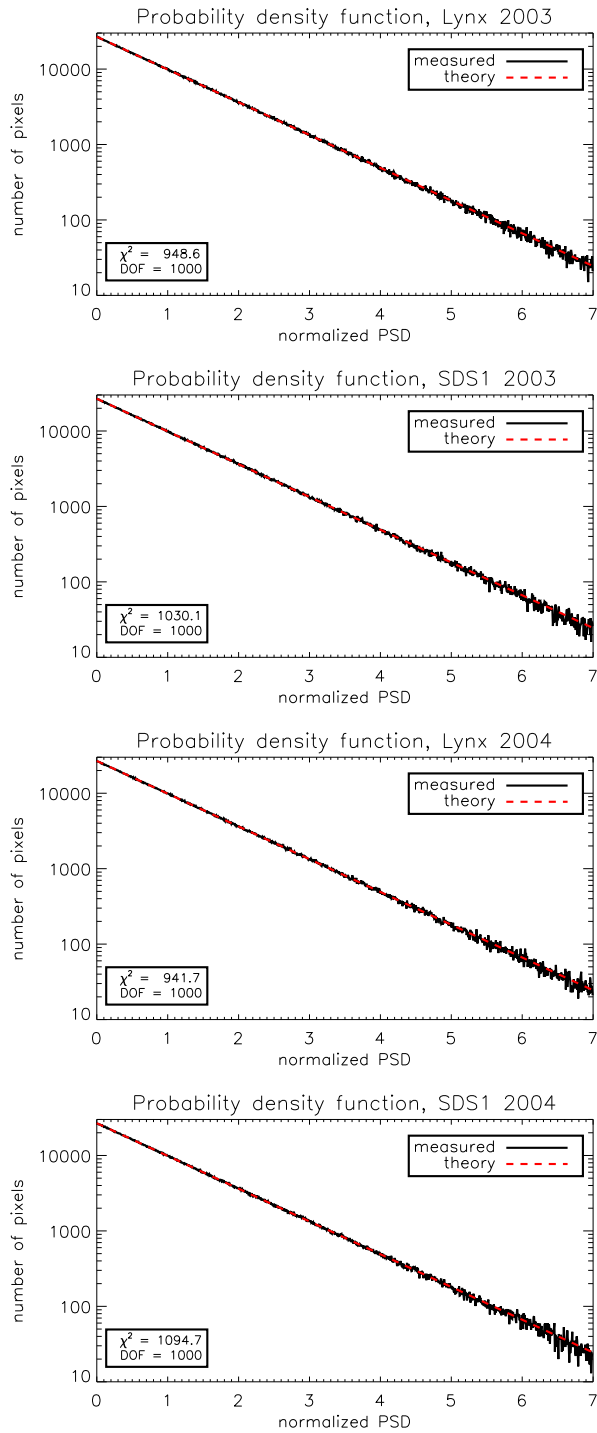


Figure 5.11: A comparison between the distribution of PSD values from the jackknifed realizations to a Gaussian PDF for the data co-added over all observations for a given observing season. From top to bottom, the plots show the data from: Lynx in 2003, SDS1 in 2003, Lynx in 2004, and SDS1 in 2004. In general the agreement is quite good, but the fits to the 2004 data are slightly worse than the fits to the 2003 data.

generated, then reverse-mapped and added into the time-stream for every observation that is co-added into m' . Next, these time-streams are processed and mapped in the same way that the original data was processed and mapped, including application of the regularizing factor²². The map made from the unmodified time-streams is then subtracted from the map made from the time-streams that include simulated signal, and this map is compared to the original simulated CMB map. More details of the calculation are given in Appendix E. Since the beam profile is the same for every observation made during a single observing season, the beam profiles, B_i s, will cancel out in Equations 5.26, 5.27, and 5.28. The B_i s will approximately cancel even when adding data from separate seasons, since the beam profile is similar in both years. Therefore, the beam profile in the final maps is the same as the beam profile used for single observation maps. Contour plots of the total astronomical signal attenuation are given in Figure 5.12 and Figure 5.13.

Compared to a single observation, the transfer functions for the final maps are much closer to being rotationally symmetric. The difference in the transfer functions is at low spatial frequencies parallel to either RA or dec, and is caused by adding observations made while scanning in perpendicular directions. This is because the modes in single observation maps, where there is a large amount of astronomical signal attenuation (i.e., at low frequency parallel to the scan direction), do not contribute much to the final map. Therefore, most of the signal at low frequency along the RA direction is obtained from maps made while scanning parallel to dec, and vice versa. This effect can be seen by comparing the plots in Figures 5.6 and 5.7 with the plots in Figure 5.12.

5.7.3 Noise from Astronomical Sources

Since the noise PSD of the final map is estimated from jackknifed realizations of the data, all of the astronomical signal will be absent from the noise PSD. This is fine for the CMB signal we are looking for, because we want to understand the noise of our system in the absence of our signal of interest. However, we need to account for the noise produced by other sources of astronomical signal, including galactic dust emission, radio point-source emission, emission from dusty submillimeter galaxies, and primary CMB anisotropies.

The amount of galactic dust emission can be estimated from maps of our science fields

²²Since the single observation PSDs, transfer functions, and beam profiles are the same for the original files and the files with simulated CMB signal, the regularizing factor will be the same for both files. Therefore, the transfer function computed in the end will account for the effects of the regularizing factor.

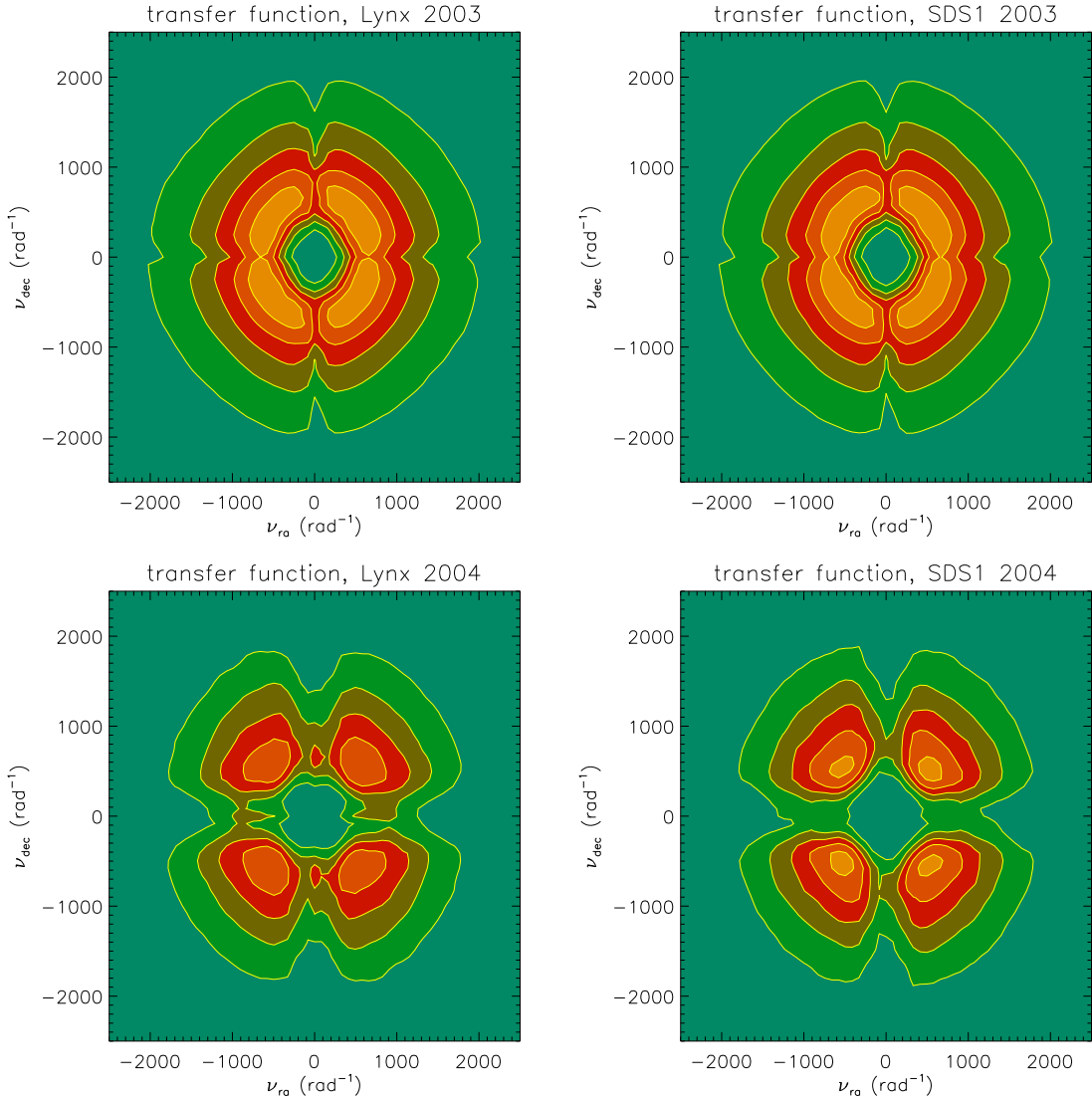


Figure 5.12: Contour plots showing the fractional amount of astronomical signal that remains in the maps made from all observations of each science field for each observing season. The astronomical signal is attenuated both by our processing and map-making algorithms, and by the Bolocam beam. Each contour line represents 0.1. Clockwise from top left, the plots show: Lynx in 2003, SDS1 in 2003, Lynx in 2004, and SDS1 in 2004. Note that the transfer functions for a given observing season are similar for each science field, because the data was processed in a similar way. However, the 2004 data processed using adaptive PCA sky subtraction has a much different transfer function than the 2003 data processed with average, planar, or quadratic sky subtraction. Note that, especially in 2003, there is a high degree of rotational symmetry compared to the single observation transfer functions in Figures 5.6 and 5.7. There is slightly more attenuation along the ν_{RA} axis compared to the ν_{dec} axis in the 2003 maps because more observations were taken while scanning parallel to RA compared to scanning parallel to dec. This asymmetry between RA and dec scans was caused by an observing error near the start of the season.

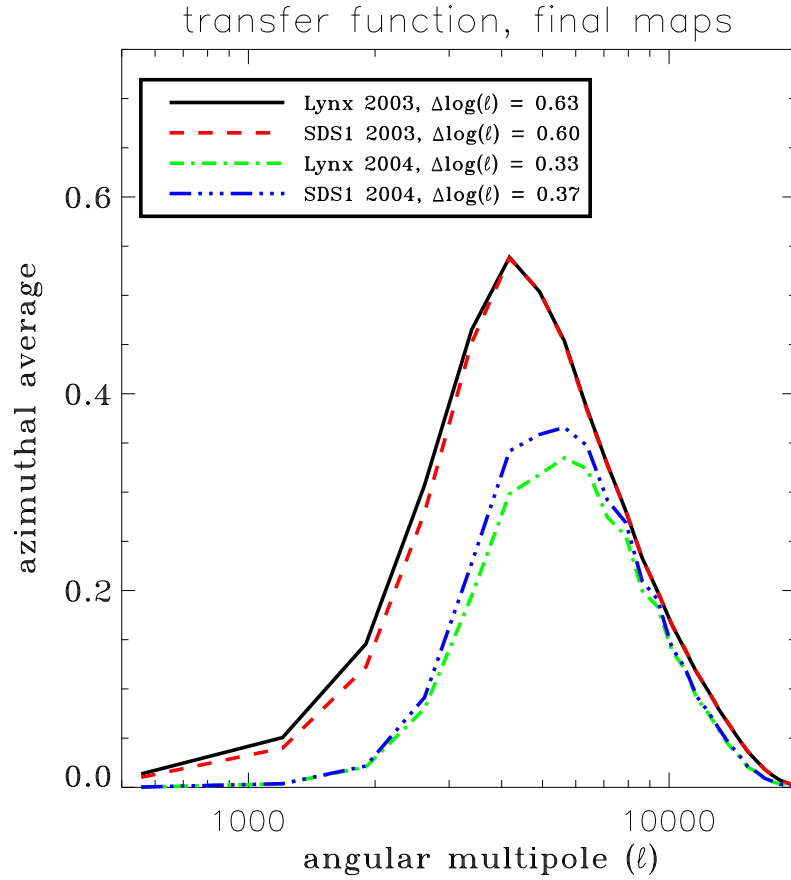


Figure 5.13: The azimuthally averaged transfer function for the map made of each science field for each observing season. Included in the legend is the value of $\Delta \log(\ell)$ for each map, which gives an estimate of the effective bandwidth of the map to a CMB signal with a flat band power in $\mathcal{C}_\ell = C_\ell \ell(\ell + 1)/2\pi$. Note that the effective bandwidth in 2003 is approximately twice the effective bandwidth in 2004.

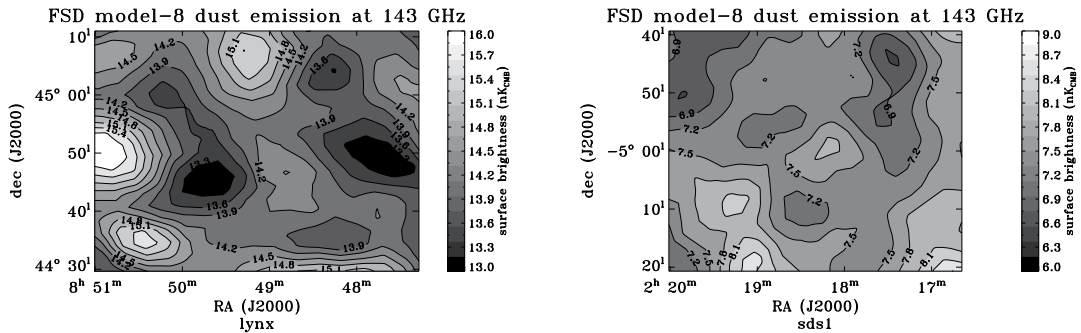


Figure 5.14: Maps of the galactic dust emission in each science field, with Lynx on the left and SDS1 on the right. Note that there is a different scale for the shading and contours for the two plots.

taken from the full-sky $100\ \mu\text{m}$ DIRBE/IRAS dust map [40,124]. To extrapolate the $100\ \mu\text{m}$ data to our band at $143\ \text{GHz} \simeq 2.1\ \text{mm}$, we have used the “model 8” extrapolation given in Finkbeiner, et al. [46]. At $100\ \mu\text{m}$, the typical surface brightness of the dust emission in our science fields is just over $1\ \text{MJy/ster}$, which corresponds to a surface brightness of around $5 - 15\ \text{nK}_{\text{CMB}}$ for Bolocam. See Figure 5.14. Using the maps that have been scaled to a surface brightness at $143\ \text{GHz}$, we determined the map-space PSD of the dust emission, which corresponds to a C_ℓ less than $10^{-6}\ \mu\text{K}_{\text{CMB}}^2$ for $\ell \gtrsim 1000$.²³ See Figure 5.15. Since this is well below the expected SZE-induced CMB anisotropy we are looking for, we will assume that there is no dust emission in our science field maps.

Emission from radio point sources will also contribute to the astronomical signal in our maps. The power spectrum from these sources can be calculated from

$$C_\ell = \int_0^{S_{\text{cut}}} S^2 N(S) dS + w_\ell I^2, \quad (5.29)$$

where S is the flux of the source, $N(S)$ is the differential number of sources at a given flux in a given solid angle, S_{cut} is an estimate of the brightest source that cannot be resolved in the map, C_ℓ is the angular power spectrum, w_ℓ is the Legendre transform of the two-point

²³Note that the resolution of the DIRBE/IRAS dust map is 6.1 arcminutes, which corresponds to HWHM in ℓ -space of $\lesssim 2000$. Therefore, we have no direct knowledge of the power spectrum on scales smaller than $\simeq 6$ arcminutes, which are the angular scales Bolocam is most sensitive to. However, the power spectrum of the dust falls rapidly at small angular scales, so the estimate at $\ell < 2000$ should provide a reasonable upper limit for the expected power spectrum at the scales Bolocam is most sensitive to.

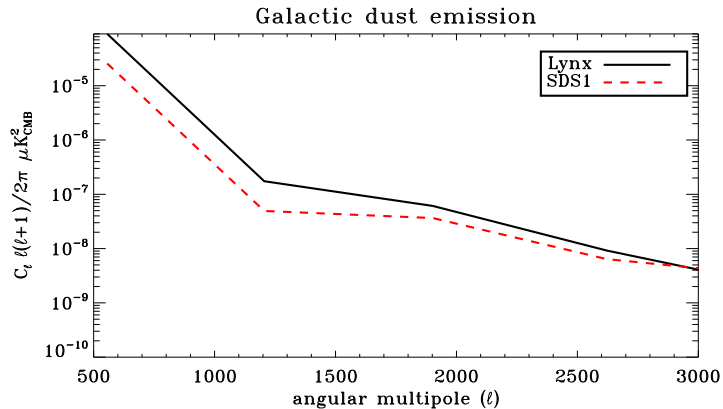


Figure 5.15: The map-space PSD of the dust emission in each science field. The dust signal is several orders of magnitude below the expected SZE-induced CMB anisotropies.

correlation function of the sources, and

$$I = \int_0^{S_{cut}} SN(S) dS \quad (5.30)$$

is the background contributed by the sources [125, 152]. We will assume $w_\ell = 0$, since there is a large amount of uncertainty in the clustering of these sources. Since any clustering will push the power spectrum to lower ℓ , which would reduce the amount of power in our band, this should be a conservative assumption. Differential number counts have been determined from measurements at 1.4, 5, and 8.44 GHz [36, 146], with

$$N(S)_{5\text{GHz}} = 150 S^{-2.5} \text{Jy}^{-1} \text{ster}^{-1}. \quad (5.31)$$

Since the spectrum of the sources is nearly flat (i.e., $S_\nu \propto \nu^\beta$ with $\beta = 0$), this equation is valid over a wide range of frequencies. Additionally, the WMAP K, Ka, and Q bands have been used to determine the differential number counts at 22, 30, and 40 GHz [9]. $N(S)$ is similar for all three WMAP bands, and is $\lesssim 70\%$ of the value of the model in Equation 5.31. The differential number counts at 40 GHz are described by

$$N(S)_{40\text{GHz}} = 33 S^{-2.7} \text{Jy}^{-1} \text{ster}^{-1}. \quad (5.32)$$

To extrapolate this equation to the Bolocam band center at 143 GHz, we will use the method described in White and Majumdar [152]. Since there is evidence of the power law

for $N(S)$ flattening out at higher frequencies, they describe the differential number counts according to²⁴

$$N(S)_{143\text{GHz}} = (20 - 33) S^{-2.3} \text{ Jy}^{-1} \text{ster}^{-1}. \quad (5.33)$$

We also need to estimate S_{cut} in order to evaluate the power spectrum in Equation 5.29. This cutoff flux will necessarily be somewhat arbitrary, but, since C_ℓ is only weakly dependent on S_{cut} , it will not significantly alter our result. We have chosen $S_{cut} = 10$ mJy, which is approximately four times the RMS fluctuations per beam in maps made from the 2003 data that have been optimally filtered for point sources. Additionally, the largest excursions in these maps are $\simeq 10$ mJy, further justifying our choice to set $S_{cut} = 10$ mJy. Inserting this value of S_{cut} into Equation 5.29, along with Equation 5.33, yields $C_\ell \simeq 1.1 - 1.9 \text{ Jy}^2 \text{ster}^{-1}$, or $C_\ell \simeq 7 - 12 \times 10^{-6} \mu\text{K}_{CMB}^2$. To compare this angular power spectrum to the expected SZE-induced CMB anisotropies, we compare the temperature fluctuation caused by C_ℓ to the temperature fluctuation caused by a constant band power in C_ℓ given our full transfer function, $W_\ell B_\ell$, in Figure 5.13. For this comparison, we compute the value of a constant C_ℓ^{eff} that would produce the same temperature fluctuation as C_ℓ , given by

$$C_\ell^{\text{eff}} = \frac{\sum_\ell C_\ell \frac{2\ell+1}{4\pi} W_\ell B_\ell}{\sum_\ell \frac{2\pi}{\ell(\ell+1)} \frac{2\ell+1}{4\pi} W_\ell B_\ell}. \quad (5.34)$$

For the radio point sources with $C_\ell = 7 - 12 \times 10^{-6} \mu\text{K}_{CMB}^2$, the effective C_ℓ given the Bolocam transfer function is $C_\ell^{\text{eff}} \simeq 35 - 60 \mu\text{K}_{CMB}^2$, which is comparable to the expected signal from the SZE-induced CMB anisotropies.

Additionally, emission from dusty submillimeter galaxies will be present in our maps. The same method used to determine the power spectrum from radio point sources can also be used to estimate the power spectrum of these sources. To calculate the differential number counts we used the number counts distribution determined by Maloney et al. [87], with

$$N(S)_{268\text{GHz}} = 42 S^{-2.7} \text{ Jy}^{-1} \text{ster}^{-1}. \quad (5.35)$$

The spectrum of these objects can be described by $S_\nu \propto \nu^\beta$, where $2.5 \lesssim \beta \lesssim 3.5$ [22],

²⁴There is some uncertainty in the spectrum of S_ν for these radio sources between 40 GHz and 143 GHz. White and Majumdar quote two spectra, one with $\beta = 0$, and one with $\beta = -0.3$. This uncertainty in the spectrum of the radio point sources results in a finite range for the normalization of the number counts after extrapolating to 143 GHz.

which gives a differential number count at 143 GHz of

$$N(S)_{143\text{GHz}} = (1.0 - 2.9) S^{-2.7} \text{ Jy}^{-1} \text{ ster}^{-1}. \quad (5.36)$$

Inserting the above formula into Equation 5.29 gives $C_\ell = 0.8 - 2.4 \text{ Jy}^2 \text{ ster}^{-1}$, or $C_\ell = 6 - 17 \times 10^{-6} \mu\text{K}_{CMB}^2$. Equation 5.34 can again be used to convert this to an effective constant \mathcal{C}_ℓ for our transfer function, giving $\mathcal{C}_\ell^{\text{eff}} \simeq 30 - 85 \mu\text{K}_{CMB}^2$. Alternatively, we can compute a power spectrum using the differential number counts derived from SHADES data at 350 GHz [31], which is described by

$$N(S)_{350\text{GHz}} = 2.2 \times 10^4 [S^2 + (5.9 \times 10^7)S^{5.8}]^{-1} \text{ Jy}^{-1} \text{ ster}^{-1}. \quad (5.37)$$

Converting this $N(S)$ to a differential number count at 143 GHz using the average spectrum of ν^3 yields a similar power spectrum, with $C_\ell = 1.0 \text{ Jy}^2 \text{ ster}^{-1}$, or $C_\ell = 8 \times 10^{-6} \mu\text{K}_{CMB}^2$.

Since there is a wide range of uncertainty in the power spectrum for both the radio and submillimeter point sources, we have not attempted to correct for this contamination in our CMB amplitude estimates. This means that the upper limits we find for the CMB amplitude will be conservative.

Finally, there will also be a signal in our map due to the primary CMB anisotropies, which are distinct from the SZE-induced anisotropies that we are looking for. The power spectrum of the primary CMB anisotropies has been measured to high precision by WMAP at $\ell \lesssim 800$ [63], by BOOMERANG at $500 \lesssim \ell \lesssim 1100$ [69], and up to $\ell \simeq 2500$ by ACBAR [78]. This measured power spectrum is well fit by theory, with only a small number of free parameters. Therefore, we have generated a template of the primary CMB power spectrum using the theoretical prediction generated by CMBFAST [29, 127, 159, 160], with the best fit values to the free parameters from WMAP, BOOMERANG, ACBAR, and other CMB measurements²⁵ [78, 132]. Since the CMBFAST routine only computes the power spectrum up to $\ell = 3000$, we fit a decaying exponential to the \mathcal{C}_ℓ versus ℓ to extrapolate the primary CMB power spectrum to higher ℓ . We can again use Equation 5.34 to convert this power spectrum to an effective constant \mathcal{C}_ℓ given our transfer function, with

²⁵The best fit values are: primordial helium fraction, $Y_{He} = 0.248$; baryon fraction, $\Omega_b = 0.0422$; cold dark matter fraction, $\Omega_{CDM} = 0.203$; dark energy fraction, $\Omega_\lambda = 0.76$; Hubble constant, $H_0 = 73 \text{ km sec}^{-1} \text{ Mpc}^{-1}$; number of effective neutrino species, $N_\nu = 3.29$; and an optical depth to the surface of last scattering of $\tau = 0.09$.

source	$\mathcal{C}_\ell^{\text{eff}}$	accounted for
galactic dust	$\lesssim 10^{-10} \mu\text{K}_{CMB}^2$	no
radio point sources	$\simeq 35 - 60 \mu\text{K}_{CMB}^2$	no
submillimeter point sources	$\simeq 30 - 85 \mu\text{K}_{CMB}^2$	no
primary CMB anisotropies	$\simeq 45 \mu\text{K}_{CMB}^2$	yes

Table 5.3: The effective constant band power in \mathcal{C}_ℓ for the Bolocam transfer function, according to Equation 5.34, for various astronomical signals.

$\mathcal{C}_\ell^{\text{eff}} \simeq 45 \mu\text{K}_{CMB}^2$. This band power is similar to what is expected from the SZE-induced CMB anisotropies. However, in contrast to the radio and submillimeter point sources, the primary CMB power spectrum is precisely known, and can be accounted for in our analysis.

A summary of the expected signal from the various astronomical sources is given in Table 5.3 and Figure 5.16.

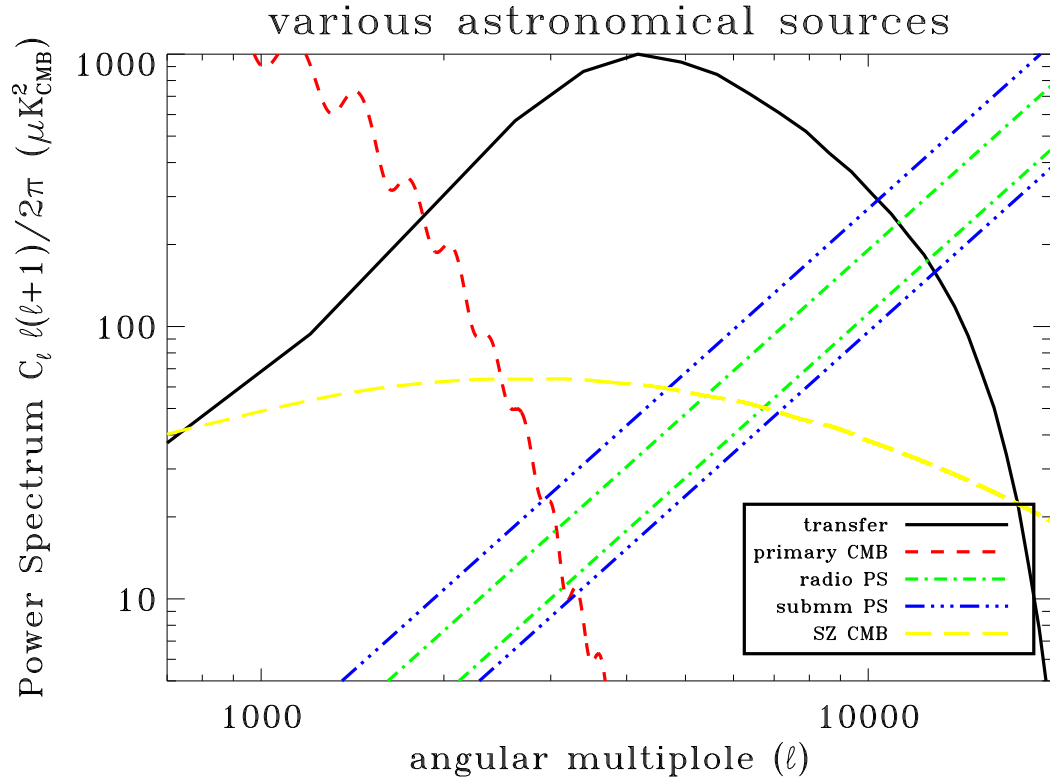


Figure 5.16: The power spectra from the primary CMB anisotropies (short red dashes), high and low estimates for radio point sources (green dash-dot), high and low estimates for submillimeter point sources (blue dot-dot-dot-dash), and the analytically predicted SZE-induced CMB anisotropies from Komatsu and Seljak [73] using the best fit value of σ_8 from Dawson, et al. [37] (long yellow dashes). Also included as a solid black line is the transfer function of the final map of the Lynx field for the 2003 observing season, with arbitrary normalization.

Chapter 6 Science Analysis

Based on the estimated non-CMB noise in our maps, the CMB signal transfer function of our maps, and the PSD of our maps we can estimate the total anisotropy (primary CMB + SZE-induced CMB + any other astronomical signal) power spectrum for the angular scales probed by our observations. Additionally, with knowledge of the expected primary CMB signal and expected spectrum of the SZE-induced CMB anisotropies, we can determine the amplitude of the SZE-induced CMB anisotropies.

6.1 Procedure

Anisotropies in the CMB, along with other unresolved astronomical signals, will produce noise in our maps. Therefore, to measure the total anisotropy power spectrum, we need to calculate the difference between the observed power spectrum of our maps and the expected power spectrum of our maps. The observed PSD, which is the squared amplitude of the Fourier transform of the final map, will be denoted by $x_{\vec{\nu}}$, where $\vec{\nu}$ is the two-dimensional Fourier space frequency in radians⁻¹. The expected PSD, $\mathcal{P}_{\vec{\nu}}$, consists of all the noise due to non-astronomical sources (i.e., the Bolocam system), as well as the noise from unwanted astronomical sources. However, we do not account for the expected noise from unwanted astronomical sources since it is not well understood, and is expected to be much smaller than the signal from the CMB anisotropies¹. The noise level of the Bolocam system has been estimated from jackknifed realizations of the data to give $\mathcal{P}_{\vec{\nu}}$, and is shown in Figure 5.10.

In order to interpret the excess power (or excess variance) in the map, the amount of astronomical signal attenuation needs to be determined. Signal is attenuated by our data processing and map-making routines, along with our finite size beam profiles, with the effective transfer functions of the map denoted by $W_{\vec{\nu}}$ and $B_{\vec{\nu}}$, respectively. We have chosen to model the CMB anisotropies according to $C_{\ell} = AS_{\vec{\nu}}$, for $\ell = 2\pi|\vec{\nu}|$ and $S_{\vec{\nu}} = 2\pi/\ell(\ell + 1)$ for a flat band power in C_{ℓ} . With these definitions, the best fit amplitude for the CMB

¹As detailed in Section 5.7.3, the noise from both radio and submillimeter point sources is not well understood, so we have not accounted for the signal from these point sources in our analysis.

anisotropy signal is determined by maximizing Equation F.8,

$$\log(\mathcal{L}) = \sum_{\vec{\nu}} \left(-\log(\mathcal{P}_{\vec{\nu}} + AS_{\vec{\nu}}B_{\vec{\nu}}W_{\vec{\nu}}) - \frac{x_{\vec{\nu}}}{\mathcal{P}_{\vec{\nu}} + AS_{\vec{\nu}}B_{\vec{\nu}}W_{\vec{\nu}}} \right),$$

with respect to A , where $x_{\vec{\nu}}$ is the measured PSD of the science field map. For reference, a detailed derivation of the above equation is given in Appendix F. Note that Equation F.8 allows for $A < 0$. Although such values are not physical, fluctuations in the noise can cause the most likely value of A to be less than zero when the signal-to-noise ratio is low.

Since our maps are real, $x_{\vec{\nu}} = x_{-\vec{\nu}}$, $\mathcal{P}_{\vec{\nu}} = \mathcal{P}_{-\vec{\nu}}$, etc., so the sum in Equation F.8 only includes half of the $\vec{\nu}$ -space pixels. Additionally, the $\vec{\nu}$ -space pixels are slightly correlated, approximately 1 - 4% for nearest-neighbor pairs of pixels and less than 1% for all other pairs of pixels. These correlations can be modeled as an effective reduction in the number of $\vec{\nu}$ -space pixels, with the effective reduction factor given by

$$N_{\text{eff}} = N_{\text{true}} / \sum_{\vec{\nu}} \sum_{\vec{\nu}'} c_{\vec{\nu}, \vec{\nu}'}, \quad (6.1)$$

where N_{true} is the total number of $\vec{\nu}$ -space pixels, N_{eff} is the effective number of $\vec{\nu}$ -space pixels, and $c_{\vec{\nu}, \vec{\nu}'}$ is the correlation between pixel $\vec{\nu}$ and pixel $\vec{\nu}'$. $c_{\vec{\nu}, \vec{\nu}'}$ is calculated from the Fourier transform of the map, M , according to

$$c_{\vec{\nu}, \vec{\nu}'} = \left| \frac{\langle M_{\vec{\nu}}^* M_{\vec{\nu}'} \rangle}{\langle |M_{\vec{\nu}}| \rangle \langle |M_{\vec{\nu}'}| \rangle} \right|. \quad (6.2)$$

Equation F.8 is divided by the ratio of N_{true} to N_{eff} to account for these correlations when calculating the Bayesian likelihood, with $N_{\text{true}}/N_{\text{eff}} \simeq 2.3$ for our data². The location of the peak in the likelihood is not affected by the value of N_{eff} , however the width of the likelihood is. Therefore, the Bayesian likelihoods we derive using N_{eff} are not used to set our final confidence level limits; they are only used as a rough estimate of these limits. Plots of \mathcal{L} versus A for each science field for each observing season are given in Figure 6.1.

Equation F.8 is useful for determining the most likely value of the CMB amplitude for each data set, but it does not provide an accurate estimate of the confidence intervals on A given our data. The reason we do not use the Bayesian model given by \mathcal{L} to estimate

²This factor of 2.3 is due entirely to these correlations, and does not include the factor of 2 due to the fact that the map is real.

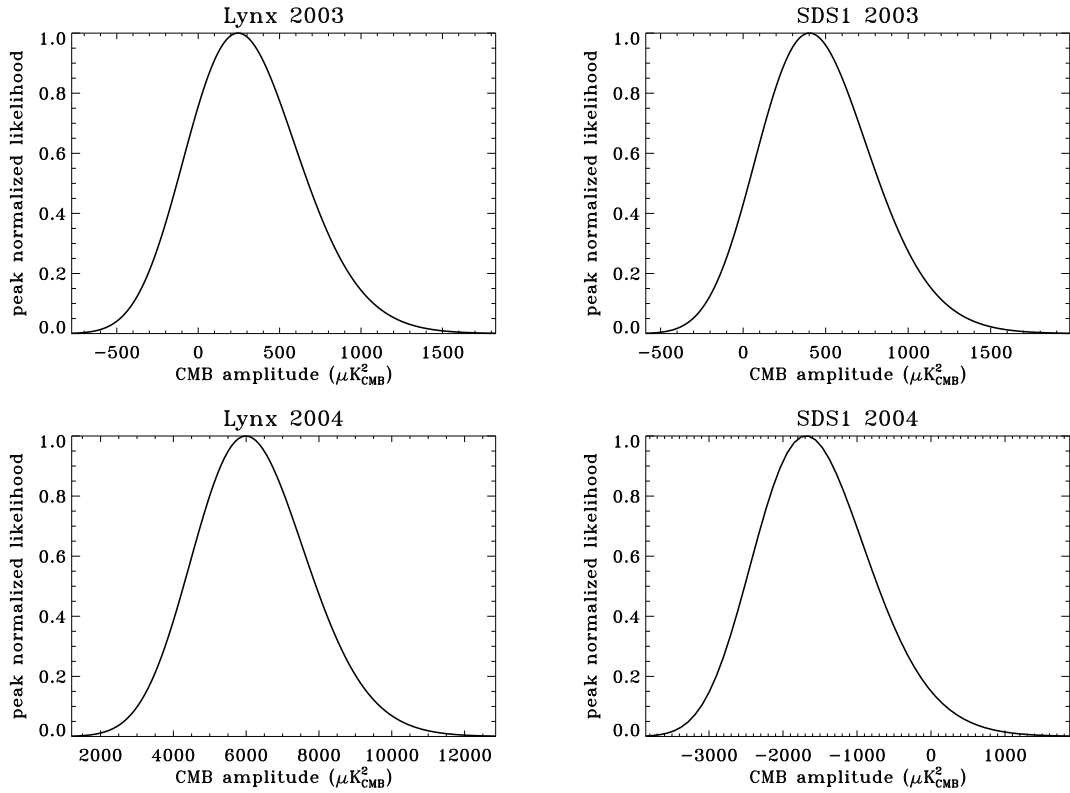


Figure 6.1: The Bayesian likelihood given by Equation F.8 for each science field for each observing season. The likelihoods have all been normalized to one at the peak. These plots should only be considered as rough estimates for determining confidence intervals, because the cosmic variance of the CMB spectra, correlations among map pixels, and the physical boundary that the CMB amplitude must be greater than or equal to zero have not been fully accounted for in the likelihood function.

the confidence intervals on A is because: 1) the correction factor $N_{\text{true}}/N_{\text{eff}}$ is only an approximate way to account for the correlations between pixels, 2) \mathcal{L} does not account for the cosmic variance on the CMB spectrum, and 3) the physical boundary that the CMB amplitude must be greater than or equal to zero is not properly dealt with in \mathcal{L} .³ Instead, we have used the following method to determine our confidence intervals, which relies on the classical interpretation of probability and the Feldman and Cousins method of dealing with physical boundaries and background signals [45]. To understand this interpretation, suppose that the most likely CMB anisotropy amplitude given our data is A_0 . Next, consider a set of experiments that are conducted under the same conditions, and have the same noise properties as our experiment, but with a CMB anisotropy amplitude of A . This set of experiments is then repeated for the full range of physically allowed values of A . We can then determine the interval, $[A_1, A_2]$, such that for any A within this interval the data from no more than α of the experiments within a given set of experiments will produce a CMB anisotropy amplitude that is more likely than A_0 . This means that given our measured data, the true value of the CMB anisotropy amplitude is within the interval $[A_1, A_2]$ at a confidence level of α .

To apply this method to our data, we first create a simulated map of the CMB for a given value of the CMB amplitude, A_{sim} , using our assumed profile $S_{\vec{\nu}}$. This simulation is produced by drawing a value for each pixel, $\vec{\nu}$, from an underlying Gaussian distribution, then multiplying it by $A_{sim}S_{\vec{\nu}}$. The PSD of this simulated map is multiplied by our full transfer function and added to the jackknifed realization of our data, $x_{i,\vec{\nu}}$.⁴ Note that a different simulated map is created for each jackknifed realization of the data to account for cosmic variance. Then, we use Equation F.8 to determine the most likely value of the CMB amplitude, \hat{A}_i , for realization i . By using jackknives of our actual data we are including all of the correlations between pixels, and by simulating the CMB maps we are accounting for the cosmic variance of the CMB spectra. For a given value of A_{sim} , we repeat this process for each jackknifed realization of the data.

At this point, we have N_{real} sets of data, each with a likelihood given by $\mathcal{L}(x_{i,\vec{\nu}}|A_{sim})$, where i is the index for each of the N_{real} jackknifed realizations of our data. We can arrange

³The standard Bayesian technique is to renormalize the likelihood to the integral over the physically allowed region, but such a renormalization is not rigorously justified [156].

⁴The reason we add the simulated CMB map to the jackknifed realization map instead of the time-streams is to reduce the amount of computational time required. Since the transfer functions of the maps are well measured, there is no reason to add the simulated data directly to the time-streams.

these data sets from most likely to least likely by ordering them according to $\mathcal{L}(x_{i,\vec{\nu}}|A_{sim})$. Classically, we can then determine what values of \hat{A}_i are within a given confidence level, α , by determining the range of \hat{A}_i for the most likely $\alpha \times N_{real}$ data realizations. However, this approach can lead to confidence intervals that contain unphysical values for an observable, or even intervals that contain no physically allowed values. Additionally, with small signals and large backgrounds it can be unclear whether an upper limit or central confidence region should be used until a result is obtained. The consequence of basing the choice of interval on the result of the data is that the intervals under-cover (i.e., do not contain a large enough range for the given confidence level) for a large range of values for the physical observable.

Therefore, to correctly determine our confidence intervals we will use the ordering method developed by Feldman and Cousins [45]. Instead of ordering data sets based on their likelihood, the data sets are ordered based on the ratio of their likelihood to the likelihood of the most probable physically allowed outcome. For example, if $\hat{A}_i < 0$, then the likelihood of the data set, $\mathcal{L}(x_{i,\vec{\nu}}|A_{sim})$, will in general be small. However, the likelihood of that data set may not be small compared to the likelihood, $\mathcal{L}(x_{i,\vec{\nu}}|0)$, of the most probable physically allowed alternative hypothesis of $\hat{A}_i = 0$. Therefore, the correct way to order the data is according to the value of

$$R_i = \frac{\mathcal{L}(x_{i,\vec{\nu}}|A_{sim})}{\mathcal{L}(x_{i,\vec{\nu}}|\hat{A}_{i,best})}, \quad (6.3)$$

where $\hat{A}_{i,best} = \max(\hat{A}_i, 0)$ is the most likely physically allowed value of A for each data realization. With this ordering principle, the confidence intervals never contain unphysical values for the observable. Additionally, there is a smooth transition from the case of an upper limit to a central confidence region, eliminating intervals that under-cover due to choosing between an upper limit and a central region based on the result.

To apply this ordering principle to our jackknifed realizations, we first calculate R_i for each of the N_{real} data sets. Then, the range of \hat{A}_i for a given confidence level is calculated from the maximum and minimum values of \hat{A}_i , denoted by $[\hat{A}_{min}, \hat{A}_{max}]$, for the $\alpha \times N_{real}$ data sets with the largest values of R_i . This means that the width of the confidence belt at A_{sim} is given by $[\hat{A}_{min}, \hat{A}_{max}]$ (i.e., if the CMB amplitude is A_{sim} and a large number of experiments are performed with the same noise properties as our experiment, then the estimated CMB amplitude for $100 \times \alpha$ percent of these experiments will fall between \hat{A}_{min}

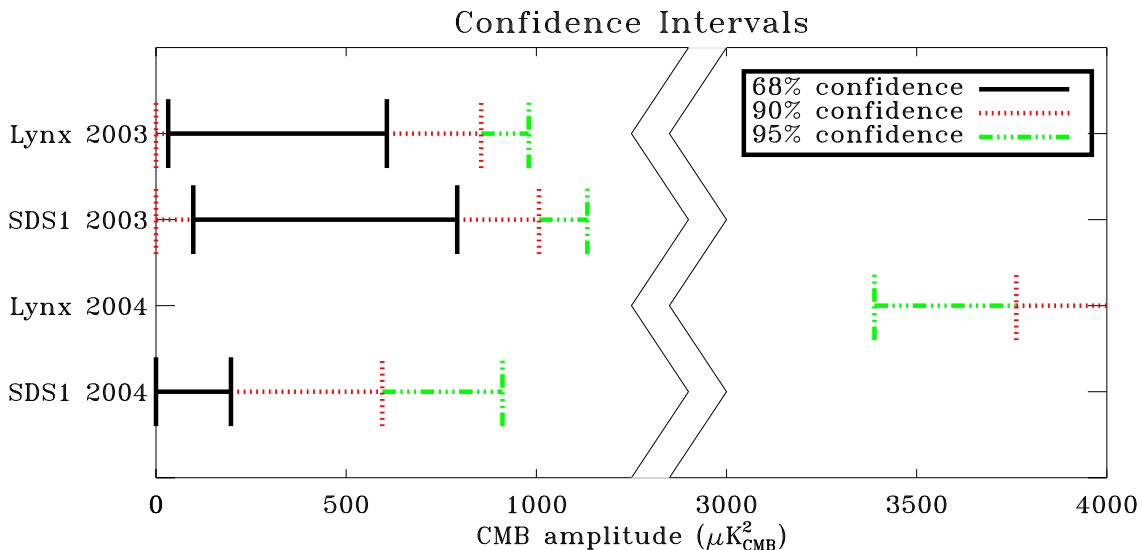


Figure 6.2: Confidence intervals for the CMB amplitude for each science field for each observing season. These values were determined from the confidence belts in Figure 6.3. Note the break in the x-axis of the plot near an amplitude of $1300 \mu\text{K}_{CMB}^2$.

and \hat{A}_{max}). By calculating $[\hat{A}_{min}, \hat{A}_{max}]$ for the full range of A_{sim} , we can construct a complete confidence belt. This confidence belt can then be used to determine the upper and lower limits at a given confidence level using the most likely value of A determined for each science field for each observing season. See Figure 6.3 and Figure 6.2.

6.2 CMB Anisotropy Results

From Figure 6.2 it is clear that the data from the Lynx field in 2004 is inconsistent with the other three data sets. Additionally, the 2004 Lynx data is inconsistent with the expected signal of $\simeq 50 - 100 \mu\text{K}_{CMB}^2$. The cause of this inconsistency in the 2004 Lynx field is not well understood, but it might be due to the adaptive PCA algorithm used to process the data or because of the excess noise that was present in the 2004 data⁵. Unfortunately, the extremely low signal-to-noise ratio of the data makes it difficult to determine the cause of the problem. At first glance, the 2004 SDS1 data appears to agree well with the 2003 data. However, the Bayesian likelihood that the CMB amplitude is greater than 0 is less than 4% for the 2004 SDS1 data. Feldman and Cousins [45] caution that their method for determining confidence intervals may not be reliable when the probability of a physically

⁵See Section 4.4 for a detailed explanation of this excess noise in the 2004 data.

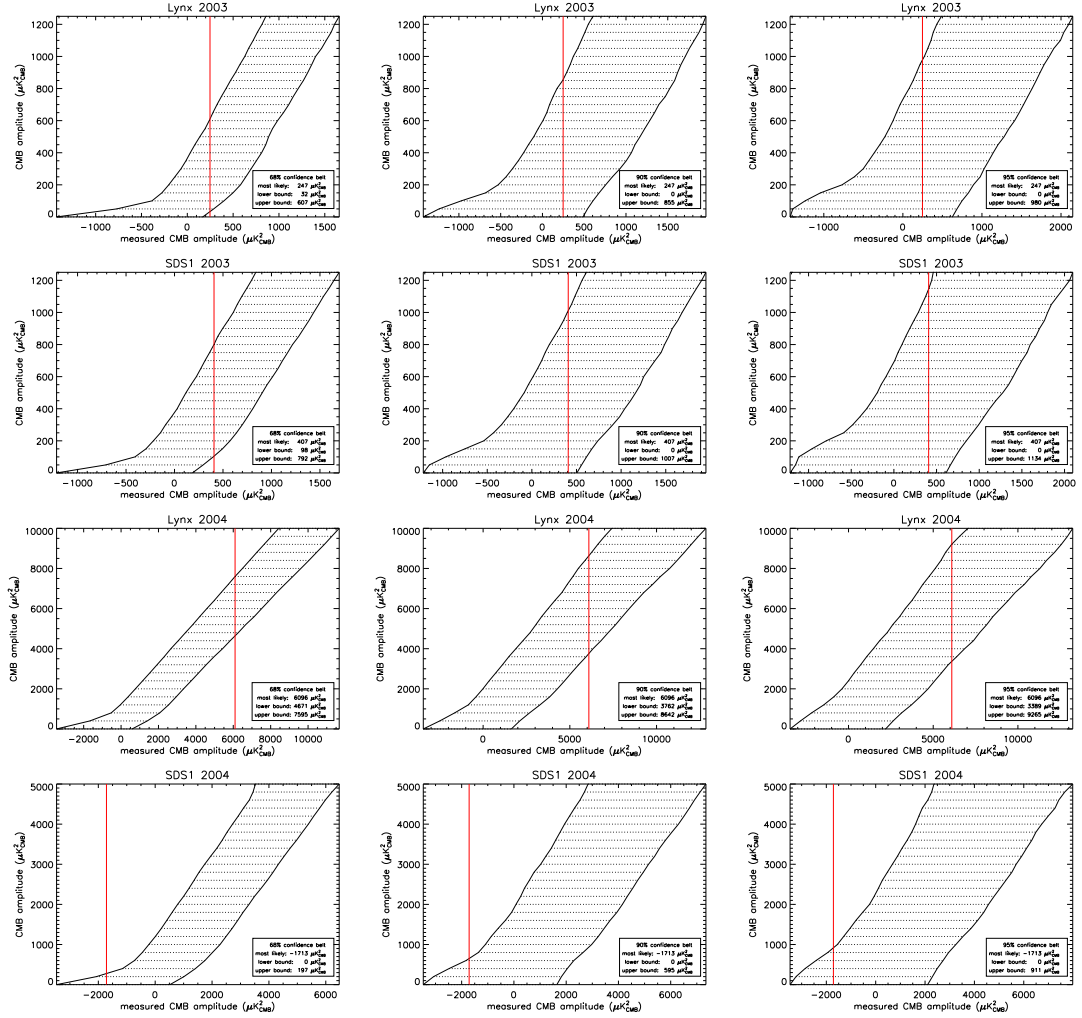


Figure 6.3: Confidence belts for the CMB amplitude for each science field for each observing season. The left row shows 68% confidence level belts, the middle row shows 90% confidence level belts, and the right row shows 95% confidence level belts. Overlaid in red on each plot is the most likely amplitude measured for each map. The upper and lower bounds of the confidence level can be determined from the intersection of this red line with the confidence belt.

allowed outcome is very small. Therefore, the 2004 SDS1 data is also inconsistent with the 2003 data, presumably for the same reason(s) that the 2004 Lynx data is inconsistent. Due to the higher noise level and larger amount of signal attenuation in the 2004 data, it is much less sensitive to the CMB signal than the 2003 data. See Figure 6.1. Even if the most likely amplitude in both 2004 data sets was $0 \mu\text{K}_{CMB}^2$, the upper limits on the CMB amplitude would drop by less than 5% compared to the upper limits found using only the 2003 data. Therefore, we have chosen to ignore the 2004 data in determining our final results.

To determine the confidence intervals for the full data set, we make a joint estimate of A using both the Lynx and SDS1 2003 data sets. The calculation was performed according to the same methods described in Section 6.1 for the single field/season data sets. A plot of the Bayesian likelihood, along with confidence belts computed using the Feldman and Cousins method are given in Figure 6.4. Uncertainties in our pointing model have already been included in these calculations, by an effective broadening of the Bolocam beam⁶. Our upper limits on the CMB amplitude are equal to 588, 755, and 828 μK_{CMB}^2 at confidence levels of 68%, 90%, and 95%.

To determine the effective angular scale of our CMB amplitude measurements we have computed our band power window function, W_ℓ^B/ℓ ,⁷ using the method given by Knox [71]. A plot of the peak normalized band power window function for the full 2003 data set is given in Figure 6.5. From this band power window function we have calculated an effective angular multipole for our data set, ℓ_{eff} , given by

$$\ell_{eff} = \frac{\sum_\ell \ell (W_\ell^B/\ell)}{\sum_\ell W_\ell^B/\ell}, \quad (6.4)$$

and equal to 5700. Additionally, the full-width half-maximum of the window function, FWHM_ℓ , is equal to 2800. A plot comparing our result to other measurements of the CMB on similar scales is shown in Figure 6.6.

⁶Uncertainties in the flux calibration have not been included here due to the standard convention. However, these uncertainties are included in our estimates of the SZE-induced anisotropies described in Section 6.3.

⁷This band power window function is defined such that $\langle C_B \rangle = \sum_\ell (W_\ell^B/\ell) C_\ell$, where $\langle C_B \rangle$ is the experimental band power measurement for the power spectrum, C_ℓ .

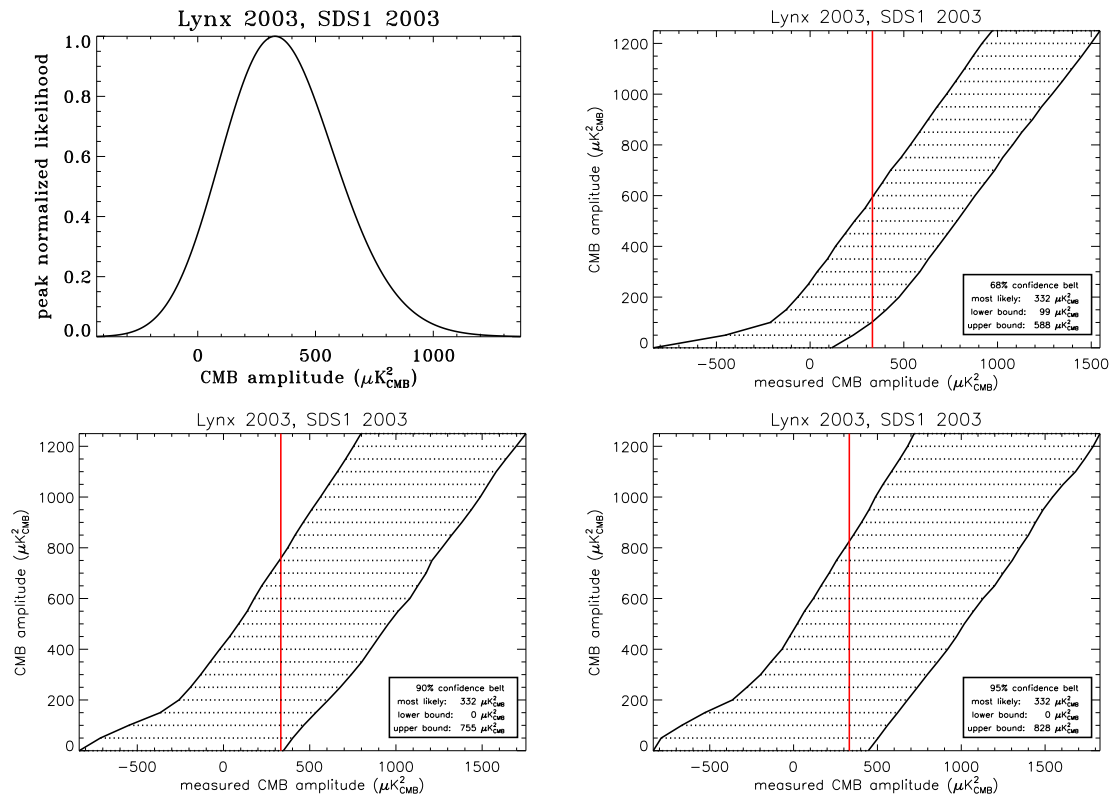


Figure 6.4: The top left plot shows the Bayesian likelihood for a range of CMB amplitudes for the full data set, which includes all of the observations made in 2003. The remaining three plots show the classical confidence belts for the full data sets, for confidence levels of 68%, 90%, and 95%.

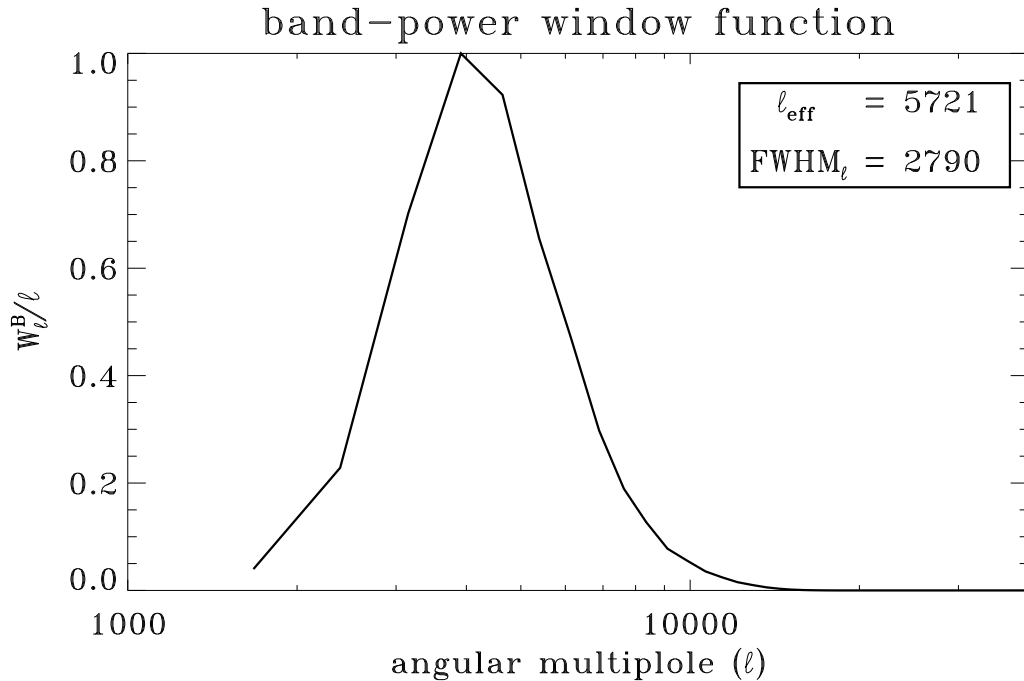


Figure 6.5: The band power window function for the full 2003 data set. We have arbitrarily peak normalized the window function.

6.3 SZE-Induced CMB Anisotropy Results

In order to determine the amplitude of the SZE-induced CMB power spectrum, we follow the same method described in Section 6.1 to determine the total amplitude of the CMB power spectrum. However, we now have to account for the signal from the primary CMB anisotropies. Following the notation from Section 6.1, the noise contributed to the map from the Bolocam system is given by $\mathcal{P}_{\vec{\nu}}$. Since the spectrum of the primary anisotropies in the CMB is well understood, we can calculate the expected noise from the primary CMB anisotropies. To calculate this noise we first create a simulated map of the primary CMB, assuming that the underlying distribution of $\vec{\nu}$ -space pixel values is Gaussian. This simulation is produced by drawing a value for each pixel, $\vec{\nu}$, from an underlying Gaussian distribution, then multiplying it by the best fit primary CMB spectrum given in Section 5.7.3. The PSD of this map is then multiplied by $W_{\vec{\nu}}B_{\vec{\nu}}$ and added to a jackknifed realization of our data, $x_{i,\vec{\nu}}$, to give $x_{i,\vec{\nu}}^{[SZE]}$. A different simulated map is generated for each jackknifed realization of the data to account for the cosmic variance in the CMB spectrum. These modified jackknifed realizations of the data can then be used to determine the expected PSD, $\mathcal{P}_{\vec{\nu}}^{[SZE]}$,

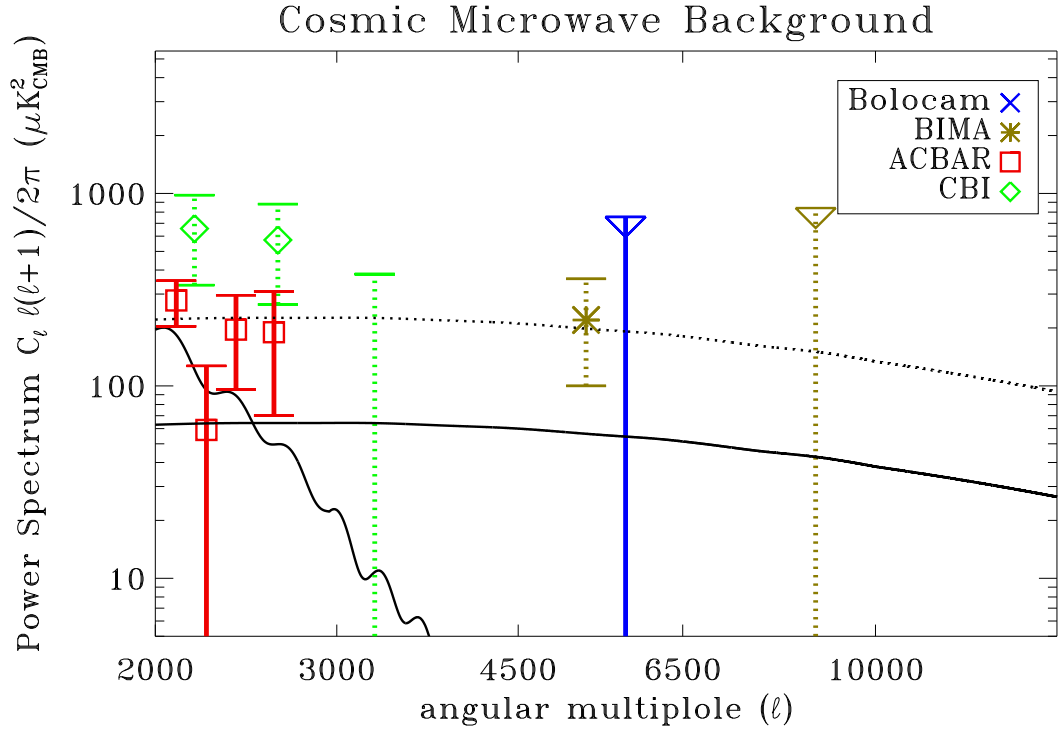


Figure 6.6: A plot of all of the current CMB anisotropy measurements above $\ell = 2000$. Solid lines represent observations made near 150 GHz, and dashed lines represent observations made near 30 GHz. The primary CMB anisotropies are represented by a solid black line on the left side of the plot, and the predicted SZE-induced CMB anisotropies are shown as solid (150 GHz) and dashed (30 GHz) black lines. The analytic model of Komatsu and Seljak [73], along with the best estimate of σ_8 from Dawson, et al. [37], were used to estimate the SZE-induced CMB anisotropies. All of the data is plotted with 1σ error bars, except for the Bolocam upper limit at $\ell = 5700$ and the BIMA upper limit at $\ell = 8748$, which are given as 90% and 95% confidence level upper limits, respectively. The ACBAR data was taken from Kuo, et al. [78], the BIMA data was taken from Dawson, et al. [37], and the CBI data was taken from Mason, et al. [88].

for the noise contributed by the Bolocam system and the primary CMB anisotropies.

Next, we select a model spectrum for the SZE anisotropies, $S_{\vec{\nu}}^{[SZE]}$. Using these new definitions, the Bayesian likelihood function in Equation F.8 can be written as

$$\log(\mathcal{L}) = \sum_{\vec{\nu}} \left(-\log(\mathcal{P}_{\vec{\nu}}^{[SZE]} + A^{[SZE]} S_{\vec{\nu}}^{[SZE]} B_{\vec{\nu}} W_{\vec{\nu}}) - \frac{x_{\vec{\nu}}^{[SZE]}}{\mathcal{P}_{\vec{\nu}}^{[SZE]} + A^{[SZE]} S_{\vec{\nu}}^{[SZE]} B_{\vec{\nu}} W_{\vec{\nu}}} \right),$$

where $A^{[SZE]}$ is the amplitude of the SZE-induced CMB anisotropies, and $B_{\vec{\nu}}$ and $W_{\vec{\nu}}$ give the transfer functions of our beam and data processing. At this point we can proceed exactly as in Section 6.1 to determine confidence intervals for $A^{[SZE]}$. As before, we create simulated SZE maps with an amplitude $A_{sim}^{[SZE]}$, add these to our jackknifed realizations after multiplying by $S_{\vec{\nu}}^{[SZE]} B_{\vec{\nu}} W_{\vec{\nu}}$, then use the ordering method developed by Feldman and Cousins [45] to determine the width of the confidence belt at $A_{sim}^{[SZE]}$. By repeating this procedure for a range of physically allowed values of $A_{sim}^{[SZE]}$ we can construct a full confidence belt that can be used to determine our confidence intervals. Examples of these confidence belts for a flat SZE spectrum are given in Figure 6.7.

Additionally, we need to account for the flux calibration uncertainty⁸. The uncertainty in the flux calibration model derived from point sources is 5.5%, and the uncertainty in the area of our beam is 3.1%. Therefore, the uncertainty in our surface brightness calibration is 6.3%. To determine the effect of this flux calibration error on our confidence intervals, we multiplied each simulated primary and SZE-induced CMB map by $\phi_i = 1 + y$, where y is drawn from a Gaussian distribution with a standard deviation equal to our flux uncertainty of 0.063. A different ϕ_i was generated for each simulated CMB map. This means that each simulated map has a different flux calibration, distributed according to our uncertainty in the calibration. New confidence belts were then calculated using the procedure described in Section 6.1⁹.

We have computed confidence intervals for two different SZE spectra: a flat spectrum, $S_{\vec{\nu}}^{[SZE]} = 2\pi/\ell(\ell + 1)$ for $\ell = 2\pi|\vec{\nu}|$ and the analytic spectrum calculated by Komatsu and Seljak [73]. The results from both of these spectra are similar, which is reasonable since the analytic spectrum is nearly flat at the scales we are most sensitive to ($4000 \lesssim \ell \lesssim 7000$).

⁸The flux calibration uncertainty was not included in our total anisotropy amplitude estimate because that is the standard convention.

⁹We have also determined the confidence intervals assuming that there is no uncertainty in the known flux of Uranus and Neptune (i.e., the only flux calibration uncertainties are due to our measurement errors and observational techniques). In this case, the flux calibration uncertainty is 3.5% instead of 6.3%.

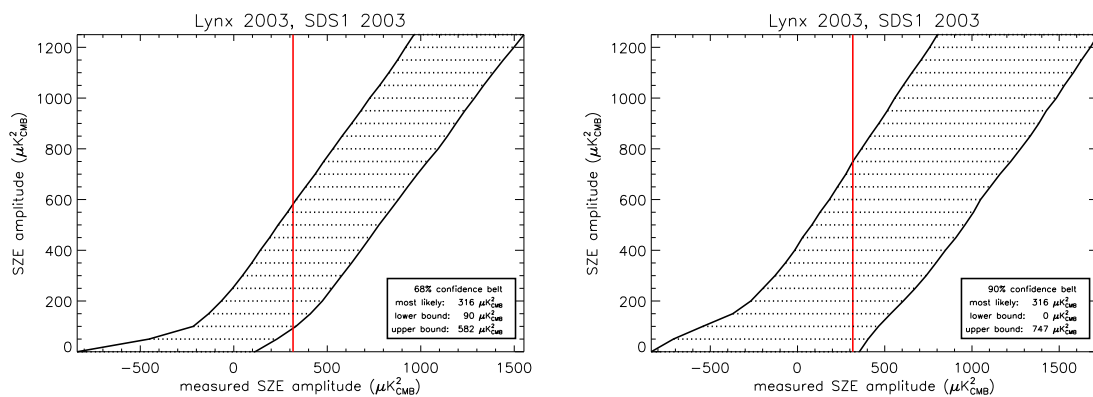


Figure 6.7: The left plot shows the 68% confidence belt for the full 2003 data set for an SZE-induced CMB amplitude for a flat SZE spectrum. The plot on the right shows the corresponding 90% confidence belt.

See Table 6.1. In addition to the analytic spectrum calculated by Komatsu and Seljak, several SZE power spectra have been determined via hydrodynamic simulations using either MMH (moving-mesh hydrodynamic) or SPH (smoothed-particle hydrodynamic) algorithms. Examples of MMH simulations can be found in Zhang, et al. (2002) [162], Seljak, et al. (2001) [126], Refregier, et al. (2000) [108], and Refregier and Teyssier [109]. Examples of SPH simulations can be found in da Silva, et al. (2001) [35] and Springel, et al. (2001) [134]. Since most of the simulated SZE spectra are approximately flat at the angular scales we are most sensitive to, we have not determined confidence levels using any of these spectra. See Figure 6.8.

6.4 Conclusions

Komatsu and Seljak determined that the amplitude of the SZE-induced CMB anisotropies scales according to $\sigma_8^7(\Omega_b h)^2$, and is relatively insensitive to all other cosmological parameters [73]. Using the results from WMAP, Boomerang, ACBAR, and other CMB experiments, the best fit values for σ_8 , Ω_b , and h are 0.78, 0.0425, and 0.729 [78]. These values produce a maximum SZE anisotropy amplitude of less than $10 \mu\text{K}_{CMB}^2$ at our band center of 143 GHz for the analytic Komatsu and Seljak spectrum. For comparison, the 90% confidence level upper limit on the analytic spectrum based on our data is $1093 \mu\text{K}_{CMB}^2$, including our flux calibration error. See Table 6.1. Based on this upper limit, assuming the scaling relation given by Komatsu and Seljak and holding all other parameters fixed, the corresponding

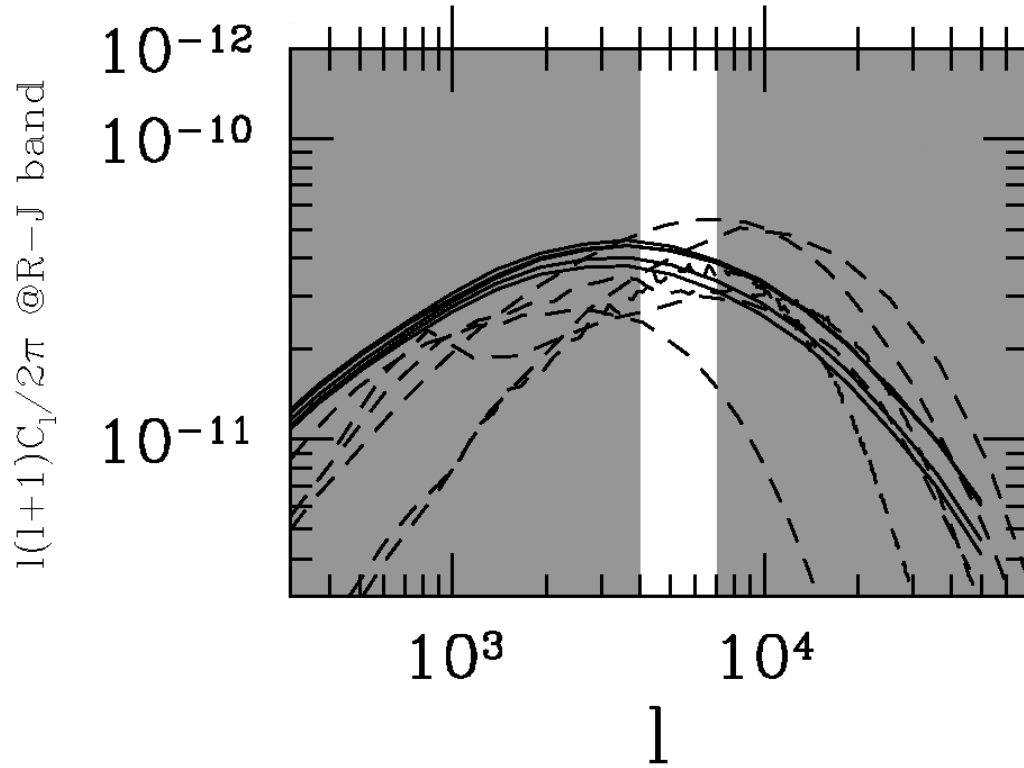


Figure 6.8: SZE spectra calculated from various MMH or SPH simulations (dashed lines) [35,108,109,126,134,162] and from the analytic model given by Komatsu and Seljak (solid lines) [73]. Each of the simulations was run with slightly different input parameters, and an analytic spectrum was calculated for each set of parameters. All of the spectra have been scaled by $\sigma_8^7(\Omega_b h)^2$, since this combination of parameters approximates the amplitude of the spectra to good precision. The highlighted region between $\ell = 4000$ and $\ell = 7000$ indicates the range of angular scales Bolocam is most sensitive to, and most of the spectra are reasonably flat within this region. Figure adapted from Komatsu and Seljak [73].

SZE-induced CMB anisotropy results

spectrum	flux uncertainty	68% CL interval	90% CL interval	95% CL interval
flat	0	$90 \leq 582 \mu\text{K}_{CMB}^2$	$0 \leq 747 \mu\text{K}_{CMB}^2$	$0 \leq 830 \mu\text{K}_{CMB}^2$
flat	3.1% (inst only)	$89 \leq 634 \mu\text{K}_{CMB}^2$	$0 \leq 794 \mu\text{K}_{CMB}^2$	$0 \leq 876 \mu\text{K}_{CMB}^2$
flat	6.3% (total)	$83 \leq 692 \mu\text{K}_{CMB}^2$	$0 \leq 956 \mu\text{K}_{CMB}^2$	$0 \leq 998 \mu\text{K}_{CMB}^2$
K-S	0	$89 \leq 625 \mu\text{K}_{CMB}^2$	$0 \leq 789 \mu\text{K}_{CMB}^2$	$0 \leq 881 \mu\text{K}_{CMB}^2$
K-S	3.1% (inst only)	$87 \leq 655 \mu\text{K}_{CMB}^2$	$0 \leq 853 \mu\text{K}_{CMB}^2$	$0 \leq 960 \mu\text{K}_{CMB}^2$
K-S	6.3% (total)	$84 \leq 842 \mu\text{K}_{CMB}^2$	$0 \leq 1093 \mu\text{K}_{CMB}^2$	$0 \leq 1143 \mu\text{K}_{CMB}^2$

Table 6.1: Confidence intervals for our estimate of the SZE-induced CMB anisotropy amplitude for both a flat SZE band power in \mathcal{C}_ℓ , and the SZE spectrum given by the analytic model of Komatsu and Seljak [73]. The limits for the analytic model refer to the peak amplitude of the SZE spectrum, and therefore make the upper limits for the analytic spectrum appear artificially high compared to the upper limits for the flat spectrum. The three rows for each spectrum give the upper limits for no uncertainty in our flux calibration, the 3.1% uncertainty in our flux calibration due to measurement error, and the 6.3% uncertainty in our flux calibration due to the combination of measurement error and uncertainty in the surface brightness of Uranus and Neptune.

90% confidence level upper limit on the three cosmological parameters is: $\sigma_8^7(\Omega_b h)^2 < 2.13$.

Individually, the best constraint can be placed on σ_8 since the amplitude depends most strongly on this parameter, with $\sigma_8 < 1.55$ at a confidence level of 90%.

Chapter 7 Other Bolocam Science

7.1 Surveys for Dusty Submillimeter Galaxies

Dusty submillimeter galaxies are high redshift, extremely luminous galaxies obscured by dust. Optical and ultraviolet radiation from young stars within the galaxy heat this dust, and thermal emission from the dust allows these galaxies to be detected at submillimeter wavelengths. The inferred formation rate of these young stars is very large, around 100 - 1000 $M_{\odot}\text{yr}^{-1}$ [16]. At these high star formation rates, all of the stars in a typical elliptical galaxy could be created on a time scale of 100 million years, so these dusty galaxies might be the progenitors of elliptical galaxies and spiral bulges [131, 140]. Therefore, knowledge of these dusty submillimeter galaxies will help provide a complete picture of galaxy formation.

Bolocam has been used at 1.1 mm to conduct two deep surveys for dusty submillimeter galaxies. One survey was conducted toward the Lockman Hole, covering $\gtrsim 300$ arcminutes² with an RMS per 30 arcsecond FWHM beam of 1.4 mJy [82]. The second survey was conducted towards the COSMOS field and covers $\simeq 1000$ arcminutes² with an RMS per 30 arcsec FWHM beam of 1.9 mJy [3]. In each survey approximately 15 sources were detected. See Figure 7.1. The inferred luminosities of these sources are $\gtrsim 10^{13} L_{\odot}$, implying star formation rates of several hundred M_{\odot} per year. Additionally, differential number counts have been calculated from these maps, with the best model from the Lockman Hole map¹ derived from a $P(D)$ analysis and given by $N_0 = 1595_{-238}^{+85} \text{ mJy}^{-1}\text{deg}^{-2}$ and $\delta = 2.7_{-0.15}^{+0.18}$ for a power law of the form $N(S) = N_0 S^{\delta}$ [87]. This $N(S)$ is a factor of 2 - 3 lower than the best fit model derived from MAMBO data at 1.2 mm [55] and the model in Blain, et al. [16] However, the MAMBO model is consistent with the Bolocam model given the flux calibration uncertainty of each data set, and the Bolocam model is consistent with the Blain model above the detection threshold in the Bolocam maps. See Figure 7.2.

¹The data from the COSMOS map is consistent with the model $N(S)$ derived from the Lockman Hole map.

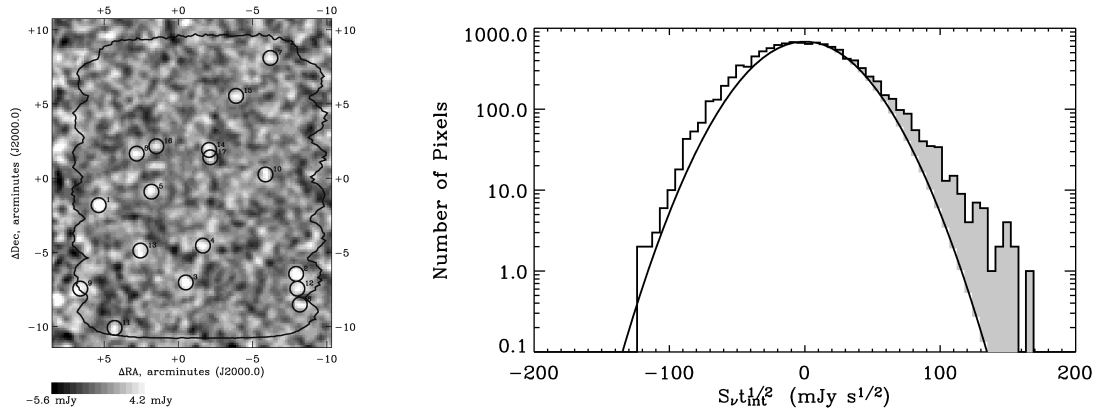


Figure 7.1: Left: The Bolocam map of the Lockman Hole, with the dusty submillimeter galaxy source detections circled. The uniform coverage region of the map is indicated by the solid black line. Right: A histogram of the pixel values in the map. The dashed line is a Gaussian fit of the noise determined from jackknifed realizations of the data, and the shaded region indicates the emission from galaxy candidates. Both plots have been taken from Laurent, et al. [82].

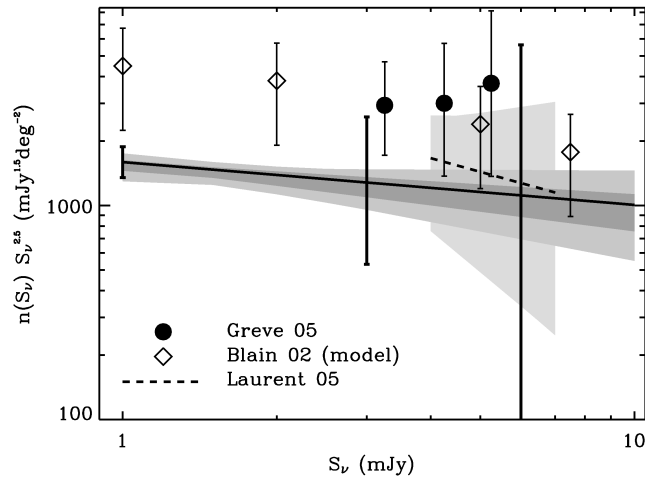


Figure 7.2: A model of the differential number counts of dusty submillimeter galaxies derived from the Bolocam Lockman Hole survey. The model is given by the solid black line, with 68% and 95% confidence limits given by the dark and light gray shaded areas. The solid circles represent the MAMBO data [55], and the open diamonds represent the model from Blain, et al. [16]. The dashed line represents the initial model derived from the Bolocam data in Laurent, et al. [82]. Figure taken from Maloney, et al. [87].

7.2 Molecular Cloud Surveys

Stars are born in molecular clouds, and the crucial step in this birth appears to be formation of dense cloud cores. Therefore, knowledge of these cores is an important step towards understanding both the efficiency and distribution of star formation [44]. These pre-stellar cores are cold, with temperatures near 10 K, so they are most easily seen at millimeter and submillimeter wavelengths. Bolocam was used to map 7.5 deg² of the Perseus cloud at 1.1 mm to an RMS of 15 mJy per beam [42], and 10.8 deg² of the Ophiuchus cloud at 1.1 mm to a non-uniform RMS of about 10 - 30 mJy per beam [158]. Approximately 60 new cores, among 122 total cores, were detected in Perseus with a 5σ mass threshold of $0.18 M_{\odot}$, and 44 cores were detected in Ophiuchus with masses as low as $0.24 M_{\odot}$. For each cloud the core mass function can be fit with a power law, and the slope of the power laws are slightly shallower than the initial mass function slope. Additionally, the total mass in these discrete cores is less than 5% of the total cloud mass, and most of the cloud contains no compact millimeter emission. Maps of the two clouds are shown in Figure 7.3.

7.3 Targeted Cluster Observations

Since November 2006, we have observed nine clusters and one blank test field at 150 GHz with Bolocam at the CSO, and each cluster has been observed for a total of approximately ten hours. We have been granted twenty nights per year for the next three years to continue this project, and we expect to image thirty more clusters assuming a weather-related observing efficiency of $\simeq 50\%$. We scanned the telescope in a Lissajous pattern, which was essentially 100% efficient mapping the center of the cluster, and 50% efficient at a radius of $\simeq 5$ arcminutes.² To remove the atmospheric noise from this data we have used the quadratic subtraction algorithm, masking off the data within 2 arcminutes of the cluster center as described in Section 5.3.1. This removal algorithm acts like a spatial high-pass filter on our data, with an effective length scale given by the eight arcmin diameter of the focal plane. From simulations, we estimate that the peak signal from a massive cluster is reduced by $\simeq 2/3$ due to our atmospheric noise removal. See Fig. 7.4. In the future we plan to use an iterative map-making procedure in order to recover more of the cluster flux.

²Bolocam must be scanned quickly in order to separate the astronomical signal from low-frequency atmospheric noise. However, if we raster scan across the cluster, then the observing efficiency is only 10 - 15% due to the time required to turn the telescope around between scans.

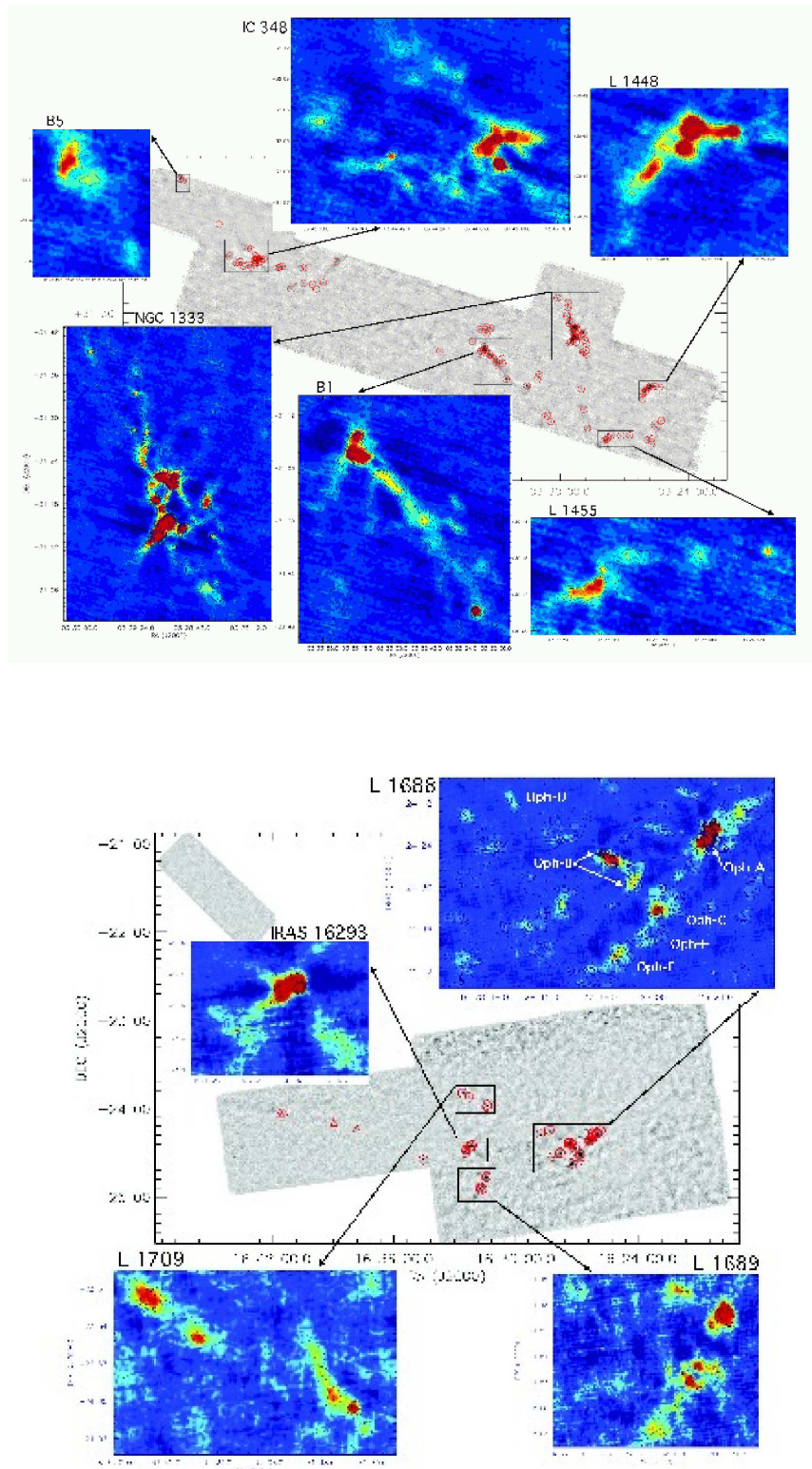


Figure 7.3: Maps of the Perseus (top) and Ophiuchus (bottom) molecular clouds made with Bolocam at 1.1 mm. The cores detected in each map are denoted by small red circles.

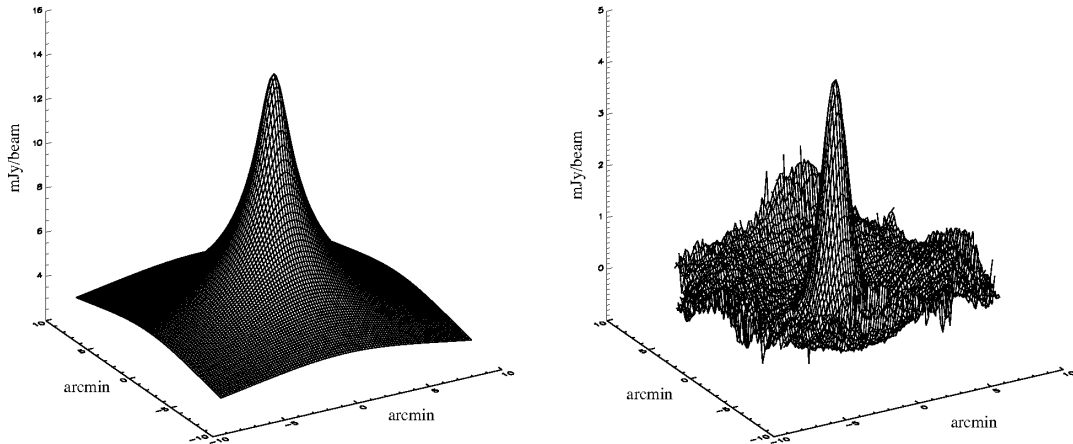


Figure 7.4: Left: Profile of a simulated cluster based on CL0016+1609. Note that the edge of the image, 10 arcmins from the center, has a brightness of around 5 mJy/beam or $50 \mu\text{K}_{CMB}$. Right: Image of the same cluster after applying our atmospheric noise removal algorithm. The peak height is reduced by a factor of $\simeq 3$, and the profile is narrowed.

However, the high-pass filter due to our atmospheric noise removal sets a fundamental limit on how much signal is attenuated; even if all of the signal on small scales is recovered the peak flux will still be reduced by a factor of $\simeq 1/3$.

To estimate the sensitivity of the maps, we have created jackknife maps, where a random half of the ten-minute-long observations are multiplied by -1. These jackknife maps are free from astronomical signal, but still maintain the noise properties of the original map under the assumption that the observations are uncorrelated. Our beam-smoothed maps have an RMS per 1.4 arcmin effective beam of $\simeq 15 - 25 \mu\text{K}_{CMB}$ (RMS in y of $5 - 10 \times 10^{-6}$), which corresponds to a signal-to-noise ratio of 10 - 15 for the typical maximum SZE decrement of $\simeq -200 \mu\text{K}_{CMB}$. See Fig. 7.5. These decrements correspond to $y_0 \simeq 75 \times 10^{-6}$, which is a factor of $\simeq 3$ below the accepted values of y_0 for the clusters we have observed, as expected from our simulations to calculate signal attenuation. For comparison, the signal-to-noise ratio of these images is comparable to the best SZE images produced to date, made with the OVRO/BIMA interferometers at 30 GHz [107]. Before we begin a rigorous analysis of the cluster images, we still need to develop a way to remove the scan-synchronous artifacts that appear with an amplitude of $\simeq 30\%$ of the cluster peak amplitude.

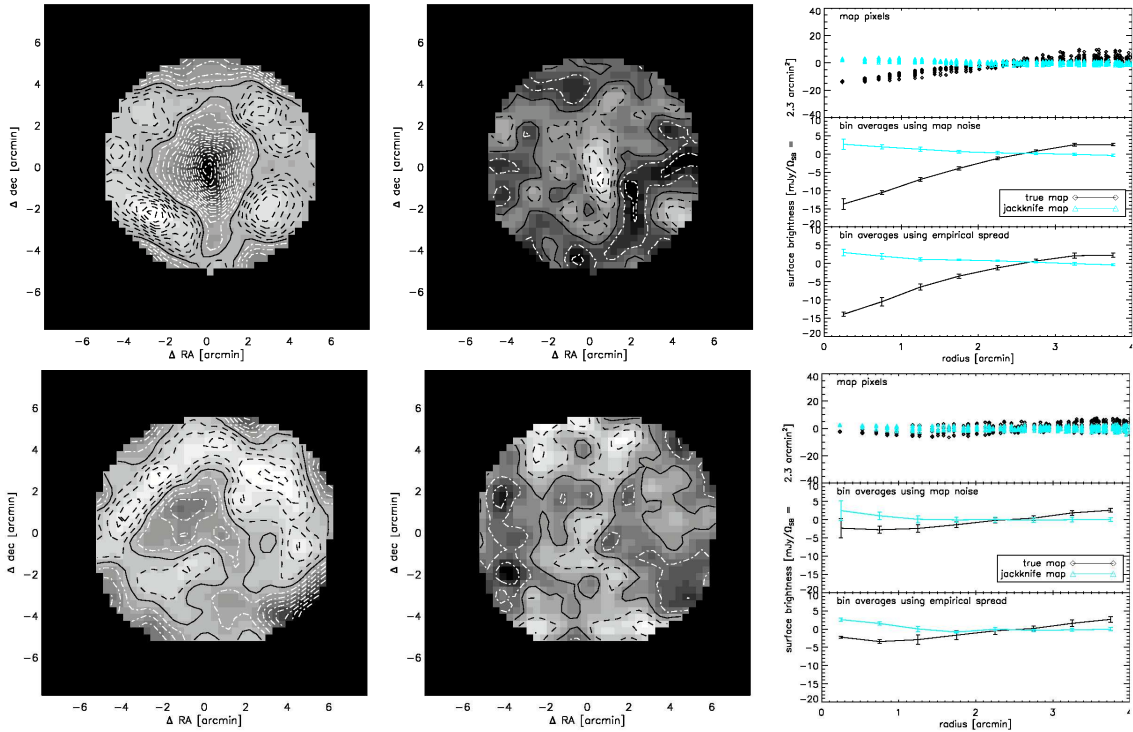


Figure 7.5: Top: Abell 697. Bottom: SDS1 (blank test field). Left: Beam-smoothed image of the cluster/test field. Center: Beam-smoothed jackknife image of the cluster/test field. The white dashed contours correspond to a S/N of -1, the black dashed contours correspond to a S/N of +1. The noise level is similar in both images, and the contours correspond to $\simeq 15 \mu K_{CMB}$. Right: Radial plots, with black for the image and blue for the jackknife image. The top plot shows a point for each map-pixel, the middle plot shows S/N weighted bin averages, and the bottom plot shows direct bin averages.

Bibliography

- [1] P. A. R. Ade, G. Pisano, C. Tucker, and S. Weaver. A review of metal mesh filters. In *Millimeter and Submillimeter Detectors and Instrumentation for Astronomy III*. J. Zmuidzinas, W. S. Holland, S. Withington, and W. D. Duncan, Eds. *Proceedings of the SPIE.*, volume 6275, page 62750U. Presented at the Society of Photo-Optical Instrumentation Engineers (SPIE) Conference, July 2006.
- [2] J. E. Aguirre. *Properties of astrophysical submillimeter emission near the South Celestial Pole from the TopHat telescope*. PhD thesis, University of Chicago, 2003.
- [3] J. E. Aguirre, J. A. Schlaerth, J. Glenn, P. A. R. Ade, H. Aussel, F. Bertoldi, J. Bird, A. W. Blain, C. Borys, C. L. Carilli, L.-H. Chien, S. R. Golwala, T. R. Greve, D. J. Haig, L. J. Hainline, O. Ilbert, G. T. Laurent, C.-J. Ma, P. R. Maloney, P. D. Mauskopf, H. T. Nguyen, P. Rossinot, D. B. Sanders, J. Sayers, M. Salvato, E. Schinnerer, K. Sheth, V. Smolčić, and P. N. Stover. The Bolocam 1.1 mm Survey in the COSMOS Field. I. First Results. for *The Astrophysical Journal Supplement Series* COSMOS Special Issue, 2007.
- [4] D. S. Akerib, M. S. Armel-Funkhouser, M. J. Attisha, C. N. Bailey, L. Baudis, D. A. Bauer, P. L. Brink, R. Bunker, B. Cabrera, D. O. Caldwell, C. L. Chang, M. B. Crisler, P. Cushman, M. Daal, R. Dixon, M. R. Dragowsky, D. D. Driscoll, L. Duong, R. Ferril, J. Filippini, R. J. Gaitskell, R. Hennings-Yeomans, D. Holmgren, M. E. Huber, S. Kamat, A. Lu, R. Mahapatra, V. Mandic, J. M. Martinis, P. Meunier, N. Mirabolfathi, H. Nelson, R. Nelson, R. W. Ogburn, T. A. Perera, M. C. Issac, E. Ramberg, W. Rau, A. Reisetter, R. R. Ross, T. Saab, B. Sadoulet, J. Sander, C. Savage, R. W. Schnee, D. N. Seitz, B. Serfass, K. M. Sundqvist, J.-P. F. Thompson, G. Wang, S. Yellin, and B. A. Young. Exclusion limits on the WIMP-nucleon cross section from the first run of the Cryogenic Dark Matter Search in the Soudan Underground Laboratory. *Physics Review D*, 72(5):052009, September 2005.
- [5] R. A. Alpher, H. Bethe, and G. Gamow. The Origin of Chemical Elements. *Physical Review*, 73:803–804, April 1948.

- [6] Ami Collaboration, R. Barker, P. Biddulph, D. Bly, R. Boysen, A. Brown, C. Clementson, M. Crofts, T. Culverhouse, J. Czeres, R. Dace, R. D'Alessandro, P. Doherty, P. Duffett-Smith, K. Duggan, J. Ely, M. Felvus, W. Flynn, J. Geisbüsch, K. Grainge, W. Grainger, D. Hammet, R. Hills, M. Hobson, C. Holler, R. Jilley, M. E. Jones, T. Kaneko, R. Kneissl, K. Lancaster, A. Lasenby, P. Marshall, F. Newton, O. Norris, I. Northrop, G. Pooley, V. Quy, R. D. E. Saunders, A. Scaife, J. Schofield, P. Scott, C. Shaw, A. C. Taylor, D. Titterington, M. Velić, E. Waldram, S. West, B. Wood, G. Yassin, and J. Zwart. High-significance Sunyaev-Zel'dovich measurement: Abell 1914 seen with the Arcminute Microkelvin Imager. *Monthly Notices of the Royal Astronomical Society*, 369:L1–L4, June 2006.
- [7] APEX-SZ website (available at <http://bolo.berkeley.edu/apexsz/index.html>).
- [8] P. Astier, J. Guy, N. Regnault, R. Pain, E. Aubourg, D. Balam, S. Basa, R. G. Carlberg, S. Fabbro, D. Fouchez, I. M. Hook, D. A. Howell, H. Lafoux, J. D. Neill, N. Palanque-Delabrouille, K. Perrett, C. J. Pritchett, J. Rich, M. Sullivan, R. Taillet, G. Aldering, P. Antilogus, V. Arsenijevic, C. Balland, S. Baumont, J. Bronder, H. Courtois, R. S. Ellis, M. Filiol, A. C. Gonçalves, A. Goobar, D. Guide, D. Hardin, V. Lusser, C. Lidman, R. McMahon, M. Mouchet, A. Mourao, S. Perlmutter, P. Ripoche, C. Tao, and N. Walton. The Supernova Legacy Survey: measurement of Ω_M , Ω_Λ and w from the first year data set. *Astronomy & Astrophysics*, 447:31–48, February 2006.
- [9] C. L. Bennett, R. S. Hill, G. Hinshaw, M. R. Nolta, N. Odegard, L. Page, D. N. Spergel, J. L. Weiland, E. L. Wright, M. Halpern, N. Jarosik, A. Kogut, M. Limon, S. S. Meyer, G. S. Tucker, and E. Wollack. First-Year Wilkinson Microwave Anisotropy Probe (WMAP) Observations: Foreground Emission. *The Astrophysical Journal Supplement Series*, 148:97–117, September 2003.
- [10] B. A. Benson. *Spectral Measurements of the Sunyaev-Zel'dovich Effect*. PhD thesis, Stanford, 2004.
- [11] B. A. Benson, S. E. Church, P. A. R. Ade, J. J. Bock, K. M. Ganga, C. N. Henson, and K. L. Thompson. Measurements of Sunyaev-Zel'dovich Effect Scaling Relations for Clusters of Galaxies. *The Astrophysical Journal*, 617:829–846, December 2004.

- [12] B. A. Benson, S. E. Church, P. A. R. Ade, J. J. Bock, K. M. Ganga, J. R. Hinderks, P. D. Mauskopf, B. Philhour, M. C. Runyan, and K. L. Thompson. Peculiar Velocity Limits from Measurements of the Sunyaev-Zeldovich Effect in Six Clusters of Galaxies. *The Astrophysical Journal*, 592:674–691, August 2003.
- [13] R. S. Bhatia, S. T. Chase, S. F. Edgington, J. Glenn, W. C. Jones, A. E. Lange, B. Maffei, A. K. Mainzer, P. D. Mauskopf, B. J. Philhour, and B. K. Rownd. A three-stage helium sorption refrigerator for cooling of infrared detectors to 280 mK. *Cryogenics*, 40:685–691, 2000.
- [14] R. S. Bhatia, S. T. Chase, W. C. Jones, B. G. Keating, A. E. Lange, P. V. Mason, B. J. Philhour, and G. Sirbi. Closed cycle cooling of infrared detectors to 250 mK. *Cryogenics*, 42:113–122, 2002.
- [15] M. Birkinshaw. The Sunyaev-Zel’dovich effect. *Physics Reports*, 310:97–195, March 1999.
- [16] A. W. Blain, I. Smail, R. J. Ivison, J.-P. Kneib, and D. T. Frayer. Submillimeter galaxies. *Physics Reports*, 369:111–176, October 2002.
- [17] J. J. Bock. *Rocket-borne observation of singly ionized carbon 158 m emission from the diffuse interstellar medium*. PhD thesis, University of California, Berkeley, 1994.
- [18] J. J. Bock, J. Glenn, S. M. Grannan, K. D. Irwin, A. E. Lange, H. G. Leduc, and A. D. Turner. Silicon nitride micromesh bolometer arrays for SPIRE. In *Advanced Technology MMW, Radio, and Terahertz Telescopes*, T. G. Phillips, Ed., volume 3357, pages 297–304. Presented at the Society of Photo-Optical Instrumentation Engineers (SPIE) Conference, July 1998.
- [19] J. J. Bock, A. E. Lange, M. K. Parikh, and M. L. Fischer. Emissivity measurements of reflective surfaces at near-millimeter wavelengths. *Applied Optics*, 34:4812–4816, August 1995.
- [20] M. Bonamente, M. K. Joy, S. J. LaRoque, J. E. Carlstrom, E. D. Reese, and K. S. Dawson. Determination of the Cosmic Distance Scale from Sunyaev-Zel’dovich Effect and Chandra X-Ray Measurements of High-Redshift Galaxy Clusters. *The Astrophysical Journal*, 647:25–54, August 2006.

- [21] J. R. Bond, C. R. Contaldi, U.-L. Pen, D. Pogosyan, S. Prunet, M. I. Ruetalo, J. W. Wadsley, P. Zhang, B. S. Mason, S. T. Myers, T. J. Pearson, A. C. S. Readhead, J. L. Sievers, and P. S. Udomprasert. The Sunyaev-Zel'dovich Effect in CMB-calibrated Theories Applied to the Cosmic Background Imager Anisotropy Power at $l > 2000$. *The Astrophysical Journal*, 626:12–30, June 2005.
- [22] C. Borys, S. Chapman, M. Halpern, and D. Scott. The Hubble Deep Field North SCUBA Super-map - I. Submillimetre maps, sources and number counts. *Monthly Notices of the Royal Astronomical Society*, 344:385–398, September 2003.
- [23] M. Bridges, A. N. Lasenby, and M. P. Hobson. WMAP 3-yr primordial power spectrum. *Monthly Notices of the Royal Astronomical Society*, 381:68–74, October 2007.
- [24] R. S. Bussmann, W. L. Holzapfel, and C. L. Kuo. Millimeter Wavelength Brightness Fluctuations of the Atmosphere above the South Pole. *The Astrophysical Journal*, 622:1343–1355, April 2005.
- [25] J. E. Carlstrom, G. P. Holder, and E. D. Reese. Cosmology with the Sunyaev-Zel'dovich Effect. *Annual Review of Astronomy and Astrophysics*, 40:643–680, 2002.
- [26] J. E. Carlstrom, M. Joy, L. Grego, G. Holder, W. L. Holzapfel, S. LaRoque, J. J. Mohr, and E. D. Reese. The Sunyaev-Zel'dovich Effect: Results and Future Prospects. *ArXiv Astrophysics e-prints*, March 2001.
- [27] R. A. Chamberlin. *Notes on the Tau sky monitors* (available at <http://www.cso.caltech.edu/taumeter.txt>).
- [28] S. E. Church. Predicting residual levels of atmospheric sky noise in ground based observations of the cosmic microwave background radiation. *Monthly Notices of the Royal Astronomical Society*, 272:551–569, February 1995.
- [29] CMBFAST Online (available at http://lambda.gsfc.nasa.gov/toolbox/tb_cmbfast_ov.cfm).
- [30] S. Cole, W. J. Percival, J. A. Peacock, P. Norberg, C. M. Baugh, C. S. Frenk, I. Baldry, J. Bland-Hawthorn, T. Bridges, R. Cannon, M. Colless, C. Collins, W. Couch, N. J. G. Cross, G. Dalton, V. R. Eke, R. De Propris, S. P. Driver, G. Efstathiou, R. S. Ellis, K. Glazebrook, C. Jackson, A. Jenkins, O. Lahav, I. Lewis, S. Lumsden, S. Maddox, D. Madgwick, B. A. Peterson, W. Sutherland, and K. Taylor. The 2dF Galaxy

Redshift Survey: power-spectrum analysis of the final data set and cosmological implications. *Monthly Notices of the Royal Astronomical Society*, 362:505–534, September 2005.

- [31] K. Coppin, E. L. Chapin, A. M. J. Mortier, S. E. Scott, C. Borys, J. S. Dunlop, M. Halpern, D. H. Hughes, A. Pope, D. Scott, S. Serjeant, J. Wagg, D. M. Alexander, O. Almaini, I. Aretxaga, T. Babbedge, P. N. Best, A. Blain, S. Chapman, D. L. Clements, M. Crawford, L. Dunne, S. A. Eales, A. C. Edge, D. Farrah, E. Gaztañaga, W. K. Gear, G. L. Granato, T. R. Greve, M. Fox, R. J. Ivison, M. J. Jarvis, T. Jenness, C. Lacey, K. Lepage, R. G. Mann, G. Marsden, A. Martinez-Sansigre, S. Oliver, M. J. Page, J. A. Peacock, C. P. Pearson, W. J. Percival, R. S. Priddey, S. Rawlings, M. Rowan-Robinson, R. S. Savage, M. Seigar, K. Sekiguchi, L. Silva, C. Simpson, I. Smail, J. A. Stevens, T. Takagi, M. Vaccari, E. van Kampen, and C. J. Willott. The SCUBA Half-Degree Extragalactic Survey - II. Submillimetre maps, catalogue and number counts. *Monthly Notices of the Royal Astronomical Society*, 372:1621–1652, November 2006.
- [32] G. Cotter, H. J. Buttery, R. Das, M. E. Jones, K. Grainge, G. G. Pooley, and R. Saunders. Observations of the Sunyaev-Zel’dovich effect in the $z=0.78$ cluster MS 1137.5+6625. *Monthly Notices of the Royal Astronomical Society*, 334:323–326, August 2002.
- [33] B. P. Crill, P. A. R. Ade, D. R. Artusa, R. S. Bhatia, J. J. Bock, A. Boscaleri, P. Cardoni, S. E. Church, K. Coble, P. de Bernardis, G. de Troia, P. Farese, K. M. Ganga, M. Giacometti, C. V. Haynes, E. Hivon, V. V. Hristov, A. Iacoangeli, W. C. Jones, A. E. Lange, L. Martinis, S. Masi, P. V. Mason, P. D. Mauskopf, L. Miglio, T. Montroy, C. B. Netterfield, C. G. Paine, E. Pascale, F. Piacentini, G. Polenta, F. Pongetti, G. Romeo, J. E. Ruhl, F. Scaramuzzi, D. Sforna, and A. D. Turner. BOOMERANG: A Balloon-borne Millimeter-Wave Telescope and Total Power Receiver for Mapping Anisotropy in the Cosmic Microwave Background. *The Astrophysical Journal Supplement Series*, 148:527–541, October 2003.
- [34] CSO Atmospheric Transmission Interactive Plotter (available at <http://www.submm.caltech.edu/cso/weather/atplot/shtml>).

- [35] A. C. da Silva, S. T. Kay, A. R. Liddle, P. A. Thomas, F. R. Pearce, and D. Barbosa. The Impact of Cooling and Preheating on the Sunyaev-Zeldovich Effect. *The Astrophysical Journal*, 561:L15–L18, November 2001.
- [36] L. Danese, A. Franceschini, L. Toffolatti, and G. de Zotti. Interpretation of deep counts of radio sources. *The Astrophysical Journal*, 318:L15–L20, July 1987.
- [37] K. S. Dawson, W. L. Holzapfel, J. E. Carlstrom, M. Joy, and S. J. LaRoque. Final Results from the BIMA CMB Anisotropy Survey and Search for a Signature of the Sunyaev-Zel'dovich Effect. *The Astrophysical Journal*, 647:13–24, August 2006.
- [38] K. S. Dawson, W. L. Holzapfel, J. E. Carlstrom, M. Joy, S. J. LaRoque, A. D. Miller, and D. Nagai. Measurement of Arcminute-Scale Cosmic Microwave Background Anisotropy with the Berkeley-Illinois-Maryland Association Array. *The Astrophysical Journal*, 581:86–95, December 2002.
- [39] P. de Bernardis, P. A. R. Ade, J. J. Bock, J. R. Bond, J. Borrill, A. Boscaleri, K. Coble, B. P. Crill, G. De Gasperis, P. C. Farese, P. G. Ferreira, K. Ganga, M. Giacometti, E. Hivon, V. V. Hristov, A. Iacoangeli, A. H. Jaffe, A. E. Lange, L. Martinis, S. Masi, P. V. Mason, P. D. Mauskopf, A. Melchiorri, L. Miglio, T. Montroy, C. B. Netterfield, E. Pascale, F. Piacentini, D. Pogosyan, S. Prunet, S. Rao, G. Romeo, J. E. Ruhl, F. Scaramuzzi, D. Sforna, and N. Vittorio. A flat Universe from high-resolution maps of the cosmic microwave background radiation. *Nature*, 404:955–959, April 2000.
- [40] DIRBE 100 μm full sky maps (available at <http://astro.berkeley.edu/marc/dust/data/data.html>).
- [41] C. D. Dowell, C. A. Allen, R. S. Babu, M. M. Freund, M. Gardner, J. Groseth, M. D. Jhabvala, A. Kovacs, D. C. Lis, S. H. Moseley, Jr., T. G. Phillips, R. F. Silverberg, G. M. Voellmer, and H. Yoshida. SHARC II: a Caltech submillimeter observatory facility camera with 384 pixels. In *Millimeter and Submillimeter Detectors for Astronomy*. T. G. Phillips and J. Zmuidzinas, Eds., volume 4855, pages 73–87. Presented at the Society of Photo-Optical Instrumentation Engineers (SPIE) Conference, February 2003.

- [42] M. L. Enoch, K. E. Young, J. Glenn, N. J. Evans, II, S. Golwala, A. I. Sargent, P. Harvey, J. Aguirre, A. Goldin, D. Haig, T. L. Huard, A. Lange, G. Laurent, P. Maloney, P. Maukopf, P. Rossinot, and J. Sayers. Bolocam Survey for 1.1 mm Dust Continuum Emission in the c2d Legacy Clouds. I. Perseus. *The Astrophysical Journal*, 638:293–313, February 2006.
- [43] S. Ettori, K. Dolag, S. Borgani, and G. Murante. The baryon fraction in hydrodynamical simulations of galaxy clusters. *Monthly Notices of the Royal Astronomical Society*, 365:1021–1030, January 2006.
- [44] N. J. Evans, II. Physical Conditions in Regions of Star Formation. *Annual Review of Astronomy and Astrophysics*, 37:311–362, 1999.
- [45] G. J. Feldman and R. D. Cousins. Unified approach to the classical statistical analysis of small signals. *Physics Review D*, 57:3873–3889, April 1998.
- [46] D. P. Finkbeiner, M. Davis, and D. J. Schlegel. Extrapolation of Galactic Dust Emission at 100 Microns to Cosmic Microwave Background Radiation Frequencies Using FIRAS. *The Astrophysical Journal*, 524:867–886, October 1999.
- [47] W. L. Freedman, B. F. Madore, B. K. Gibson, L. Ferrarese, D. D. Kelson, S. Sakai, J. R. Mould, R. C. Kennicutt, Jr., H. C. Ford, J. A. Graham, J. P. Huchra, S. M. G. Hughes, G. D. Illingworth, L. M. Macri, and P. B. Stetson. Final Results from the Hubble Space Telescope Key Project to Measure the Hubble Constant. *The Astrophysical Journal*, 553:47–72, May 2001.
- [48] W. K. Gear, J. A. Stevens, D. H. Hughes, S. J. Litchfield, E. I. Robson, H. Terasranta, E. Valtaoja, H. Steppe, M. F. Aller, and H. D. Aller. A Comparison of the Radio / Submillimetre Spectra of BL-Lacertae Objects and Flat Spectrum Radio Quasars. *Monthly Notices of the Royal Astronomical Society*, 267:167, March 1994.
- [49] J. Glenn, P. A. R. Ade, M. Amarie, J. J. Bock, S. F. Edgington, A. Goldin, S. Golwala, D. Haig, A. E. Lange, G. Laurent, P. D. Maukopf, M. Yun, and H. Nguyen. Current status of Bolocam: a large-format millimeter-wave bolometer camera. In *Millimeter and Submillimeter Detectors for Astronomy*. T. G. Phillips, and J. Zmuidzinas, Eds.,

volume 4855, pages 30–40. Presented at the Society of Photo-Optical Instrumentation Engineers (SPIE) Conference, February 2003.

- [50] J. Glenn, J. J. Bock, G. Chattopadhyay, S. F. Edgington, A. E. Lange, J. Zmuidzinas, P. D. Mauskopf, B. Rownd, L. Yuen, and P. A. Ade. Bolocam: a millimeter-wave bolometric camera. In *Advanced Technology MMW, Radio, and Terahertz Telescopes*. T. G. Phillips, Ed., volume 3357, pages 326–334. Presented at the Society of Photo-Optical Instrumentation Engineers (SPIE) Conference, July 1998.
- [51] J. Glenn, G. Chattopadhyay, S. F. Edgington, A. E. Lange, J. J. Bock, P. D. Mauskopf, and A. T. Lee. Numerical optimization of integrating cavities for diffraction-limited millimeter-wave bolometer arrays. *Applied Optics*, 41:136–142, January 2002.
- [52] A. B. Goldin, M. S. Kowitt, E. S. Cheng, D. A. Cottingham, D. J. Fixsen, C. A. Inman, S. S. Meyer, J. L. Puchalla, J. E. Ruhl, and R. F. Silverberg. Whole-Disk Observations of Jupiter, Saturn, and Mars in Millimeter/Submillimeter Bands. *The Astrophysical Journal*, 488:L161, October 1997.
- [53] S. Golwala. *Internal memo*.
- [54] A. M. Green. Determining the weakly interacting massive particles mass using direct detection experiments. *Journal of Cosmology and Astro-Particle Physics*, 8:22–+, August 2007.
- [55] T. R. Greve, R. J. Ivison, F. Bertoldi, J. A. Stevens, J. S. Dunlop, D. Lutz, and C. L. Carilli. A 1200- μm MAMBO survey of ELAISN2 and the Lockman Hole - I. Maps, sources and number counts. *Monthly Notices of the Royal Astronomical Society*, 354:779–797, November 2004.
- [56] M. J. Griffin, P. A. R. Ade, G. S. Orton, E. I. Robson, W. K. Gear, I. G. Nolt, and J. V. Radostitz. Submillimeter and millimeter observations of Jupiter. *Icarus*, 65:244–256, March 1986.
- [57] M. J. Griffin and G. S. Orton. The near-millimeter brightness temperature spectra of Uranus and Neptune. *Icarus*, 105:537, October 1993.
- [58] A. H. Guth. Inflationary universe: A possible solution to the horizon and flatness problems. *Physics Review D*, 23:347–356, January 1981.

- [59] D. J. Haig, P. A. R. Ade, J. E. Aguirre, J. J. Bock, S. F. Edgington, M. L. Enoch, J. Glenn, A. Goldin, S. Golwala, K. Heng, G. Laurent, P. R. Maloney, P. D. Mauskopf, P. Rossinot, J. Sayers, P. Stover, and C. Tucker. Bolocam: status and observations. In *Millimeter and Submillimeter Detectors for Astronomy II*. J. Zmuidzinas, W. S. Holland, and S. Withington, Eds., volume 5498, pages 78–94. Presented at the Society of Photo-Optical Instrumentation Engineers (SPIE) Conference, October 2004.
- [60] N. W. Halverson, E. M. Leitch, C. Pryke, J. Kovac, J. E. Carlstrom, W. L. Holzapfel, M. Dragovan, J. K. Cartwright, B. S. Mason, S. Padin, T. J. Pearson, A. C. S. Readhead, and M. C. Shepherd. Degree Angular Scale Interferometer First Results: A Measurement of the Cosmic Microwave Background Angular Power Spectrum. *The Astrophysical Journal*, 568:38–45, March 2002.
- [61] S. Hanany, P. Ade, A. Balbi, J. Bock, J. Borrill, A. Boscaleri, P. de Bernardis, P. G. Ferreira, V. V. Hristov, A. H. Jaffe, A. E. Lange, A. T. Lee, P. D. Mauskopf, C. B. Netterfield, S. Oh, E. Pascale, B. Rabbii, P. L. Richards, G. F. Smoot, R. Stompor, C. D. Winant, and J. H. P. Wu. MAXIMA-1: A Measurement of the Cosmic Microwave Background Anisotropy on Angular Scales of 10^{-5} deg. *The Astrophysical Journal*, 545:L5–L9, December 2000.
- [62] E. R. Harrison. Fluctuations at the threshold of classical cosmology. *Physics Review D*, 1:2726–2730, 1970.
- [63] G. Hinshaw, M. R. Nolta, C. L. Bennett, R. Bean, O. Doré, M. R. Greason, M. Halpern, R. S. Hill, N. Jarosik, A. Kogut, E. Komatsu, M. Limon, N. Odegard, S. S. Meyer, L. Page, H. V. Peiris, D. N. Spergel, G. S. Tucker, L. Verde, J. L. Weiland, E. Wollack, and E. L. Wright. Three-Year Wilkinson Microwave Anisotropy Probe (WMAP) Observations: Temperature Analysis. *The Astrophysical Journal Supplement Series*, 170:288–334, June 2007.
- [64] W. S. Holland, E. I. Robson, W. K. Gear, C. R. Cunningham, J. F. Lightfoot, T. Jenness, R. J. Ivison, J. A. Stevens, P. A. R. Ade, M. J. Griffin, W. D. Duncan, J. A. Murphy, and D. A. Naylor. SCUBA: a common-user submillimetre camera operating on the James Clerk Maxwell Telescope. *Monthly Notices of the Royal Astronomical Society*, 303:659–672, March 1999.

- [65] F. Hoyle and R. J. Tayler. The Mystery of the Cosmic Helium Abundance. *Nature*, 203:1108, 1964.
- [66] E. Hubble. A Relation between Distance and Radial Velocity among Extra-Galactic Nebulae. *Proceedings of the National Academy of Science*, 15:168–173, March 1929.
- [67] N. Itoh, Y. Kohyama, and S. Nozawa. Relativistic Corrections to the Sunyaev-Zeldovich Effect for Clusters of Galaxies. *The Astrophysical Journal*, 502:7, July 1998.
- [68] JCMT Planet Flux Calculator (available at <http://www.jach.hawaii.edu/jacbin/planetflux.pl>).
- [69] W. C. Jones, P. A. R. Ade, J. J. Bock, J. R. Bond, J. Borrill, A. Boscaleri, P. Cabella, C. R. Contaldi, B. P. Crill, P. de Bernardis, G. De Gasperis, A. de Oliveira-Costa, G. De Troia, G. di Stefano, E. Hivon, A. H. Jaffe, T. S. Kisner, A. E. Lange, C. J. MacTavish, S. Masi, P. D. Mauskopf, A. Melchiorri, T. E. Montroy, P. Natoli, C. B. Netterfield, E. Pascale, F. Piacentini, D. Pogosyan, G. Polenta, S. Prunet, S. Ricciardi, G. Romeo, J. E. Ruhl, P. Santini, M. Tegmark, M. Veneziani, and N. Vittorio. A Measurement of the Angular Power Spectrum of the CMB Temperature Anisotropy from the 2003 Flight of BOOMERANG. *The Astrophysical Journal*, 647:823–832, August 2006.
- [70] M. Kamionkowski and A. Kosowsky. The Cosmic Microwave Background and Particle Physics. *Annual Review of Nuclear and Particle Science*, 49:77–123, 1999.
- [71] L. Knox. Cosmic microwave background anisotropy window functions revisited. *Physics Review D*, 60(10):103516, November 1999.
- [72] A. N. Kolmogorov. The Local Structure of Turbulence in an Incompressible Fluid with Very Large Reynolds Number. *ANSSSR*, 30:301–305, 1941.
- [73] E. Komatsu and U. Seljak. The Sunyaev-Zel’dovich angular power spectrum as a probe of cosmological parameters. *Monthly Notices of the Royal Astronomical Society*, 336:1256–1270, November 2002.
- [74] A. Kosowsky. The Atacama Cosmology Telescope. *New Astronomy Review*, 47:939–943, December 2003.

- [75] A. Kovacs. *SHARC-2 350 micron observations of distant submillimeter-selected galaxies and techniques for the optimal analysis and observing of weak signals*. PhD thesis, Caltech, 2006.
- [76] J. D. Kraus. *Radio Astronomy*. Cygnus-Quasar Books, Powell, Ohio, 2nd edition, 1986.
- [77] E. Kreysa, H.-P. Gemuend, J. Gromke, C. G. Haslam, L. Reichertz, E. E. Haller, J. W. Beeman, V. Hansen, A. Sievers, and R. Zylka. Bolometer array development at the Max-Planck-Institut fuer Radioastronomie. In *Advanced Technology MMW, Radio, and Terahertz Telescopes*. T. G. Phillips, Ed., volume 3357, pages 319–325. Presented at the Society of Photo-Optical Instrumentation Engineers (SPIE) Conference, July 1998.
- [78] C. L. Kuo, P. A. R. Ade, J. J. Bock, J. R. Bond, C. R. Contaldi, M. D. Daub, J. H. Goldstein, W. L. Holzapfel, A. E. Lange, M. Lueker, M. Newcomb, J. B. Peterson, C. Reichardt, J. Ruhl, M. C. Runyan, and Z. Staniszewski. Improved Measurements of the CMB Power Spectrum with ACBAR. *The Astrophysical Journal*, 664:687–701, August 2007.
- [79] C. L. Kuo, P. A. R. Ade, J. J. Bock, C. Cantalupo, M. D. Daub, J. Goldstein, W. L. Holzapfel, A. E. Lange, M. Lueker, M. Newcomb, J. B. Peterson, J. Ruhl, M. C. Runyan, and E. Torbet. High-Resolution Observations of the Cosmic Microwave Background Power Spectrum with ACBAR. *The Astrophysical Journal*, 600:32–51, January 2004.
- [80] A. P. Lane. Submillimeter Transmission at South Pole. In G. Novak and R. Landsberg, editors, *Astrophysics From Antarctica*, volume 141, page 289. Astronomical Society of the Pacific Conference Series, 1998.
- [81] S. J. LaRoque, M. Bonamente, J. E. Carlstrom, M. K. Joy, D. Nagai, E. D. Reese, and K. S. Dawson. X-Ray and Sunyaev-Zel’dovich Effect Measurements of the Gas Mass Fraction in Galaxy Clusters. *The Astrophysical Journal*, 652:917–936, December 2006.

- [82] G. T. Laurent, J. E. Aguirre, J. Glenn, P. A. R. Ade, J. J. Bock, S. F. Edgington, A. Goldin, S. R. Golwala, D. Haig, A. E. Lange, P. R. Maloney, P. D. Mauskopf, H. Nguyen, P. Rossinot, J. Sayers, and P. Stover. The Bolocam Lockman Hole Millimeter-Wave Galaxy Survey: Galaxy Candidates and Number Counts. *The Astrophysical Journal*, 623:742–762, April 2005.
- [83] O. P. Lay and N. W. Halverson. The Impact of Atmospheric Fluctuations on Degree-Scale Imaging of the Cosmic Microwave Background. *The Astrophysical Journal*, 543:787–798, November 2000.
- [84] M. Leong, R. Peng, M. Houde, H. Yoshida, R. Chamberlin, and T. G. Phillips. A CSO submillimeter active optics system. In *Millimeter and Submillimeter Detectors and Instrumentation for Astronomy III*. J. Zmuidzinas, W. S. Holland, S. Withington, and W. D. Duncan, Eds., volume 6275. Presented at the Society of Photo-Optical Instrumentation Engineers (SPIE) Conference, July 2006.
- [85] M. S. Longair. *Galaxy Formation*. Springer-Verlag, Berlin, 1998.
- [86] C. J. MacTavish, P. A. R. Ade, J. J. Bock, J. R. Bond, J. Borrill, A. Boscaleri, P. Cabella, C. R. Contaldi, B. P. Crill, P. de Bernardis, G. De Gasperis, A. de Oliveira-Costa, G. De Troia, G. di Stefano, E. Hivon, A. H. Jaffe, W. C. Jones, T. S. Kisner, A. E. Lange, A. M. Lewis, S. Masi, P. D. Mauskopf, A. Melchiorri, T. E. Montroy, P. Natoli, C. B. Netterfield, E. Pascale, F. Piacentini, D. Pogosyan, G. Polenta, S. Prunet, S. Ricciardi, G. Romeo, J. E. Ruhl, P. Santini, M. Tegmark, M. Veneziani, and N. Vittorio. Cosmological Parameters from the 2003 Flight of BOOMERANG. *The Astrophysical Journal*, 647:799–812, August 2006.
- [87] P. R. Maloney, J. Glenn, J. E. Aguirre, S. R. Golwala, G. T. Laurent, P. A. R. Ade, J. J. Bock, S. F. Edgington, A. Goldin, D. Haig, A. E. Lange, P. D. Mauskopf, H. Nguyen, P. Rossinot, J. Sayers, and P. Stover. A Fluctuation Analysis of the Bolocam 1.1 mm Lockman Hole Survey. *The Astrophysical Journal*, 635:1044–1052, December 2005.
- [88] B. S. Mason, T. J. Pearson, A. C. S. Readhead, M. C. Shepherd, J. Sievers, P. S. Udomprasert, J. K. Cartwright, A. J. Farmer, S. Padin, S. T. Myers, J. R. Bond, C. R. Contaldi, U. Pen, S. Prunet, D. Pogosyan, J. E. Carlstrom, J. Kovac, E. M.

- Leitch, C. Pryke, N. W. Halverson, W. L. Holzapfel, P. Altamirano, L. Bronfman, S. Casassus, J. May, and M. Joy. The Anisotropy of the Microwave Background to $l = 3500$: Deep Field Observations with the Cosmic Background Imager. *The Astrophysical Journal*, 591:540–555, July 2003.
- [89] C. R. Masson. Atmospheric Effects and Calibrations. In M. Ishiguro and J. Welch, editors, *IAU Colloq. 140: Astronomy with Millimeter and Submillimeter Wave Interferometry*, volume 59, page 87. Astronomical Society of the Pacific Conference Series, 1994.
- [90] J. C. Mather, E. S. Cheng, D. A. Cottingham, R. E. Eplee, Jr., D. J. Fixsen, T. Hewagama, R. B. Isaacman, K. A. Jensen, S. S. Meyer, P. D. Noerdlinger, S. M. Read, L. P. Rosen, R. A. Shafer, E. L. Wright, C. L. Bennett, N. W. Boggess, M. G. Hauser, T. Kelsall, S. H. Moseley, Jr., R. F. Silverberg, G. F. Smoot, R. Weiss, and D. T. Wilkinson. Measurement of the cosmic microwave background spectrum by the COBE FIRAS instrument. *The Astrophysical Journal*, 420:439–444, January 1994.
- [91] J. C. Mather, E. S. Cheng, R. E. Eplee, Jr., R. B. Isaacman, S. S. Meyer, R. A. Shafer, R. Weiss, E. L. Wright, C. L. Bennett, N. W. Boggess, E. Dwek, S. Gulkis, M. G. Hauser, M. Janssen, T. Kelsall, P. M. Lubin, S. H. Moseley, Jr., T. L. Murdock, R. F. Silverberg, G. F. Smoot, and D. T. Wilkinson. A preliminary measurement of the cosmic microwave background spectrum by the Cosmic Background Explorer (COBE) satellite. *The Astrophysical Journal*, 354:L37–L40, May 1990.
- [92] P. D. Mauskopf. *Measurements of Anisotropies in the Cosmic Microwave Background at Small and Intermediate angular scales with Bolometric Receivers at mm Wavelengths*. PhD thesis, University of California at Berkeley, 1997.
- [93] P. D. Mauskopf, J. J. Bock, H. del Castillo, W. L. Holzapfel, and A. E. Lange. Composite infrared bolometers with Si 3 N 4 micromesh absorbers. *Applied Optics*, 36:765–771, February 1997.
- [94] M. McKinnon. *MMA memo 40*, 1987.
- [95] A. D. Miller, R. Caldwell, M. J. Devlin, W. B. Dorwart, T. Herbig, M. R. Nolta, L. A. Page, J. Puchalla, E. Torbet, and H. T. Tran. A Measurement of the Angular

- Power Spectrum of the Cosmic Microwave Background from $L = 100$ to 400. *The Astrophysical Journal*, 524:L1–L4, October 1999.
- [96] F. Murtagh and A. Heck. *Multivariate Data Analysis*. Kluwer Academic Publishers, Boston, 1987.
- [97] P. Natoli, G. de Gasperis, C. Gheller, and N. Vittorio. A Map-Making algorithm for the Planck Surveyor. *Astronomy & Astrophysics*, 372:346–356, June 2001.
- [98] C. B. Netterfield, P. A. R. Ade, J. J. Bock, J. R. Bond, J. Borrill, A. Boscaleri, K. Coble, C. R. Contaldi, B. P. Crill, P. de Bernardis, P. Farese, K. Ganga, M. Giacometti, E. Hivon, V. V. Hristov, A. Iacoangeli, A. H. Jaffe, W. C. Jones, A. E. Lange, L. Martinis, S. Masi, P. Mason, P. D. Mauskopf, A. Melchiorri, T. Montroy, E. Pascale, F. Piacentini, D. Pogosyan, F. Pongetti, S. Prunet, G. Romeo, J. E. Ruhl, and F. Scaramuzzi. A Measurement by BOOMERANG of Multiple Peaks in the Angular Power Spectrum of the Cosmic Microwave Background. *The Astrophysical Journal*, 571:604–614, June 2002.
- [99] K. A. Olive, G. Steigman, and T. P. Walker. Primordial nucleosynthesis : theory and observations. *Physics Reports*, 333:389–407, 2000.
- [100] G. S. Orton, M. J. Griffin, P. A. R. Ade, I. G. Nolt, and J. V. Radostitz. Submillimeter and millimeter observations of Uranus and Neptune. *Icarus*, 67:289–304, August 1986.
- [101] J. R. Pardo, J. Cernicharo, and E. Serabyn. Atmospheric transmission at microwaves (ATM): an improved model for millimeter/submillimeter applications. *IEEE Transactions on Antennas and Propagation*, 49:1683–1694, December 2001.
- [102] B. Peng, A. Kraus, T. P. Krichbaum, and A. Witzel. Long-term monitoring of selected radio sources. *Astronomy and Astrophysics Supplement Series*, 145:1–10, July 2000.
- [103] A. A. Penzias and R. W. Wilson. A Measurement of Excess Antenna Temperature at 4080 Mc/s. *The Astrophysical Journal*, 142:419–421, July 1965.
- [104] J. B. Peterson, S. J. E. Radford, P. A. R. Ade, R. A. Chamberlin, M. J. O’Kelly, K. M. Peterson, and E. Schartman. Stability of the Submillimeter Brightness of the Atmosphere above Mauna Kea, Chajnantor, and the South Pole. *Publications of the Astronomical Society of the Pacific*, 115:383–388, March 2003.

- [105] PolarBear website (available at <http://bolo.berkeley.edu/polarbear/>).
- [106] S. J. Radford and R. A. Chamberlin. *ALMA memo 334*, 2000.
- [107] E. D. Reese, J. E. Carlstrom, M. Joy, J. J. Mohr, L. Grego, and W. L. Holzapfel. Determining the Cosmic Distance Scale from Interferometric Measurements of the Sunyaev-Zeldovich Effect. *The Astrophysical Journal*, 581:53–85, December 2002.
- [108] A. Refregier, E. Komatsu, D. N. Spergel, and U.-L. Pen. Power spectrum of the Sunyaev-Zel’dovich effect. *Physics Review D*, 61(12):123001, June 2000.
- [109] A. Refregier and R. Teyssier. Numerical and Analytical Predictions for the Large-Scale Sunyaev-Zel’dovich Effect. *ArXiv Astrophysics e-prints*, December 2000.
- [110] P. L. Richards. Bolometers for infrared and millimeter waves. *Journal of Applied Physics*, 76:1–24, July 1994.
- [111] A. G. Riess, A. V. Filippenko, P. Challis, A. Clocchiatti, A. Diercks, P. M. Garnavich, R. L. Gilliland, C. J. Hogan, S. Jha, R. P. Kirshner, B. Leibundgut, M. M. Phillips, D. Reiss, B. P. Schmidt, R. A. Schommer, R. C. Smith, J. Spyromilio, C. Stubbs, N. B. Suntzeff, and J. Tonry. Observational Evidence from Supernovae for an Accelerating Universe and a Cosmological Constant. *Astronomical Journal*, 116:1009–1038, September 1998.
- [112] A. G. Riess, L.-G. Strolger, J. Tonry, S. Casertano, H. C. Ferguson, B. Mobasher, P. Challis, A. V. Filippenko, S. Jha, W. Li, R. Chornock, R. P. Kirshner, B. Leibundgut, M. Dickinson, M. Livio, M. Giavalisco, C. C. Steidel, T. Benítez, and Z. Tsvetanov. Type Ia Supernova Discoveries at $z > 1$ from the Hubble Space Telescope: Evidence for Past Deceleration and Constraints on Dark Energy Evolution. *The Astrophysical Journal*, 607:665–687, June 2004.
- [113] M. S. Roberts and R. N. Whitehurst. The rotation curve and geometry of M31 at large galactocentric distances. *The Astrophysical Journal*, 201:327–346, October 1975.
- [114] D. J. Rudy. *Mars: High Resolution VLA Observations at Wavelengths of 2 and 6 cm and Derived Properties*. PhD thesis, Caltech, 1987.

- [115] D. J. Rudy, D. O. Muhleman, G. L. Berge, B. M. Jakosky, and P. R. Christensen. Mars - VLA observations of the northern hemisphere and the north polar region at wavelengths of 2 and 6 CM. *Icarus*, 71:159–177, July 1987.
- [116] J. Ruhl, P. A. R. Ade, J. E. Carlstrom, H.-M. Cho, T. Crawford, M. Dobbs, C. H. Greer, N. w. Halverson, W. L. Holzapfel, T. M. Lanting, A. T. Lee, E. M. Leitch, J. Leong, W. Lu, M. Lueker, J. Mehl, S. S. Meyer, J. J. Mohr, S. Padin, T. Plagge, C. Pryke, M. C. Runyan, D. Schwan, M. K. Sharp, H. Spieler, Z. Staniszewski, and A. A. Stark. The South Pole Telescope. In *Millimeter and Submillimeter Detectors for Astronomy II*. J. Zmuidzinas, W. S. Holland, and S. Withington, Eds., volume 5498, pages 11–29. Presented at the Society of Photo-Optical Instrumentation Engineers (SPIE) Conference, October 2004.
- [117] M. C. Runyan. *A Search for Galaxy Clusters Using the Sunyaev-Zel'dovich Effect*. PhD thesis, Caltech, 2002.
- [118] M. C. Runyan, P. A. R. Ade, R. S. Bhatia, J. J. Bock, M. D. Daub, J. H. Goldstein, C. V. Haynes, W. L. Holzapfel, C. L. Kuo, A. E. Lange, J. Leong, M. Lueker, M. Newcomb, J. B. Peterson, C. Reichardt, J. Ruhl, G. Sirbi, E. Torbet, C. Tucker, A. D. Turner, and D. Woolsey. ACBAR: The Arcminute Cosmology Bolometer Array Receiver. *The Astrophysical Journal Supplement Series*, 149:265–287, December 2003.
- [119] J. Ruze. Antenna tolerance theory - A review. *Proceedings of the IEEE*, pages 633–640, April 1966.
- [120] R. K. Sachs and A. M. Wolfe. Perturbations of a Cosmological Model and Angular Variations of the Microwave Background. *The Astrophysical Journal*, 147:73, January 1967.
- [121] G. Sandell. Secondary calibrators at submillimetre wavelengths. *Monthly Notices of the Royal Astronomical Society*, 271:75–80, November 1994.
- [122] S. Sasaki. A New Method to Estimate Cosmological Parameters Using the Baryon Fraction of Clusters of Galaxies. *Publications of the Astronomical Society of Japan*, 48:L119–L122, December 1996.

- [123] R. Saunders, R. Kneissl, K. Grainge, W. F. Grainger, M. E. Jones, A. Maggi, R. Das, A. C. Edge, A. N. Lasenby, G. G. Pooley, S. J. Miyoshi, T. Tsuruta, K. Yamashita, Y. Tawara, A. Furuzawa, A. Harada, and I. Hatsukade. A measurement of H_0 from Ryle Telescope, ASCA and ROSAT observations of Abell 773. *Monthly Notices of the Royal Astronomical Society*, 341:937–940, May 2003.
- [124] D. J. Schlegel, D. P. Finkbeiner, and M. Davis. Maps of Dust Infrared Emission for Use in Estimation of Reddening and Cosmic Microwave Background Radiation Foregrounds. *The Astrophysical Journal*, 500:525, June 1998.
- [125] D. Scott and M. White. Implications of SCUBA observations for the Planck Surveyor. *Astronomy & Astrophysics*, 346:1–6, June 1999.
- [126] U. Seljak, J. Burwell, and U.-L. Pen. Sunyaev-Zeldovich effect from hydrodynamical simulations: Maps and low order statistics. *Physics Review D*, 63(6):063001, March 2001.
- [127] U. Seljak and M. Zaldarriaga. A Line-of-Sight Integration Approach to Cosmic Microwave Background Anisotropies. *The Astrophysical Journal*, 469:437, October 1996.
- [128] E. Serabyn. A wide-field relay optics system for the Caltech Submillimeter Observatory. *International Journal of Infrared and Millimeter Waves*, 18:273–284, February 1997.
- [129] J. L. Sievers, J. R. Bond, J. K. Cartwright, C. R. Contaldi, B. S. Mason, S. T. Myers, S. Padin, T. J. Pearson, U.-L. Pen, D. Pogosyan, S. Prunet, A. C. S. Readhead, M. C. Shepherd, P. S. Udomprasert, L. Bronfman, W. L. Holzappel, and J. May. Cosmological Parameters from Cosmic Background Imager Observations and Comparisons with BOOMERANG, DASI, and MAXIMA. *The Astrophysical Journal*, 591:599–622, July 2003.
- [130] J. Silk. Cosmic Black-Body Radiation and Galaxy Formation. *The Astrophysical Journal*, 151:459, February 1968.
- [131] I. Smail, R. J. Ivison, A. W. Blain, and J.-P. Kneib. The nature of faint submillimetre-selected galaxies. *Monthly Notices of the Royal Astronomical Society*, 331:495–520, March 2002.

- [132] D. N. Spergel, R. Bean, O. Doré, M. R.olta, C. L. Bennett, J. Dunkley, G. Hinshaw, N. Jarosik, E. Komatsu, L. Page, H. V. Peiris, L. Verde, M. Halpern, R. S. Hill, A. Kogut, M. Limon, S. S. Meyer, N. Odegard, G. S. Tucker, J. L. Weiland, E. Wollack, and E. L. Wright. Three-Year Wilkinson Microwave Anisotropy Probe (WMAP) Observations: Implications for Cosmology. *The Astrophysical Journal Supplement Series*, 170:377–408, June 2007.
- [133] Spider website (available at http://www.astro.caltech.edu/lgg/spider_front.htm).
- [134] V. Springel, M. White, and L. Hernquist. Hydrodynamic Simulations of the Sunyaev-Zeldovich Effect(s). *The Astrophysical Journal*, 549:681–687, March 2001.
- [135] S. A. Stanford, B. Holden, P. Rosati, P. Tozzi, S. Borgani, P. R. Eisenhardt, and H. Spinrad. The Intracluster Medium in $z > 1$ Galaxy Clusters. *The Astrophysical Journal*, 552:504–507, May 2001.
- [136] A. A. Stark, J. Bally, S. P. Balm, T. M. Bania, A. D. Bolatto, R. A. Chamberlin, G. Engargiola, M. Huang, J. G. Ingalls, K. Jacobs, J. M. Jackson, J. W. Kooi, A. P. Lane, K.-Y. Lo, R. D. Marks, C. L. Martin, D. Mumma, R. Ojha, R. Schieder, J. Staguhn, J. Stutzki, C. K. Walker, R. W. Wilson, G. A. Wright, X. Zhang, P. Zimmermann, and R. Zimmermann. The Antarctic Submillimeter Telescope and Remote Observatory (AST/RO). *Publications of the Astronomical Society of the Pacific*, 113:567–585, May 2001.
- [137] G. Steigman. BBN and the CBR Probe the Early Universe. In *AIP Conference Proceedings*, volume 903, pages 40–47. Presented at SUSY06: The 14th International Conference on Supersymmetry and the Unification of Fundamental Interactions, April 2007.
- [138] M. E. Sulkanen. Galaxy Cluster Shapes and Systematic Errors in H_0 Measured by the Sunyaev-Zeldovich Effect. *The Astrophysical Journal*, 522:59–65, September 1999.
- [139] R. A. Sunyaev and Y. B. Zeldovich. The Observations of Relic Radiation as a Test of the Nature of X-Ray Radiation from the Clusters of Galaxies. *Comments on Astrophysics and Space Physics*, 4:173, November 1972.

- [140] A. M. Swinbank, I. Smail, S. C. Chapman, A. W. Blain, R. J. Ivison, and W. C. Keel. The Rest-Frame Optical Spectra of SCUBA Galaxies. *The Astrophysical Journal*, 617:64–80, December 2004.
- [141] V. I. Tatarskii. *Wave Propagation in a Turbulent Medium*. McGraw-Hill, New York, 1961.
- [142] A. C. Taylor. Clover A B-mode polarization experiment. *New Astronomy Review*, 50:993–998, December 2006.
- [143] M. Tegmark. How to Make Maps from Cosmic Microwave Background Data without Losing Information. *The Astrophysical Journal*, 480:L87, May 1997.
- [144] M. Tegmark, M. R. Blanton, M. A. Strauss, F. Hoyle, D. Schlegel, R. Scoccimarro, M. S. Vogeley, D. H. Weinberg, I. Zehavi, A. Berlind, T. Budavari, A. Connolly, D. J. Eisenstein, D. Finkbeiner, J. A. Frieman, J. E. Gunn, A. J. S. Hamilton, L. Hui, B. Jain, D. Johnston, S. Kent, H. Lin, R. Nakajima, R. C. Nichol, J. P. Ostriker, A. Pope, R. Scranton, U. Seljak, R. K. Sheth, A. Stebbins, A. S. Szalay, I. Szapudi, L. Verde, Y. Xu, J. Annis, N. A. Bahcall, J. Brinkmann, S. Burles, F. J. Castander, I. Csabai, J. Loveday, M. Doi, M. Fukugita, J. R. I. Gott, G. Hennessy, D. W. Hogg, Ž. Ivezić, G. R. Knapp, D. Q. Lamb, B. C. Lee, R. H. Lupton, T. A. McKay, P. Kunszt, J. A. Munn, L. O’Connell, J. Peoples, J. R. Pier, M. Richmond, C. Rockosi, D. P. Schneider, C. Stoughton, D. L. Tucker, D. E. Vanden Berk, B. Yanny, and D. G. York. The Three-Dimensional Power Spectrum of Galaxies from the Sloan Digital Sky Survey. *The Astrophysical Journal*, 606:702–740, May 2004.
- [145] The Planck Collaboration. The Scientific Programme of Planck. *ArXiv Astrophysics e-prints*, April 2006.
- [146] L. Toffolatti, F. Argueso Gomez, G. de Zotti, P. Mazzei, A. Franceschini, L. Danese, and C. Burigana. Extragalactic source counts and contributions to the anisotropies of the cosmic microwave background: predictions for the Planck Surveyor mission. *Monthly Notices of the Royal Astronomical Society*, 297:117–127, June 1998.
- [147] D. Tytler, J. M. O’Meara, N. Suzuki, and D. Lubin. Review of Big Bang Nucleosynthesis and Primordial Abundances. *Physica Scripta Volume T*, 85:12, 2000.

- [148] P. S. Udomprasert, B. S. Mason, A. C. S. Readhead, and T. J. Pearson. An Unbiased Measurement of H_0 through Cosmic Background Imager Observations of the Sunyaev-Zel'dovich Effect in Nearby Galaxy Clusters. *The Astrophysical Journal*, 615:63–81, November 2004.
- [149] S. van den Bergh. The Early History of Dark Matter. *Publications of the Astronomical Society of the Pacific*, 111:657–660, June 1999.
- [150] P. G. van Dokkum, S. A. Stanford, B. P. Holden, P. R. Eisenhardt, M. Dickinson, and R. Elston. The Galaxy Population of Cluster RX J0848+4453 at $Z=1.27$. *The Astrophysical Journal*, 552:L101–L104, May 2001.
- [151] R. V. Wagoner, W. A. Fowler, and F. Hoyle. On the Synthesis of Elements at Very High Temperatures. *The Astrophysical Journal*, 148:3, April 1967.
- [152] M. White and S. Majumdar. Point Sources in the Context of Future SZ Surveys. *The Astrophysical Journal*, 602:565–570, February 2004.
- [153] E. L. Wright. Recalibration of the far-infrared brightness temperatures of the planets. *The Astrophysical Journal*, 210:250–253, November 1976.
- [154] M. C. H. Wright. Atmospheric Phase Noise and Aperture Synthesis Imaging at Millimeter Wavelengths. *Publications of the Astronomical Society of the Pacific*, 108:520, June 1996.
- [155] J. C. Wyant and K. Creath. *Applied Optics and Optical Engineering*, volume XI, chapter Basic Wavefront Aberration Theory. Academic Press, San Diego, CA, 1992.
- [156] W.-M. Yao, C. Amsler, D. Asner, R.M. Barnett, J. Beringer, P.R. Burchat, C.D. Carone, C. Caso, O. Dahl, G. D'Ambrosio, A. DeGouvea, M. Doser, S. Eidelman, J.L. Feng, T. Gherghetta, M. Goodman, C. Grab, D.E. Groom, A. Gurtu, K. Hagiwara, K.G. Hayes, J.J. Hernández-Rey, K. Hikasa, H. Jawahery, C. Kolda, Kwon Y., M.L. Mangano, A.V. Manohar, A. Masoni, R. Miquel, K. Mönig, H. Murayama, K. Nakamura, S. Navas, K.A. Olive, L. Pape, C. Patrignani, A. Piepke, G. Punzi, G. Raffelt, J.G. Smith, M. Tanabashi, J. Terning, N.A. Törnqvist, T.G. Trippe, P. Vogel, T. Watari, C.G. Wohl, R.L. Workman, P.A. Zyla, B. Armstrong,

- G. Harper, V.S. Lugovsky, P. Schaffner, M. Artuso, K.S. Babu, H.R. Band, E. Barbério, M. Battaglia, H. Bichsel, O. Biebel, P. Bloch, E. Blucher, R.N. Cahn, D. Casper, A. Cattai, A. Ceccucci, D. Chakraborty, R.S. Chivukula, G. Cowan, T. Damour, T. DeGrand, K. Desler, M.A. Dobbs, M. Drees, A. Edwards, D.A. Edwards, V.D. Elvira, J. Erler, V.V. Ezhela, W. Fetscher, B.D. Fields, B. Foster, D. Froidevaux, T.K. Gaisser, L. Garren, H.-J. Gerber, G. Gerbier, L. Gibbons, F.J. Gilman, G.F. Giudice, A.V. Gritsan, M. Grünewald, H.E. Haber, C. Hagmann, I. Hinchliffe, A. Höcker, P. Igo-Kemenes, J.D. Jackson, K.F. Johnson, D. Karlen, B. Kayser, D. Kirkby, S.R. Klein, K. Kleinknecht, I.G. Knowles, R.V. Kowalewski, P. Kreitz, B. Krusche, Yu.V. Kuyanov, O. Lahav, P. Langacker, A. Liddle, Z. Ligeti, T.M. Liss, L. Littenberg, L. Liu, K.S. Lugovsky, S.B. Lugovsky, T. Mannel, D.M. Manley, W.J. Marciano, A.D. Martin, D. Milstead, M. Narain, P. Nason, Y. Nir, J.A. Peacock, S.A. Prell, A. Quadt, S. Raby, B.N. Ratcliff, E.A. Razuvaev, B. Renk, P. Richardson, S. Roesler, G. Rolandi, M.T. Ronan, L.J. Rosenberg, C.T. Sachrajda, S. Sarkar, M. Schmitt, O. Schneider, D. Scott, T. Sjöstrand, G.F. Smoot, P. Sokolsky, S. Spanier, H. Spieler, A. Stahl, T. Stanev, R.E. Streitmatter, T. Sumiyoshi, N.P. Tkachenko, G.H. Trilling, G. Valencia, K. van Bibber, M.G. Vincet, D.R. Ward, B.R. Webber, J.D. Wells, M. Whalley, L. Wolfenstein, J. Womersley, C.L. Woody, A. Yamamoto, O.V. Zenin, J. Zhang, and R.-Y. Zhu. Review of Particle Physics. *Journal of Physics G*, 33:1+, 2006.
- [157] K. W. Yoon, P. A. R. Ade, D. Barkats, J. O. Battle, E. M. Bierman, J. J. Bock, J. A. Brevik, H. C. Chiang, A. Crites, C. D. Dowell, L. Duband, G. S. Griffin, E. F. Hivon, W. L. Holzappel, V. V. Hristov, B. G. Keating, J. M. Kovac, C. L. Kuo, A. E. Lange, E. M. Leitch, P. V. Mason, H. T. Nguyen, N. Ponthieu, Y. D. Takahashi, T. Renbarger, L. C. Weintraub, and D. Woolsey. The Robinson Gravitational Wave Background Telescope (BICEP): a bolometric large angular scale CMB polarimeter. In *Millimeter and Submillimeter Detectors and Instrumentation for Astronomy III*. J. Zmuidzinas, W. S. Holland, S. Withington, and W. D. Duncan, Eds., volume 6275. Presented at the Society of Photo-Optical Instrumentation Engineers (SPIE) Conference, July 2006.
- [158] K. E. Young, M. L. Enoch, N. J. Evans, II, J. Glenn, A. Sargent, T. L. Huard,

- J. Aguirre, S. Golwala, D. Haig, P. Harvey, G. Laurent, P. Mauskopf, and J. Sayers. Bolocam Survey for 1.1 mm Dust Continuum Emission in the c2d Legacy Clouds. II. Ophiuchus. *The Astrophysical Journal*, 644:326–343, June 2006.
- [159] M. Zaldarriaga and U. Seljak. CMBFAST for Spatially Closed Universes. *The Astrophysical Journal Supplement Series*, 129:431–434, August 2000.
- [160] M. Zaldarriaga, U. Seljak, and E. Bertschinger. Integral Solution for the Microwave Background Anisotropies in Nonflat Universes. *The Astrophysical Journal*, 494:491, February 1998.
- [161] Y. B. Zeldovich. A hypothesis, unifying the structure and the entropy of the Universe. *Monthly Notices of the Royal Astronomical Society*, 160:1P, 1972.
- [162] P. Zhang, U.-L. Pen, and B. Wang. The Sunyaev-Zeldovich Effect: Simulations and Observations. *The Astrophysical Journal*, 577:555–568, October 2002.
- [163] F. Zwicky. Die Rotverschiebung von extragalaktischen Nebeln. *Helvetica Physica Acta*, 6:110–127, 1933.

Appendix A Astronomical Flux and Surface Brightness Conversion Factors

Our data was calibrated against the flux of point sources, so the default is for our maps to be made in units of mJy. However, flux density is not always the most useful calibration for the maps. To convert from flux density in mJy to surface brightness in mJy/ster, we divide by the Bolocam beam area, with

$$NESB = \frac{NEFD}{\Omega_{beam}} = \left(9.33 \times 10^{-8} \frac{\text{mJy/ster}}{\text{mJy}} \right) NEFD \quad (\text{A.1})$$

for our beam area of $\Omega_{beam} = 3968 \text{ arcsec}^2$. See Figure 3.15. It is also possible to convert to surface brightness units relative to the temperature of a blackbody in the Raleigh-Jeans limit, with

$$NET_{RJ} = NESB \left(\frac{dB_{\nu}^{RJ}}{dT} \Big|_{\nu=\nu_0} \right)^{-1}, \quad (\text{A.2})$$

where $B_{\nu}^{RJ} = 2k_B T \nu^2 / c^2$ is the surface brightness of a blackbody in the Raleigh-Jeans limit. k_B is Boltzmann's constant, T is the temperature of the blackbody, and $\nu_0 = 143 \text{ GHz}$ is the effective band center for Bolocam. See Table 2.2. Equation A.2 can be rewritten in terms of the $NEFD$ as

$$NET_{RJ} = \frac{NEFD}{\Omega_{beam}} \left(\frac{c^2}{2k_B \nu_0^2} \right) = \left(17.1 \frac{\mu\text{K}}{\text{mJy}} \right) NEFD. \quad (\text{A.3})$$

A similar relation can be used to convert to surface brightness units relative to the temperature of the CMB, with

$$NET_{CMB} = NESB \left(\frac{dB_{\nu}^{CMB}}{dT_{CMB}} \Big|_{\nu=\nu_0} \right)^{-1}, \quad (\text{A.4})$$

where

$$B_{\nu}^{CMB} = 2k_B T_{CMB} \frac{\nu^2}{c^2} \frac{x}{e^x - 1} \quad (\text{A.5})$$

is the surface brightness of the CMB, $T_{CMB} = 2.73$ K is the temperature of the CMB, and $x = h\nu/k_B T_{CMB}$ where h is Planck's constant. Again, we can relate NET_{CMB} to NEFD, with

$$NET_{CMB} = \frac{NEFD}{\Omega_{beam}} \left(\frac{c^2}{2k_B\nu_0^2} \right) \frac{(e^x - 1)^2}{x^2 e^x} = \left(28.3 \frac{\mu\text{K}_{CMB}}{\text{mJy}} \right) NEFD \quad (\text{A.6})$$

using

$$\left. \frac{dB_\nu^{CMB}}{dT_{CMB}} \right|_{\nu=\nu_0} = 2k_B \frac{\nu^2}{c^2} \frac{x^2 e^x}{(e^x - 1)^2}, \quad (\text{A.7})$$

for $NEFD$ in mJy and NET_{CMB} in μK . Finally, to convert to surface brightness units relative to the SZE y parameter,

$$NEy = -\frac{1}{2} \frac{NEFD}{\Omega_{beam}} \frac{c^2}{2k_B\nu^2 T_{CMB}} = \left(-3.14 \times 10^{-6} \frac{1}{\text{mJy}} \right) NEFD, \quad (\text{A.8})$$

for $NEFD$ in mJy.

Appendix B Data Synchronization

There are two data synchronization problems that must be addressed prior to analyzing Bolocam data. The first synchronization issue arises because of the finite time it takes for the multiplexer in our data acquisition system to sample each channel. So, up to 0.02 seconds can elapse between when the signal from the first and last bolometer are recorded for a given sample. Since we scan at 240 arcseconds/sec, this 20 ms timing error can create a pointing error of 5 arcseconds, which is non-negligible compared to our 5 arcsecond pointing uncertainty. The second synchronization issue arises because the pointing information is recorded by the telescope computer while the bolometer information is recorded by our data acquisition computer. Therefore, these two data streams need to be aligned in order to create a map from the bolometer data.

B.1 Data Acquisition System Multiplexer

Bolocam uses a National Instruments SCXI-1001 multiplexer to read the 300+ channels of bolometer signals, bias signals, etc. Each signal is sampled at 50 Hz, or once every 20 ms. The multiplexer can sample at 20000 Hz, or once every 50 μ s, which means that it takes approximately 15 ms to sample every channel. The end result is that the first bolometer signal is digitized about 15 ms before the last bolometer signal, which translates to a pointing difference of around 4 arcseconds with our scan speed of 240 arcseconds/sec. This is not a huge effect since our beams have a FWHM of approximately 60 arcseconds, but it is large enough to detect.

During the 2003 observing run we collected data while the dewar was capped, which means each bolometer was exposed to the same optical signal. Therefore, the time-streams of all bolometers will be the same (ignoring small differences in gain, responsivity, etc.), except they will be shifted relative to each other according to when the multiplexer reads their signals. This shift can be determined by the phase of the cross PSD between the bolometer pairs, with the results shown in Figure B.1. Additionally, this effect can be seen by plotting the phase angle of each bolometer pair versus the physical angle between them

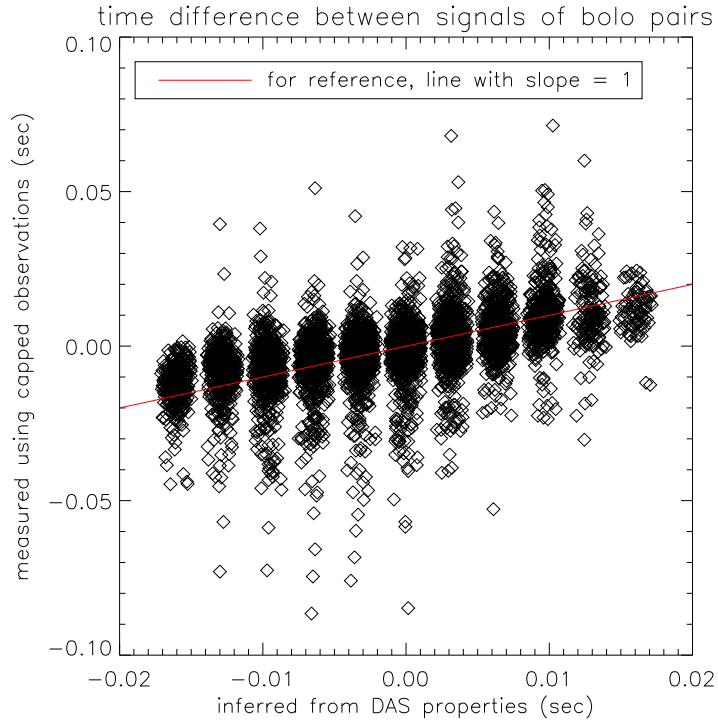


Figure B.1: Scatter plot of time offset between bolometer pairs for capped observations taken during the Fall 2003 observing run. The vertical axis is the measured offset, the horizontal axis is the offset predicted from the sampling properties of the multiplexer. Note that the scale of the two axes is different. A line with a slope of 1 and intercept of 0 is plotted for reference.

on the focal plane, since the multiplexer orders the channels by hexant (see Figure B.2).

In order to correct for this offset between the bolometer signals, we linearly interpolate each bolometer time-stream between consecutive 50 Hz samples. Since the data acquisition system (DAS) computer is aligned with the telescope computer based on a logic signal that is digitized by both computers, the time when this logic signal is digitized by the DAS computer is chosen as the zero point for the interpolation. For example, if a given bolometer is sampled Δt_b seconds after the reference logic signal, then we will interpolate the time-stream according to

$$d'_n = \left(1 - \left|\frac{\Delta t_b}{\Delta t}\right|\right) d_n + \left|\frac{\Delta t_b}{\Delta t}\right| d_{n+\Delta t_b/\Delta t} \quad (\text{B.1})$$

where d'_n is the interpolated data time-stream, d_n is the original data time-stream, Δt is the time between samples, and n is the sample number. Since $\Delta t_b < \Delta t$, we do not need to worry about shifting the data by more than one sample. Alternatively, this shift can be

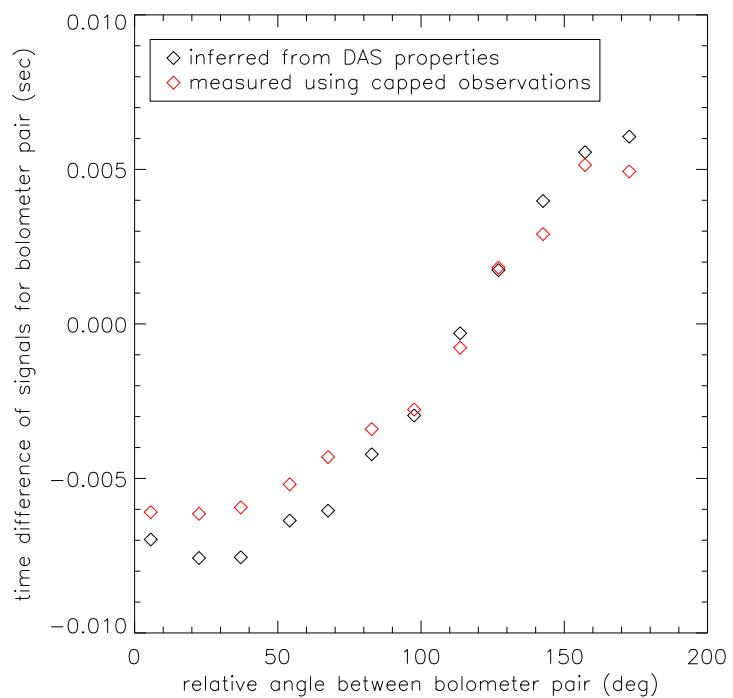


Figure B.2: Plot of relative bolometer pair angle on the focal plane versus time offset for capped observations during the 2003 observing run. The red diamonds show the measured values and the black diamonds show the predicted values from the properties of the multiplexer.

performed in frequency space by applying

$$S_m = \left(1 - \left| \frac{\Delta t_b}{\Delta t} \right| + \left| \frac{\Delta t_b}{\Delta t} \right| e^{-\text{sign}(\Delta t_b) i 2\pi f_m \Delta t} \right) \quad (\text{B.2})$$

to the Fourier transform of the time-stream data, where f_m is frequency in Hz and m is the frequency-space index. S_m acts like a filter, and for all non-zero frequencies $|S_m| < 1$. Therefore, to preserve the noise properties of our data, we divide the Fourier transform of the shifted time-stream by $|S_m|$. In summary, we shift the time-stream data according to Equation B.1, then correct for the filtering effects of this shift in frequency-space by dividing by $|S_m|$.

B.2 Aligning the Telescope and DAS Computer Data Streams

In order to align the time-streams from the telescope computer (mostly pointing information) and the DAS computer (mostly bolometer signals), each computer digitizes the same logic signal¹. This logic signal is low only when the telescope is scanning, so there is a transition at the start and end of each scan. Since each scan is roughly 10 seconds in length, the transitions of this logic signal are fairly frequent. Each transition allows us to align the two data streams to within 0.02 seconds, because the DAS data is sampled at 50 Hz. In order to improve the alignment, we investigated some of the subtleties involved in analyzing the offset in the logic transition for the two computers.

B.2.1 Results

First, note that the telescope data is digitized at 100 Hz instead of 50 Hz. Without loss of generality, assume that the telescope data is digitized at $t=0.00, 0.01, \text{etc.}$, while the DAS data is digitized at $t=0.00+\Delta t, 0.02+\Delta t, \text{etc.}$, where Δt is a uniformly distributed random variable between 0 and .02 and t is measured by the telescope clock. The reason for Δt is that the DAS clock runs about 94 ms/hour slower than the telescope clock, so in general no DAS sample is digitized at the same absolute time as a telescope sample. However, since Δt is slowly varying it is reasonable to assume it is constant for a single scan. Further, assume that the telescope sample at $t=0.00$ is the first sample with a logic low, signaling the start of a scan. We down-sample the telescope data by a factor of 2 before storing it to

¹The logic signal is sent via a physical cable from the telescope to our DAS computer.

disk, so we select every other sample from the telescope. This means that we are equally likely to select the sample at $t=0.00$ as we are to select the sample at $t=0.01$. Therefore, the average start time of the scan according to the telescope computer is $t=0.005$.

The DAS digitizes the logic signal of the telescope computer, so the signal will be recorded as low by the DAS computer the first time it digitizes the signal after the telescope has gone low. This means that the start time of the scan according to the DAS will be Δt . Recall that Δt is a uniformly distributed random variable between 0 and .02, so on average the DAS will think the scan starts at $t=0.01$. This means that when we calculate the offset between the two computers based on the tracking logic signals, the DAS will be 5 ms behind the telescope on average².

However, this is not the way that we calculate the start of a scan. The method described above provides a first guess of the start (and end) of each scan. Then, each scan is forced to be a certain length (e.g., if the scan is 600 arcseconds long and the scan speed is 240 arcseconds/sec then the scan should contain 125 50-Hz samples). Next, the offset, in number of 50 Hz frames, between the DAS computer and the telescope computer is constrained to be the same for both the start and end of each scan. The end result is that every scan contains the correct number of frames, and the offset between the computers is a perfect step function. Here is a simple example. For a given scan the DAS computer has 124 frames and the telescope computer has 125 frames. The offset, DAS start frame minus telescope start frame, between the computers is 12 50-Hz samples at the start of the scan and 11 samples at the end of the scan. If the average offset of the 2 previous and 2 subsequent scans is 12 samples, then the assumption is made that 12 is the true offset of this scan. So, if a frame is added to the end of the DAS scan, then the DAS scan will have the correct number of frames and the offset will be correct.

The complexity of determining the time delay of the scan on the DAS compared to the telescope is daunting when the scan information is calculated in the manner described above (note that this time delay is calculated after accounting for the offset of 12 frames). Therefore, a simulation was run to determine the time delay, which was calculated by the simulation to be $9.770 \pm .002$ ms. To test for this delay the centroids produced from observations of Uranus and Neptune were compared for left-going and right-going scans. A time offset between the pointing information and the bolometer data would show up as a

²Simulations produce an average time delay of $4.991 \pm .004$ ms for the DAS.

pointing offset along the scan direction for the two sets of scans. The 21 centroids from these observations give a time delay of $9.1 \pm .9$ ms, consistent with our prediction of 9.77 ms.³

B.2.2 Details of the Simulation

A 100 Hz string of logic signals, representing the telescope time-stream before it is down-sampled to 50 Hz, is produced. Each scan in this time-stream contains one less sample than it should (e.g., if the scan should have 125 50-Hz samples then the simulation produces scans with 249 samples), and each scan starts randomly on either an odd or even sample number. These two input parameters to the simulation are justified below. This simulated logic signal is generated to have the same number of scans and same number of samples per scan as our real data. Next, a 100 Hz string (telescope) of times, in seconds relative to the first frame, is generated to correspond to the time when each logic signal was taken. Additionally, a 50 Hz string (DAS) of times is created, with the start frame randomly offset by an amount between 0 and 0.02 seconds and every frame multiplied by a factor to account for the DAS running slower than the telescope by 94 ms/hour. Then, a 50 Hz logic signal (DAS) is generated by giving each sample the value of the 100 Hz logic sample (telescope) with the closest earlier time. Recall that this is how the DAS logic signal is actually digitized. Finally, the telescope logic signal is down-sampled to 50 Hz, and the two logic signals are input to the same program used to calculate the scan information for real data. The time delay of the DAS was calculated by differencing the time according to the DAS computer when the scan starts with the time according to the telescope computer when the scan starts. The results of this simulation are given in Table B.1, and agree well with our real data.

Randomly starting the scan on odd-or even-numbered samples is reasonable because the number of 50 Hz frames between scans varies by approximately 100 for a single observation. Since the time between scans varies by such a large amount from one scan to the next it seems reasonable that the start frame will be randomly either even or odd. The only justification for making each scan with one fewer frame than it should have, is that any other reasonable assumption does not fit the data. The following possibilities, in addition to

³After correcting for a 9.77 ms time delay, the 21 observations give an average time delay of $-.36 \pm .93$ ms. The reason the new time delay was not $9.1 - 9.770 = -.67$ ms is that the time delay is calculated by centroiding a binned map, and therefore depends on the binning, which changes when the time delay is corrected. For reference, the average pointing error in the direction perpendicular to the scan is $.208 \pm .191$ arcseconds (or $.87 \pm .79$ ms after dividing by the scan speed).

	planet obs		pointing obs		science field obs	
	data	simulation	data	simulation	data	simulation
total scans	1792	1792	11592	11592	18960	18960
DAS/tel wrong length	905	901.3 ± 21.6	5654	5798.2 ± 90.8	9467	9500.5 ± 114.2
tel scan too short	460	435.1 ± 14.9	2814	2877.1 ± 64.8	4680	4600.4 ± 79.8
tel scan too long	0	0.0 ± 0.0	0	0.0 ± 0.0	0	0.0 ± 0.0
DAS scan too short	445	466.2 ± 15.7	2840	2921.1 ± 63.7	4786	4900.1 ± 81.7
DAS scan too long	0	0.0 ± 0.0	0	0.0 ± 0.0	1	0.0 ± 0.0
add to tel start	458	433.9 ± 15.0	2781	2833.8 ± 65.2	4621	4515 ± 80.2
sub from tel start	0	0.0 ± 0.0	0	0.0 ± 0.0	0	0.0 ± 0.0
add to tel end	2	1.3 ± 1.0	33	43.3 ± 10.7	59	85.4 ± 14.7
sub from tel end	0	0.0 ± 0.0	0	0.0 ± 0.0	0	0.0 ± 0.0
add to DAS start	1	1.3 ± 1.0	28	53.5 ± 11.8	67	95.7 ± 15.6
sub from DAS start	0	0.0 ± 0.0	0	0.0 ± 0.0	0	0.0 ± 0.0
add to DAS end	444	464.9 ± 15.8	2812	2867.6 ± 64.4	4719	4804 ± 82.1
sub from DAS end	0	0.0 ± 0.0	0	0.0 ± 0.0	1	0.0 ± 0.0
DAS time lag (ms)	N/A	$9.912 \pm .002$	N/A	9.744 ± 0.003	N/A	$9.606 \pm .003$

Table B.1: Actual scan data compared to simulations. In each simulation the total number of scans is normalized to be the same as the data. The data includes all observations taken at 240 arcseconds/sec in October 2003. The errors are the 1 sigma statistical errors on the simulated values due to the finite length of each simulation.

how the simulation was actually performed, were attempted in every possible combination: scan length is always the number of 100 Hz frames it should be, scan length is randomly within one of the correct number of frames, scan length is randomly one less or equal to the correct number of frames, the start of each scan is an even-numbered frame, the start of each scan is an odd-numbered frame, the start of each scan is randomly odd or even for the entire observation. Only when the number of frames in the scan is one less than it should be and when the start of each scan is randomly either odd or even does the simulation match the data.

Appendix C Computing Power Spectra and Cross Power Spectra

Power spectral densities (PSDs) and cross power spectral densities (xPSDs) are mentioned throughout this thesis, and were calculated using the conventions described in this appendix. I will present the formalism for the one-dimensional case, but the generalization to two dimensions is trivial. First, consider a set of data of the form d_n , where n is the sample number. The amplitude of the Bolocam data will generally be given in units of voltage (V), flux (Jy), or surface brightness (T_{CMB}), and the samples will be evenly spaced in either time (sec) or distance (arcseconds). The Fourier transform of d_n is given by

$$D_m = \frac{1}{N_s} \sum_{n=0}^{n=N_s-1} d_n e^{-i2\pi nm/N_s}, \quad (\text{C.1})$$

where N_s is the number of samples in the data and m is the Fourier space index ranging from $-(N_s - 1)/2$ to $N_s/2$. D_m can be transformed back to d_n according to

$$d_n = \sum_{m=-(N_s-1)/2}^{m=N_s/2} D_m e^{i2\pi nm/N_s}. \quad (\text{C.2})$$

Often, we apply a Hanning window to the data prior to Fourier transforming. The Hanning window is applied so that the data smoothly transitions to zero at the endpoints¹. With this window, Equation C.1 becomes

$$D_m = \frac{1}{N_s} \sqrt{\frac{1}{\bar{h}^2}} \sum_{n=0}^{n=N_s-1} d_n h_n e^{-i2\pi nm/N_s}, \quad (\text{C.3})$$

where h_n is the Hanning window defined by $h_n = \frac{1}{2}(1 - \cos(2\pi n/N_s))$ and $\bar{h}^2 = \frac{1}{N_s} \sum_{n=0}^{n=N_s-1} h_n^2$.

Note that D_m has units of amplitude. Also, since d_n is purely real, $D_m^* = D_{-m}$ where D_m^*

¹The Hanning window reduces the Fourier-space resolution of the transform, but it also reduces the amount of leakage between signals at different Fourier-space indices. This windowing is important because a lot of the Bolocam data has a steeply rising profile at low frequency, which means the signals at low frequency can easily contaminate the signals at high frequency.

is the complex conjugate of D_m . A PSD can be directly computed from D_m , with

$$PSD_f = \frac{2D_{m_f}^* D_{m_f}}{\Delta f} = \frac{2D_{-m_f} D_{m_f}}{\Delta f}, \quad (\text{C.4})$$

and has units of amplitude²/frequency. m_f is still the Fourier space index, and the subscript f signifies that it corresponds to a particular Fourier space frequency with units of 1/time or 1/distance. The Fourier space frequency is defined by $f = m/N_s \Delta t$, where Δt is the spacing between data points, d_n , in units of time or distance. Δf is the frequency resolution, given by $\Delta f = \frac{1}{N_s \Delta t}$. The factor of 2 is added because all of the spectra are converted to one-sided spectra, containing only positive frequencies. One-sided spectra are used because $PSD_f = PSD_{-f}$. Often, the square root of the PSD, in units of amplitude/ $\sqrt{\text{frequency}}$, is quoted in place of the PSD. Since PSDs are purely real, no phase information is lost by taking this square root.

The cross PSD between two data sets serves as a useful tool for determining the correlations between them. For two sets of data, $d_n^{[1]}$ and $d_n^{[2]}$, the cross PSD is defined as

$$xPSD_f^{[12]} = \frac{2(D_{m_f}^{[1]})^* D_{m_f}^{[2]}}{\Delta f}, \quad (\text{C.5})$$

where $D_{m_f}^{[1]}$ and $D_{m_f}^{[2]}$ are calculated from Equation C.1 or C.3. Again, the factor of 2 is added to account for the conversion from a two-sided spectra to a one-sided spectra. Since the cross spectra are generally used to determine correlations between data, it is more useful to compute the relative cross spectra,

$$\text{rel } xPSD_f^{[12]} = \frac{xPSD_f^{[12]}}{\sqrt{PSD_f^{[1]}} \sqrt{PSD_f^{[2]}}}. \quad (\text{C.6})$$

As an example, consider $d_n^{[1]} = (1 - \alpha)r_n^{[1]} + \alpha c_n$ and $d_n^{[2]} = (1 - \alpha)r_n^{[2]} + \alpha c_n$, where $|\alpha| < 1$, and c_n , $r_n^{[1]}$ and $r_n^{[2]}$ are uncorrelated and have similar amplitudes and spectra. The corresponding transforms will be $D_f^{[1]} = (1 - \alpha)R_f^{[1]} + \alpha C_f$ and $D_f^{[2]} = (1 - \alpha)R_f^{[2]} + \alpha C_f$. If we ignore the cross terms, which are uncorrelated and will average to zero, then the relative

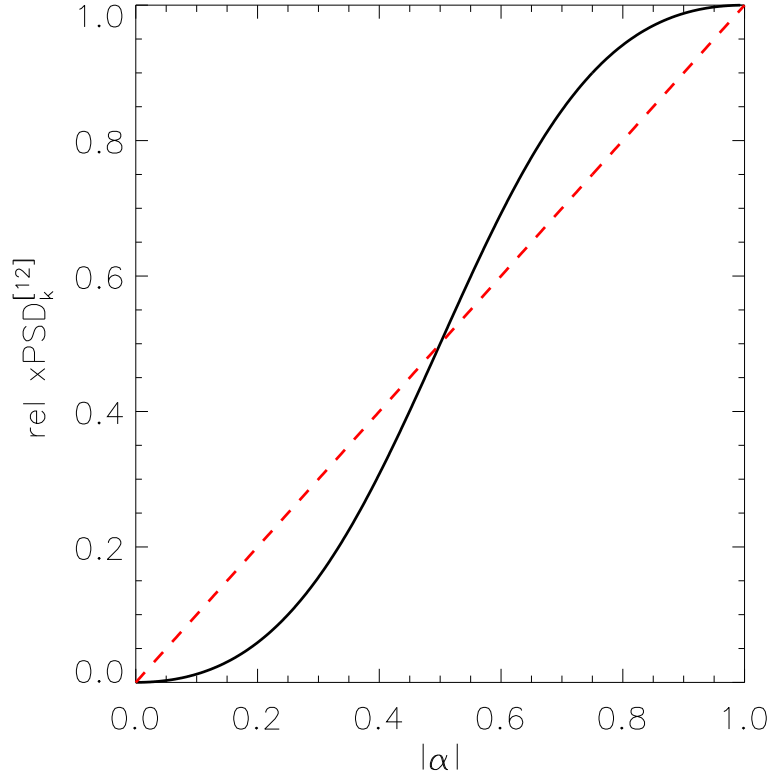


Figure C.1: A plot of the relative cross power spectra versus the relative amplitude of the correlated signal. The relative amplitude of the correlated signal, α , is described in the text. The relative cross power spectra is a good indicator of the relative PSD of the correlated portion of the signal in each of the two data sets. For reference, the red dashed line corresponds to the relative amplitude of the correlated signal, α .

cross spectra will be

$$\text{rel } xPSD^{[12]} = \frac{|\alpha|^2 |C_f|^2}{\sqrt{|1 - \alpha|^2 |R_f^{[1]}|^2 + |\alpha|^2 |C_f|^2} \sqrt{|1 - \alpha|^2 |R_f^{[2]}|^2 + |\alpha|^2 |C_f|^2}}. \quad (\text{C.7})$$

Since $|R_f^{[1]}|^2$, $|R_f^{[2]}|^2$, and $|C_f|^2$ are roughly equal to each other, Equation C.7 can be reduced to $\text{rel } xPSD_f^{[12]} \simeq \frac{|\alpha|^2}{1 - \alpha - \alpha^* + 2|\alpha|^2}$. Except at very small correlations, this expression is approximately equal to the relative amplitude of the correlated portion of the signal, α . This can be seen in Figure C.1.

As another example, consider two data sets that are identical, but shifted in time or space relative to each other. These data sets could be written as $d_n^{[1]} = d_n$ and $d_n^{[2]} = d_{n+\delta n}$. From Equation C.1 or C.3, the corresponding transforms would be D_m and $D_m e^{-i2\pi m \delta n / N_s}$,

and the relative cross PSD of these two sets is $\text{rel } xPSD_f^{[12]} = e^{-i2\pi(m_f)(\delta n)/N_s}$. Therefore, if two data sets are highly correlated, the relative cross PSD can be used to determine the temporal or spatial delay between the two sets.

Appendix D Atmospheric Noise Removal Algorithms

This Appendix will describe how the various atmospheric noise removal algorithms are implemented. In each case, the data is parsed into scans prior to removing the atmospheric noise, where each scan is 12.5 seconds long.

D.1 Average/Planar/Quadratic Subtraction

For average/planar/quadratic subtraction, the data is modeled according to

$$\vec{d}_n = \mathbf{S}\vec{p}_n, \quad (\text{D.1})$$

where \vec{d}_n is a vector with n_b elements representing the bolometer data, \mathbf{S} is an $n_{params} \times n_b$ element matrix and \vec{p}_n is a vector with n_{params} elements. n_b is the number of bolometers, n is the sample number within the 12.5-second-long scan, and n_{params} is the number of fit parameters. \mathbf{S} is based on the geometry of the focal plane, with $n_{params} = 1/3/6$ for average/planar/quadratic subtraction and

$$\begin{aligned} \text{average: } \mathbf{S} &= (\vec{1}) \\ \text{planar: } \mathbf{S} &= (\vec{1}, \vec{x}, \vec{y}) \\ \text{quadratic: } \mathbf{S} &= (\vec{1}, \vec{x}, \vec{y}, \vec{x}\vec{y}, \vec{x}^2, \vec{y}^2), \end{aligned}$$

where \vec{x} (\vec{y}) are vectors with n_b elements that contain the x (y) coordinate of each bolometer. The \vec{p}_n are the n_{params} atmospheric noise templates, which are obtained by minimizing

$$\chi_n^2 = (\vec{d}_n - \mathbf{S}\vec{p}_n)^T (\vec{d}_n - \mathbf{S}\vec{p}_n) \quad (\text{D.2})$$

with respect to \vec{p}_n .¹ Each \vec{p}_n can be thought of as a time-dependent trace that corresponds to a particular spatial dependence over the focal plane. To minimize Equation D.2, we set

¹The reason there is not a noise covariance matrix in Equation D.2 is that we have assumed the instrumental noise is constant in time. Since this noise is approximately white, this should be a reasonable assumption. If the instrumental noise is time-dependent, then our estimate of the atmospheric templates will be noisier, but it will not be biased.

the gradient of χ_n^2 with respect to \vec{p}_n equal to zero, with

$$\vec{\nabla}_{\vec{p}_n} \chi^2 = -2\mathbf{S}^T \vec{d}_n + 2\mathbf{S}^T \mathbf{S} \vec{p}_n. \quad (\text{D.3})$$

Solving Equation D.3 for \vec{p}_n yields

$$\vec{p}_n = (\mathbf{S}^T \mathbf{S})^{-1} \mathbf{S}^T \vec{d}_n. \quad (\text{D.4})$$

Once \vec{p}_n is known, we can construct an atmospheric template analogous to Equation 4.15 for each bolometer according to

$$\vec{T}_n = \mathbf{S} \vec{p}_n. \quad (\text{D.5})$$

At this point, the process continues exactly like the average subtraction algorithm given in Section 4.6.1. A correlation coefficient is computed for each bolometer according to Equation 4.16, the data is weighted by this correlation coefficient, and a new template is computed. The process is repeated until the fractional change in the values of the correlation coefficients is less than one part in 10^8 . Some examples of the typical power spectra of the \vec{p}_i are shown in Figure D.1.

D.2 Adaptive PCA Subtraction

Consider the bolometer data to be a matrix, \mathbf{d} , with $n_b \times n_s$ elements. As usual, n_b denotes the number of bolometers and n_s denotes the number of samples in a scan. For our adaptive PCA algorithm, we first calculate a covariance matrix, \mathbf{C} , with $n_b \times n_b$ elements according to

$$\mathbf{C} = \mathbf{d} \mathbf{d}^T. \quad (\text{D.6})$$

Next, \mathbf{C} is decomposed in the standard way to produce a set of eigenvalues (λ_i) and eigenvectors ($\vec{\phi}_i$), where i is the index of the eigenvector and $\vec{\phi}$ contains n_b elements. A transformation matrix, \mathbf{R} , is then formed from the eigenvectors according to

$$\mathbf{R} = (\vec{\phi}_0, \vec{\phi}_1, \dots, \vec{\phi}_{n_b}). \quad (\text{D.7})$$

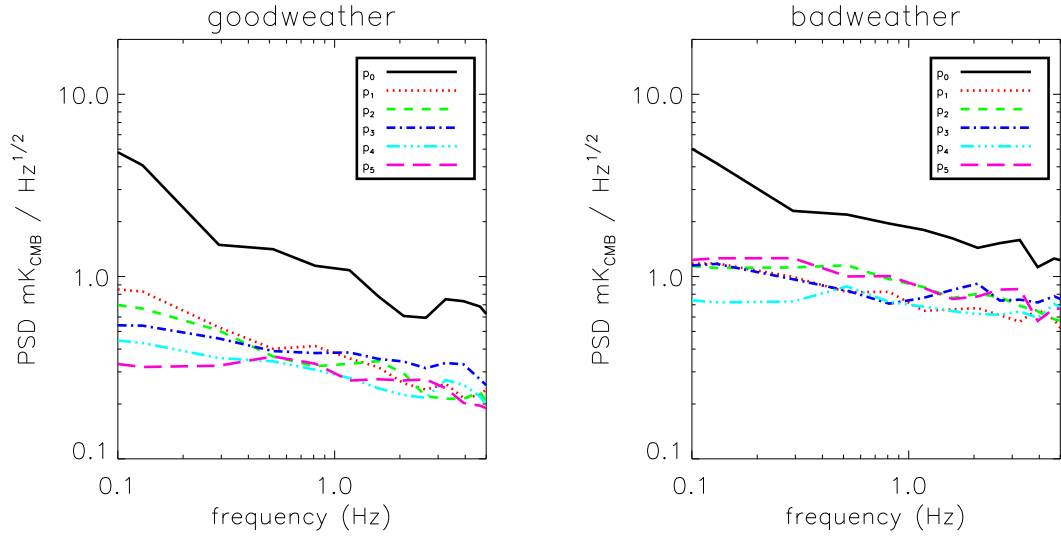


Figure D.1: Power spectra for the templates generated by the quadratic sky subtraction algorithm. The plot on the left represents an observation taken in good weather on November 10, 2003, and the plot on the right represents an observation taken in bad weather on December 7, 2003. All six elements of \vec{p}_i are plotted, with labels given in the upper right of each plot. The higher-order elements in \vec{p}_i are shown for a bolometer approximately half-way between the array center and the edge of the array. Therefore, the PSDs for these \vec{p}_i will be larger for bolometers at the edge of the focal plane, and they will be zero for a bolometer at the center of the focal plane. Note that the magnitude of the higher-order templates in bad weather is a factor of $\simeq 2$ larger than the magnitude of the higher-order templates in good weather.

This transformation matrix is used to decompose the data into eigenfunctions, $\vec{\Phi}_i$, with

$$(\vec{\Phi}_0, \vec{\Phi}_1, \dots, \vec{\Phi}_{n_b})^T = \mathbf{\Phi} = \mathbf{d}\mathbf{R}^T. \quad (\text{D.8})$$

At this point, we compute the logarithm for all of the eigenvalues, and then determine the standard deviation of that distribution. All of the eigenvalues with a logarithm more than three standard deviations from the mean are cut, and then a new standard deviation is calculated. The process is repeated until there are no more outliers with large eigenvalues. Next, all of the eigenvector columns, $\vec{\phi}_i$, in \mathbf{R} that correspond to the cut eigenvalues are set to zero, yielding a new transformation matrix, \mathbf{R}' . When reconstructing the data, setting these columns in \mathbf{R} equal to zero is equivalent to discarding the cut eigenvectors. Finally, we transform back to the original basis, with the adaptive PCA cleaned data, \mathbf{d}' , computed according to

$$\mathbf{d}' = \mathbf{\Phi}\mathbf{R}'. \quad (\text{D.9})$$

In general, the eigenfunction, $\vec{\Phi}_i$, corresponding to the largest eigenvalue is nearly equal to the template created for average sky subtraction. See Figure D.2. Therefore, the physical interpretation of the leading order eigenfunction is fairly well understood. However, it is not obvious what signal(s) the lower-order eigenfunctions correspond to. Our lack of an intuitive understanding of what signals are removed by adaptive PCA subtraction is one more reason why it was not used to analyze the data collected in 2003².

²The main reason we do not use PCA subtraction for the 2003 data set is because the ratio of attenuated noise to attenuated astronomical signal is low compared to the other subtraction methods.

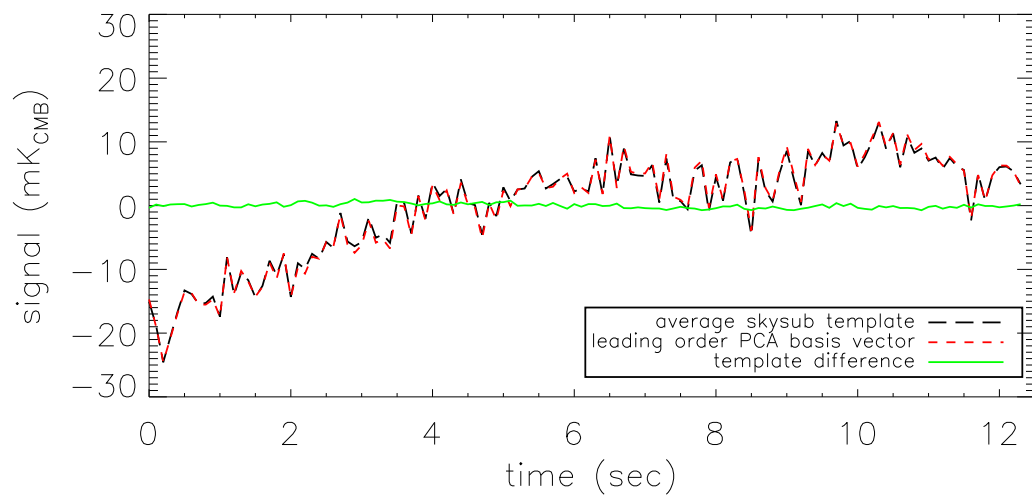


Figure D.2: This plot was generated from the data for a single scan taken during an observation on November 10, 2003. The long-dashed black line represents the average sky subtraction template, and the short-dashed red line represents the leading order adaptive PCA basis vector. The solid green line represents the difference between the two templates, which is minimal.

Appendix E Data Processing: Signal Attenuation Versus Signal Amplitude

E.1 Theory

This section describes the theory of the average sky subtraction algorithm for removing atmospheric noise. The theory becomes slightly more complicated for the more advanced planar and quadratic sky subtraction algorithms. However, the general idea of these algorithms is the same, and the results of simulations show that they behave in similar ways to changes in the amplitude of the astronomical signal.

Assume that our data is of the form

$$d_{i,n} = \alpha_i A_n + N_{i,n} + S_{i,n}, \quad (\text{E.1})$$

where i denotes the bolometer number and n denotes the sample number. α_i is the relative responsivity of bolometer i , A_n is the atmospheric signal that is common to all bolometers, $N_{i,n}$ is noise that is uncorrelated between bolometers, and $S_{i,n}$ is the astronomical signal. Recall from Section 4.6.1 that we remove atmospheric noise to create a new set of data, \tilde{d}_i , according to the following equation:

$$\tilde{d}_{i,n} = d_{i,n} - c_i T_n, \quad (\text{E.2})$$

with

$$c_i = \frac{\sum_u d_{i,u} T_u}{\sum_v T_v^2} \quad \text{and} \quad T_n = \frac{\sum_i c_i d_{i,n}}{\sum_i c_i}. \quad (\text{E.3})$$

Since $N_{i,n}$ will average to zero when summed over i , and since all of the c_i are approximately equal to one, we have

$$T_n \simeq \frac{1}{N_{bolos}} \sum_i (\alpha_i A_n + S_{i,n}) = \bar{\alpha} A_n + \tilde{S}_n \quad (\text{E.4})$$

where $\bar{\alpha} = \frac{1}{N_{bolos}} \sum_i \alpha_i$ and $\tilde{S}_n = \sum_i S_{i,n}$. Now, we can rewrite c_i from Equation E.2 as

$$c_i = \frac{\sum_v (\alpha_i A_v + N_{i,v} + S_{i,v})(\bar{\alpha} A_v + \tilde{S}_v)}{\sum_w (\bar{\alpha} A_w + \tilde{S}_w)^2} \quad (\text{E.5})$$

using Equation E.4. On average, none of the terms in the numerator or denominator will be correlated with each other, so all the cross terms will average to zero. However, since A_n and \tilde{s}_n both have a steep $1/f$ profile, at least for $S_{i,n}$ due to the CMB, the cross terms between these factors will not average to zero very quickly. Therefore, we will discard all the cross terms except those between A_n and \tilde{S}_n and Equation E.5 will reduce to

$$c_i = \frac{\sum_v \alpha_i \bar{\alpha} A_v^2 + \alpha_i A_v \tilde{S}_v + \bar{\alpha} A_v S_{i,v} + S_{i,v} \tilde{S}_v}{\sum_w \bar{\alpha}^2 A_w^2 + 2\bar{\alpha} A_w \tilde{S}_w + \tilde{S}_w^2}. \quad (\text{E.6})$$

Next, we define $\overline{A^2} = \bar{\alpha}^2 \sum_n A_n^2$, $\overline{S^2} = \sum_n \tilde{S}_n^2$, $\overline{AS} = \bar{\alpha} \sum_n A_n \tilde{S}_n$, $\overline{\mathbb{A}S_i} = \bar{\alpha} \sum_n A_n S_{i,n}$, and $\overline{\mathbb{S}_i^2} = \sum_n \tilde{S}_n S_{i,n}$. This allows us to rewrite Equation E.6 as

$$c_i = \frac{\frac{\alpha_i}{\bar{\alpha}} (\overline{A^2} + \overline{AS}) + \overline{\mathbb{A}S_i} + \overline{\mathbb{S}_i^2}}{\overline{A^2} (1 + \frac{2\overline{AS} + \overline{S^2}}{\overline{A^2}})} \quad (\text{E.7})$$

$\overline{A^2}$ is much greater than \overline{AS} , $\overline{S^2}$, $\overline{\mathbb{A}S_i}$, or $\overline{\mathbb{S}_i^2}$ since the atmospheric noise is about 10^4 times larger than the astronomical signal we are looking for. Therefore, we will approximate the above equation as

$$c_i = \frac{1}{\overline{A^2}} \left(1 - \frac{2\overline{AS} + \overline{S^2}}{\overline{A^2}} + 8 \frac{(\overline{AS})^2}{(\overline{A^2})^2} + \mathcal{O}\left(\frac{S^3}{A^3}\right) \right) \left(\frac{\alpha_i}{\bar{\alpha}} (\overline{A^2} + \overline{AS}) + \overline{\mathbb{A}S_i} + \overline{\mathbb{S}_i^2} \right) \quad (\text{E.8})$$

which can be further simplified as

$$c_i = \frac{\alpha_i}{\bar{\alpha}} + \frac{\overline{\mathbb{A}S_i} - \frac{\alpha_i}{\bar{\alpha}} \overline{AS}}{\overline{A^2}} + \frac{\overline{\mathbb{S}_i^2} - \frac{\alpha_i}{\bar{\alpha}} \overline{S^2}}{\overline{A^2}} + \frac{6 \frac{\alpha_i}{\bar{\alpha}} (\overline{AS})^2 - 2(\overline{AS})(\overline{\mathbb{A}S_i})}{(\overline{A^2})} + \mathcal{O}\left(\frac{S^3}{A^3}\right). \quad (\text{E.9})$$

So, the leading order correction to c_i due to the astronomical signal $S_{i,n}$ will be of order $S/A \simeq 10^{-4}$, and the next correction will be of order $S^2/A^2 \simeq 10^{-8}$. Now, if we consider what is removed from the data, $c_i T_n$, we find that

$$c_i T_n = \alpha_i A_n + \frac{\alpha_i}{\bar{\alpha}} \tilde{S}_n + (\bar{\alpha} \overline{\mathbb{A}S_i} - \alpha_i \overline{AS}) \frac{A_n}{\overline{A^2}} + \mathcal{O}\left(\frac{S^2}{A}\right). \quad (\text{E.10})$$

Again, since $A/S \simeq 10^4$, the first term in the equation above will be approximately 10^4 times larger than the second and third terms, and approximately 10^8 times larger than any of the terms that are quadratic in S . Therefore, we can safely conclude that our atmospheric noise removal algorithm will be nearly constant for any reasonable range of possible signal values, with the leading order deviations being linear with respect to signal strength.

E.2 Results From Simulations

To test the theory outlined in Section E.1, we have run some simulations using simulated realizations of the expected CMB signal. For all but the largest angular scales probed by Bolocam, the CMB signal is likely to be dominated by emission from the thermal SZE, which we have approximated as a flat band power in $\mathcal{C}_\ell = C_\ell \ell(\ell + 1)/2\pi$. To run the simulations we first generated a simulated CMB map realization, m_{CMB} . Next, we reverse map this realization into a time-stream using the pointing information for a real observation, and then add it to the time-stream data for that observation. We then propagate this time-stream through our data processing algorithms, and make a map, m_{simCMB} . Then, we make a map of the same observation using the original time-streams, called m_{noCMB} . Finally, we determine the difference between the map with no simulated CMB signal and the one with the simulated signal.

First, we determined how much the correlation coefficient in the atmospheric noise removal algorithm, c_i in Equation E.3, is distorted by the addition of a simulated CMB signal using the quantity

$$\Delta c = \text{median} \left(\left| \frac{c_{i,simCMB} - c_{i,noCMB}}{c_{i,noCMB}} \right| \right). \quad (\text{E.11})$$

The results, with the median taken over ten observations, twenty scans per observation, five CMB realizations, and 114 bolometers are given in Table E.1 and Figure E.1. We found that for $S/A \lesssim 10^{-1}$ Δc is of the same order of magnitude as S/A , as predicted by the theory. Additionally, this relationship holds not only for average sky subtraction, but also for the slightly more advanced planar and quadratic algorithms. For larger values of S/A the median value of Δc approaches a constant.

We also looked at the distribution of $(c_{i,simCMB} - c_{i,noCMB})/c_{i,noCMB}$ to determine if there is any systematic difference in the values, or if the nonzero values of Δc are just caused

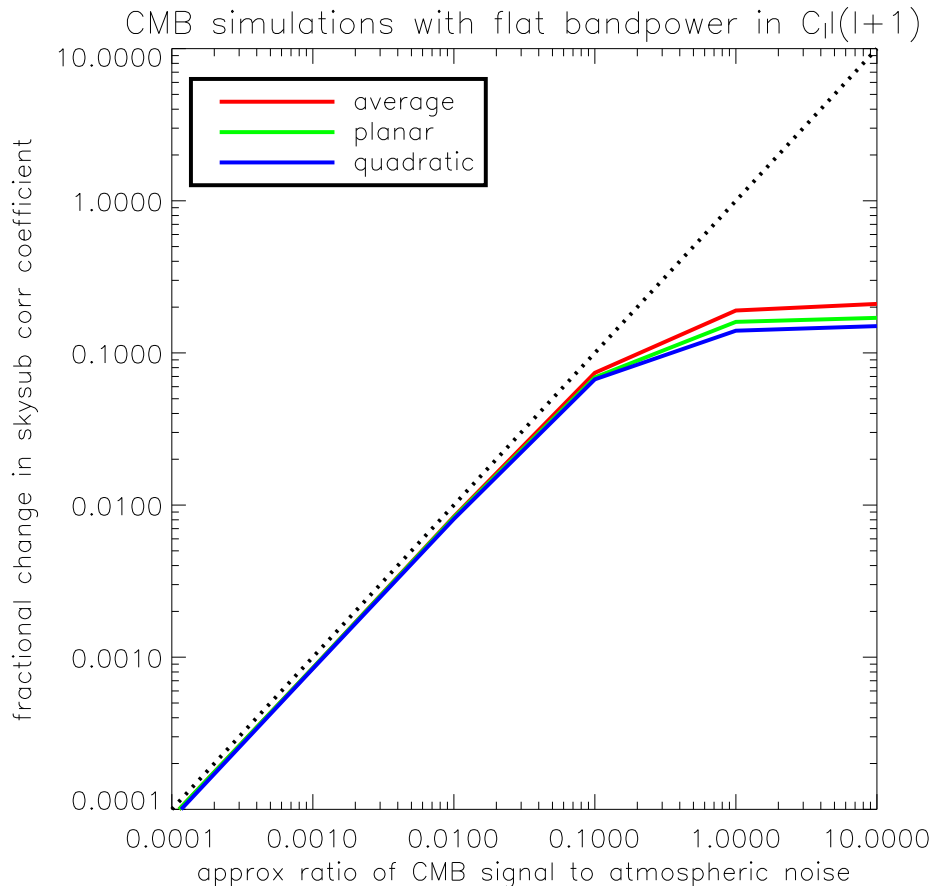


Figure E.1: Plot of the data in Table E.1.

$C_{\ell}(\ell+1)$	approx. S/A	Δc_{ave}	Δc_{planar}	$\Delta c_{quadratic}$
$5 \times 10^1 \mu K^2$	1×10^{-4}	0.89×10^{-4}	0.89×10^{-4}	0.86×10^{-4}
$5 \times 10^3 \mu K^2$	1×10^{-3}	0.85×10^{-3}	0.85×10^{-3}	0.84×10^{-3}
$5 \times 10^5 \mu K^2$	1×10^{-2}	0.84×10^{-2}	0.83×10^{-2}	0.81×10^{-2}
$5 \times 10^7 \mu K^2$	1×10^{-1}	0.74×10^{-1}	0.69×10^{-1}	0.67×10^{-1}
$5 \times 10^9 \mu K^2$	1×10^0	0.19×10^0	0.16×10^0	0.14×10^0
$5 \times 10^{11} \mu K^2$	1×10^1	0.021×10^1	0.017×10^1	0.015×10^1

Table E.1: The median fractional change in the atmospheric noise subtraction correlation coefficient for each of the three atmospheric noise removal algorithms (average, planar, and quadratic) when simulated CMB realizations of six different amplitudes were added to the data. The first column gives the flat band power of the CMB realization and the second column gives the approximate ratio of the CMB signal to the atmospheric signal. Notice that at small values of S/A , the median fractional change in the correlation coefficient is of the same order of magnitude as S/A , as predicted by the theory.

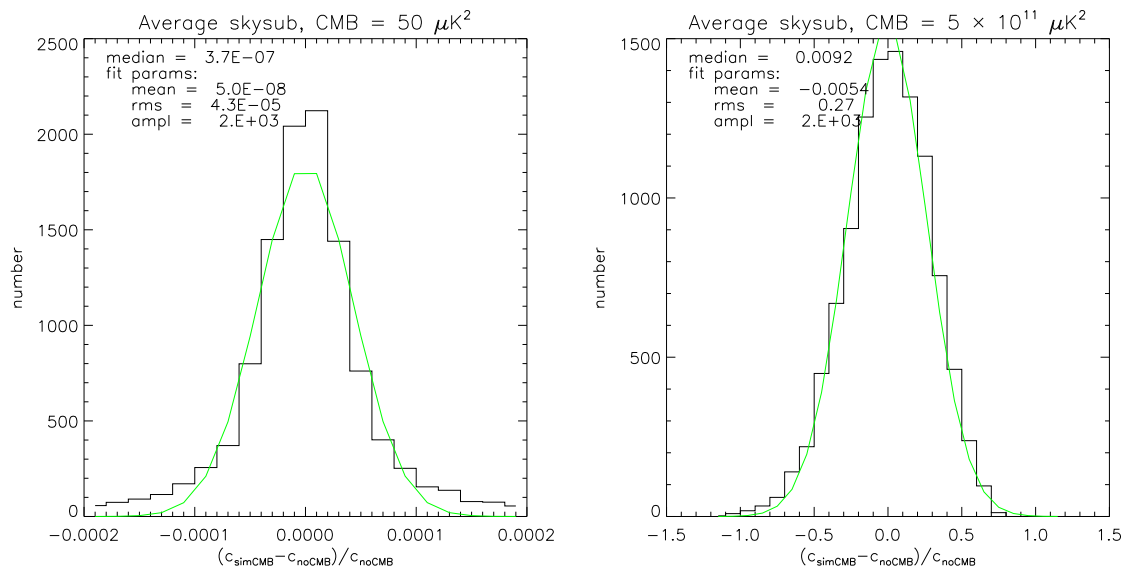


Figure E.2: Histograms of the distribution of $(c_{i,simCMB} - c_{i,noCMB})/c_{i,noCMB}$ for two amplitudes of CMB realizations. The histogram on the left shows the distribution for a flat CMB band power of $50 \mu K^2_{CMB}$ ($S/A \simeq 10^{-4}$), while the histogram on the right shows the distribution for a flat CMB band power of $5 \times 10^{11} \mu K^2_{CMB}$ ($S/A \simeq 10$). In both cases the mean of the distribution is consistent with 0, indicating that there is no systematic difference between the value of $c_{i,simCMB}$ and $c_{i,noCMB}$.

by $c_{i,simCMB}$ fluctuating around the value of $c_{i,noCMB}$. The result is that the distribution is consistent with zero for any value of S/A that we tried (see Figure E.2). This is due to the fact that the SZE-induced CMB power spectrum and the atmosphere are both beam-filling sources with steeply falling spectra at high spatial frequency. This means that on average, the CMB signal and/or the atmosphere will produce the same value of c_i .

Additionally, it should be noted that any primary CMB signal observed by Bolocam will also be a beam-filling signal that falls steeply at high frequency, since the largest angular scales probed by Bolocam correspond to $\ell \simeq 1500$. Actually, the primary CMB power spectrum falls much more steeply than the SZE-induced CMB power spectrum, which means it will be even more similar to the atmospheric signal. Therefore, the small amount of primary CMB signal in the time-stream data will not have a large effect on the c_i s we determine to remove atmospheric noise.

We have shown that the deviations in c_i are of the same magnitude as S/A , which means they will be very small for our expected astronomical signals. But, it is also important to know if the effective transfer function of our atmospheric noise removal algorithms is affected by changes in the amplitude of the astronomical signal. To test this, we computed a transfer

function for each observation according to

$$Xfer = \frac{|M_{diff}|^2}{|M_{CMB}|^2}, \quad (\text{E.12})$$

where M denotes the two-dimensional Fourier transform of the map m . The results are given in Figure E.3. We find that the transfer function is not affected by the amplitude of the CMB signal, even for $S/A \simeq 10$. Again, this is because the spectrum of the CMB signal is very similar to the spectrum of the atmospheric signal, and any combination of the two signals will produce the same value of c_i on average. Therefore, a transfer function computed for a given signal amplitude will be valid for any signal amplitude.

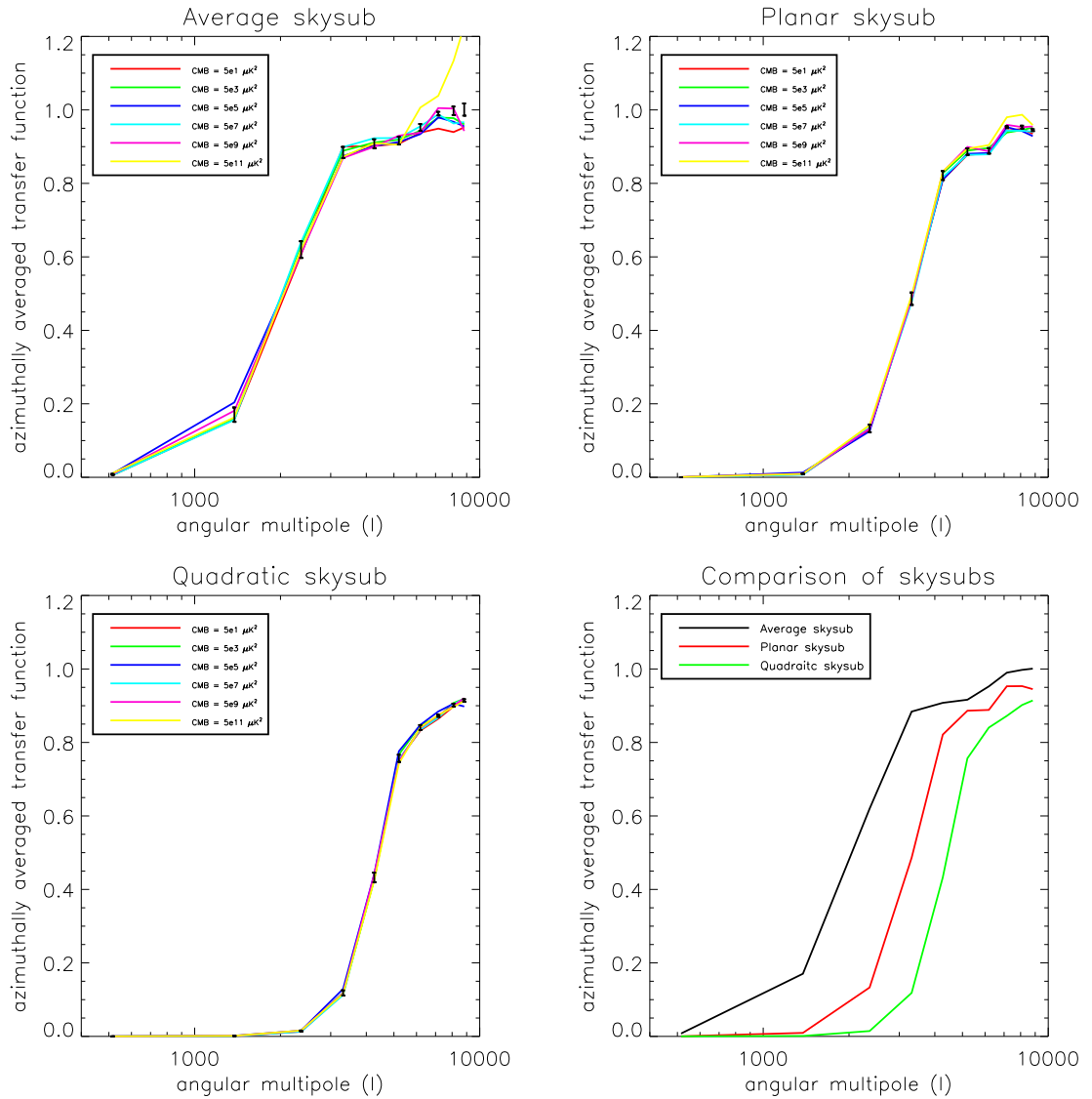


Figure E.3: Plots of the transfer function of the Bolocam software pipeline. The plots in the upper left, upper right, and lower left show the transfer function when average sky subtraction, planar sky subtraction, or quadratic sky subtraction is applied to data with a CMB realization added to the time-stream. Six different amplitudes of CMB realizations were tested, with the results of each shown in the plots. The black error bars show the average error for that bin for a single CMB amplitude. Note that the transfer functions at different CMB amplitudes are consistent with each other given the uncertainties, indicating the transfer function is independent of signal amplitude. For reference, the plot on the lower right shows the average transfer function for each of the three cleaning methods.

Appendix F Algorithm for Calculating An Excess Map Variance

The goal of our analysis is to determine the amplitude of the power spectrum due to emission from astronomical sources¹ by measuring an excess variance in the maps of the science fields. This excess variance is the difference between the actual variance of the map, and the expected variance of the map based on measurements of the noise in the Bolocam system and knowledge of the expected signal spectrum. Therefore, we need measurements of the following quantities:

- $x_{\vec{\nu}}$: The measured PSD of the science field map at pixel $\vec{\nu}$ in units of μK_{CMB}^2 . $\vec{\nu}$ is a two-dimensional value, $\vec{\nu} = (\nu_{RA}, \nu_{dec})$, describing a location in the spatial Fourier transform of the map, and has units of 1/radians.
- $\mathcal{P}_{\vec{\nu}}$: The predicted PSD of the science field map at pixel $\vec{\nu}$ in the absence of the desired astronomical signal. $\mathcal{P}_{\vec{\nu}}$ is estimated from jackknife realizations, along with the PSDs of unwanted astronomical sources in the map (i.e., primary CMB anisotropies).
- $\mathcal{S}_{\vec{\nu}}$: The spectral profile of the expected astronomical signal. For a flat band power $\mathcal{S}_{\vec{\nu}} = 2\pi/(\ell(\ell + 1))$, where the angular multipole ℓ is described by $\ell = 2\pi|\vec{\nu}|$.
- $B_{\vec{\nu}}$: The peak-normalized square of the $\vec{\nu}$ -space Bolocam beam profile. Since astronomical signals are attenuated by the beam, $B_{\vec{\nu}}$ acts like a window function or filter. Note that the broadening of the beam in map-space due to our pointing uncertainty is included in $B_{\vec{\nu}}$.
- $W_{\vec{\nu}}$: The effective transfer function, or window function, of the data processing applied to the time-stream data. Analogous to $B_{\vec{\nu}}$, $W_{\vec{\nu}}$ describes how much astronomical signal is attenuated.

With this convention, the expected PSD of the map can be described by

$$\langle x_{\vec{\nu}} \rangle = \mathcal{P}_{\vec{\nu}} + AS_{\vec{\nu}}B_{\vec{\nu}}W_{\vec{\nu}}, \quad (\text{F.1})$$

¹This power spectrum is thought to be dominated by primary and SZE-induced anisotropies in the CMB. See Section 5.7.3.

where A is the amplitude of the CMB variance, in μK_{CMB}^2 .

The CMB amplitude can be estimated by determining what value of A maximizes the likelihood of the measured map PSD, $x_{\vec{\nu}}$. Therefore, we need to determine the probability density function (PDF) describing $x_{\vec{\nu}}$, given A . First, note that

$$|x_{\vec{\nu}}| = |\alpha + i\beta|^2, \quad (\text{F.2})$$

where α is the real part of the Fourier transform of the science field map and β is the imaginary part of the Fourier transform of the science field map. If we assume that the noise properties of the map are Gaussian², then the PDFs for α and β are the same and are given by

$$f(\alpha) = \frac{1}{\sqrt{2\pi\sigma^2}} e^{-\alpha^2/2\sigma^2} \quad \text{and} \quad f(\beta) = \frac{1}{\sqrt{2\pi\sigma^2}} e^{-\beta^2/2\sigma^2}, \quad (\text{F.3})$$

where $\sigma^2 = \langle x_{\vec{\nu}} \rangle / 2$. Next, after a change of variables to $\alpha = r \cos(\theta)$ and $\beta = r \sin(\theta)$, the PDF in Equation F.3 becomes

$$f(r, \theta) = \frac{1}{2\pi\sigma^2} r e^{-r^2/2\sigma^2}. \quad (\text{F.4})$$

Since the θ dependence of $f(r, \theta)$ is trivial, we can reduce the above PDF to $f(r) = 2\pi f(r, \theta)$, with

$$f(r) = \frac{r}{\sigma^2} e^{-r^2/2\sigma^2}. \quad (\text{F.5})$$

Finally, after one more change of variables using the relation $x_{\vec{\nu}} = r^2$, we find that the PDF for $x_{\vec{\nu}}$ is equal to

$$f(x_{\vec{\nu}}) = \frac{1}{2\sigma^2} e^{-x_{\vec{\nu}}/2\sigma^2}, \quad (\text{F.6})$$

where the factor of r has been replaced by $1/2$ due to the change in the differential element. Equation F.6 can be written in terms of our measured parameters as

$$f(x_{\vec{\nu}}|A) = \frac{1}{\mathcal{P}_{\vec{\nu}} + AS_{\vec{\nu}}B_{\vec{\nu}}W_{\vec{\nu}}} \exp\left(\frac{-x_{\vec{\nu}}}{\mathcal{P}_{\vec{\nu}} + AS_{\vec{\nu}}B_{\vec{\nu}}W_{\vec{\nu}}}\right) \quad (\text{F.7})$$

²This is an extremely good assumption. See Figure 5.11.

using Equation F.1. Note that we have made use of the fact that $2\sigma^2 = \langle x_{\vec{\nu}} \rangle = \mathcal{P}_{\vec{\nu}} + AS_{\vec{\nu}}B_{\vec{\nu}}W_{\vec{\nu}}$ to go from Equation F.6 to Equation F.7.

The next step is to calculate a likelihood function, \mathcal{L} , from Equation F.7 by multiplying $f(x_{\vec{\nu}}|A)$ over all of the $\vec{\nu}$ -space pixels. This product can be turned into a sum by taking the logarithm of \mathcal{L} , with

$$\log(\mathcal{L}) = \sum_{\vec{\nu}} \left(-\log(\mathcal{P}_{\vec{\nu}} + AS_{\vec{\nu}}B_{\vec{\nu}}W_{\vec{\nu}}) - \frac{x_{\vec{\nu}}}{\mathcal{P}_{\vec{\nu}} + AS_{\vec{\nu}}B_{\vec{\nu}}W_{\vec{\nu}}} \right). \quad (\text{F.8})$$

Then, the most probable value of the CMB amplitude for our measured map PSD can be determined by maximizing $\log(\mathcal{L})$ with respect to A . In practice, we maximize Equation F.8 by evaluating $\log(\mathcal{L})$ at a range of values for A . Since the number of $\vec{\nu}$ -space pixels is $\lesssim 10000$, the computational time required to evaluate $\log(\mathcal{L})$ at each value of A is minimal, which means that we can determine the best fit value of A to almost any desired precision using this numerical method.

However, it is also instructive to analytically approximate the value of A that maximizes Equation F.8. To start, we take the derivative of $\log(\mathcal{L})$ with respect to A , yielding

$$\left. \frac{\partial \log(\mathcal{L})}{\partial A} \right|_{A=\hat{A}} = \sum_{\vec{\nu}} \frac{\Theta_{\vec{\nu}}}{(\mathcal{P}_{\vec{\nu}} + A\Theta_{\vec{\nu}})^2} (x_{\vec{\nu}} - \mathcal{P}_{\vec{\nu}} - A\Theta_{\vec{\nu}}) \Big|_{A=\hat{A}} = 0, \quad (\text{F.9})$$

where $\Theta_{\vec{\nu}} = S_{\vec{\nu}}B_{\vec{\nu}}W_{\vec{\nu}}$ and \hat{A} is the best fit value of A . For any given $\vec{\nu}$ -space pixel, $\mathcal{P}_{\vec{\nu}} \gg A\Theta_{\vec{\nu}}$ for any physically reasonable value of A . Therefore, we can simplify Equation F.9 to

$$\sum_{\vec{\nu}} \frac{\Theta_{\vec{\nu}}}{\mathcal{P}_{\vec{\nu}}^2} \left(1 - \frac{2A\Theta_{\vec{\nu}}}{\mathcal{P}_{\vec{\nu}}} + \mathcal{O}\left(\frac{A^2\Theta_{\vec{\nu}}^2}{\mathcal{P}_{\vec{\nu}}^2}\right) \right) (x_{\vec{\nu}} - \mathcal{P}_{\vec{\nu}} - A\Theta_{\vec{\nu}}) \Big|_{A=\hat{A}} \simeq 0 \quad (\text{F.10})$$

by making some approximations. If we rearrange some terms, and again keep only the lowest order terms in $A\Theta_{\vec{\nu}}/\mathcal{P}_{\vec{\nu}}$, then we find

$$\hat{A} \simeq \frac{\sum_{\vec{\nu}} \frac{\Theta_{\vec{\nu}}^2}{\mathcal{P}_{\vec{\nu}}^2} \left(\frac{x_{\vec{\nu}} - \mathcal{P}_{\vec{\nu}}}{\Theta_{\vec{\nu}}} \right)}{\sum_{\vec{\nu}} \frac{\Theta_{\vec{\nu}}^2}{\mathcal{P}_{\vec{\nu}}^2} \left(\frac{2x_{\vec{\nu}} - \mathcal{P}_{\vec{\nu}}}{\mathcal{P}_{\vec{\nu}}} \right)}. \quad (\text{F.11})$$

Finally, because $A\Theta_{\vec{v}} \ll \mathcal{P}_{\vec{v}}$, we can make the approximation that $\langle x_{\vec{v}} \rangle \simeq \mathcal{P}_{\vec{v}}$, which means that $\langle 2x_{\vec{v}} - \mathcal{P}_{\vec{v}} \rangle \simeq \mathcal{P}_{\vec{v}}$. With this approximation we find

$$\hat{A} \simeq \frac{\sum_{\vec{v}} \frac{\Theta_{\vec{v}}^2}{\mathcal{P}_{\vec{v}}^2} \left(\frac{x_{\vec{v}} - \mathcal{P}_{\vec{v}}}{\Theta_{\vec{v}}} \right)}{\sum_{\vec{v}} \frac{\Theta_{\vec{v}}^2}{\mathcal{P}_{\vec{v}}^2}}. \quad (\text{F.12})$$

To understand this result, consider that for a single \vec{v} -space pixel the best estimate of A is $(x_{\vec{v}} - \mathcal{P}_{\vec{v}})/\Theta_{\vec{v}}$. Therefore, Equation F.12 determines the weighted mean of A over all pixels, assuming that the uncertainty on the value of A for each \vec{v} -space pixel is proportional to $\mathcal{P}_{\vec{v}}/\Theta_{\vec{v}}$, which is a reasonable assumption. This means that the variance on \hat{A} implied by Equation F.12 is proportional to

$$\sigma_{\hat{A}}^2 \propto \frac{1}{\sum_{\vec{v}} \frac{\Theta_{\vec{v}}^2}{\mathcal{P}_{\vec{v}}^2}}. \quad (\text{F.13})$$